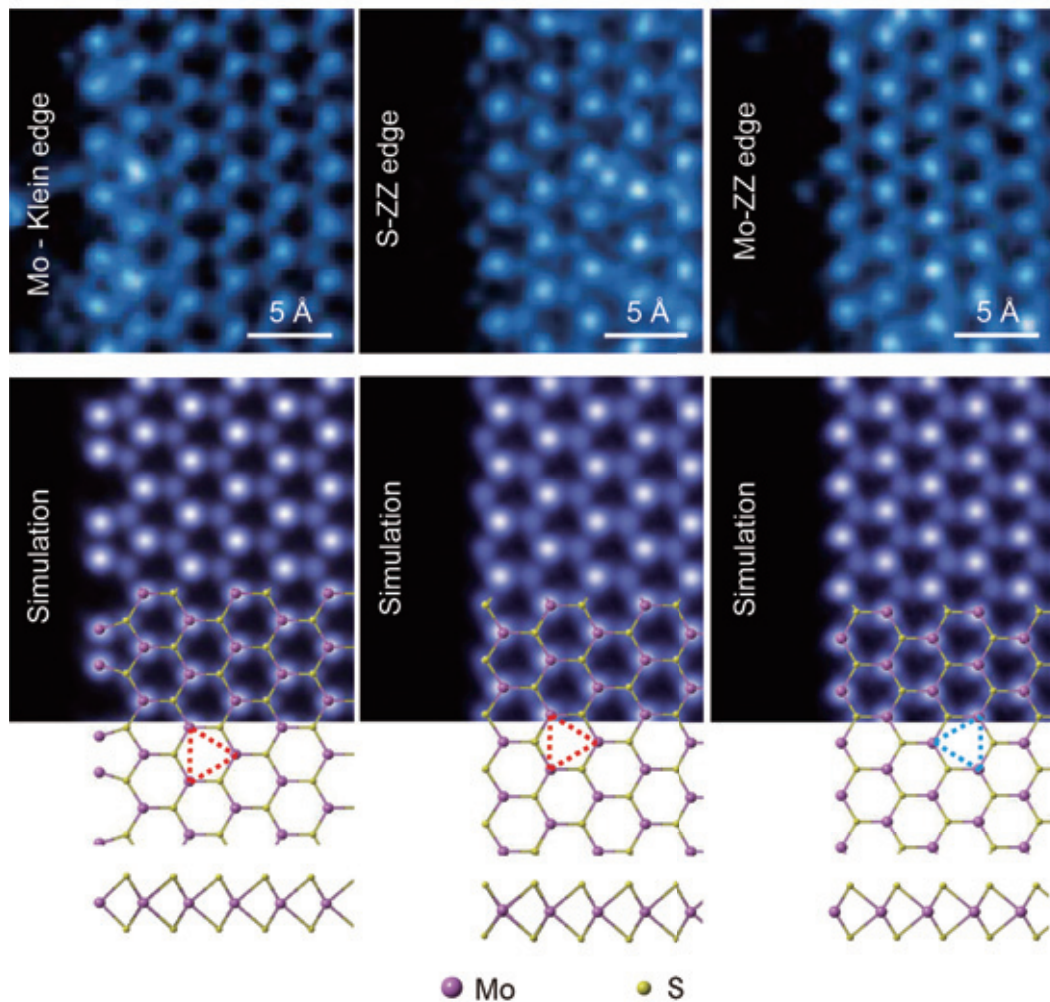




## JEOL 70th Anniversary Issue

### Topological Edges in MoS<sub>2</sub>





**Angus I Kirkland**

Professor of Materials, Oxford University  
Science Director, Electron Physical Science Imaging Centre, Diamond Lightsource Ltd.  
President, The International Federation of Societies for Microscopy

## **Congratulatory Message for the 70<sup>th</sup> Anniversary of JEOL**

It gives me great pleasure to write to congratulate JEOL on the occasion of their 70<sup>th</sup> anniversary.

Over the last 70 years, electron microscopy in its many forms has changed beyond recognition. The first JEOL instrument, the DA1 was delivered to the Mitsubishi Chemical company in 1947 with a resolution of approximately 5 nm at 50 kV. The latest generation of aberration corrected instruments installed at Oxford and at other major laboratories around the globe have a resolution two orders of magnitude higher and operate between 30 and 300 kV. Of course costs have risen but much more slowly than resolution has improved and, factoring for inflation, shows that today's instruments are also better value for money than those of 1947!

Alongside these substantial advances in electron optical instrumentation, JEOL have themselves grown to a major international corporation employing over 3000 staff, with multiple subsidiaries on every continent except the Arctic and Antarctica. They now manufacture a wide range of electron optical and analytical instruments together with precision fabrication and characterisation tools used in a variety of industries.

Science in the 21<sup>st</sup> century requires a close collaboration, based on mutual trust and respect between instrument manufacturers and developers, and academic and industrial research laboratories. JEOL have fostered this symbiotic relationship through a number of large scale research collaborations. In the UK they have been a key partner in the David Cockayne Centre at Oxford, the National electron Physical Sciences Imaging centre at Diamond Lightsource, the York Nanoscience Centre and the Centre for Ultrastructure Imaging at Kings College London. Most recently they have actively engaged in the design and construction of novel instruments for the Rosalind Franklin Centre to be completed in 2020. However, JEOL's scientific engagement with the research community extends beyond the supply of state-of-the-art instrumentation. They have an outstanding team of engineers and applications specialists who not only ensure that the instruments operate at peak performance throughout their lives but who also provide training and education to research students and scientists thus contributing to a lasting legacy for the electron microscopy community.

JEOL can be justifiably proud of their technology and their contributions to science. They have an international reputation as innovators in instrument design and as valued collaborators.

I wish JEOL well on the occasion of this important historical landmark and I look forward to many more years of fruitful science using JEOL instruments.



**Miguel Jose Yacaman**

Lutcher Brown Endowed Professor  
Physics Department University of Texas at San Antonio

## **Congratulatory Message for the 70<sup>th</sup> Anniversary of JEOL**

In the early seventies I was working in my PhD thesis and I spent time at the University of Warwick in the UK and had the chance to use a JEOL JEM-7 TEM. That was my first interaction with JEOL and will be the first of many more. The JEM-7 was a great instrument in which I obtained the most important results of my dissertation. In those years most of the microscope alignment was mostly mechanical and we spent a lot of time preparing the machine for obtaining data. My previous experience with the Elmiskop1 was kind of painful. It was a fantastic machine but very difficult to align. The JEM-7 included a device for electric alignment of the lenses. Since my scholarship was running out I needed to complete my experiments fast enough and I was able to do it because the improvements on the operation.

In the late seventies the National University of Mexico decided to purchase 6 microscopes to push the biological and materials research. JEOL won the bid and a new TEM JEM-100C ended on my lab. That machine had an amazing resolution and was friendly to use. It became the instrument in which many young scientists were trained. Then along my career I had many other JEOL machines including among others, the JEM-100CX in which nanodiffraction was possible for the first time, The JEOL JEM-4000EX (which became a classical high resolution Machine), the Field emission TEM JEM-2010F and finally the JEM-ARM200F which incorporated probe aberration correction. My lab in the University of Texas at San Antonio was the first one to be installed in USA. Other manufacturers told me about the great risk that I was taking in a microscope that was not even in demo. However I knew of the great quality values of the company and I trusted them. The result was amazing and I was thrilled when we got into the Pico meter resolution.

I have seen JEOL grow as my career advanced and clearly have demonstrated to be always to be a company always producing new technology and supporting the researchers to obtain important discoveries.

Congratulations to JEOL in its 70-anniversary and which the best for the future many new surprises will come out of the JEOL hat.





**Gon-emon Kurihara**

Chairman and CEO

JEOL Ltd.

## **Evolving in the 70<sup>th</sup> Year**

In May 1949, not long after the end of World War II, Japan Electron Optics Laboratory (forerunner of JEOL) was founded for developing and manufacturing electron microscopes. Since then, owing to great support by many people around the world, JEOL has marked its 70<sup>th</sup> anniversary this year. Based on “Creativity” and “Research and Development” which our company philosophy states, JEOL has continued to contribute to the progress of Science and Human Society. Nowadays, JEOL instruments are used at universities and laboratories in as many as more than 130 countries, and we are highly regarded as a true global enterprise. I am deeply aware that our long-time corporate development is primarily due to a great number of persons who have continually supported and guided us. On this occasion, I would like to express my heartfelt gratitude to all of them.

Analytical instruments and scientific instruments are essential tools for development of scientific technology and manufacturing industries. I strongly recognize that the responsibility of JEOL is significantly high under a circumstance where every country is aimed at becoming a science-oriented nation. JEOL is now pushing forward with the YOKOGUSHI (cross-sectional collaboration) strategy, which utilizes its strength of diversified products lineup of high-end instruments, including electron microscopes, nuclear magnetic resonance spectrometers, mass spectrometers and surface analysis instruments. The YOKOGUSHI strategy aims to supply customers with instruments as well as applications and services, so that the customers can use our variety of instruments in a multi-faceted manner for obtaining their research accomplishments timely and accurately, in the midst of the recent historical background where research and development is increasingly advanced. In this context, we are providing *JEOL News* to users, as well as attending and organizing various exhibitions, seminars and conferences worldwide.

Japan has entered into a new “Reiwa Era” from “Heisei Era” in the year of our 70<sup>th</sup> anniversary. Positioning this memorable year as our turning point, we are announcing the key concept, “Evolving in the 70<sup>th</sup> Year”. That is, on the basis of our core technologies cultivated in the academia market, JEOL will expand its instrument business and service business to the bigger markets, such as semiconductor & industrial equipment and medical equipment. We are determined to continually make hard efforts to serve to all of you. Finally, I sincerely hope for your candid evaluations and warm assistance.

A handwritten signature in black ink, appearing to read "G. Kurihara". The signature is fluid and cursive, written in a professional style.



**Izumi Oi**

President and COO  
JEOL Ltd.

## **Celebrating JEOL's 70<sup>th</sup> Anniversary**

JEOL celebrated its 70<sup>th</sup> anniversary in May this year. Since its founding, JEOL has dedicated its resources to the development of state-of-the-art scientific/metrology instruments under the mission: Contributing to the progress in both science and society. In the past 70 years, we have received generous support from countless individuals and corporations including users, shareholders, and business partners. We are truly grateful for their guidance and support.

The scientific and technical infrastructure JEOL has provided throughout the years, such as electron microscope and NMR, not only serves as fundamental technology in creating new industries but also contributes to the SDGs, the goals set by the UN for a global community. This demonstrates that JEOL will continue to play an increasingly important role in society.

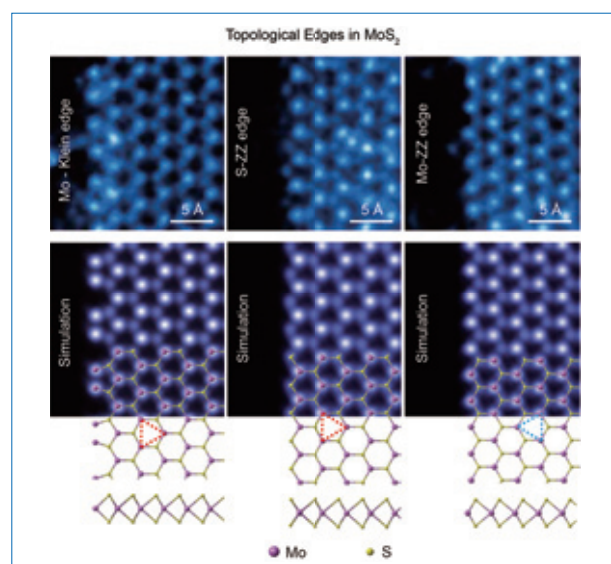
Under these circumstances, JEOL has launched a new mid-term business plan, Triangle Plan 2022, this fiscal year. Using "Evolving in the 70<sup>th</sup> Year," as a keyword, the plan intends to strengthen our advanced R&D capability in analysis/metrology as our core technology, and to utilize it actively to explore growing markets such as semiconductor fabrication, industrial equipment, biological and medical equipment to accelerate our business growth. JEOL's core technology has the potential for significant growth and development. We will seek to strengthen it further under your continued guidance and support.

We are also aware that superior customer support is equally important as sophisticated instruments. We review users' applications and research objectives to design valuable services, and provide individual users with total solutions unique to JEOL.

Through our high performance products and solutions, we are committed to contributing to the advance of science and society. We look forward to your continued patronage in the future.

A handwritten signature in black ink, appearing to read "I. Oi", written in a cursive style.

- Atomic-Resolution Imaging and Spectroscopy on Materials of Various Dimensions by Aberration-Corrected Scanning Transmission Electron Microscopy .....6  
Mengsha Li, Shoucong Ning, Changjian Li, Jiadong Dan, Xiaoxu Zhao, Chunhua Tang, Stephen J. Pennycook  
Department of Materials Science and Engineering, National University of Singapore
- Probe Corrected STEM Structural Imaging and Chemical Analysis of Materials at Atomic Resolution .....15  
E. J. Olivier, J. H. Neethling and J. H. O'Connell Centre for HRTEM, Nelson Mandela University
- Analytical SEM and TEM: Applications in Product-related Material Development.....21  
Jörg Kaspar Fraunhofer IWS Dresden, Germany
- Practical Solutions in Electron Beam Lithography with the JBX-9500FS and the JBX-6300FS .....28  
D. M. Tennant, A. Banerjee, C. Treichler and A. R. Bleier Cornell NanoScale Science and Technology Facility
- Development of New Operando Measurement System by Combining Reaction-Science High-Voltage Electron Microscopy and Quadrupole Mass Spectrometry .....35  
Shunsuke Muto<sup>1,2,4</sup>, Shigeo Arai<sup>2</sup>, Testuo Higuchi<sup>3</sup>, Shigemasa Ohta<sup>4</sup>, and Koji Orita<sup>5</sup>  
<sup>1</sup>Advanced Measurement Technology Center, Institute of Materials and Systems for Sustainability, Nagoya University  
<sup>2</sup>High-Voltage Electron Microscopy Laboratory, Institute of Materials and Systems for Sustainability, Nagoya University  
<sup>3</sup>JEOL Ltd. <sup>4</sup>JEOL USA, Inc. <sup>5</sup>Graduate School of Engineering, Nagoya University
- Development of Low-Voltage TEM/STEM for Single Carbon Atom Analysis under the 3C Project .....40  
Kazu Suenaga National Institute of Advanced Industrial Science and Technology (AIST)
- High-Field DNP Using Closed-Cycle Helium MAS System .....46  
Yoh Matsuki and Toshimichi Fujiwara Institute for Protein Research, Osaka University
- Application of "operando-ESR" to Organic Electronics Materials .....53  
Junto Tsurumi NIMS  
Shun Watanabe Department of Advanced Materials Science, Graduate School of Frontier Sciences, The University of Tokyo,  
National Institute of Advanced Industrial Science and Technology (AIST)-University of Tokyo Advanced  
Operando-Measurement Technology Open Innovation Laboratory (OPERANDO-OIL), AIST and JST, PRESTO\*
- YOKOGUSHI (Multifaceted) Analysis of Biomimetic Materials by Using PyGC/MS and XPS  
– Characterization of Biomimetic Lacquer – .....61  
Noriyasu Niimura Application Management Department, JEOL Ltd.
- Development of Cryo High-Resolution Transmission Electron Microscope CRYO ARM™ 300,  
Equipped with Cold Field Emission Gun for Structural Biology .....68  
Sohei Motoki EM Business Unit, JEOL Ltd.
- Observation and Analysis at Low Accelerating Voltage Using Ultra High Resolution FE-SEM JSM-7900F .....72  
Hironobu Niimi, Yusuke Sakuda, Natsuko Asano, Shunsuke Asahina EP Business Unit, JEOL Ltd.
- Development of an Integrated Analysis Method for the JMS-T200GC High Mass-Resolution  
GC-TOFMS by Electron Ionization and Soft Ionization Methods .....83  
Masaaki Ubukata and Yoshihisa Ueda MS Business Unit, JEOL Ltd.
- Development of a Gas Chromatograph Triple Quadrupole Mass Spectrometer JMS-TQ4000GC .....90  
Kiyotaka Konuma MS Business Unit, JEOL Ltd.



### Cover micrograph

ADF-STEM images of various different edge structures found in nanoporous MoS<sub>2</sub> (upper panels) with corresponding simulated images (lower panels) with overlaid density functional theory (DFT) optimized atomic structures (see Fig. 4 on page 9).

# Atomic-Resolution Imaging and Spectroscopy on Materials of Various Dimensions by Aberration-Corrected Scanning Transmission Electron Microscopy

Mengsha Li, Shoucong Ning, Changjian Li, Jiadong Dan, Xiaoxu Zhao, Chunhua Tang, Stephen J. Pennycook

Department of Materials Science and Engineering, National University of Singapore

The modern aberration corrected scanning transmission electron microscope (STEM) can dramatically accelerate the development of novel functional nanomaterials, the properties of which are determined by their atomic scale compositions and structures. The combination of a field emission gun and fifth order aberration corrector pushes the spatial resolution down to the sub-Ångström level, making atomic scale structural imaging practically a routine operation. Furthermore, retaining the sub-Ångström resolution at low electron acceleration voltage greatly broadens the application of STEM due to the reduction of beam damage, especially with two-dimensional materials. More recently, the combination of STEM optical depth sectioning and sophisticated STEM simulation makes possible the atomic scale three-dimensional imaging of defects in crystalline materials. Together with enhanced spectrometer collection efficiency and energy resolution, atomic scale chemical information can simultaneously be unveiled *via* spectrum imaging. In this paper, several recent materials research advances are presented, utilizing the JEOL JEM-ARM200F aberration corrected electron microscope installed in the National University of Singapore. The importance and impact of aberration corrected STEM imaging is very clearly demonstrated by these examples from different classes of functional materials with different dimensionalities.

## Introduction

On the occasion of the 70<sup>th</sup> birthday of the Japan Electron Optics Laboratory Company (JEOL), perhaps a brief history can bring perspective to the remarkable performance of the modern microscope column, having capabilities which not very long ago would have been just a dream (for a more extensive history see [1]). The first prototype of a microscope using a beam of electrons was invented by Max Knoll and Ernst Ruska in 1932, initiating the field of transmission electron microscopy (TEM) for which Ruska later received the Nobel prize [2, 3]. A few years later, in 1935, Knoll produced the first scanning electron microscope (SEM) [4], and shortly after that Manfred Von Ardenne combined the features of both by developing the first scanning transmission electron microscope (STEM) [5, 6]. He fully realized the advantage of the STEM in having no imaging lenses after the sample, meaning the image would not suffer from chromatic aberration as in the Ruska TEM. However, he

soon abandoned the STEM due to the inability to get enough current into the probe to provide a useable image, taking up the Ruska TEM concept instead [7, 8]. Thus the development of the electron microscope lay solely in the domain of the TEM for several decades. Rapid development took place in many countries, including Japan, and the founding of the Japan Electron Optics Laboratory Company (JEOL) in 1949. With increasing resolution, the first lattice images were achieved in 1956 [9]. Three years later, Richard Feynman put out the challenge to improve the resolution of the electron microscope one hundred times [10], and although we are not there yet, we have essentially achieved his goal to be able to just look at an image and see where the atoms are. Primarily, it is the STEM that has brought Feynman's goal closest to reality, with its ability to provide atomic-resolution images that are incoherent in nature, and hence directly interpretable to a first approximation.

However, the STEM only became a viable form of microscope with the development of the cold field emission gun by Albert

Crewe in 1968 [11], and shortly afterwards the first images of individual heavy atoms were obtained [12, 13]. Crewe and his team in Chicago also introduced the annular dark field (ADF) detector, simultaneous electron energy loss spectroscopy (EELS), and the term Z-contrast was coined, referring to a ratio image between the elastic (ADF) and inelastic (EELS) signals, which at least for single atoms is proportional to atomic number Z [14]. But it was much later before a commercial STEM achieved atomic resolution. John Cowley published the first STEM bright field image of a gold crystal resolving 2.04 Å fringes using a VG Microscopes HB5 [15]. Later he published corresponding STEM bright field and ADF images of  $\text{Ti}_2\text{Nb}_{10}\text{O}_{29}$ , commenting on the enhanced resolution of the ADF image but not on any incoherent characteristics such as the thickness and focus dependence of the image [16]. This was left to the Oak Ridge group, building on work at the Cavendish Laboratory by Mike Treacy and Archie Howie who were investigating the high angle annular detector for improving the visibility of catalyst particles [17, 18]. With the installation of a VG Microscopes HB501UX in Oak Ridge National Laboratory, equipped with a high-resolution pole piece, images of high-temperature superconductors and Si did indeed show the focus and thickness characteristics of an incoherent image, and over the next few years the detailed reasons were elucidated [19-24]. Atomic resolution EELS was also achieved with VG Microscopes columns, both in a compositional profile and in variation of fine structure [25,26]. In 1993, a 300 kV VG Microscopes machine was installed at Oak Ridge, the HB603U, allowing resolution of the “dumbbells” in the  $\langle 110 \rangle$  projection of semiconductors [27-29]. Then in 1996, VG Microscopes ceased business, and it was the JEOL company who stepped in to fulfil an order for a high-resolution STEM from Nigel Browning in Chicago with a JEM-2010F [30].

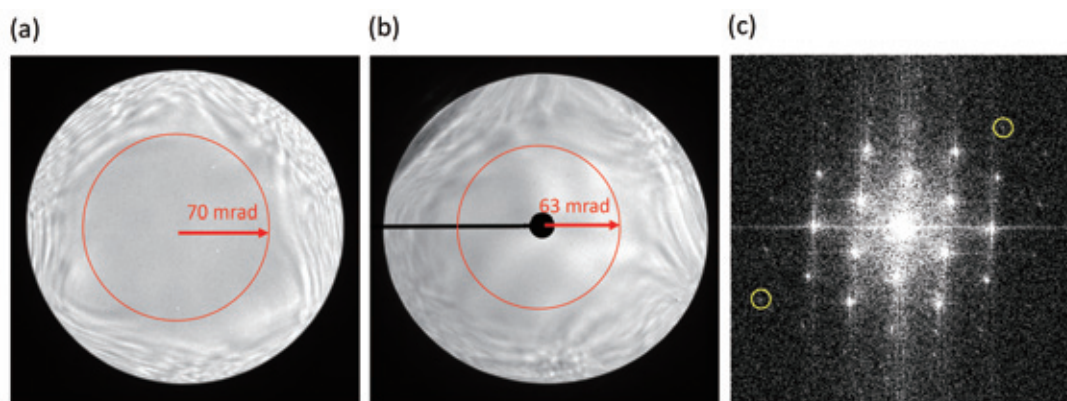
Nevertheless, STEM images remained rather noisy compared to the high-resolution lattice images obtained in the conventional TEM. It was the development of aberration correction for the STEM, led by Ondrej Krivanek, that largely overcame the noise problem and enabled the STEM to achieve sub-Ångström resolution for the first time [31, 32], surpassing the highest resolution achieved by the TEM, and nicely demonstrating the enhanced resolution that incoherent imaging should allow compared to coherent imaging. In addition, aberration correction improved EELS sensitivity allowing single atoms to be identified within individual atomic columns of a crystal [33], and the first two-dimensional elemental mapping was achieved at atomic

resolution [34]. With the development of 5<sup>th</sup> order correctors, the STEM resolution has pushed down to 0.5 Å and even below [35-37], and also atomic-level resolution has become feasible at low accelerating voltages [38]. The JEM-ARM200F installed in the National University of Singapore (NUS) in 2015 was the first to be supplied by JEOL with a CEOS 5<sup>th</sup> order corrector (named the Advanced STEM CORrector, or ASCOR). A prototype had been installed by CEOS on a similar machine at the Stuttgart Centre for Electron Microscopy and had demonstrated aberration correction to a 70 mrad semiangle [39]. JEOL kindly agreed to supply this configuration to NUS, equipped with a cold-field emission gun (CFEG) and ultra-high resolution (UHR) pole piece. The higher order geometrical aberrations can therefore be corrected while chromatic aberration is not too severe, allowing larger illumination convergence angles even at low accelerating voltages. **Figure 1**(a) and (b) show Ronchigrams of amorphous carbon films from the NUS system at 200 kV and 60 kV, respectively. Clearly, the “flat field” region, *i.e.* aberration free area, reaches to 70 mrad at 200 kV, and even maintains a 63 mrad semiangle at 60 kV. Most spectacular is the sub-Ångström resolution demonstrated at only 40 kV accelerating voltage. In Fig. 1(c), a fast Fourier Transform (FFT) of a raw high angle annular dark field (HAADF) STEM image (as shown in **Fig. 3**) shows information transfer to a spacing of 0.95 Å, indicating the sub-Ångström capability even at low accelerating voltage. Besides the lateral resolution, it is well known that large convergence angles also improve depth-resolution to the nm-scale [40-43]. Therefore, the advanced aberration-corrected (AC) STEM is a versatile tool to obtain atomic-resolution images and spectra of materials with different dimensions, from zero to three, as we demonstrate in the examples below.

### Zero-dimensional (0D) materials: Imaging single atoms in catalysts

Single-atom catalysts (SACs) represent one of the most promising developments in heterogeneous catalysis. The presence of clusters as small as single atoms was first demonstrated by STEM even before aberration correction [44], although the sensitivity is of course remarkably improved with AC-STEM [45]. Due to the unique electronic environment of a single atom bonded to a substrate, unique catalytic performance can be tuned, resulting in properties different from those of the same atoms in nanoparticle form, for a review see [46].

**Fig. 1**



Observed Ronchigrams of amorphous carbon films from the JEM-ARM200F equipped with a CFEG and ASCOR corrector at 200 kV (a) and 60 kV (b), respectively. Data courtesy Chunhua Tang. (c) The FFT image from the HAADF-STEM image of  $\text{MoSe}_2$  in Fig. 3 at 40 kV. The dots which are marked by yellow circles correspond to the 0.95 Å {300} (lower left) and 1.27 Å {210} (upper right) lattice spacings respectively. Data courtesy Jiadong Dan.

However, there are some key challenges when developing SACs. The most important one is how to realize and control the dispersion of single metal atoms on the substrates. Because aggregation of the single atoms will remove their unique electronic environment, the atomic resolution of AC-STEM gives us an opportunity to directly observe the dispersion of these single atoms. **Figure 2(a)** shows the raw HAADF-STEM image of Ni single atoms embedded in a carbon matrix observed at 200 kV accelerating voltage. It is obvious that the Ni single atoms are atomically dispersed on the matrix. The histograms extracted from seven single atoms are shown in Fig. 2(b), and each histogram is fitted with a Gaussian function. After the Gaussian fitting, the average full width at half maximum (FWHM) reveals the sub-Ångström probe size (0.6 Å) at the 200 kV accelerating voltage. Therefore, due to the efficient aberration correction, the atomic resolution AC-STEM becomes one of the most useful techniques for the study of SACs.

## Two-dimensional (2D) materials: Imaging defects in MoSe<sub>2</sub> and MoS<sub>2</sub>

The discovery of graphene opened the door to the whole family of two-dimensional (2D) materials [47, 48]. Their advantageous properties make them potential materials for many applications for example low-dimensional spintronic or valleytronic devices [49]. Defects, however, which are inevitably induced during the growth of these materials, can significantly affect device performance [50, 51]. Therefore, direct observation of these defects is critically important when developing 2D materials-based devices with specific desired properties. Although a high accelerating voltage provides high STEM image quality, it is above the threshold for knock-on damage in most 2D materials. To minimize knock-on damage, low-voltage AC-STEM is usually employed to investigate these kinds of materials at the atomic level. Nevertheless, ionization damage effects can still occur leading to the generation and agglomeration of vacancies, but such effects are often sufficiently slow to enable their detailed dynamics to be investigated [52-57]. A recent example of utilizing such processes for fabricating new materials is the

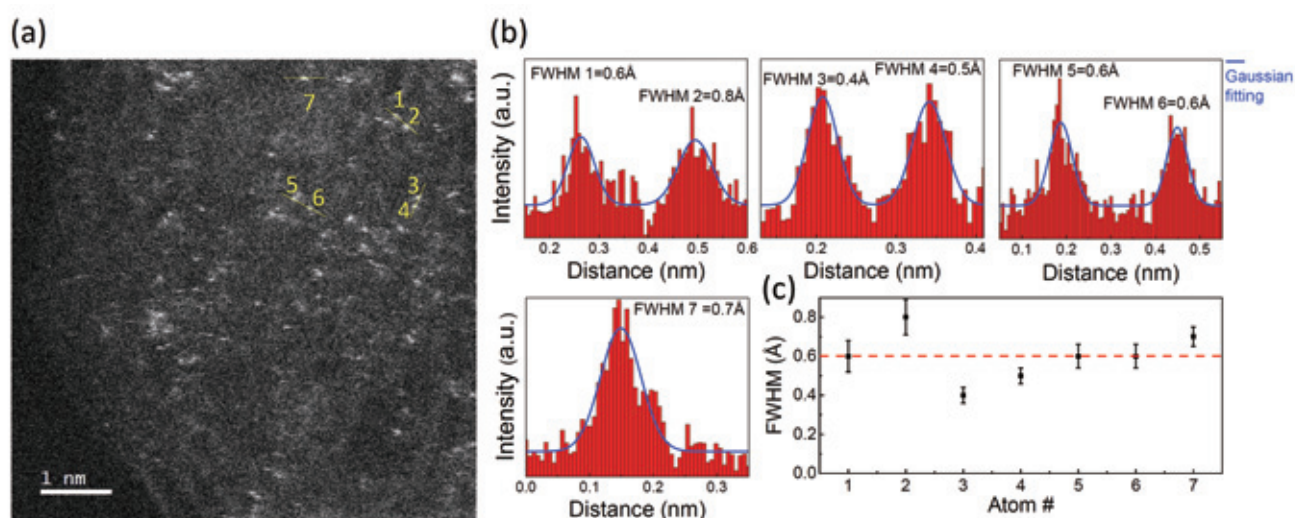
electron beam sputtering of Se atoms from MoSe<sub>2</sub> to create monolayer Mo metal [58].

Figure 3 shows a raw HAADF-STEM image of MoSe<sub>2</sub> at 40 kV. The dark regions are labeled by red triangles in Fig. 3(a), indicating double Se vacancies, while the orange dots clearly show single Se vacancies in Fig. 3(b). Apart from vacancies, defects such as edges and boundaries in 2D materials may have unpaired electrons which can also have a major influence on the interplay between materials structures and chemical properties. **Figure 4** shows four types of edges in monolayer nanoporous MoS<sub>2</sub> [59]. Besides conventional Mo- and S-terminated zigzag structures, two new edge structures, the distorted T (DT) edge (Fig. 4a) and the Mo-Klein edge (Fig. 4b), are observed. Here, 60 kV is used to slightly improve the image resolution and signal to noise ratio. These Mo-terminated edges not only impart unexpected magnetic properties to the nanoporous MoS<sub>2</sub>, but also lead to excellent activity for the hydrogen evolution reaction. The low voltage AC-STEM provides an excellent pathway to explore new properties and improve the performance of 2D materials and devices.

## Three-dimensional (3D) materials I: 3D imaging of defects in metal oxide thin films

Although nowadays the resolution of AC-STEM is sufficient for many insightful materials studies, the STEM image is a 2D projection of a 3D sample structure, missing important information along the beam direction. Many efforts have been made to determine atomic structure in 3D by tilting the sample and reconstructing the data, a process referred to as tilt series reconstruction, which has recently achieved atomic resolution, although the required dose and data collection time is high [60-66]. An alternative approach is optical sectioning, which requires no tilt and maintains atomic resolution in the 2D plane, albeit with only nanoscale resolution in the z-direction. Thanks to the 5<sup>th</sup> order aberration correction of the probe-forming lens, our illumination angles have increased substantially (as shown in Fig. 1). A simple definition of the depth of field,  $\Delta z$ , is the

**Fig. 2**



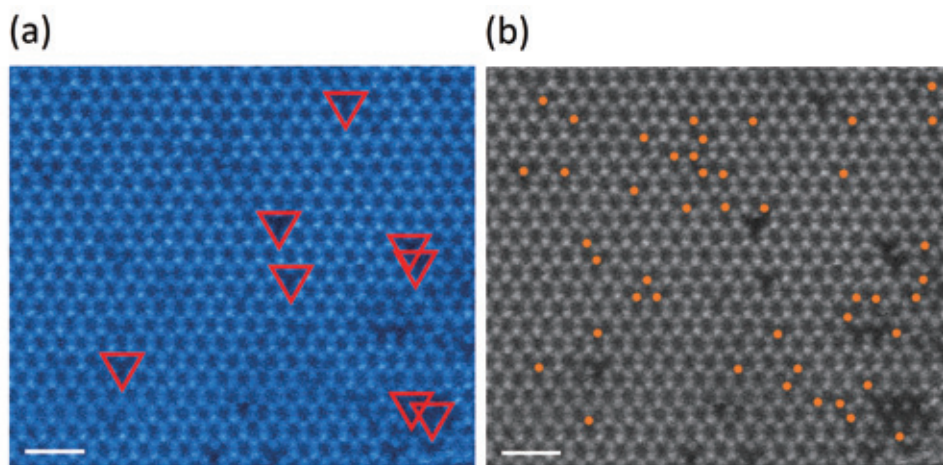
(a) HAADF-STEM image of metallic Ni single atoms embedded in a carbon matrix obtained at 200 kV accelerating voltage and a probe-forming semiangle of 31 mrad. (b) Histograms of the single atoms which are labelled in (a). (c) The average FWHM of the histograms in (b) after Gaussian fitting is 0.6 Å. Data courtesy Chunhua Tang.

range of defocus when the image contrast does not significantly decrease and a change of less than 20% is usually used [67]. Based on this,  $\Delta z$  can be expressed as  $\Delta z \approx \frac{\lambda}{\theta^2}$ , where  $\lambda$  is the wavelength of the incident electrons and  $\theta$  is the illumination angle [41, 67]. The depth resolution is usually taken as twice this figure, based on two point objects along the z axis showing a dip in intensity between them in a focal series [68]. Thus, the significant decrease of the depth of field to the nanoscale provides an opportunity to explore information along the third dimension [43]. It might be expected that the strong dynamical diffraction occurring at a zone axis orientation would destroy the ability to focus at specific depths [69], however, at such large probe angles most of the beam is not channeled and optical sectioning is surprisingly effective, as we show below.

$ABO_3$  perovskite thin films and their interfaces exhibit various properties different from bulk materials [70], such as ferromagnetism [71], ferroelectricity and superconductivity [72,

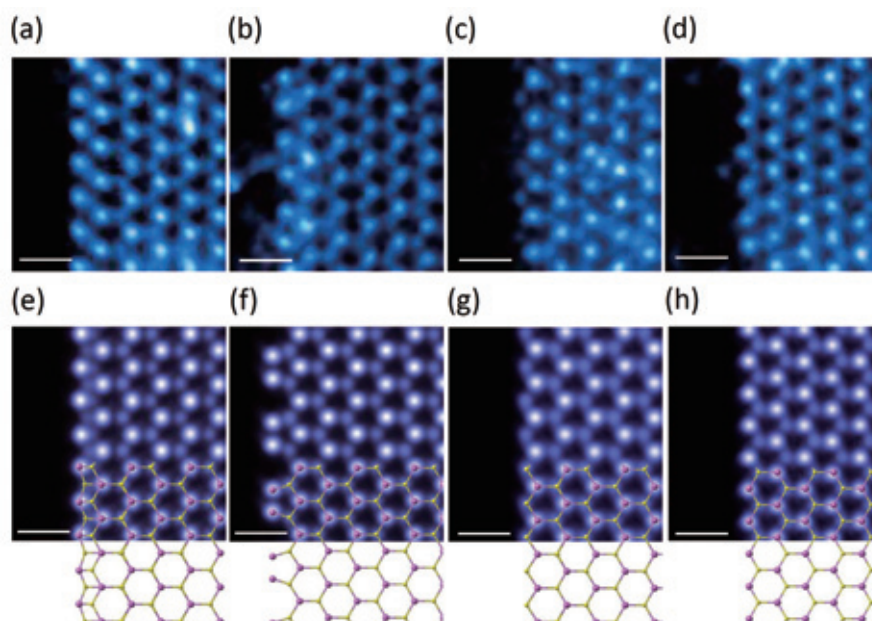
73]. However, these properties are always affected by defects in the structures, including interdiffusion, vacancies [74], and dislocations [75-78], which form to release mismatch strain [79]. Atomic displacements around screw dislocations have already been visualized by optical sectioning [80, 81]. We show here some progress towards determining the 3D structure of interface dislocations and impurity segregation through optical sectioning combined with image simulations. **Figure 5** shows a focal series of images of a dislocation loop at a  $La_{0.7}Sr_{0.3}MnO_3/STO$  (LSMO/STO) interface in a (LSMO/STO) superlattice structure. It is noticeable that the dislocation region shows darker contrast than the perfect lattice, which may be due to different chemical composition and/or an electron dechannelling effect [68, 82]. Applying inverse FFT images and strain ( $\epsilon_{yy}$ ) maps extracted from the HAADF images it is possible to distinguish the emergence and disappearance of this dislocation loop, as shown in Fig. 5(b) and (c), respectively.

**Fig. 3**



Raw HAADF-STEM images of monolayer  $MoSe_2$  at 40 kV. The red triangles in (a) represent double Se vacancies. The orange dots in (b) show single Se vacancies. Data courtesy Jiadong Dan. Scale bars: 1 nm.

**Fig. 4**



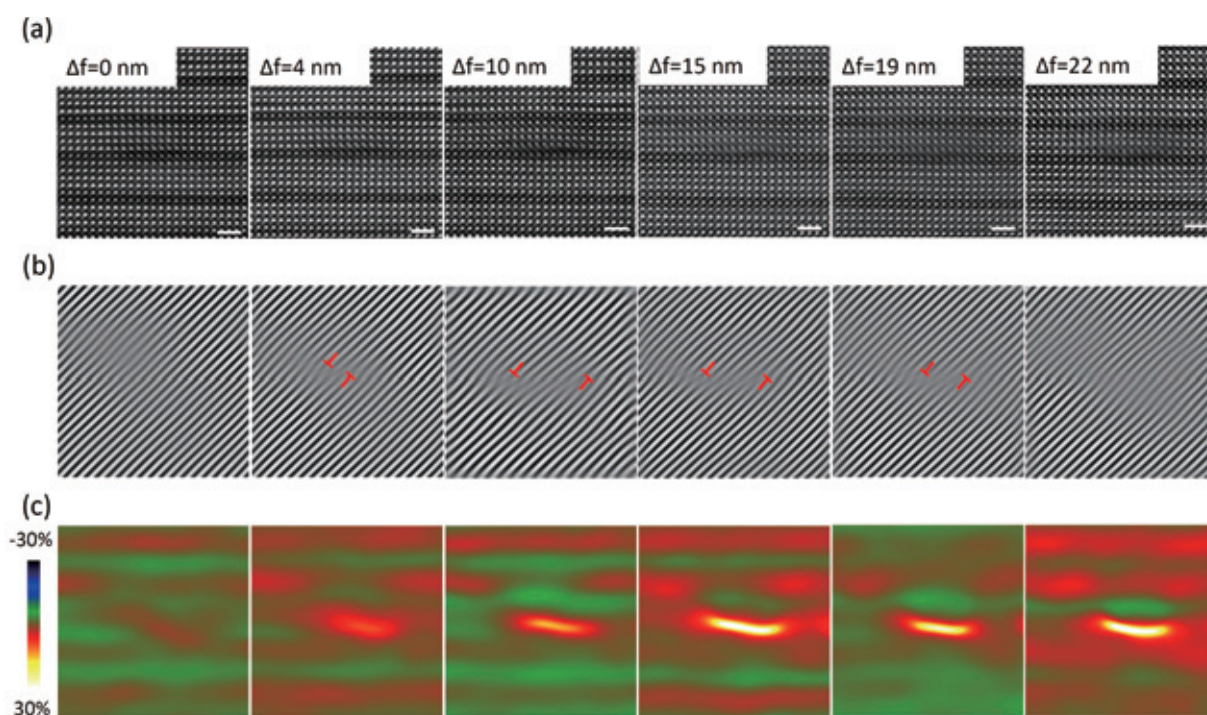
(a-d) Atomic-resolution ADF-STEM images of nanoporous  $MoS_2$  showing the (a) DT, (b) Mo-Klein, (c) S-ZZ and (d) Mo-ZZ edges. (e-h) The corresponding simulated images with overlaid density functional theory (DFT) optimized atomic structures of the four kinds of edges. Scale bars: 0.5 nm. Reproduced from Zhao *et al.* 2017. Copyright 2017 American Chemical Society.

Another example of optical-sectioning is a dislocation at the  $\text{PbTiO}_3$ (PTO)/  $\text{La}_{0.7}\text{Sr}_{0.3}\text{MnO}_3$  (LSMO) interface grown on a  $\text{NdGaO}_3$  (NGO) substrate. The HAADF-STEM image in Fig. 6(a) shows the PTO/LSMO/NGO heterostructure. It is noticeable that the LSMO layer is not uniform. Some regions in this layer have become  $\text{La}_2\text{O}_3$  instead of LSMO. Due to the large lattice parameter of  $\text{La}_2\text{O}_3$ , the lattice mismatch between the PTO and LSMO layer increases. Therefore, the dislocation, which is marked by the yellow rectangle in Fig. 6(a), appears to release strain. In order to acquire detailed information on the dislocation, a STEM focal series with 4 nm defocus interval (Fig. 6(c)) and a corresponding STEM simulation (Fig. 6(d)) are required. For simplicity, we use the  $\text{La}_2\text{O}_3$  structure in the LSMO layer in the STEM simulation, and we incline the dislocation to see if we should expect sufficient depth resolution to image the core at different depths, i.e., we should see the core located at different distances from the interface. The cudaEM software package with multiple GPU support is adopted to simulate the STEM focal series. This software package, which is developed in our group, is optimized for various electron microscopy simulations, especially STEM simulation. The 3D atomic model is given in Fig. 6(b). The y-z view shows that the edge dislocation starts at 4 nm depth and reaches the surface at 24 nm depth. The simulated images and inverse FFT images, Fig. 6(d, e) show that we do expect clear images from each focus value, and the core indeed moves away from the interface with increasing defocus. The simulations match the experimental images only if the Burgers vector is  $a[101]$ . The presence of the screw component is necessary to reproduce the symmetric blurring of the atomic columns each side of the core. Therefore, by combining the experimental STEM data with simulated images, we can achieve a more detailed understanding of the extended 3D structure of materials.

## Three-dimensional (3D) materials II: Atomic resolution imaging and spectroscopy of oxide thin films

Although Z-contrast images are able to provide elemental information from the intensity of atom columns, it is still a challenge to distinguish different atoms when they have similar atomic numbers. Simultaneously acquiring EELS/energy-dispersive X-ray spectroscopy (EDS) and the ADF signal by AC-STEM is a promising and precise approach to identify elements, as well as their valence, even at the atomic-scale. In order to obtain statistically significant results, sufficient signal levels need to be collected for EDS and EELS analysis, meaning that the probe current is much higher than usually used for ADF imaging. Thanks to the improved correction of high order aberrations, AC-STEM is capable of generating a high probe current while maintaining atomic resolution, which significantly increases the data collection efficiency to enable high quality elemental mapping. Figure 7(a) shows an example of atomically-resolved EDX mappings, indicating an atomically sharp  $\text{LaAlO}_3$  (LAO)/ $\text{SrTiO}_3$  (STO) interface. This sharp interface is important to avoid charge localization that may hamper the operation of oxide-based devices [83]. Besides such information on elemental distribution, AC-STEM equipped with EELS also creates the possibility to analyze the valence of elements from one atom column to another. Figure 7(b) shows the HAADF-STEM image produced concurrently with EELS acquisition, while Figure 7(c) indicates the corresponding EELS results for the  $\text{Ti-L}_{2,3}$  energy loss near edge structure (ELNES) in the STO layer at a LAO/STO interface with a 15 unit cell (uc) LAO layer. According to the polar catastrophe model [84], the electrons transferred from the LAO layer always sit in Ti  $d$  orbitals, leading to a change of  $\text{Ti}^{4+}$  to  $\text{Ti}^{3+}$ . To obtain the

**Fig. 5**



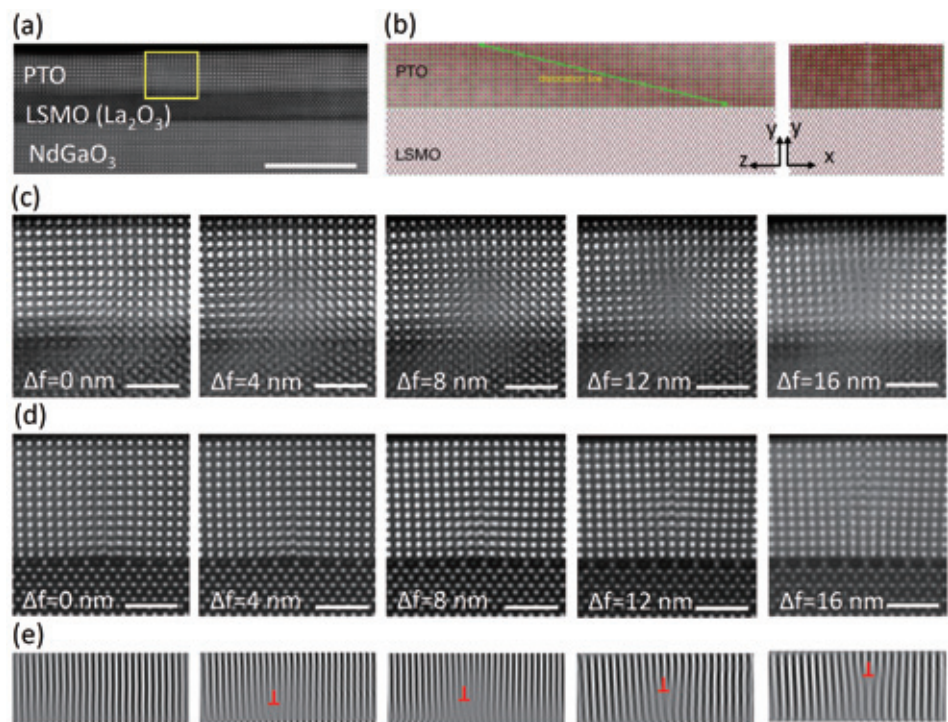
(a) Through focal series of HAADF-STEM images of a LSMO/STO superlattice structure with an interfacial dislocation loop (scale bars: 1 nm). (b,c) The corresponding inverse FFT images and strain ( $\epsilon_{yy}$ ) maps extracted from (a), respectively.

valence change of Ti near the LAO/STO interface, the  $Ti-L_{2,3}$  EEL spectra were extracted from different  $TiO_2$  planes in the STO layer. It is noticeable that the spectra close to the LAO/STO interface are similar to the spectrum of the  $Ti^{3+}$  reference, while the spectra far away from the interface region show the same appearance as the  $Ti^{4+}$  reference. It perfectly confirms the presence of a two-dimensional electron gas (2DEG) at the LAO/STO interface. These results strongly highlight how analyzing elemental composition and valence at the atomic-scale with AC-STEM provides fundamental insights into the electronic as well as atomic structure of interfaces, and can point to new directions for investigation.

## Conclusions

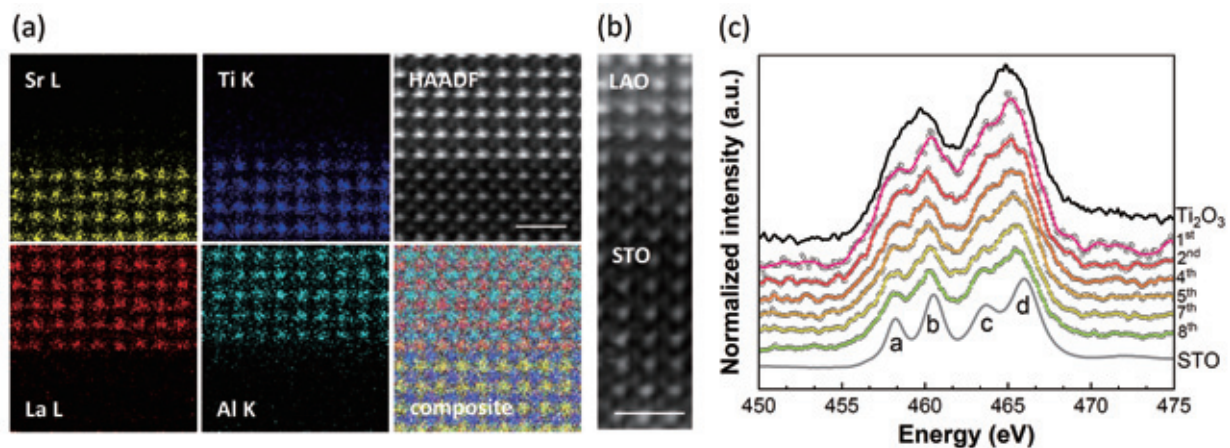
In summary, with the improvement of aberration correction, AC-STEM is finding wide application across many active areas of materials research, including single-atom catalysts, 2D materials and perovskite thin films and devices. It is also demonstrated that the larger convergence angles enable us to explore sample information along the third dimension through optical sectioning, resulting in improved determination of the 3D structures of extended defects in materials. Furthermore, with the associated AC-STEM techniques of EELS and EDX, we can obtain more useful data such as elemental compositions, bonding

**Fig. 6**



(a) HAADF-STEM image of the LSMO/PTO//NGO heterostructure (scale bar: 10 nm). (b) The 3D atomic model of the dislocation. (c,d) Through focal series of HAADF-STEM images and the corresponding simulated images of the dislocation at the PTO/LSMO interface (scale bars: 2 nm). (e) The corresponding inverse FFT images of the PTO layer in (d) show the core to move away from the interface with increasing defocus. Data courtesy Changjian Li and simulation courtesy Shoucong Ning.

**Fig. 7**



(a) EDX images of a LAO/STO interface, with total acquisition time of 10 min. Reproduced from Pennycook *et al.* Copyright 2018 Springer Berlin Heidelberg. (b) The ADF image produced concurrently with EELS acquisition. (c) Comparison of the STO  $Ti-L_{2,3}$  ELNES at different  $TiO_2$  planes at the LAO/STO interface with a 15 uc LAO layer. The black dots are the experimental data, and coloured lines are smoothed by Fast Fourier Transform. Solid black lines are reference spectra from STO and  $Ti_2O_3$  used to extract the  $Ti^{3+}$  fraction. The a, b, c and d peaks represent electron transitions from  $2p_{3/2}$  to  $3d_{2g}$ ,  $2p_{3/2}$  to  $3d_{e_g}$ ,  $2p_{1/2}$  to  $3d_{t_{2g}}$ ,  $2p_{1/2}$  to  $3d_{e_g}$ , respectively (scale bars 1 nm). Data courtesy Mengsha Li.

and oxidation states of the atoms. We hope these examples have demonstrated that, thanks to the enhanced sensitivity at the single-atom level, the advanced AC-STEM has become one of the most powerful techniques in nanomaterials research, invaluable for researchers to optimize material properties and create new materials.

We wish JEOL every success for the next 70 years, and look forward to the further development of improved aberration correctors, monochromators and other new imaging modes, for example, the use of pixelated detectors for field free magnetic imaging or ptychography to name just a few [85-87]. Never before in history we have been able to view the “atomic circus” with such clarity [88], observing materials complexity at the atomic scale, including atomic dynamics. Understanding such behavior will surely enable the development of better materials and processes. Perhaps we will also see the emergence of the STEM as a nanofabrication tool, able not just to image but to manipulate atoms in 3D as well. We are already seeing much progress in this direction [89]. But we have not yet realized Richard Feynman’s dream [90], and improving resolution, especially the depth resolution, will surely bring yet greater precision in locating atoms in 3D, solving the structures of amorphous materials, metallic glasses, etc. To quote Freeman Dyson, “The great advances in science usually result from new tools rather than new doctrines” [91].

## Acknowledgments

All authors are grateful to their collaborators on the work shown in this article. C.J.L. would like to acknowledge financial support from the Lee Kuan Yew Postdoctoral Fellowship through the Singapore Ministry of Education Academic Research Fund Tier 1 (R-284-000-158-114). S.J.P would like to acknowledge financial support by the Ministry of Education, Singapore under its Tier 2 Grant (Grant No. MOE2017-T2-2-139), under its Tier 1 grant (R-284-000-175-112), and by the National University of Singapore.

## References

- [ 1 ] Pennycook S.J., Nellist P.D., Scanning transmission electron microscopy imaging and analysis, Springer Science & Business Media, London, 2011, pp. 1-91.
- [ 2 ] Knoll M., Ruska E., Das Elektronenmikroskop, *Zeitschrift für Physik*, **78** (1932) 318-339.
- [ 3 ] Ruska E., The development of the electron microscope and of electron microscopy, *Reviews of Modern Physics*, **59** (1987) 627-638.
- [ 4 ] Knoll M., Aufladepotential und Sekundäremission elektronenbestrahlter Körper. *Zeitschrift für technische Physik*, **16** (1935) 467-475.
- [ 5 ] von Ardenne M., Das Elektronen-Rastermikroskop. Praktische Ausführung, *Zeitschrift für technische Physik*, **19** (1938) 407-416.
- [ 6 ] von Ardenne M., Das Elektronen-Rastermikroskop. Theoretische Grundlagen, *Zeitschrift für Physik*, **109** (1938) 553-572.
- [ 7 ] von Ardenne M., Über ein Universal-Elektronenmikroskop für Hellfeld-, Dunkelfeld- und Stereobild-Betrieb, *Zeitschrift für Physik A Hadrons and Nuclei*, **115** (1940) 339-368.
- [ 8 ] Ardenne M.V., 4.4 Reminiscences on the origins of the scanning electron microscope and the electron microprobe, *Advances in Imaging and Electron Physics*, **96** (1996) 635-652.
- [ 9 ] Menter J., The direct study by electron microscopy of crystal lattices and their imperfections, *Proceedings of the Royal Society of London, Series A: Mathematical and Physical Sciences*, **236** (1956) 119-135.
- [10] Feynman R.P., There's plenty of room at the bottom, *Journal of Microelectromechanical Systems*, **1** (1992) 60-66.
- [11] Crewe A.V., Eggenberger D.N., Wall J., Welter L.M., Electron gun using a field emission source. *Review of Scientific Instruments* **39** (1968) 576-583.
- [12] Crewe A.V., Wall J., Langmore J., Visibility of single atoms, *Science*, **168** (1970) 1338-1340.
- [13] Wall J., Langmore J., Isaacson M., Crewe A., Scanning-transmission electron-microscopy at high-resolution, *Proceedings of the National Academy of Sciences of the United States of America*, **71** (1974) 1-5.
- [14] Crewe A.V., High resolution scanning microscopy of biological specimens, *Philosophical Transactions of the Royal Society B*, **261** (1971) 61-70.
- [15] Cowley J.M., High resolution electron microscopy of crystals, today and tomorrow, *Journal of the Crystallography Society of Japan*, **20** (1978) 241-259.
- [16] Cowley J.M., Scanning transmission electron microscopy and microdiffraction techniques, *Bulletin of Materials Science*, **6** (1984) 477-490.
- [17] Treacy M., Imaging with Rutherford scattered electrons in the scanning-transmission electron-microscope, *Scanning Electron Microscopy*, (1981) 185-197.
- [18] Treacy M.M.J., Howie A., Pennycook S.J., Z-contrast of supported catalyst particles on the STEM, *Journal of Physics: Conference Series*, **52** (1980) 261-266.
- [19] Pennycook S.J., Boatner L.A., Chemically sensitive structure-imaging with a scanning transmission electron microscope, *Nature*, **336** (1988) 565-567.
- [20] Pennycook S.J., Z-contrast STEM for materials science, *Ultramicroscopy*, **30** (1989) 58-69.
- [21] Pennycook S.J., Jesson D.E., High-resolution incoherent imaging of crystals. *Physical Review Letters*, **64** (1990) 938-941.
- [22] Pennycook S.J., Jesson D.E., High-resolution Z-contrast imaging of crystals, *Ultramicroscopy*, **37** (1991) 14-38.
- [23] Jesson D.E., Pennycook S.J., Incoherent imaging of thin specimens using coherently scattered electrons, *Proceedings of the Royal Society of London, Series A: Mathematical and Physical Sciences*, **441** (1993) 261-281.
- [24] Jesson D.E., Pennycook S.J., Incoherent imaging of crystals using thermally scattered electrons, *Proceedings of the Royal Society A: Mathematical Physical and Engineering Sciences*, **449** (1995) 273-293.
- [25] Browning N.D., Chisholm M.F., Pennycook S.J., Atomic-resolution chemical analysis using a scanning transmission electron microscope, *Nature*, **366** (1993) 143-146.
- [26] Pennycook S.J., Browning N.D., Jesson D.E., Chisholm M.F., McGibbon A.J., Atomic-resolution imaging and spectroscopy of semiconductor interfaces, *Applied Physics A*, **57** (1993) 385-391.
- [27] Batson P.E., Simultaneous STEM imaging and electron energy-loss spectroscopy with atomic-column sensitivity, *Nature*, **366** (1993) 727-728.
- [28] von Harrach H.S., Nicholls A.W., Jesson D.E., Pennycook S.J., First results of a 300 kV high-resolution field-emission STEM, *Electron Microscopy and Analysis*, (1993) 499-502.
- [29] von Harrach H.S., Development of the 300-kV Vacuum Generator STEM (1985-1996), *Advances in Imaging and Electron Physics*, **159** (2009) 287-323.

- [30] James E.M., Browning N.D., Nicholls A.W., Kawasaki M., Xin Y., Stemmer S., Demonstration of atomic resolution Z-contrast imaging by a JEOL JEM-2010F scanning transmission electron microscope, *Journal of Electron Microscopy*, **47** (1998) 561.
- [31] Batson P.E., Dellby N., Krivanek O.L., Sub-ångstrom resolution using aberration corrected electron optics, *Nature*, **418**, 617–620 (2002).
- [32] Nellist P.D., Chisholm M.F., Dellby N., Krivanek O.L., Murfitt M.F., Szilagy Z.S., Lupini A.R., Borisevich A., Sides W.H., Pennycook S.J., Direct sub-ångstrom imaging of a crystal lattice, *Science*, **305** (2004) 1741-1741.
- [33] Varela M., Findlay S.D., Lupini A.R., Christen H.M., Borisevich A.Y., Dellby N., Krivanek O.L., Nellist P.D., Oxley M.P., Allen L.J., Pennycook S.J., Spectroscopic imaging of single atoms within a bulk solid, *Physical Review Letters*, **92** (2004) 095502.
- [34] Bosman M., Keast V.J., Garcia-Munoz J.L., Alfonso D'A. J., Findlay S.D., Allen L.J., Two-dimensional mapping of chemical information at atomic resolution, *Physical Review Letters*, **99** (2007) 086102.
- [35] Erni R., Rossell M.D., Kisielowski C., Dahmen U., Atomic-resolution imaging with a sub-50-pm electron probe, *Physical Review Letters*, **102** (2009) 096101.
- [36] Sawada H., Tanishiro Y., Ohashi N., Tomita T., Hosokawa F., Kaneyama T., Kondo Y., Takayanagi K., STEM imaging of 47-pm-separated atomic columns by a spherical aberration-corrected electron microscope with a 300-kV cold field emission gun, *Journal of Electron Microscopy*, **58** (2009) 357-361.
- [37] Sawada H., Shimura N., Hosokawa F., Shibata N., Ikuhara Y., Resolving 45-pm-separated Si-Si atomic columns with an aberration-corrected STEM, *Microscopy*, **64** (2015) 213-217.
- [38] Krivanek O.L., Chisholm M.F., Nicolosi V., Pennycook T.J., Corbin G.J., Dellby N., Murfitt M.F., Own C.S., Szilagy Z.S., Oxley M.P., Pantelides S.T., Pennycook S.J., Atom-by-atom structural and chemical analysis by annular dark-field electron microscopy, *Nature*, **464** (2010) 571-574.
- [39] Peter A. van Aken, private communication.
- [40] Borisevich A.Y., Lupini A.R., Pennycook S.J., Depth sectioning with the aberration-corrected scanning transmission electron microscope, *Proceedings of the National Academy of Sciences of the United States of America*, **103** (2006) 3044-3048.
- [41] van Benthem K., Lupini A.R., Oxley M.P., Findlay S.D., Allen L.J., Pennycook S.J., Three-dimensional ADF imaging of individual atoms by through-focal series scanning transmission electron microscopy, *Ultramicroscopy*, **106** (2006) 1062-1068.
- [42] Ishikawa R., Lupini A.R., Hinuma Y., Pennycook S.J., Large-angle illumination STEM: toward three-dimensional atom-by-atom imaging, *Ultramicroscopy*, **151** (2015) 122-129.
- [43] Ishikawa R., Pennycook S.J., Lupini A.R., Findlay S.D., Shibata N., Ikuhara Y., Single atom visibility in STEM optical depth sectioning, *Applied Physics Letters* **109** (2016) 163102.
- [44] Nellist P.D., Pennycook S.J., Direct imaging of the atomic configuration of ultradispersed catalysts, *Science*, **274** (1996) 413-415.
- [45] Pennycook S.J., The impact of STEM aberration correction on materials science, *Ultramicroscopy*, **180** (2017) 22-33.
- [46] Yan H., Su C., He J., Chen W., Single-atom catalysts and their applications in organic chemistry, *Journal of Materials Chemistry A*, **6** (2018) 8793-8814.
- [47] Geim A.K., Novoselov K.S., The rise of graphene, *Nature Materials*, **6** (2007) 183-191.
- [48] Tiwari J.N., Tiwari R.N., Kim K.S., Zero-dimensional, one-dimensional, two-dimensional and three-dimensional nanostructured materials for advanced electrochemical energy devices, *Progress in Materials Science* **57** (2012) 724-803.
- [49] Zeng H., Dai J., Yao W., Xiao D., Cui X., Valley polarization in MoS<sub>2</sub> monolayers by optical pumping. *Nature Nanotechnology*, **7** (2012) 490-493.
- [50] Komsa H.P., Kotakoski J., Kurasch S., Lehtinen O., Kaiser U., Krasheninnikov A.V., Two-dimensional transition metal dichalcogenides under electron irradiation: defect production and doping, *Physical Review Letters* **109** (2012) 035503.
- [51] Hong J., Hu Z., Probert M., Li K., Lv D., Yang X., Gu L., Mao N., Feng Q., Xie L., Zhang J., Wu D., Zhang Z., Jin C., Ji W., Zhang X., Yuan J., Zhang Z., Exploring atomic defects in molybdenum disulphide monolayers. *Nature Communications*, **6** (2015) 6293.
- [52] Lee J., Zhou W., Pennycook S.J., Idrobo J.C., Pantelides S.T., Direct visualization of reversible dynamics in a Si<sub>6</sub> cluster embedded in a graphene pore, *Nature Communications*, **4** (2013) 1650.
- [53] Pennycook S.J., Zhou W., Pantelides S.T., Watching atoms work-nanocluster structure and dynamics, *ACS Nano*, **9**(10) (2015) 9437-9440.
- [54] Yang Z., Yin L., Lee J., Ren W., Cheng H.-M., Ye H., Pantelides S.T., Pennycook S.J., Chisholm M.F., Direct observation of atomic dynamics and silicon doping at a topological defect in graphene, *Angewandte Chemie International Edition*, **53** (2014) 8908-8912.
- [55] Kurasch S., Kotakoski J., Lehtinen O., Skákalová V., Smet J., Krill C.E., Krasheninnikov A.V., Kaiser U., Atom-by-atom observation of grain boundary migration in graphene, *Nano Letters*, **12** (2012) 3168-3173.
- [56] Hong J., Pan Y., Hu Z., Lv D., Jin C., Ji W., Yuan J., Zhang Z., Direct imaging of kinetic pathways of atomic diffusion in monolayer molybdenum disulfide, *Nano Letters*, **17** (2017) 3383-3390.
- [57] Lin J., Cretu O., Zhou W., Suenaga K., Prasai D., Bolotin K.I., Cuong N.T., Otani M., Okada S., Lupini A.R., Idrobo J.-C., Caudel D., Burger A., Ghimire N.J., Yan J., Mandrus D.G., Pennycook S.J., Pantelides S.T., Flexible metallic nanowires with self-adaptive contacts to semiconducting transition-metal dichalcogenide monolayers, *Nature Nanotechnology*, **9** (2014) 436-442.
- [58] Zhao X., Dan J., Chen J., Ding Z., Zhou W., Loh K.P., Pennycook S.J., Atom-by-atom fabrication of monolayer molybdenum membranes, *Advanced Materials*, **5** (2018) 1707281-7.
- [59] Zhao X., Fu D., Ding Z., Zhang Y.Y., Wan D., Tan S.J.R., Chen Z., Leng K., Dan J., Fu W., Geng D., Song P., Du Y., Venkatesan T., Pantelides S.T., Pennycook S.J., Zhou W., Loh K.P. Mo-terminated edge reconstructions in nanoporous molybdenum disulfide film, *Nano Letters*, **18** (2017) 482-490.
- [60] Van Aert S., Batenburg K.J., Rossell M.D., Erni R., Van Tendeloo G., Three-dimensional atomic imaging of crystalline nanoparticles, *Nature*, **470** (2011) 374-377.
- [61] Bals S., Casavola M., Van Huis M.A., Van Aert S.,

- Batenburg K.J., Van Tendeloo G., Vanmaekelbergh D., Three-dimensional atomic imaging of colloidal core-shell nanocrystals, *Nano Letters*, **11** (2011) 3420-3424.
- [62] Goris B., De Backer A., Van Aert S., Gómez-Graña S., Liz-Marzan L.M., Van Tendeloo G., Bals S., Three-dimensional elemental mapping at the atomic scale in bimetallic nanocrystals, *Nano Letters* **13** (2013) 4236-4241.
- [63] Scott M.C., Chen C.-C., Mecklenburg M., Zhu C., Xu R., Ercius P., Dahmen U., Regan B.C., Miao J., Electron tomography at 2.4-ångström resolution, *Nature*, **483** (2012) 444-447.
- [64] Bals S., Goris B., De Backer A., Van Aert S., Van Tendeloo G., Atomic resolution electron tomography. *MRS Bulletin*, **41** (2016) 525-530.
- [65] Yang Y., Chen C.-C., Scott M. C., Ophus C., Xu R., Pryor A., Wu L., Sun F., Theis W., Zhou J., Eisenbach M., Kent P.R.C., Sabirianov R.F., Zeng H., Ercius P., Miao J., Deciphering chemical order/disorder and material properties at the single-atom level, *Nature*, **542** (2017) 75-79.
- [66] Xu R., Chen C.-C., Wu L., Scott M.C., Theis W., Ophus C., Bartels M., Yang Y., Ramezani-Dakhel H., Sawaya M.R., Heinz H., Marks L. D., Ercius P., Miao J., Three-dimensional coordinates of individual atoms in materials revealed by electron tomography, *Nature Materials*, **14** (2015) 1099-1103.
- [67] Snyder S.H., Whitten D.G., Flexible bilayers with spontaneous curvature lead to lamellar gels and spontaneous vesicles, *Proceedings of the National Academy of Sciences of the United States of America*, **103** (2006) 19213.
- [68] Perovic D.D., Rossouw C.J., Howie A., Imaging elastic strains in high-angle annular dark field scanning transmission electron microscopy, *Ultramicroscopy*, **52** (1993) 353-359.
- [69] Borisevich A.Y., Depth sectioning of aligned crystals with the aberration-corrected scanning transmission electron microscope, *Journal of Electron Microscopy*, **55** (2006) 7-12.
- [70] Song K., Du K., Ye H., Atomic structure and chemistry of a[100] dislocation cores in  $\text{La}_{2/3}\text{Sr}_{1/3}\text{MnO}_3$  films. *Micron*, **96** (2017) 72-76.
- [71] Tanaka H., Zhang J., Kawai T., Giant electric field modulation of double exchange ferromagnetism at room temperature in the perovskite manganite/titanate p-n junction, *Physical Review Letters*, **88** (2001) 027204.
- [72] Tybell T., Ahn C.H., Triscone J.M., Ferroelectricity in thin perovskite films. *Applied Physics Letters*, **75** (1999) 856-858.
- [73] Sandstrom R.L., Giess E.A., Gallagher W.J., Segmüller A., Cooper E.I., Chisholm M.F., Gupta A., Shinde S., Laibowitz R.B., Lanthanum gallate substrates for epitaxial high-temperature superconducting thin films. *Applied Physics Letters*, **53** (1988) 1874-1876.
- [74] Cantoni C., Gazquez J., Miletto Granozio F., Oxley M.P., Varela M., Lupini A.R., Pennycook S.J., Aruta C., di Uccio U.S., Perma P., Maccariello D., Electron transfer and ionic displacements at the origin of the 2D electron gas at the LAO/STO interface: direct measurements with atomic-column spatial resolution, *Advanced Materials*, **24** (2012) 3952-3957.
- [75] Kim M., Duscher G., Browning N.D., Sohlberg K., Pantelides S.T., Pennycook S.J., Nonstoichiometry and the electrical activity of grain boundaries in  $\text{SrTiO}_3$ , *Physical Review Letters*, **86** (2001) 4056-4059.
- [76] Klie R.F., Buban J.P., Varela M., Franceschetti A., Jooss C., Zhu Y., Browning N.D., Pantelides S.T., Pennycook S.J., Enhanced current transport at grain boundaries in high- $T_c$  superconductors, *Nature*, **435** (2005) 475-478.
- [77] Szot K., Speier W., Bihlmayer G., Waser R., Switching the electrical resistance of individual dislocations in single-crystalline  $\text{SrTiO}_3$ , *Nature Materials*, **5** (2006) 312-320.
- [78] Metlenko V., Ramadan A.H., Gunkel F., Du H., Schraknepper H., Hoffmann-Eifert S., Dittmann R., Waser R., De Souza R.A., Do dislocations act as atomic autobahns for oxygen in the perovskite oxide  $\text{SrTiO}_3$ ? *Nanoscale*, **6** (2014) 12864-12876.
- [79] Kaya M., Atici Y., Studies of lattice mismatch and threading dislocations in GaAs/Si grown by MBE, *Superlattices and Microstructures*, **35** (2004) 35-44.
- [80] Lozano J.G., Yang H., Guerrero-Lebrero M.P., D'Alfonso A.J., Yasuhara A., Okunishi E., Zhang S., Humphreys C.J., Allen L.J., Galindo P.L., Hirsch P.B., Nellist P.D., Direct observation of depth-dependent atomic displacements associated with dislocations in gallium nitride, *Physical Review Letters*, **113** (2014) 135503.
- [81] Yang H., Lozano J.G., Pennycook T.J., Jones L., Hirsch P.B., Nellist P.D., Imaging screw dislocations at atomic resolution by aberration-corrected electron optical sectioning, *Nature Communications*, **6** (2015) 7266.
- [82] Chisholm M.F., Pennycook S.J., Direct imaging of dislocation core structures by Z-contrast STEM, *Philosophical Magazine*, **86** (2006) 4699-4725.
- [83] Ron A., Hevroni A., Maniv E., Mograbi M., Jin L., Jia C.L., Urban K.W., Garkovich G., Dagan Y., Solution monolayer epitaxy for tunable atomically sharp oxide interfaces., *Advanced Materials Interfaces*, **4** (2017) 1700688.
- [84] Harrison W.A., Kraut E.A., Waldrop J.R., Grant R.W., Polar heterojunction interfaces, *Physical Review B*, **18** (1978) 4402-4410.
- [85] Krajnak M., McGrouther D., Maneuski D., Shea V.O., McVitie S., Pixelated detectors and improved efficiency for magnetic imaging in STEM differential phase contrast, *Ultramicroscopy*, **165** (2016) 42-50.
- [86] Pennycook T.J., Lupini A.R., Yang H., Murfitt M.F., Jones L., Nellist P.D., Efficient phase contrast imaging in STEM using a pixelated detector. Part I: Experimental demonstration at atomic resolution, *Ultramicroscopy*, **151** (2015) 160-167.
- [87] Yang H., Pennycook T.J., Nellist P.D., Efficient phase contrast imaging in STEM using a pixelated detector. Part II: optimisation of imaging conditions, *Ultramicroscopy*, **151** (2015) 232-239.
- [88] Wu H., Zhao X., Guan C., Zhao L.-D., Wu J., Song D., Li C., Wang J., Loh K.P., Venkatesan T.V., Pennycook S.J., The atomic circus: small electron beams spotlight advanced materials down to the atomic scale, *Advanced Materials*, **30** (2018) 1802402-11.
- [89] Kalinin S.V., Pennycook S.J., Single-atom fabrication with electron and ion beams: from surfaces and two-dimensional materials toward three-dimensional atom-by-atom assembly, *MRS Bulletin*, **42** (2017) 637-643.
- [90] Pennycook S.J., Fulfilling Feynman's dream: "Make the electron microscope 100 times better"-Are we there yet? *MRS Bulletin*, **40** (2015) 71-78.
- [91] Dyson F., The Scientist as Rebel, *The American Mathematical Monthly*, 1996, pp. 800.

# Probe Corrected STEM Structural Imaging and Chemical Analysis of Materials at Atomic Resolution

E. J. Olivier, J. H. Neethling and J. H. O'Connell

Centre for HRTEM, Nelson Mandela University

This paper provides a brief overview of materials science problems solved by imaging and analysis with Cs-corrected scanning transmission electron microscopy (STEM) with special focus on the palladium and silver transport mechanisms in Tristructural Isotropic (TRISO) coated fuel particles. The JEOL JEM-ARM200F used is equipped with two CEOS spherical aberration (Cs) correctors for probe and image correction as well as an Oxford Instruments X-Max 100 TLE large angle energy dispersive X-ray spectrometry (EDS) detector with a collection angle of  $\sim 0.72$  Sr. The improved collection efficiency of the large angle EDS detector proved to be essential for the detection of low concentrations of silver along SiC grain boundaries. The better counting statistics over a shorter analysis time allowed the use of lower probe currents for the detection of silver, before the STEM probe could cause the dispersion of the silver accumulations. In addition, the microscope is fitted with a Gatan Quantum 965 ERS image filter (GIF) with dual electron energy loss spectroscopy (EELS) capability. EELS was used to obtain information about the chemical bonding characteristics of elements in extended lattice defects.

## Introduction

The development of Cs-corrected STEM with high angle annular dark field (HAADF) imaging mode has provided a powerful technique for obtaining structural and chemical information at atomic resolution. The range of useful techniques includes atomic scale and Z-contrast imaging and chemical analysis using EDS and EELS. The acquisition of a double Cs-corrected JEOL JEM-ARM200F in South Africa in 2011 enabled the solving of several long-standing materials problems of technological interest. These problems include the following examples. The atomic arrangement in nitrogen containing {001} platelet defects in natural type Ia diamond is a problem that has been investigated for more than 60 years. By studying the atomic arrangement across the platelet line at a spatial resolution of better than 89 pm (required to resolve the atomic columns of the defect along the  $\langle 110 \rangle$  direction) we were able to match the observed atomic positions to one of the leading structural models proposed earlier by other workers. Comparisons of the HAADF STEM images with simulated platelet model images revealed that it agrees closely with a structural model called the zigzag model [1]. The electron energy-loss near-edge fine structure of both carbon K- and nitrogen K-edges obtained from the platelet core is consistent with the atomic bond arrangement of the zigzag structure model [1]. The second example is the phase of a Ag-Pt alloy, which could only be determined by using probe corrected Z-contrast imaging [2]. The correct phase diagram of the Ag-Pt alloy is essential for the identification of new novel uses of this alloy. Despite many years of research on the silver-

platinum system, it was until recently not well understood since earlier attempts to determine its crystal structure were not successful [2]. By using atomic resolution HAADF STEM, we showed that the Ag-Pt alloy consists of nanometre-sized domains with  $L1_1$  ordering [2].

The nature of small dislocation loops in proton, electron and neutron irradiated n-type GaAs may be determined unambiguously by Cs-corrected HAADF STEM since the image characteristics are much less dependent on foil thickness and defocus values as is the case for HRTEM imaging. Cs-corrected HAADF STEM imaging of {110} and {111} dislocation loops in neutron irradiated and annealed (600 °C for 20 minutes) n-type GaAs revealed that the {110} loop consists of two layers of Ga and As atoms, which is consistent with the model for a {110} pure-edge interstitial dislocation loop in GaAs. The {111} interstitial loop consists of one layer of Ga and As atoms while the stacking sequence across the loop is consistent with that of an extrinsic stacking fault. The positions of the Ga and As atoms (obtained by using EEL spectrum imaging) across the extrinsic stacking fault plane of the {111} loop indicate polarity continuation across the loop and the preservation of charge neutrality [3]. This study generated valuable information related to defect evolution in irradiated GaAs, which has applications in GaAs based space solar cell technologies.

This paper focuses on the successful use of Cs-corrected HAADF STEM and EDS to provide a deeper understanding of the palladium and silver transport mechanisms in TRISO fuel particles. The finding, more than three decades ago, that silver ( $^{110m}\text{Ag}$ , a radioactive fission product) can be released

by reputedly intact TRISO nuclear fuel particles [4], has led to significant research efforts to determine the silver transport mechanism in SiC. The TRISO-coated particle is used in generation IV high temperature gas cooled reactors (HTGR) and consists of a fuel kernel and coating layers of porous pyrolytic carbon (PyC), inner high-density PyC (IPyC), silicon carbide (SiC) and outer high density PyC (OPyC) [5]. The SiC layer serves as the main barrier to fission product release. The diffusion coefficients of Ag in SiC determined from the fractional release of  $^{110m}\text{Ag}$  from irradiated TRISO fuel are about three orders of magnitude higher than that measured for Ag in SiC in out-of-reactor diffusion experiments. [6]. Despite more than four decades of studies of the transport mechanism of Ag in irradiated SiC, many researchers feel that a satisfactory explanation has not yet been found [6]. This paper presents results of a high-resolution analytical STEM study of irradiated TRISO particle SiC layers. The approach followed to analyse fission products at inter- and intra-granular sites are discussed. The finding that Ag was mostly found to co-exist with Pd at SiC grain boundaries [5], is consistent with the earlier Pd-assisted Ag transport mechanism proposed by the authors [7, 8, 9].

## Experimental

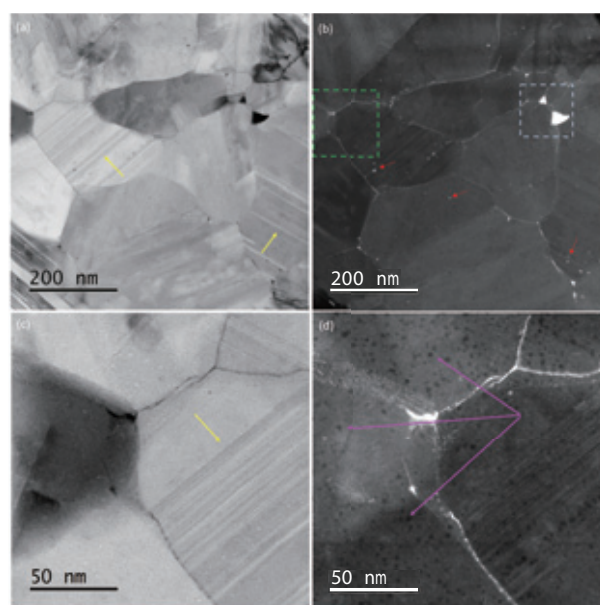
The TRISO fuel particle used in this study was from the first advanced gas reactor (AGR-1) experiment [5]. The particle was irradiated to 19.38% fissions per initial metal atom (FIMA) average burnup, 1072 °C time average, volume-averaged temperature; 1182 °C time average, peak temperature and an average fast fluence of  $4.13 \times 10^{21}$  n/cm<sup>2</sup>. Electron transparent lamellae were prepared at the Electron Microscopy Laboratory (EML) at the Materials and Fuels Complex (MFC) of Idaho National Laboratory (INL) using a dual-beam Quanta 3D FEG focused ion beam (FIB). HRSTEM investigations were performed at the Centre for HRTEM at the Nelson Mandela University (NMU) in South Africa using a double Cs-corrected JEOL JEM-ARM200F operated at 200 kV. This microscope is equipped with two CEOS spherical aberration (Cs) correctors for correction in TEM and STEM modes, as well as an Oxford Instruments X-Max 100 TLE large angle energy dispersive X-ray spectrometer (EDS) with a collection angle of  $\sim 0.72$  Sr. The improved collection efficiency of large angle EDS detectors results in better counting statistics, allowing for shorter STEM-EDS analysis times which enable the detection of small concentrations of elements before beam induced dispersion of beam sensitive elements might occur. The electron dose experienced by the sample can also be reduced since lower probe currents can be used. In addition, the microscope is fitted with a Gatan Quantum 965 ERS image filter (GIF) with dual EELS capability. Imaging and analysis of the samples were done using a sub-angstrom sized probe with a probe current between 68 pA and 281 pA. The convergence semi-angle of the probe used was fixed at 21 mrad with acceptance semi-angles of the GIF and dark-field detector being 84 mrad and 34 to 137 mrad respectively. EDS was used for element identification and compositional analysis due to the relative accessibility of the higher energy K-lines for Ag and Pd which enabled their easy identification due to sufficient separation between the respective X-ray peaks. The possibility of simultaneous acquisition of bright field (BF) and high angle annular dark field (HAADF) STEM images aided in the identification of grain boundaries in conjunction with elemental atomic number contrast imaging. EELS spectrum imaging was used to study the nature of Si and C bonds to fission products present at grain boundaries.

## Results and discussion

Figure 1(a)-(d) show complimentary BF and HAADF STEM images of an area within the SiC layer investigated. Figure 1 (c) and (d) are magnified views of the area indicated in Fig. 1 (b) by the green square. The contrast observed in the bright field images is due to diffraction contrast generated by grains in different orientations as well as extended defects in the grains. Cubic SiC, due to its low stacking fault energy, normally has a high density of planar defects (stacking faults and twins) which are visible as sets of parallel lines running across the grains as indicated by the yellow arrows in Figs. 1 (a) and (c). Radiation induced voids are visible as bright and dark spots in (c) BF and (d) HAADF images respectively. The presence of voids in SiC after irradiation by high-energy neutrons at elevated temperatures is consistent with the findings of other workers [9, 10]. The bright regions along grain boundaries in the HAADF STEM images (Fig. 1 (b) and (d)), are evidence for the presence of heavy metal fission product agglomerations. Larger fission product agglomerates are visible at grain boundary triple points while the fission product agglomerations along grain boundaries connecting the triple points show a variation in HAADF image intensity indicating a variation in the agglomerate volume along the grain boundary. The fission products observed in the SiC layer are produced in the fuel kernel from where they migrate through the pyrolytic carbon layers to the SiC layer. The fission product agglomerates were analyzed previously and found to contain typically Pd and U, with trace amounts of Ag, Cd, P, Ni and Mo which are similar to the results of other AGR-1 fuel particles analyses [5, 11-13].

The identification of metallic fission products is generally carried out by using TEM EDS point analysis and mapping.

**Fig. 1**



(a) BF STEM image of an area in the SiC layer. (b) HAADF STEM image of the same area in (a). (c) Bright-field STEM image of the area in (b) indicated by the green square. (d) HAADF STEM image of the same area shown in (c). Yellow arrows in (a) and (c) indicate the positions of planar defects. Purple arrows in (d) shows examples of voids present in the SiC grain (Originally published by van Rooyen et al. (2016) [5]).

**Figure 2** shows complimentary BF and DF (top left, bottom left respectively) images of the area indicated in Fig. 1 (b) by the light blue square. EDS spectra of the positions indicated by the red arrows as 1, 2 and 3 are also shown (right-hand side of Fig. 2). Each spectrum contains at least 100,000 counts for an energy range of 0 to 40 keV to ensure accurate identification of elements. As mentioned before, detection of Ag in Pd containing agglomerates was done using the higher energy K-edges situated at 21.2 keV for Pd and 22.2 keV for Ag in order to avoid complications that may arise with the use of L-edges due to a significant overlap of Pd and Ag L-edges (2.8 keV for Pd, 3 keV for Ag). An additional complication is the presence of a U M-edge at 3.2 keV. The EDS spectra in Fig. 2 indicate the presence of Pd (K-edge, L-edge) and U (M-edge) along with Si (K-edge) and C (K-edge) at the three regions indicated by the red arrows (bottom left). In addition, the presence of Ag (L-edge) and Cd (L-edge) was identified at position 3 from a sub 5 nm fission product precipitate. The concentration of the Ag and Cd at position 3 was below the EDS quantification limit.

The improved collection efficiency of the large angle, windowless EDS detector, as well as enhanced sensitivity enabled the detection of small concentrations of elements before beam-induced dispersion of beam sensitive elements could occur. This system made it possible to identify fission products from sub 5 nm precipitates or agglomerates in SiC.

**Figure 3** (a) to (d) show HAADF and ADF images of areas in the SiC layers containing nanometer sized fission product agglomerates along with their associated EDS spectra. Figure 3 (a) shows the presence of a Ni rich fission product cluster in a SiC grain. Figure 3 (b) shows the presence of a Cs containing precipitate along a SiC grain boundary and Fig. 3 (c) shows a triple point agglomeration containing Pd, U, Ag and Cd. Fig. 3 (d) is a HAADF STEM lattice image showing a small Pd atomic cluster in a SiC grain. The accurate identification of low concentrations of fission products and their location in the SiC lattice provides essential information needed to develop fission product transport models in the SiC layer of TRISO particles.

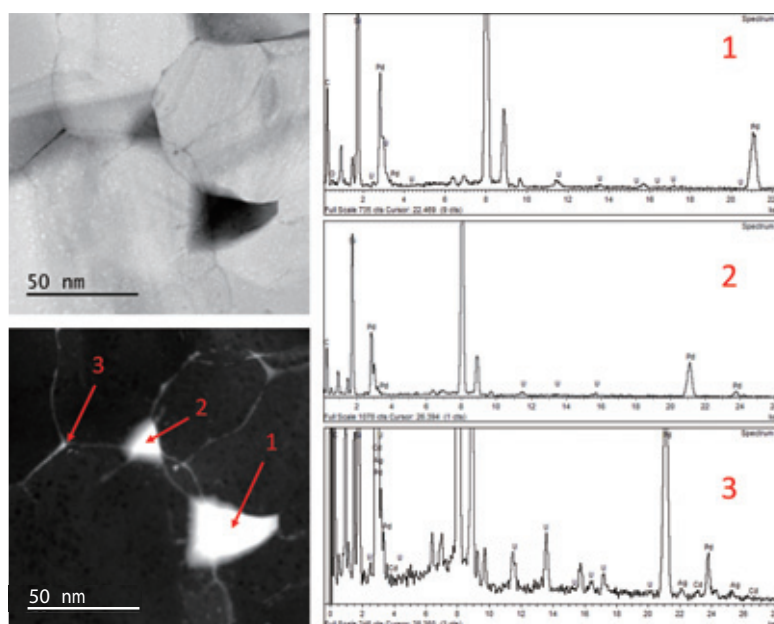
**Figure 4** (a) and (b) shows complimentary atomic resolution BF and HAADF STEM images of fission products present along the SiC grain boundaries. The fission products are visible as

sub nanometer-size agglomerations with single fission product atoms observed at certain points (e.g., indicated by yellow arrow in Fig. 4(b)). The EDS spectrum (Fig. 4 (c), obtained from area indicated by the red oval in Fig. 4 (b)) indicates that the fission product agglomerations consist mainly of Pd with U, which is consistent with earlier publications [5, 11-13]. The presence of fission product agglomerates along SiC grain boundaries may indicate that grain boundary diffusion is the dominant diffusion mechanism, however, contributions from intra-granular diffusion routes cannot be excluded since these fission product diffusants would most likely coalesce at sinks such as grain boundaries.

**Figure 5** (a) and (b) shows two HAADF images of fission products present in a SiC grain. Figure 5 (a) shows the EDS identification a Pd precipitate in the SiC lattice while Fig. 5 (b) shows a faceted palladium silicide in the SiC lattice with corresponding EDS spectrum. A fast Fourier transform of the faceted palladium silicide is shown on the right-side of Fig. 5 (b). The palladium silicide phase was identified as Pd<sub>2</sub>Si. These results indicate that intragranular bulk diffusion of Pd in SiC occurs as well as the precipitation of the Pd at sinks inside the grains.

**Figure 6** (a) shows a HAADF STEM image of an area in the SiC grain containing sub-nanometer size fission product precipitates seen as bright regions in the lattice. Furthermore, it is observed that a high concentration of twins and stacking faults with dislocations (Fig. 6 (b)) associated with its termination points in the SiC lattice are present in the area. Figure 6 (c) shows an inverse fast Fourier transform (FFT) filtered and false coloured image of the area shown in Fig. 6 (a) by the red square, generated using spatial frequencies associated with principle crystallographic planes. The resultant image provides a clearer view of the positions and lattice termination points of planar defects in this area. From this image, the position of fission products (precipitates as well as single atom columns) is seen to coincide with the positions of the termination points of planar defects in Fig. 6 (c). The presence of fission products at the dislocations associated with twins or stacking faults is consistent with diffusion along dislocation cores, but contributions from bulk diffusion to sinks such as the dislocation cores cannot be excluded. Stacking faults in 3C-SiC are bounded by Shockley

**Fig. 2**



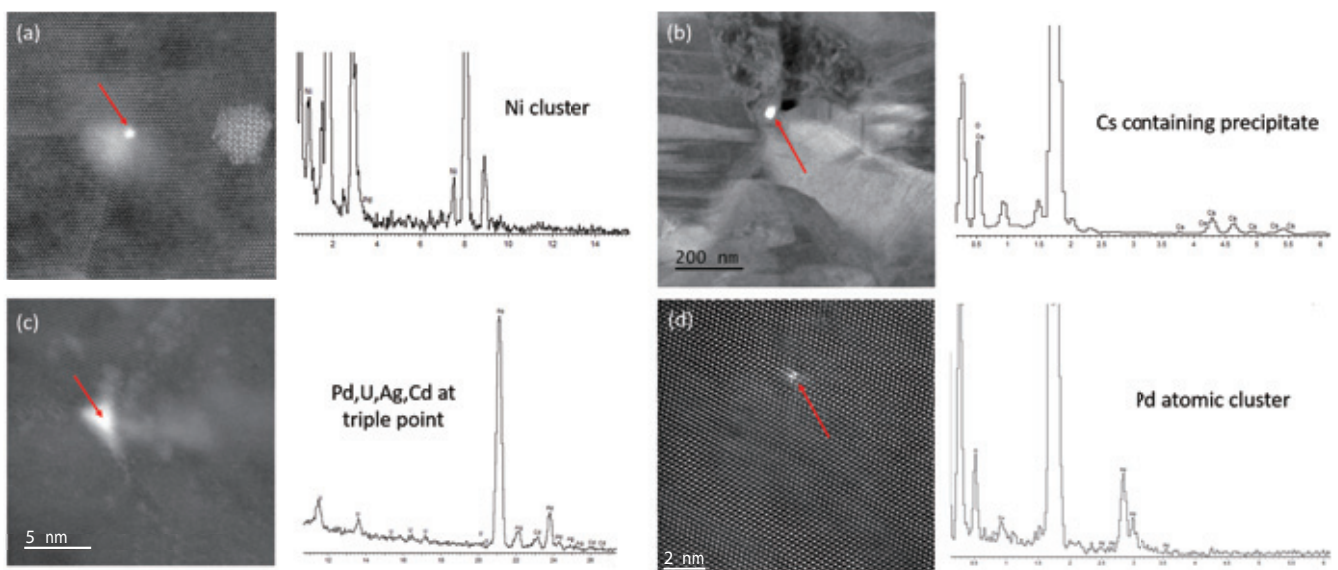
Complimentary BF and DF (top left, bottom left respectively) images of the area indicated in Fig. 1 (b) by the light blue square. EDS spectra of the positions indicated by the red arrows as 1, 2 and 3 are shown (right-hand side of Fig. 2) (Originally published by van Rooyen et al. (2016) [5])

partial dislocations. When Shockley partial dislocations from two intersecting {111} planes react, a pure edge dislocation lying parallel to the <110> line of intersection is formed. This dislocation is called a Lomer-Cottrell dislocation [14]. Figure 6 (b) is a view along the core of an unoccupied Lomer-Cottrell dislocation present at the intersection of two stacking faults.

To gain a better understanding of the chemical bonding characteristics of atomic fission products at SiC grain boundaries, an EELS spectrum imaging study of an area containing fission product agglomerations was carried out. **Figure 7** (a) shows a SiC grain boundary containing the fission product atoms Pd and U, as identified by EDS. The green rectangle indicates the area from which the spectrum image was obtained. The acquisition was done using an energy range of 0

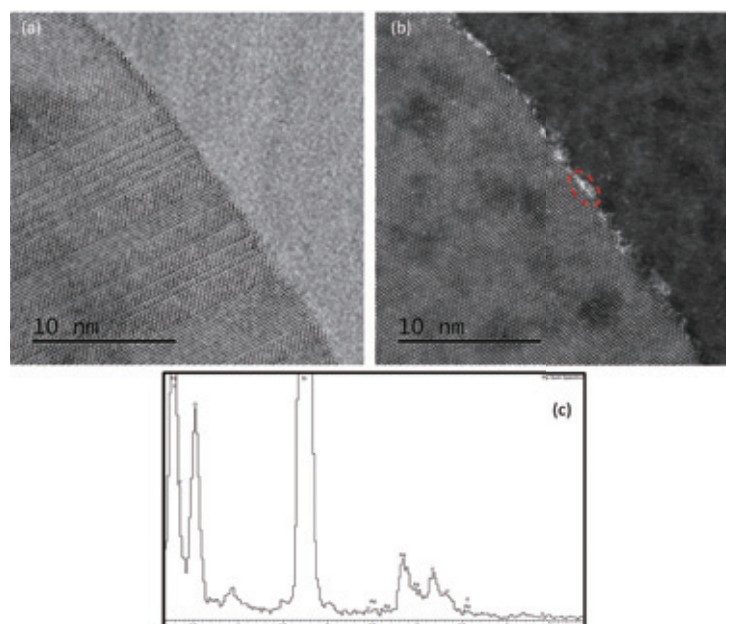
to 550 eV energy loss and an energy channel width of 0.25 eV. Figure 7 (b) shows the electron energy loss spectra for the Si L and C K edges obtained from the SiC matrix (blue spectrum) and from the fission product containing boundary (red spectrum). The inset in Fig. 7 (b) is a magnification of the C K spectra. The fine structure of both the Si L and C K edges for the fission product containing boundary differs significantly from the spectrum representing the SiC matrix. Pronounced rounding of both edges in the spectrum structure is observed. This indicates a change in the bonding environment that is different from the SiC matrix crystal. The change in the fine structure of the C K edge is accompanied by the presence of a pre-edge feature situated at 278 eV energy loss. This is indicative of a  $\pi$  bonding state, most likely due to the presence of C-C bonding, as found in graphite

**Fig. 3**



HAADF and ADF images of areas in the SiC layers containing nanometer sized fission product agglomerates along with their associated EDS spectra. (a) Ni rich fission product cluster in a SiC grain, (b) Cs containing precipitate along a SiC grain boundary, (c) Triple point agglomeration containing Pd, U, Ag and Cd, (d) HAADF STEM lattice image showing a small Pd atomic cluster in a SiC grain.

**Fig. 4**



Complimentary atomic resolution (a) BF and (b) HAADF STEM images of fission products present along the SiC grain boundaries. (c) EDS spectrum from the area indicated by the red oval in (b).

or amorphous carbon. It has been reported by other workers that during high-temperature corrosion of SiC by Pd, Pd reacts with Si to form a silicide, while the carbon atoms precipitate as carbon clusters [15, 16].

Figure 7 (c) and (d) show maps of the spatial distribution of matrix bonded Si L and  $\pi$  bonded C in the area investigated. Figure 7 (c) was obtained by doing a multiple linear least squares (MLLS) fitting on the area using the reference Si L edge obtained from the SiC matrix area. A low index of fitting is observed at the fission product boundary area due to the previously mentioned change in bonding environment. Figure 7 (d) was obtained by mapping the residual signal above background obtained from a 5 eV energy window fitted over the  $\pi$  bonding related pre-edge as discussed. A definitive increase in signal is obtained at the fission product boundary position. Figure 7 (e) is a map of metallic fission products (FPs) along the SiC boundary area. This was generated by contrast thresholding of the simultaneously obtained HAADF image of the area due to its contrast dependence on atomic number. From these findings it may be inferred that the fission product agglomeration could consist of a disordered solid solution due to a change in the Si bonding environment and the identification of possible C-C type bond arrangements.

The ongoing research confirming the role of Pd in enhancing Ag transport in irradiated SiC, has important implications for HTGRs. TRISO coated fuel particles are used in both the Chinese pebble bed core [17] and the Japanese prismatic core (HTTR) [18] HTGRs. We believe that the presence of palladium along SiC grain boundaries provide fast diffusion paths for silver, hence small modifications to the TRISO particles and prismatic fuel assemblies should increase its retention capabilities of the fission products Pd and Ag.

## Conclusions

The acquisition of an analytical double Cs-corrected JEOL JEM-ARM200F in South Africa enabled us to solve several long-standing materials problems of technological interest. These problems include the atomic arrangement in nitrogen containing {001} platelet defects in type Ia diamond, the phase of Ag-Pt alloys, nature of small dislocation loops in neutron irradiated n-type GaAs and the transport mechanism of silver in the 3C-SiC layer of irradiated TRISO particles. Analytical Cs-corrected STEM has without doubt established itself as an essential technique for the analysis of materials at the nanoscale. The range of useful techniques includes atomic scale and

**Fig. 5**

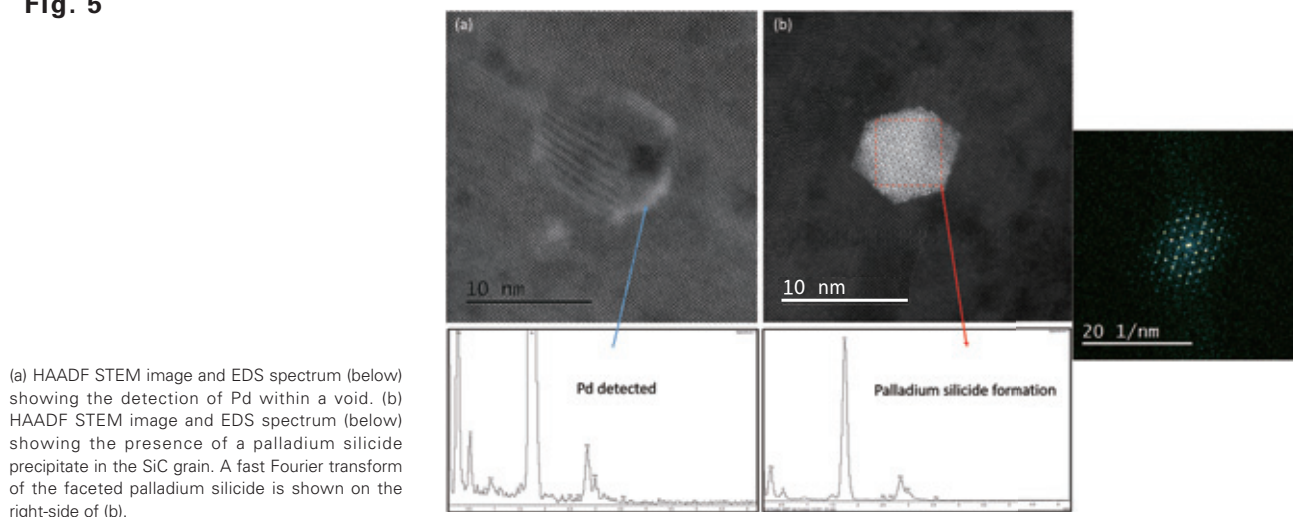


**Fig. 6**

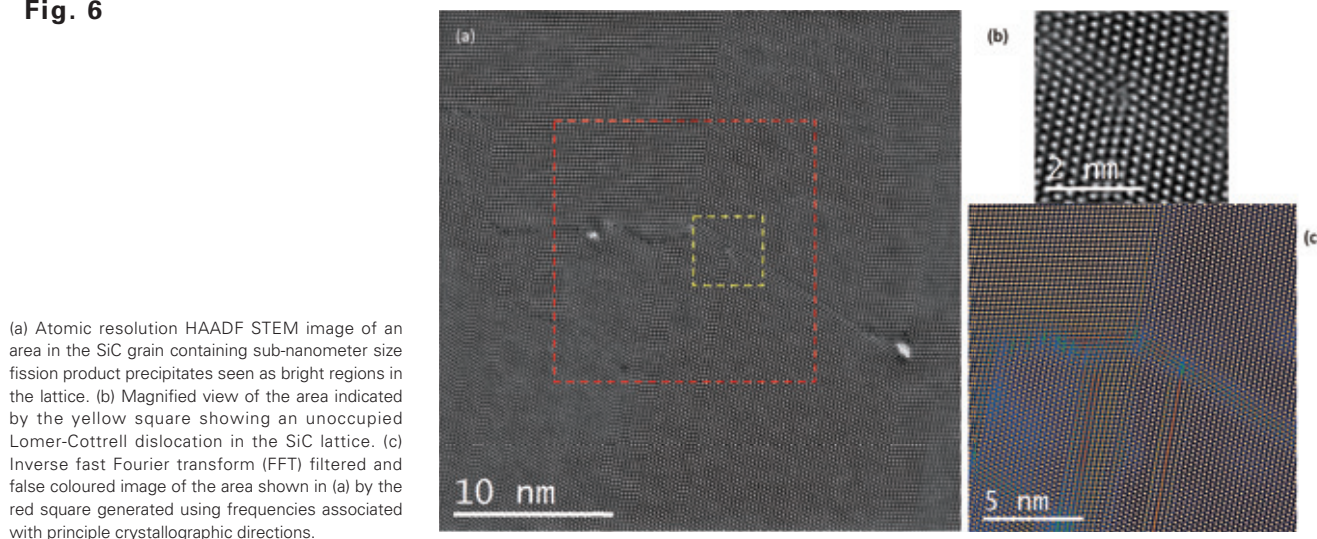
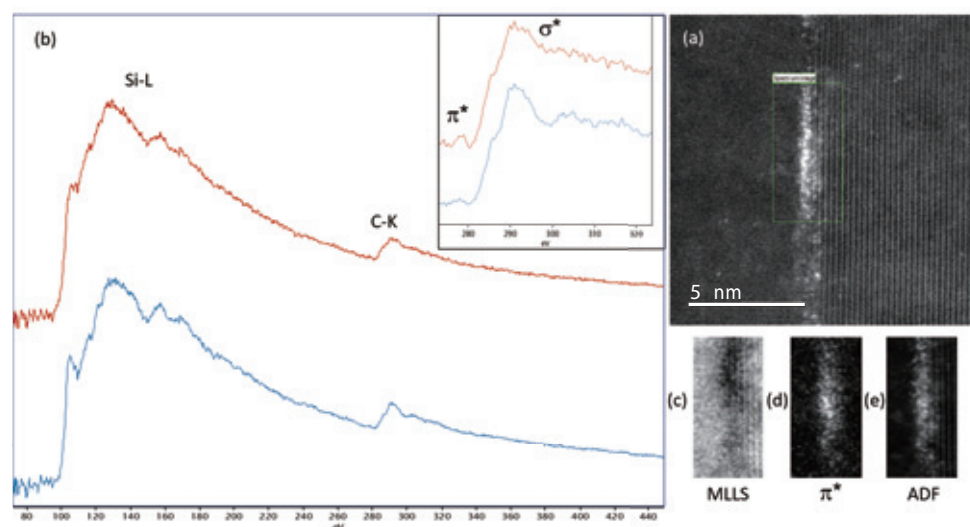


**Fig. 7**

(a) SiC grain boundary containing the fission product atoms Pd and U. The green rectangle indicates the area from which the EELS spectrum image was obtained. (b) Electron energy loss spectra for the Si L and C K edges obtained from the SiC matrix (blue spectrum) and from the fission product containing boundary (red spectrum). Inset in (b) is a magnification of the C K spectra. (c) Multiple linear least squares (MLLS) fitting on the area using the reference Si L edge obtained from the SiC matrix area. (d) Map of the residual signal above background obtained from a 5 eV energy window fitted over the  $\pi$  bonding related pre-edge situated at 278 eV. (e) Map of metallic fission products (FPs) along the SiC boundary area obtained using contrast thresholding.



Z-contrast imaging, chemical analysis using EDS and EELS and atomic bonding characteristics using EELS.

## Acknowledgments

The National Research Foundation, the Department of Science and Technology of South Africa and Sasol are acknowledged for their financial support. The authors would like to thank our collaborator at Idaho National Laboratory (US), Dr Isabella van Rooyen, for the SiC sample that was cut from an AGR-1 TRISO particle.

## References

- [ 1 ] E. J. Olivier, J. H. Neethling, R. E. Kroon, S. R. Naidoo, C. S. Allen, H. Sawada, P. A. van Aken and A. I. Kirkland, Imaging the Atomic Structure and Local Chemistry of Platelets in Natural Type Ia Diamond, *Nature Materials* **17**, 243-248 (2018).
- [ 2 ] G. L. W. Hart, L. J. Nelson, B. J. Campbell, R. R. Vanfleeter, M. Sluiter, J. H. Neethling, E. J. Olivier, S. Allies, C. Lang, B. Meredig and C. Wolverton, Revisiting the revised Ag-Pt phase diagram, *Acta Materialia* **124**, 325-332 (2017).
- [ 3 ] J. H. Neethling, A. Janse van Vuuren, E. J. Olivier and P. A. van Aken, TEM and HAADF STEM Imaging of Dislocation Loops in Irradiated GaAs, *Acta Physica Polonica A* (in press, 2019).
- [ 4 ] H. Nabelek, P. E. Brown and P. Offerman Silver Release from Coated Particle Fuel Nucl. Technol. **35**, 483-493 (1977).
- [ 5 ] I. J. Van Rooyen, E. J. Olivier and J. H. Neethling, Fission products silver, palladium and cadmium identification in neutron irradiated SiC TRISO particles using a Cs corrected HRTEM, *J. Nucl. Mater.* **476**, 93-101 (2016).
- [ 6 ] B. G. Kim, S. Yeo, Y. W. Lee and M. S. Cho, Comparison of Diffusion Coefficients and Activation Energies for Ag Diffusion in SiC, *Nucl. Eng. Technol.* **47**, 608-616 (2015).
- [ 7 ] J. H. Neethling, J. H. O'Connell and E. J. Olivier, Palladium Assisted Silver Transport in Polycrystalline SiC, *Nucl. Eng. Des.* **251**, 230-234 (2012).
- [ 8 ] E. J. Olivier and J. H. Neethling, The Role of Pd in the Transport of Ag in SiC, *J. Nucl. Mater.* **432**, 252-260 (2013).
- [ 9 ] J. H. O'Connell and J. H. Neethling, Ag Transport in High Temperature Neutron Irradiated 3C- SiC, *J. Nucl. Mater.* **455**, 20-25 (2014).
- [ 10 ] P. J. Price, Neutron irradiation-induced voids in b-Silicon Carbide, *J. Nucl. Mater.* **48**, 47-57 (1973).
- [ 11 ] H. Wen and I. J. van Rooyen, Distribution of fission products palladium, silver, cerium, and cesium in the un-corroded areas of the locally corroded SiC layer of a neutron irradiated TRISO fuel particle, *J. Eur. Ceram. Soc.* **37**, 3271-3284 (2017).
- [ 12 ] B. Leng, I. J. van Rooyen, Y.Q. Wu, I. Szlufarska and K. Sridharan STEM/EDS analysis of fission products in irradiated TRISO-coated particles of the AGR-1 experiment *J. Nucl. Mater.* **475**, 62-70 (2016).
- [ 13 ] H. Wen, I. J. van Rooyen, J. D. Hunn and T. J. Gerczak, Electron microscopy study of Pd, Ag, and Cs in carbon areas in the locally corroded SiC layer in a neutron-irradiated TRISO fuel particle, *J. Eur. Ceram. Soc.* **38**, 4173-4188 (2018).
- [ 14 ] J. Yamasaki, S. Inamoto, Y. Nomura, H. Tamaki and N. Tanaka, Atomic structure analysis of stacking faults and misfit dislocations at 3C-SiC/Si(001) interfaces by aberration-corrected transmission electron microscopy, *J. Phys. D: Appl. Phys.* **45**, 494002 (2012).
- [ 15 ] K. Minato, T. Ogawa, S. Kashimura, K. Fukuda, M. Shimizu, Y. Tayama and I. Takahashi, Fission product palladium-silicon carbide interaction in HTGR fuel particles, *J. Nucl. Mater.* **172**, 184-196 (1990).
- [ 16 ] K. Bhanumurthy and R. Schmid-Fetzer, Experimental study of ternary Pd-Si-C phase equilibria and Pd/SiC interface reactions, *Zeitschrift Fur Metallkunde*, **87**, 244-253 (1996).
- [ 17 ] Z. Zhang, Z. Wu, D. Wang, Y. Xu, Y. Sun, F. Li and Y. Dong, Current status and technical description of Chinese 2x250MWth HTR-PM demonstration plant, *Nucl. Eng. Des.* **239**, 1212-1219 (2009).
- [ 18 ] K. Sawa and S. Ueta, Research and development on HTGR fuel in the HTTR project, *Nucl. Eng. Des.* **233**, 163-172 (2004).

# Analytical SEM and TEM: Applications in Product-related Material Development

Jörg Kaspar | Fraunhofer IWS Dresden, Germany

The present article sums up several years of experience of Fraunhofer IWS Dresden employing JEOL high resolution electron microscopes (JSM-7800F, JIB-4610F, JEM-2100) for characterization in product-related material development. After the introduction of the used microscopical, analytical and preparative equipment several examples of structural analysis from research projects in welding, surface hardening, additive manufacturing as well as thin films and coatings technology are presented. The achieved results show the capabilities and the benefit of advanced analytical electron microscopy in development and optimization of processes in advanced laser and surface technology.

## Introduction

Materials and material research form the background for many technological innovations. The desired materials properties depend, to a large extent, on their microscopic structure, making micro and nano analytical tools a necessity. Analytical scanning and transmission electron microscopy (SEM and TEM) play a key role as they provide profound structural information down to the nanoscale, and in the case of TEM, even to atomic level. Moreover, SEM and TEM allow to combine the three fundamental analytical methods of imaging, diffraction and spectroscopy in the same tool, collecting complementary information from surface and bulk and thus enabling for comprehensive analyses.

Electron microscopy has significantly contributed to tailoring the structure of materials with regard to their application-relevant properties. Electron microscopic methods are not only advantageous to address fundamental research but can also be used for further developing material-dependent manufacturing processes (e.g. joining, additive manufacturing, surface engineering), quality evaluation and improvement of the production process as well as failure analysis. In this respect, it is the goal, to utilize SEM and TEM for product-related material development and to offer this particular expertise to our customers and their product driven issues.

At Fraunhofer IWS the analytical electron microscopy is combined with comprehensive metallographic capacities, modern ion beam and electrolytic polishing sample preparation facilities and state-of-the-art materials testing capacities. The present article gives an overview of research activities in the field of material-related process and product development and demonstrates the excellent performance of the used JEOL electron microscopes and preparation techniques.

## Equipment

For the work presented in this paper the JSM-7800F SEM, the JIB-4610F multi beam system and the JEM-2100 TEM were used (**Fig. 1**). Our JSM-7800F is configured with an in-lens Schottky emitter delivering up to 400 nA beam current at 30 kV and a so-called “Gentle Beam Super High Resolution” (GBSH) function allowing a resolution of 0.7 nm guaranteed down to an acceleration voltage of 1 kV. It is equipped with a set of in-lens detectors for low-kV imaging and retractable backscattered (BSE) and scanning transmission (STEM) detectors. For elemental analysis we utilized energy and wavelength dispersive X-ray spectroscopy (EDS and WDS) systems AZtec X-Max and IncaWave by Oxford Instruments. Additionally, in our work SEM analysis was conducted with the JIB-4610F presenting a combination of a high power focused ion beam (FIB) machine and field emission (FE) SEM. In addition to an Aztec X-Max EDS system our JIB-4610F is equipped with an AZtec Electron Backscatter Diffraction (EBSD) analysis system allowing to study crystallographic structural information. TEM analysis was performed in a standard JEM-2100 (LaB<sub>6</sub>) electron microscope configured with a high resolution polepiece (HRP) and an AZtec X-Max EDS system.

Sample preparation for SEM analysis was performed by standard metallographic procedures including a sequence of cutting, grinding, polishing and sometimes etching. For advanced BSE imaging and EBSD analysis the samples were additionally electrolytically or vibratory polished in order to completely remove preparation induced artefacts and deformations. For the analysis of thin films and coatings as well as very heterogeneous materials, the IB-09010CP CROSS SECTION POLISHER™ (CP), based on Argon (Ar) ion beam bombardment was very successfully applied delivering clean, smooth and deformation

free transverse sections. Samples for TEM analysis were thinned to electron transparency by a sequence of grinding, polishing and Ar ion beam thinning in a Precision Ion Polishing System “PIPS695” (Gatan Inc.). For some applications electrolytic polishing with a “TenuPol-3” system (Struers) or the FIB lift-out specimen preparation technique in the JIB-4610F was utilized to obtain the TEM samples.

## Results and applications

The Fraunhofer IWS Dresden stands for innovations in laser and surface technology. The research fields include PVD and nanotechnology, chemical surface and reaction technology, thermal surface technology, generation and printing, joining, laser ablation and separation as well as microtechnology. All these activities benefit from a thorough structural characterization by electron microscopy. In the following a few revealing examples of this work will be given in order to demonstrate the potential of modern electron microscopic methods in product-related material characterization and development.

### Welding of dissimilar metals

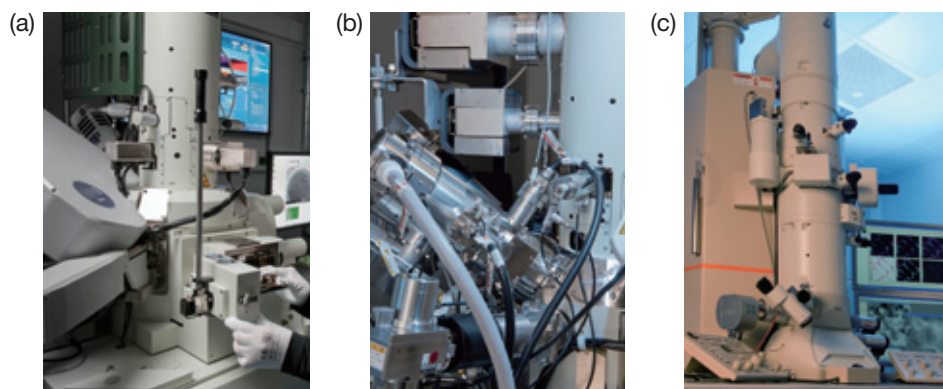
New materials and material combinations require efficient methods for the realization of dissimilar joints. In this regard Fraunhofer IWS focuses on such promising new technologies as laser beam welding, electromagnetic pulse welding (MPW), friction stir welding (FSW) and laser induction roll plating (LIRP) [1-3]. For example, the effective joining of aluminium (Al) with copper (Cu) is one of the central technical tasks involved in electromobility. However, the joining of these metals by conventional fusion welding is challenging because of

poor weldability arising from different chemical, mechanical and thermal properties of the materials. Especially the formation of pronounced intermetallic phases, which cause a drastic decrease of the mechanical strength, is identified as a major obstacle.

Comparing the different joining technologies, all of them seem basically suited to realize a dissimilar metal joint consisting of Al and Cu plates with reproducible bond quality. Generally, the formation of an intermetallic phase seam cannot be completely prevented. However, its size depends on the joining technology chosen and can be controlled in a certain range by optimizing process parameters and joint geometry. Applying laser welding, even with brilliant lasers in the kW power range and choosing high welding speeds it is not possible to reduce the thickness of the intermetallic interface layer in the laser weld below 10 μm [3]. As a consequence the strength of the mixed joint is always lower than that of the original Al material and the laser welded connection is very brittle.

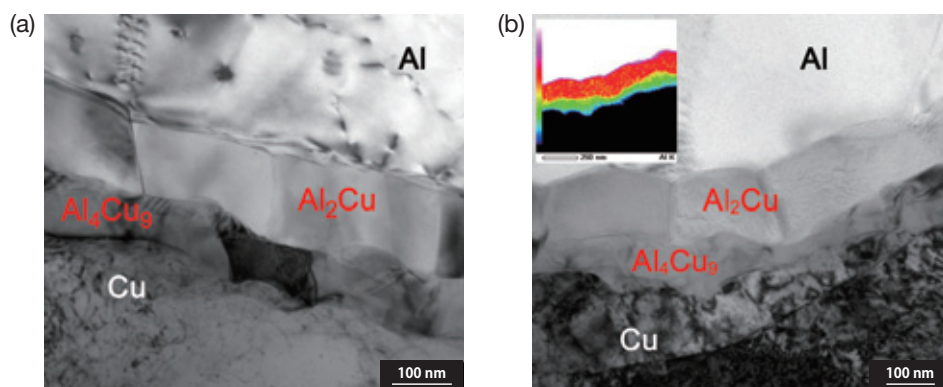
On the contrary, applying friction stir welding, laser induction roll plating or electromagnetic pulse welding for the joining task, the size of the intermetallic phase seam could be significantly reduced. Avoiding the massive melting of both joining partners it was possible to control the phase seam at 1 μm thickness or even below. As a result, the mechanical strength of the Al-Cu joint could be significantly improved if compared to the laser welded joints. TEM analysis including electron diffraction provided valuable information about the growth process and the nature of the phases formed (Fig. 2). For all three advanced joining technologies the seam is split into an Al<sub>2</sub>Cu phase on the Al side and Al<sub>4</sub>Cu<sub>9</sub> phase facing the Cu side. Besides ensuring a good and reliable joint quality and strength this kind of narrow phase seam also guarantees the low contact resistance mandatory for applications in electromobility.

Fig. 1



Equipment utilized for SEM and TEM analysis:  
a) JSM-7800F (SEM), b) JIB-4610F (dual-beam),  
c) JEM-2100 (TEM)

Fig. 2



Joining Al and Cu (overlap joints): TEM analysis of the intermetallic phase seam consisting of thin Al<sub>2</sub>Cu and Al<sub>4</sub>Cu<sub>9</sub>: a) Friction stir welding, b) Laser induction roll plating

## Surface strengthening of precipitation hardening steels

Precipitation-hardening martensitic stainless steels offer a good combination of strength, ductility and toughness, good fabrication characteristics and corrosion resistance as well as superior fatigue performance. Unlike quenched and tempered steels which gain their strength by the formation of carbon martensite, in precipitation hardening martensitic stainless steels small precipitations considerably contribute to strength. Hence, these steels contain precipitation-forming elements like Cu, Al, titanium (Ti) or niobium (Nb). In many applications precipitation hardening martensitic stainless steels must guarantee high ductility and toughness as well as low susceptibility to stress corrosion cracking. For this reason these steels are typically used in an overaged but not in the peak aged condition. However, if the application requires high wear resistance common surface heat treatments are not applicable for this kind of material. To overcome this drawback an effective surface modification technique has been developed at Fraunhofer IWS Dresden, which allows the selective generation of wear resistant surface regions up to several millimeters in depth without altering mechanical properties in the bulk of the material [4]. This surface age hardening technique consists first of selective short-time laser surface solution annealing (austenitization) at temperatures close to the melting point (approx. 1300 °C) to completely dissolve the precipitations in the near surface region and maintain a solid solution condition upon rapid self-quenching and phase transformation to lath martensite. It is followed, secondly, by an aging treatment at relatively low temperatures to optimally strengthen the laser annealed surface regions but leaving the bulk structure unchanged.

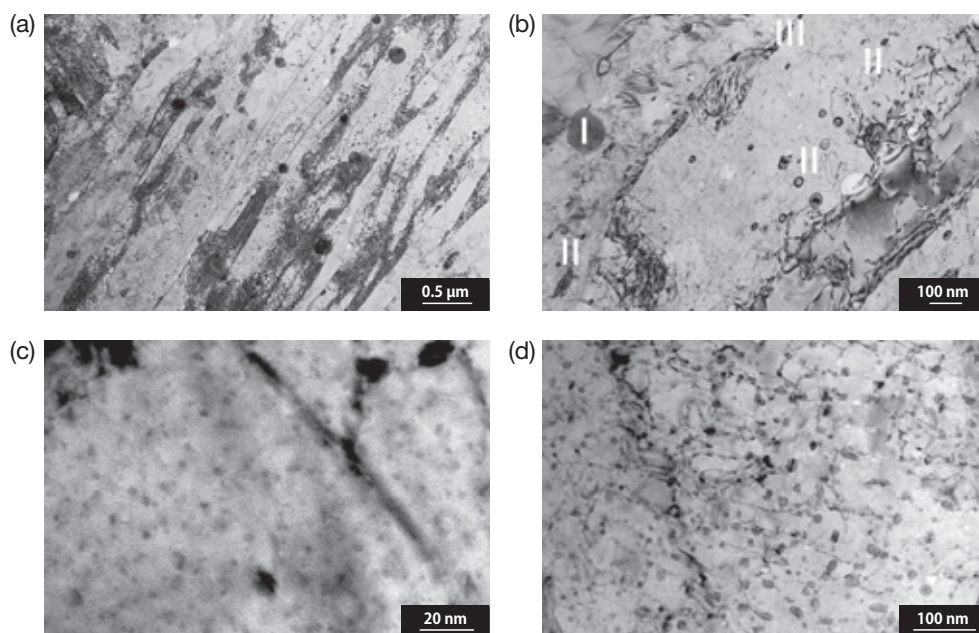
By choosing the appropriate laser and aging treatment, the hardness of precipitation-hardening steels (17-4 PH and PH 13-8) can be increased by more than 150 HV up to a depth of 4 mm. TEM analysis of the conventionally heat treated samples of the 17-4 PH steel (solution annealing 1050 °C / 0.5 h, aging 560 °C / 3 h) revealed a lath martensitic structure exhibiting a high dislocation density and small amounts of reverted austenite along the boundaries of the lath martensite (Figs. 3a and b). The precipitation structure consists of spherical NbC particles

(50-200 nm) and fine spherical fcc  $\epsilon$ -phase Cu precipitates varying in size from 10 to 50 nm (Fig. 3b). Figures 3c and 3d reveal that in the surface age hardened region the size of the Cu precipitates is much smaller, the precipitation density is much higher and the precipitation distribution is more homogenous than in conventionally heat treated samples. Peak-aging at 480 °C for 8 h predominately led to the formation of a very high amount of Cu-rich clusters only about 1-3 nm in size and homogeneously formed within the laths of the martensite. Overaging at 550 °C for 3 h resulted in a precipitation structure that is characterized by a dense and homogenous arrangement of fcc  $\epsilon$ -phase Cu-rich precipitations about 20 nm in size. Consequently, even if the aging conditions of conventional heat treatment and surface age hardening are comparable in the surface age hardened regions the precipitation density is significantly higher whereas the size of the Cu particles is much smaller than in the conventional state leading to the observed hardening. Similar results could be obtained for the PH 13-8 precipitation hardening steel even though the precipitations are of the Ni<sub>3</sub>Al type and not Cu. It could be shown that the surface age hardening treatment increases the cavitation erosion resistance of 17-4 PH by more than a factor of three [5]. Because of this encouraging result the novel surface age hardening technique was adjusted and successfully applied for the wear protection of low pressure turbine blades made of this steel.

## Laser metal deposition of high entropy alloys (HEA)

A new alloy design concept allowing several principal elements simultaneously (usually more than five) has stimulated the start of exploration of a vast composition space about 15 years ago [6, 7]. In this new field the term High Entropy Alloys (HEAs) is used if single-phase solid solution microstructures with simple crystal structures are intended. A special type of these alloys are refractory metal HEAs that usually contain four or more of the refractory elements Ti, V, Cr, Zr, Nb, Mo, Hf, Ta and W. Refractory metal HEAs are intended as new high temperature structural materials making use of their exceptionally high melting temperatures and strengths [8]. A typical representative of a body-centered cubic (bcc) single

**Fig. 3**



TEM analysis of the microstructure of 17-4 PH steel exhibiting different heat treatments: a and b) As-delivered: solution annealed (1050 °C / 0.5 h) and aged (560 °C / 3 h): I = NbC, II = Cu precipitates, III = reverted austenite c) Surface age hardening: laser annealed (1300 °C / 10 s) and aged (480 °C / 8 h) d) Surface age hardening: laser annealed (1300 °C / 10 s) and aged (550 °C / 3 h)

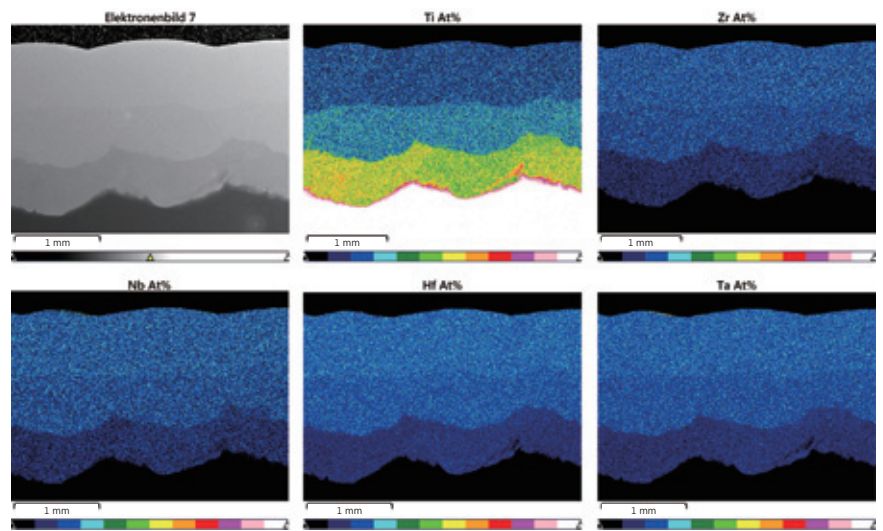
phase HEA is TiZrNbHfTa [9]. Because classical synthesis routes like casting are very complex and alloy fabrication is very costly it appears that additive manufacturing (AM), which can reduce material costs solely by local application, is a proper synthesis route for HEA utilization on an industrial scale. In a current study researchers at Fraunhofer IWS utilized for the first time laser wire deposition (LWD) for the synthesis of refractory type TiZrNbHfTa coatings on titanium substrate material.

Single and multiple tracks and layers of TiZrNbHfTa were successfully cladded on a substrate of cp Ti. Using optimized parameter settings it was possible to achieve defect free structures and a good adhesion to the substrate. Quantitative EDS maps demonstrate a rather homogeneous chemical composition within the individual cladded layers (Fig. 4). Due to the dilution with the titanium substrate material the chemical composition changes up to the third layer. In the first layer the Ti content is still about 52 at%, in the second layer about 26 at% and in the third layer about 18 at%. Already in the third layer a nearly equal atomic composition of all five elements was established. Generally,

macroscopic segregation did not occur in the laser cladded regions. Only on the microscopic scale a slight segregation of tantalum could be verified.

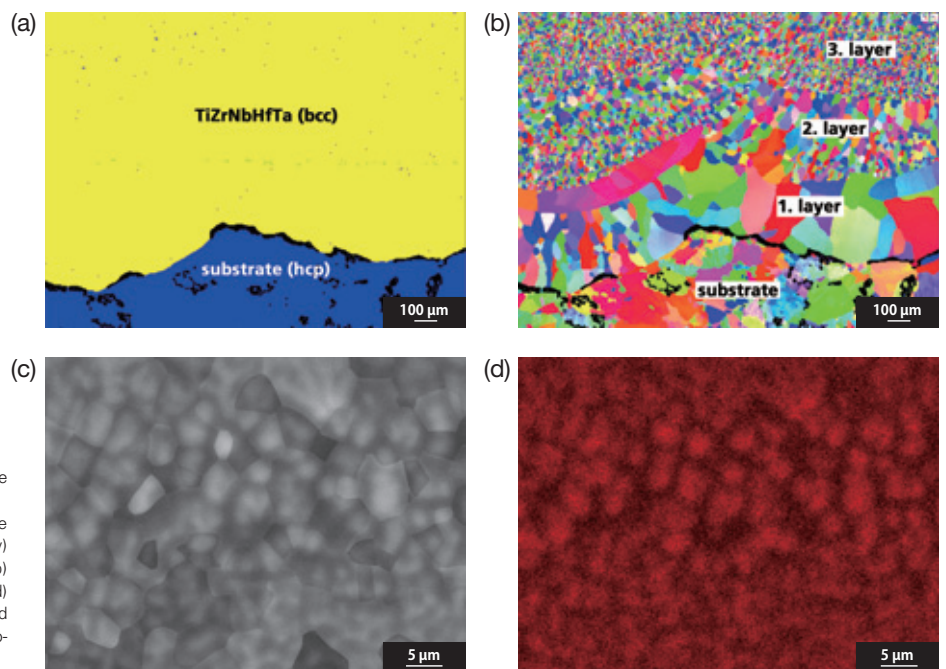
EBSD analysis revealed that all layers completely exhibit a solid solution bcc structure, independent of their different chemical compositions (Fig. 5). Consequently, no signs of second phase formation or precipitation could be revealed. The first Ti-rich layer reveals a coarse grained structure. Already in the second layer the grains are significantly smaller. In the third layer with nearly equal atomic composition a very fine-grained equiaxed microstructure has formed showing an average grain size of about  $20 \pm 5 \mu\text{m}$ . Furthermore, the micro-segregation of the heaviest constituent Ta is clearly revealed by the SEM analysis. The laser cladded layers exhibited hardness values up to 600 HV. Further microstructural analysis by means of TEM is intended in order to clarify if precipitation hardening took place during the cladding experiments or if the hardness of the laser cladded TiZrNbHfTa is mainly caused by the strong intrinsic solid solution hardening effect of HEA.

Fig. 4



Cross section of LWD samples of refractory type HEA alloy TiZrNbHfTa showing the elemental distribution within the individual layers analyzed by EDS mapping

Fig. 5



SEM structural analysis of LWD refractory type HEA alloy TiZrNbHfTa:  
 a) EBSD phase map (overview) showing the single phase bcc structure of the cladded layers (yellow) and the hcp structure of the Ti substrate (blue), b) EBSD orientation map (overview), c) BSE image & d) Ta elemental map (detail) showing the fine grained structure in the third cladded layer and the micro-segregation of Ta

## Development of nanometer multilayers and hard coatings for various applications

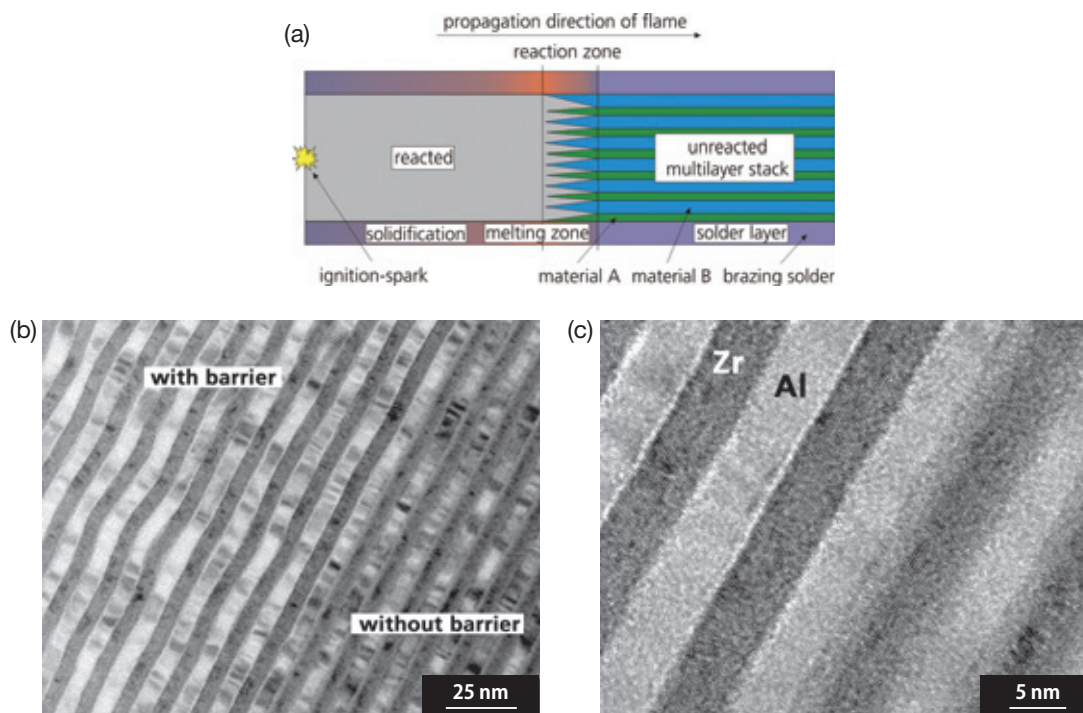
The Fraunhofer IWS develops and researches processes to synthesize various coatings based on physical vapor deposition (PVD). The range of work includes the fabrication of ultra-precise multilayer stacks using magnetron and ion beam sputtering techniques, various processes to deposit amorphous carbon coatings and high rate deposition techniques.

The first example visualizes the development of so-called reactive multilayer systems (RMS), which are applied in low heat impact joining processes for various material combinations [10]. Basically, the RMS consists of many single layers with nanometer thickness of at least two different materials (Fig. 6a). The ignition of the RMS initiates an exothermic reaction, which delivers heat very locally and only for the duration of milliseconds. This energy can be used to join various components including brass-brass, Al-Cu, Ti-Ti, Al-Ti, Si-ceramics or different plastic-metal combinations without significantly heating the main components. By designing the RMS, it is possible to influence the propagation velocity of the reaction, the released amounts of heat and the peak temperature. Thus it is possible to optimize the RMS for a specific application. This can be done by the choice of the material system (e.g. Ni/Al, Zr/Si or Zr/Al), the stoichiometric ratio of the two elements and the thickness of the whole stack. Another important aspect during the development of RMS is the suppression of inter-diffusion between the individual layers during fabrication. Figures 6b and c show bright field TEM images of a Zr/Al RMS stack in transverse section. Both, Zr and Al form crystalline layers having thicknesses of only about 5 nm and 6 nm, respectively. TEM analysis furthermore revealed the high precision of the nanometer multilayers over the whole stack. However, if the individual Al and Zr films are deposited directly on the top of each other a strong inter-diffusion takes place leading to transition zones of up to 2 nm thickness. This unfavorable inter-

diffusion, that strongly reduces the efficiency of the chemical reaction, can be completely inhibited by the application of a specific barrier layer.

The second example describes the development of wear-reducing hard coatings applied for cutting, machining and forming tools (Fig. 7a). Hard coatings based on metal nitrides (e.g. TiN, AlTiN, CrN) are usually fabricated up to approx. 10 µm thickness by PVD and CVD based processes. For many applications thicker coatings would offer a better wear protection than these conventional thin films. The difficulties associated with the synthesis of thick hard coatings are (I) residual stresses, (II) the strong columnar structure and (III) the growth of defects within the coating. With the help of analytical SEM and TEM studies engineers at the Fraunhofer IWS succeeded to control these critical aspects, which enabled them to fabricate hard coatings with a thickness of more than 100 µm [11]. The first approach for structural optimization involved the generation of a nano-layered structure for the system AlCrN/TiN (Fig. 7b). In the laboratory such stacks can be produced by arc evaporation of two different targets in a nitrogen atmosphere, either by alternately using the sources or by turning the samples past the simultaneous employed targets. Hardness as well as residual stress levels can be controlled by choosing appropriate period thicknesses. The second aim of structural optimization was the suppression of the strong columnar grain growth. This was achieved by adding small amounts of Si to the AlCrN/TiN system which restricted the dimensions of the nitride grains to some ten nanometers or even smaller (Fig. 7c). Finally, the IWS researchers also found solutions for the suppression of the harmful defect growth. Already the nano-layered structural design very effectively hinders defect growth in the hard coatings. Another innovative approach to defect growth suppression is the utilization of highly ionized plasmas. For instance, using enhanced arc deposition processes highly charged plasma particles remove unwanted

**Fig. 6**



Development and TEM characterization of Zr/Al RMS multilayer

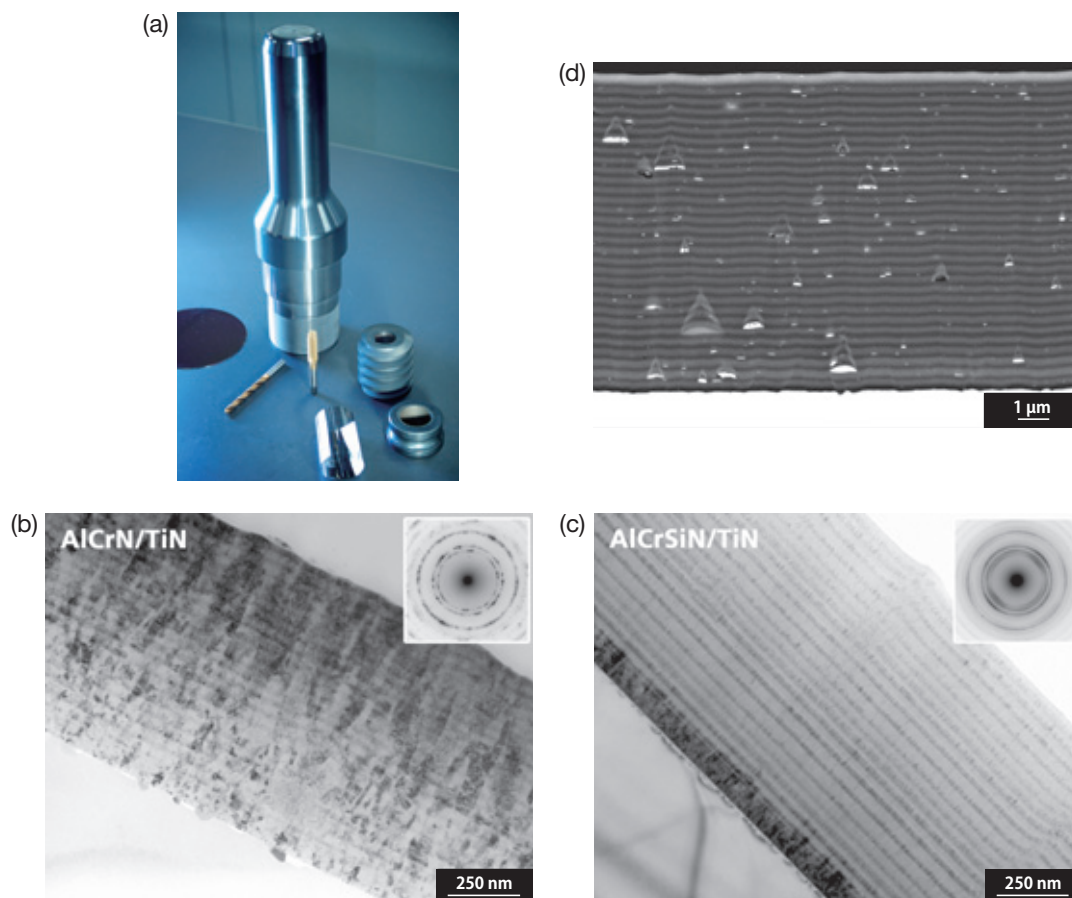
a) Schematic of the setup and principle of RMS, b and c) TEM micrographs (overview and detail) of cross sections through the multilayer coating (left: with barrier coating, right: without barrier coating)

roughness resulting from droplets deposited and embedded in the coating. SEM analysis verifies that these inhomogeneities are covered and flattened in the course of the layer growth by the combined effect of nano-multilayers and high ionization energies (Fig. 7d). Various laboratory and application tests have demonstrated that the IWS hard coatings show high hardness and abrasion wear resistance and stability at high surface pressures [12].

Even though nano-structured hard coatings allow high hardness and effective abrasive wear protection the adhesion against metals, characterized by the friction coefficient in dry contact, nevertheless, remains on a rather high level of 0.5 to 0.8 [12]. A significant reduction to values below 0.2 or even below 0.1 is feasible with covalently bonded carbon films. Scientists at Fraunhofer IWS have developed a laser arc method by which tetrahedrally bonded amorphous carbon films (ta-C) can be efficiently deposited [13]. For the ta-C material it is characteristic, that it shows the tetrahedral diamond structure only in the near range, without forming long-range crystallites. The resulting hardness of 40 to 80 GPa lies only little below the diamond top value but is far above the level of conventional hard coatings. In application such coatings have to endure severe conditions regarding loads and environment. One major demand on the coating is a good adhesive strength. For this purpose different designs of bonding layers have been evaluated and characterized by means of scratch test and SEM surface analysis [14]. Furthermore, for detailed analysis of the interfaces between substrate, bond layer and ta-C coating thorough SEM

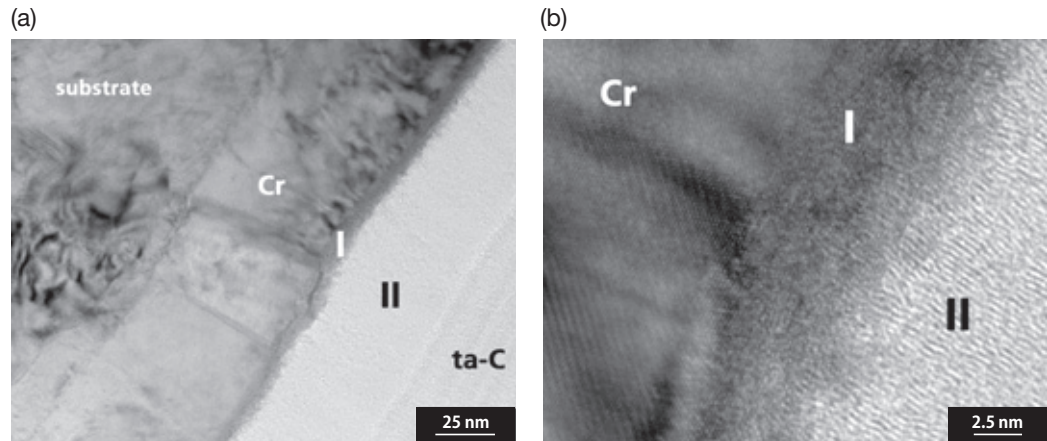
and TEM investigations of transverse sections have been conducted. High resolution SEM analysis revealed that one predominant de-bonding mechanism is cohesive failure shortly above the bond layer in the ta-C film. TEM analysis reveals the complex structure of the interface region. Typically, directly on the substrate material, usually being a tool steel or a hard metal, a carbide forming metal like Cr, Ti or W is deposited as first part of the bonding layer (Fig. 8a). This metal layer is usually some hundreds of nanometers thick and exhibits a columnar grain structure. The transition zone between metallic bonding layer and ta-C coating characteristically consists of two specific sub-areas. Figure 8b visualizes that an approx. 5-10 nm thick nearly amorphous Chromium carbide ( $\text{CrC}_x$ ) film forms directly on the metallic layer. Remarkably, a further transition zone has developed directly above this carbide film, where actually the amorphous ta-C coating should start. Within this typically 10-40 nm thick zone the structure strongly differs from the typical amorphous structure of the remaining ta-C coating. Consequently, this transition zone shows a graphene like structure with a strong orientation of the graphitic layers in growth direction. It is concluded, that the transition zone between the metallic bonding layer and the ta-C functional coating plays a decisive role for the bonding strength of ta-C coated tools in industrial applications. In a recent publication the high potential of ta-C coatings for friction reduction down to the superlubricity level has been established, using environment friendly and renewable fatty acid-based lubricants on ta-C coated surfaces [15].

**Fig. 7**



Multilayer hard coatings for wear reduction of tools

a) Examples of coated tools, b and c) TEM and diffraction (inserts) micrographs of hard coatings exhibiting different grain growth (b: AlCrN/TiN: columnar structure, c: AlCrSiN/TiN: nanocrystalline structure), d) SEM Cross section: Self-healing capacity reducing the detrimental effects of defects in the coating

**Fig. 8**

TEM micrographs of cross sections through the bonding zone of ta-C hard coatings deposited on components of tools steels: (from left: steel substrate, bcc Cr layer, nearly amorphous  $\text{CrC}_x$  (I), graphene like modified C (II), ta-C coating)

## Summary

This article demonstrates the capabilities and the benefit of advanced analytical electron microscopy in the development of processes and technologies which depend on materials or material properties. Furthermore, the presented work shows how the materials characterization group at Fraunhofer IWS applies its methods and its know-how to provide materials research for product development across different technologies. This is visualized through several examples of electron microscopic investigations in the research fields of welding, surface hardening, additive manufacturing and thin films and coatings. It is concluded that the conducted microscopic characterization enables us to achieve a profoundly increased understanding of process-structure-property relations. This knowledge is a prerequisite for the successful development of new material-dependent technologies as well as process optimization and validation.

## Acknowledgments

The author would like to thank his colleagues Prof. Berndt Brenner, Georg Dietrich, Volker Fux, Andreas Grimm, Dr. Frank Kaulfuss, Dr. Liliana Kotte, Erik Pflug, Dr. Jens Standfuss, Dr. Otmar Zimmer and Dr. Volker Weihnacht for the described technological development from which the samples were taken for analysis and Dr. Jörg Bretschneider, Anja Mittag, Martin Kuczyk, Dr. Arnold Luft and Andrea Ostwaldt for contributing to the analysis as well as performing the challenging and time consuming sample preparation.

## References

- [ 1 ] M. Krätzsch, J. Standfuß, A. Klotzbach, J. Kaspar, B. Brenner, E. Beyer, "LBW with high frequency beam oscillation: Welding of dissimilar materials with brilliant fibre lasers", *Phys. Proc.*, **12**, 142-149 (2011).
- [ 2 ] G. Göbel, E. Beyer, J. Kaspar, B. Brenner, "Dissimilar metal joining: Macro- and microscopic effects of MPW", *Proceedings of the Int. Conf. on High Speed Forming (ICHSF)*, **5**, 179-188 (2012).
- [ 3 ] J. Kaspar, M. Zimmermann, A. Ostwaldt, G. Goebel, J. Standfuß, Brenner, "Challenges in joining aluminium with copper for applications in electro mobility", *Materials Science Forum*, **783-786**, 1747-1752 (2014).
- [ 4 ] B. Brenner, F. Tietz, "A method for producing wear resistant surface layers of hardenable materials", German

Patent DE10030433C2, 2002.

- [ 5 ] J. Kaspar, B. Brenner, A. Luft, F. Tietz, J. Bretschneider, "Enhanced wear resistance of precipitation hardening steels by laser solution annealing and subsequent aging treatment", *Proc. Of the Int. Symp. on Friction, Wear and Wear Protection*, Eds. A. Fischer, K. Bobzin, Wiley-VCH GmbH & Co. KGaA, 654-659 (2008).
- [ 6 ] B. Cantor, I.T.H. Chang, P. Knigh, A.J.B. Vincent, "Microstructural development in equiatomic multicomponent alloys," *Mater. Sci. Eng., A* **375-377**, 213-218 (2004).
- [ 7 ] J.-W. Yeh, S.K. Chen, S.J. Lin, J.Y. Gan, T.S. Chin, T.T. Shun, C.H. Tsau, S.Y. Chang, "Nanostructured high-entropy alloys with multiple principal elements: Novel alloy design concepts and outcomes", *Adv Eng Mater.*, **6**, 299-303 (2004).
- [ 8 ] D. B. Miracle, O.N. Senkov, "A critical review of high entropy alloys and related concepts", *Acta Materialia*, **122**, 448-511 (2017).
- [ 9 ] O. N. Senkov, J.M. Scotta, S.V. Senkova, D.B. Miracle, C.F. Woodward, "Microstructure and room temperature properties of a high-entropy TaNbHfZrTi alloy", *Journal of Alloys and Compounds*, **509**, 6043-6048 (2011).
- [ 10 ] G. Dietrich, M. Rühl, S. Braun, A. Leson, "Reactive nanometer multilayers for high-precision bonding", *Vakuum in Forschung und Praxis*, **24**, 9-15 (2012).
- [ 11 ] T. Krülle, F. Kaulfuss, O. Zimmer, C. Leyens "Nano-Design für Makroschichten: Anwendungsperspektiven für PVD-Beschichtungen bis 100  $\mu\text{m}$  Dicke", *Vakuum in Forschung und Praxis*, **30**, 46-49 (2018).
- [ 12 ] F. Kaufuss, O. Zimmer, "Temperaturstabile Hartstoffschichten zur Standzeitverlängerung von Schmiedewerkzeugen", E. Leuze Verlag, *Jahrbuch Oberflächentechnik*, **70**, 61-70 (2014).
- [ 13 ] A. Leson, G. Englberger, D. Hammer, S. Makowski, C.-F. Meyer, M. Leonhard, H.-J. Scheibe, V. Weihnacht, "Diamond-like carbon thin films enhance efficiency - Laser arc deposition of ta-C", *Vakuum in Forschung und Praxis*, **27**, 24-28 (2015).
- [ 14 ] M. Zawischa, S. Makowski, N. Schwarzer, V. Weihnacht, "Scratch resistance of superhard carbon coatings – A new approach to failure and adhesion evaluation", *Surface and Coatings Technology*, **308**, 341-348 (2016).
- [ 15 ] S. Makowski, F. Schaller, V. Weihnacht, G. Englberger, M. Becker, "Tribochemical induced wear and ultra-low friction of superhard ta-C coatings", *Wear*, **392-393**, 139-151 (2017).

# Practical Solutions in Electron Beam Lithography with the JBX-9500FS and the JBX-6300FS

D. M. Tennant, A. Banerjee, C. Treichler and A. R. Bleier

Cornell NanoScale Science and Technology Facility

State of the art electron beam lithography instruments such as the JEOL JBX-9500FS are higher resolution, faster, and more precise than previous generation tools. As such, modern electron beam lithography systems are finding widespread use in R&D facilities to pattern devices and structures for many novel interdisciplinary projects. But as highly experienced practitioners have come to know, there can be very important elements that must go into solving some of the more challenging lithographic applications, many of them related to how the pattern data are generated and manipulated in specialized software. This paper introduces some of the data centric solutions that the staff at the Cornell NanoScale Science and Technology Facility (CNF) have implemented, and now make available, to make tedious data manipulation more automated and to solve two specific issues that users at our facility posed to us. One issue relates to sharpening of lithographically patterned geometric shapes as the features are made smaller where they would normally smooth out. The other describes a method of patterning on 3D surfaces such as a tilted surface or a spherical lens.

## Introduction

The Cornell NanoScale Science and Technology Facility is an open, shared laboratory where users from the world over come to fabricate their novel research and development devices. Among its 180 research instruments are included two state-of-the-art electron beam lithography systems, the JEOL JBX-6300FS and the JEOL JBX-9500FS. The JBX-9500FS is a flagship tool that combines high resolution, 100 MHz deflections speed, and a precise laser interferometer controlled stage that, when taken together, can produce very fine and very accurately placed patterns. As such, modern electron beam lithography systems are finding widespread use in R&D facilities to pattern devices and structures for many novel interdisciplinary projects. But as highly experienced practitioners have come to know, there can be very important elements that must go into achieving the goals of some of the more challenging lithographic applications. Many of these elements relate to how the pattern data are generated and manipulated in specialized software. To facilitate the various scenarios that we have seen from among our many user projects over the past decade one of us (J. C. Treichler) has written a freeware lithographic software package called JETStream [1]. It is a software tool that can generate industry standard data format, GDSII files, with a program or a script. It contains a java library that can be used with another java program or, with proper configuration, a python script. Below we describe how JETStream might be used and give both a simple illustration of its use, and follow that with an example of how it was applied to the task of calibrating and focusing an exposure in which the e-beam writing takes place on non-planar substrates such

as a ramp or a spherical surface. In a second application we describe the use of GenISys BEAMER software [2] to meet a very different challenge. One in which geometric shapes such as squares, hexagons and triangles, etc. were losing their sharp vertices as the size of the structures was patterned below 50 nm. Using the advanced features of BEAMER, modifications of the pattern fracturing were made to help restore these features.

## Introduction to JETStream

JETStream allows for its users to automate the creation or modification of GDSII files. For some researchers, this is the preferred way to generate most of their CAD. These users can also create libraries of parametric parts or graphical interfaces for other users. For example, at the CNF we write reticles for our steppers. The steppers require certain marks, barcodes, labels ... to be able to use the reticles. We have written a graphical program that asks the user to select the target tool for the reticle, type in the label and barcode and then the program generates the desired reticle frame. The frame generating function that is used by the graphical program is in a library of parametric parts and could be used directly by someone programming their CAD. The structure of a program to create CAD is similar to the structure of a GDSII file. A library, the document that contains the CAD, is created and a "cell" is added to it. Each cell should have a unique name. A cell can contain polygons and/or references to other cells. A reference to a cell sets the position, mirroring, magnitude and possible arraying of the cell. JETStream supports non-orthogonal arrays. The polygons can be defined by a series of points and a layer, or as paths defined by series of points, a width and a layer. There

are convenience methods that create regular polygons, rectangles and text shaped polygons. Vectorized fonts on the computer running the program are available allowing for non-English labels. These polygons and paths may also have segments that are a cubic or quadratic Bezier curve. These curved segments will get “flattened” to multiple linear segments with a user specified maximum error when written to GDSII. Polygons can be modified with Boolean operations with other polygons or transformed by mirroring, translating, scaling, growing/shrinking or applying an affine transform. Boolean operators can work through hierarchy to generate polygons from the logical combinations of the shape of flattened cells extracted by layer or layers. It is also possible to extract a layer with the hierarchy preserved. This can keep a file much smaller than extracting a layer by flattening the hierarchy.

Here is a sample java program that will generate a GDSII file called Hello.gds. The file will contain a cell called top that has polygons on layer 2 that look like the text “Hello World” shown in Fig. 1 that are 200 µm tall.

```
import JetStream.Poly;
import JetStream.Lib;
import JetStream.Cell;

public class GettingStarted {

    public static void main(String[] args) {
        Lib lib = new Lib();
        Cell top = new Cell("top", Poly.text("Hello World", 2, 200));
        lib.add(top);
        System.out.println(" Saved to " + lib.GDSOut("Hello"));
    }
}
```

JETStream can also be used to modify GDSII created

elsewhere. The following line illustrates how compactly JETStream can perform powerful tasks. This example gets a cell named “PM” from the file “PM.gds” and then creates a new cell, named “NewPM”, constructed with a polygon made from the area on layer 1 of cell PM.

```
Cell pm = new Cell("NewPM", Lib.GDSIn("PM.gds").
getCellNamed("PM").toPoly(1));
```

Below we show a few examples of CAD layouts performed using JETStream that would otherwise be tedious to generate. Figure 2(a) is a group of optical apertures defined by an analytical expression with different parameters for each. Figure 2(b) is a wiring pattern for pad frames with Verniers, labels, ebeam marks, and spline leads. Figure 2(c) is a hexagonal array of holes made with 3 non-orthogonal arrays as may be found in a photonic crystal. Circle sizes and spacings can readily be changed and arrayed. Figure 2(d) is a branching fluidic pattern that is a fractal pattern drawn with spline curves. These would each present a challenge using standard CAD drawing tools.

### Case I: Applying JETStream to non-planar ebeam exposures:

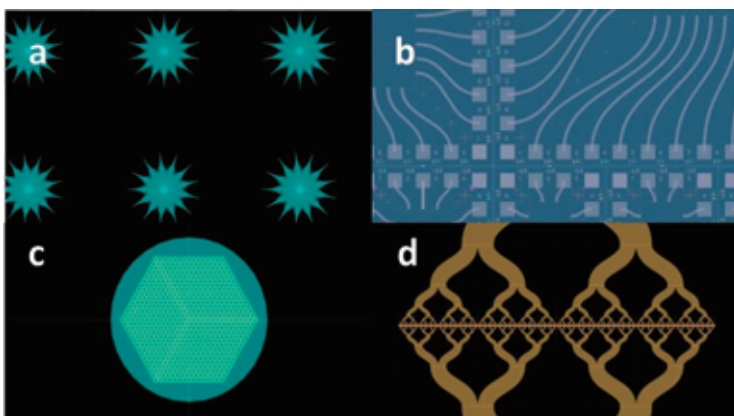
Writing on a nonplanar substrate is on high demand due to its various applications in the fields of optics, bioengineering, sensing and imaging and flexible electronics. There are already several methods that have been used such as laser lithography, soft lithography, nano imprinting lithography, replica molding etc. High resolution patterning on lenses with large height variation has also been demonstrated using EBL by first using a commercial laser probe microscope to map the surface [3]. Writing on a nonplanar substrate is always a challenge using an EBL system due to limited depth of focus of the electron beam. If a substrate has more than a few tens of microns of variation in height, the resulting pattern often is out of focus and exhibits poor field stitching and distortion. Therefore, writing on surfaces with varying height requires changing the focus of the beam, a magnification change in the scan field along with a rotation correction, and it is necessary to parse the pattern data and coordinate the pattern with the appropriate EBL hardware settings. In detail this can occur on a curved, angled, or other non-flat surface and requires breaking the image to be exposed into areas that correspond to certain height ranges on the surface. Typically, each range includes the area that falls within the depth of focus for a certain height offset. This can be accomplished

Fig. 1



Screen image of graphical output of the JETStream script above.

Fig. 2



Computer aided design patterns created using JETStream (a). An array of apertures defined by the same function; (b). Wiring patterns for pad frames; (c). A non-cartesian (hexagonal) array of holes; and (d). a fractal pattern for use in fluidics.

using proprietary optical interferometer measurements and dedicated application software [3]. However, in an effort to use open source solutions, one approach could be to cut up the intended exposure pattern into multiple patterns using Boolean operations with a vectorized contour map of the surface. In the easiest implementation, this would remove all hierarchy from the design. Another approach would be to generate the multiple patterns needed using the known surface contour as a parameter. This approach would leave some hierarchy in the generated files, making them smaller and more manageable. It also allows the programmer to control where the cuts happen, minimizing their undesirable effects. It does require that the design be generated by a program.

In this paper, as a proof of principle, we explore the possibility of writing on a slanted sample by using our JEOL JBX-6300FS and an analytical approach without the use of a dedicated external measurement system. We tested the approach on flat but tilted sample with a height variation of  $\sim 550 \mu\text{m}$ , well beyond the normal depth of focus.

The sample was mounted on a piece holder with slit width of 12 mm. It was tilted at an angle of 2.62 degrees. The designed layout consisted of Verniers, gratings, checker board structures, holes, and squares, extending  $\pm 4$  mm along the tilt from the center of the sample. We used our openly available scripting platform, JETStream, described above to generate the layout in GDS format. GenSys BEAMER was used for proximity effect correction and generation of the JEOL52 (V3.0) file.

To prepare for patterning, a piece of Si wafer was baked at  $170^\circ\text{C}$  for 4 min to remove water from the surface and cleaned with acetone and then IPA for 45 s. We used ZEP 520A resist from Zeon Corporation for our imaging layer. ZEP 520A was diluted in anisole in a 1:3 ratio to obtain around 50 nm thick film on silicon. It was spun at 3000 rpm for 45 s followed by a pre-exposure bake on hot plate at  $170^\circ\text{C}$  for 2 min.

The JBX-6300FS at Cornell is configured with both a graphical user interface and a scripting language interface. The latter can be exploited to automate the parameter changes during exposure. For this proof of concept demonstration, the height values at different points on the sample were obtained manually. To accomplish this, a test sample was coated with gold particles at the middle and edge along the tilted (y) axis. The height coefficients [difference between objective lens value on BE mark (a gold cross reference height mark on the stage) and objective lens value on each specific point of the sample] were obtained and plotted against the physical height variations from the three measurement areas. We observed that the height coefficient varied linearly with height change. Repeated measurements from the edges and the center of the sample were near identical. Next, another sample with the same tilt was mounted onto the cassette and height coefficients were again measured along the tilted direction at  $+6$  mm (highest point measured) from the center position and at  $-6$  mm (lowest point measured) from the center position. Height coefficient vs. height change data was then interpolated based on the linear equation determined earlier. With the scripting interface, the dies were then placed adjacent to each

other over a region spanning from  $+4$  mm to  $-4$  mm along the tilted direction. Height correction syntax [height coefficient, gain x, gain y, rotation x, rotation y] were calculated for each die with the script for easier manipulation of data.

Gain and rotation values are functions of height coefficient, objective lens value conversion coefficient, and gain and rotation values from primary deflectors [PDEF gain x, PDEF gain y, PDEF rotation x and PDEF rotation y]. Conversion coefficient and PDEF gain and rotation values were obtained by running a subprogram called INIEBX through the JBX-6300FS calibration program. For a fixed tilt, these numbers are constants. Using scripting, the job files were created with changing height coefficients, gains and rotations for each focus change interval.

The sample was finally exposed with 100 kV accelerating voltage, beam current of 2 nA, shot pitch of 4 nm, a field size of  $500 \mu\text{m} \times 500 \mu\text{m}$  and dose of  $300 \mu\text{C}/\text{cm}^2$ . After exposure, the sample was developed in hexyl acetate for 2 min followed by an IPA rinse for 45 s.

**Figure 3** shows our experimental setting on the JBX-6300FS cassette holder in order to tilt the sample. In our first exposure, we wrote our gratings along the slope of the Si piece without incorporating any height correction to adjust the focal plane. Results from this experiment came out as expected. In **Fig. 4**, we see the pattern features are in focus at height =  $0 \mu\text{m}$  (surface level) and the adjacent fields within the die are well stitched where the two patterns meet at a field boundary, as indicated by the Vernier measurement in the Fig. 4(d) inset. In **Fig. 5** and **Fig. 6**, we see that the uncorrected patterns  $220 \mu\text{m}$  above (Fig. 5(a), (b)) and  $220 \mu\text{m}$  below (Fig. 6(a), (b)) the center point, respectively, are unresolved due to poor focus and the stitching is also poor.

Next, we measured the height ( $-Z$  direction) at the center of the sample and corrected focus, gain and rotation for that specific point using the HEIGHT command, and we incorporated changes in height, PDEF gain and PDEF rotation into the job file during exposure. The corrected patterns Fig. 5(c), (d) (at  $+220 \mu\text{m}$ ) and Fig. 6(c), (d) (at  $-220 \mu\text{m}$ ) are all in sharp focus and exhibit excellent stitching in the Vernier pattern between the two adjacent areas written with separately provided focus, gain, and rotation parameters.

To generalize the approach, one could take any layout and (for the hardware settings used here) slice it into 2 mm strips (for unidirectional tilt) or into zones for (multidirectional tilts) using our JETStream platform. The software can generate a table with varying focus parameters for each of these strips or zones that are then applied during exposure using the python based JBX-6300FS scripting interface. This approach can then provide well resolved and reasonably well stitched patterns over a curved surface.

## Case II: CAD Solution to restore sharp vertices in nanolithography

Our next example of an application specific software solution is in response to a rising demand to fabricate unconventional features by e-beam lithography. We find that as we decrease the

**Fig. 3**

Experimental setting on JEOL JBX-6300FS cassette holder, showing that moving right along the tilt axis (y) corresponds to higher z and left (-y) corresponds to lower z.

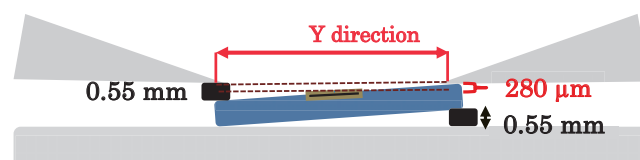
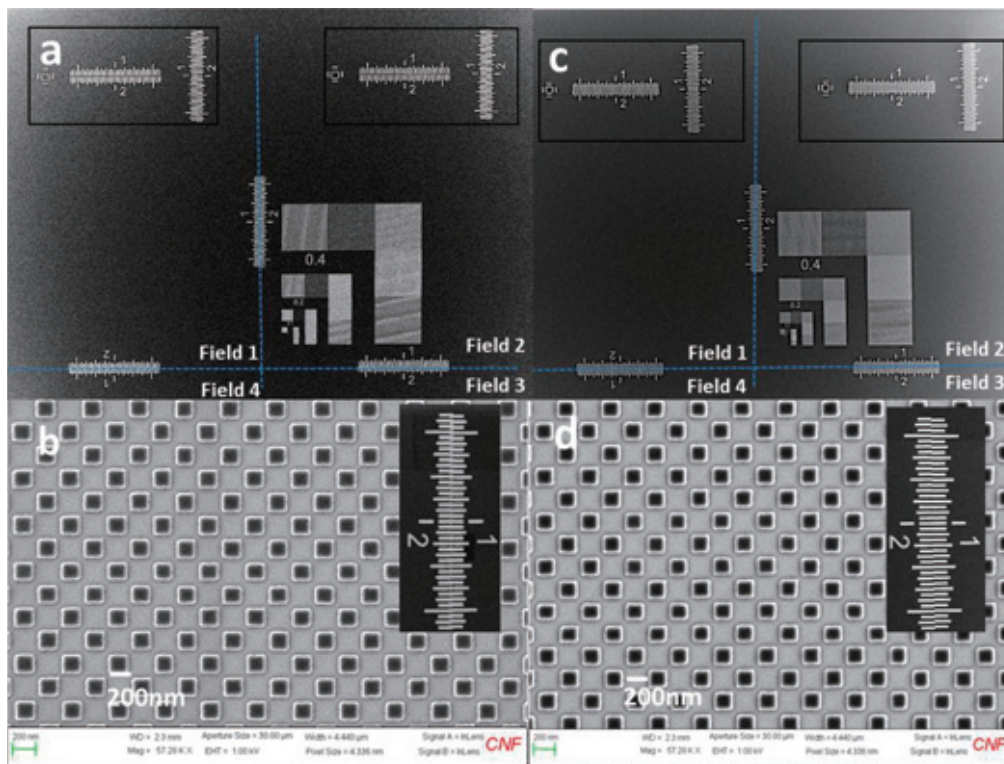
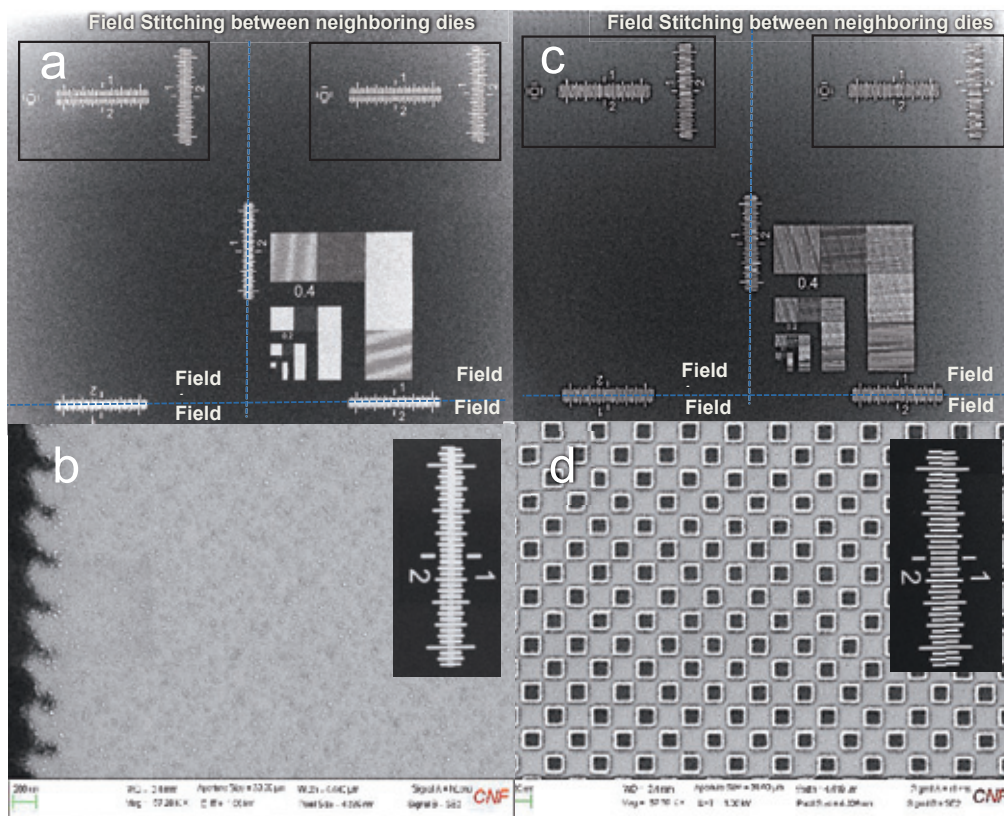


**Fig. 4**



SEM images of height uncorrected (a, b) and corrected (c, d) samples at reference focal plane ( $z=0$ ). Figure 4(a) and 4(c) show field stitching accuracy within a die (blue dotted lines). Verniers inside black rectangular boxes shows field stitching between neighboring dies with different focal planes. Image (b) and (d) show small features obtained after exposure. Verniers in the insets of (b) and (d) show field placement accuracy.

**Fig. 5**



SEM images of height uncorrected (a, b) and corrected (c, d) samples at reference focal plane ( $z = +220 \mu\text{m}$ ). Figure 5(a) and 5(c) show field stitching accuracy within a die (blue dotted lines). Verniers inside black rectangular boxes shows field stitching between neighboring dies with different focal planes. Image (b) and (d) show small features obtained after exposure. Verniers in the insets of (b) and (d) show field placement accuracy.

required size scale of various distinctive shapes of the designed features below about 50 nm, maintaining pattern fidelity is more challenging. Well established recipes, with e-beam resists, do not provide the expected patterns. This is the result of a number of factors including the contrast in the latent image, the developer effects on partially exposed resist, short range electron scattering, strain in polymer films after development, etc. To resolve this issue, we wanted to develop a process flow that would help users write sub 50 nm features with various shapes by a single e-beam lithography exposure. The objective is to obtain features that are as close to the actual designed layout as possible. This is partially achieved by using proximity correction software such as BEAMER. This data manipulation step helps to more uniformly adjust the energy deposited in the resist at the perimeter of the patterned objects. It does this by using the modeled electron scattering (proximity) function to iteratively adjust and correct for the contribution of scattered electrons to the exposure in each cell of the pattern. This correction primarily addresses the dose variation issue, however. To explore the possibility of a more complete correction, we have designed a layout consisting of right-angled triangles, squares, hexagons and L shapes all with 40 nm sides and 80 nm spacing. We used our java based scripting platform, JETStream, to generate a layout in GDS format. These test patterns were then exposed after two levels of data manipulation, the global proximity correction described above, and an additional correction

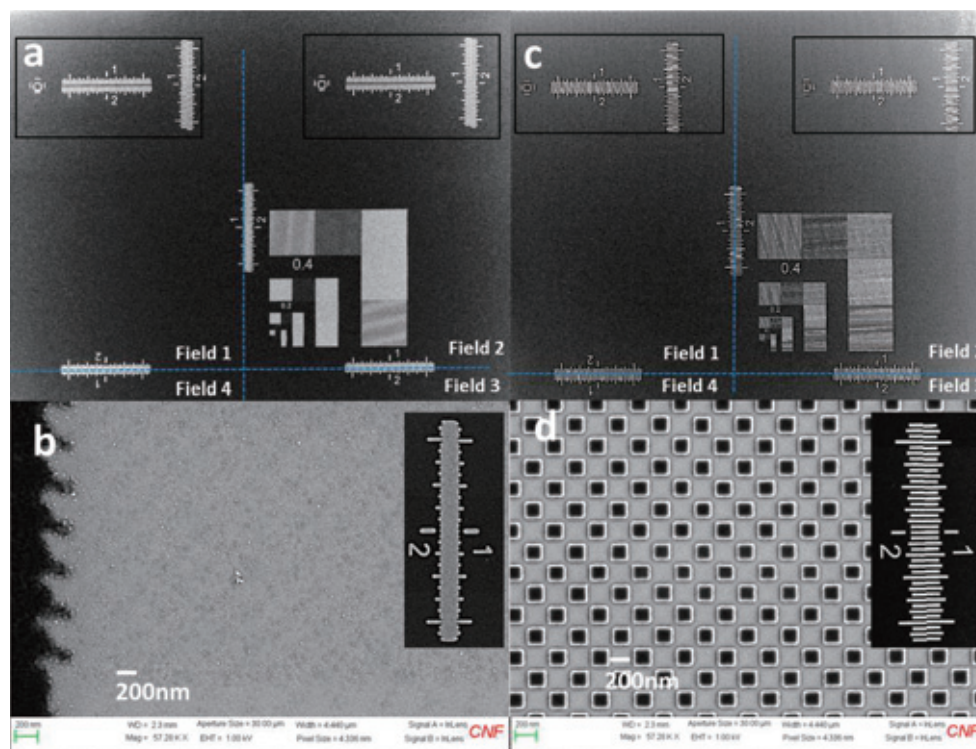
To prepare for patterning, a Si wafer was baked at 170 °C for 4 min to remove any water from the surface and cleaned with acetone and then IPA for 45 s. We then spin coated HSQ resist [4]. HSQ was diluted in MIBK with 1:4 ratio to obtain a ~25 nm thin film after spinning at 2000 rpm for 45 s and this was followed by a hot plate bake at 170 °C for 2 min. We exposed in the JBX-6300FS at 100 kV, a beam current of 0.5 nA, at a base dose of 20,000  $\mu\text{C}/\text{cm}^2$ , and developed our samples using *salty*

*developer* [5] for 2 min followed by DI water rinse for 4 min and IPA rinse for 2 min.

The exposures in **Figs. 7, 9, 10** were performed with a shot pitch of 2 nm, and a field size of 62.5  $\mu\text{m} \times 62.5 \mu\text{m}$ . We created JBX machine readable JEOL52 (V3.0) files by using GenISys BEAMER software. Initially we used only proximity effect correction (PEC) to create our JEOL52 (V3.0) file [Fig. 7(a), (b), (c) and (d)]. Proximity correction requires that the scattering of the electrons be modeled for the particular material and electron energy being employed. We obtained this proximity function as a PSF file to perform PEC by first using GenISys Monte Carlo simulation software called TRACER. Proximity effect correction in BEAMER is an edge-correction method. PEC connects the threshold exposure of the resist to the resist development to where the resist edge will land. This means for PEC the absorbed energy of the resist is analyzed in the CAD pattern and dose assignments are made such that the absorbed constant energy at threshold lands at the edge of the intended pattern design. The PEC module provides a set of features for correction of effects not only caused by electron scattering, but also process blur and the pattern transfer process. It provides great flexibility for handling both forward scattering (short range effects) and backward scattering (long range effects).

Using PEC alone, we can clearly see a difference in the appearance of each shape and the uniformity among the groups was good. However, the vertices of these features were not resolved as sharply as desired. To remedy this, we used a newer module in BEAMER called corner-PEC. The corner-PEC module facilitates corner sharpening by rule-based dose adjustments at feature edges and corners. The correction method uses the model based correction with Gaussian parameters and combines a rule based correction by breaking down the layout and giving dose multiplication factors. The breakdown of the layout is done using the Size parameter. This Size parameter creates a bulk, edge and corner element (inner corner and outer

**Fig. 6**



SEM images of height uncorrected (a, b) and corrected (c, d) samples at reference focal plane ( $z = -220 \mu\text{m}$ ). Figure 6(a) and 6(c) show field stitching accuracy within a die (blue dotted lines). Verniers inside black rectangular boxes shows field stitching between neighboring dies with different focal planes. Image (b) and (d) show small features obtained after exposure. Verniers in the insets of (b) and (d) show field placement accuracy.

corner). The size of the corner element depends on the corner angle. For each of these elements a dose factor is defined. The layout is corrected as a whole, decomposed and then the dose factors are applied on those areas. These dose adjustments compensate for areas that were found to pull back or bulge even though they were calculated by the PEC software to receive the optimum dose.

**Figure 8** shows a detail of the corner PEC correction for an individual shape to illustrate the method. The figure helps illustrate how unexpected resist effects can be out maneuvered using phenomenologically determined adjustments. Using a combination of size biasing near edges and dose “boosts” near vertices, dramatic improvements in shape retention can be obtained. The shape depicted is that of a single triangle used in the exposure series above in which the data underwent Corner PEC correction after standard PEC.

As can be observed in Fig. 9, the corner-PEC adjustment did indeed improve the sharpness of the vertices in each feature. The enhanced lithography results are due to the subsequent dose changes that can be observed in the refractured CAD data (see Fig. 8). These adjustments offset the non-ideal behavior (such as stress, short range electrons, developer effects, etc.) that manifest in the developed resist, especially when patterns are

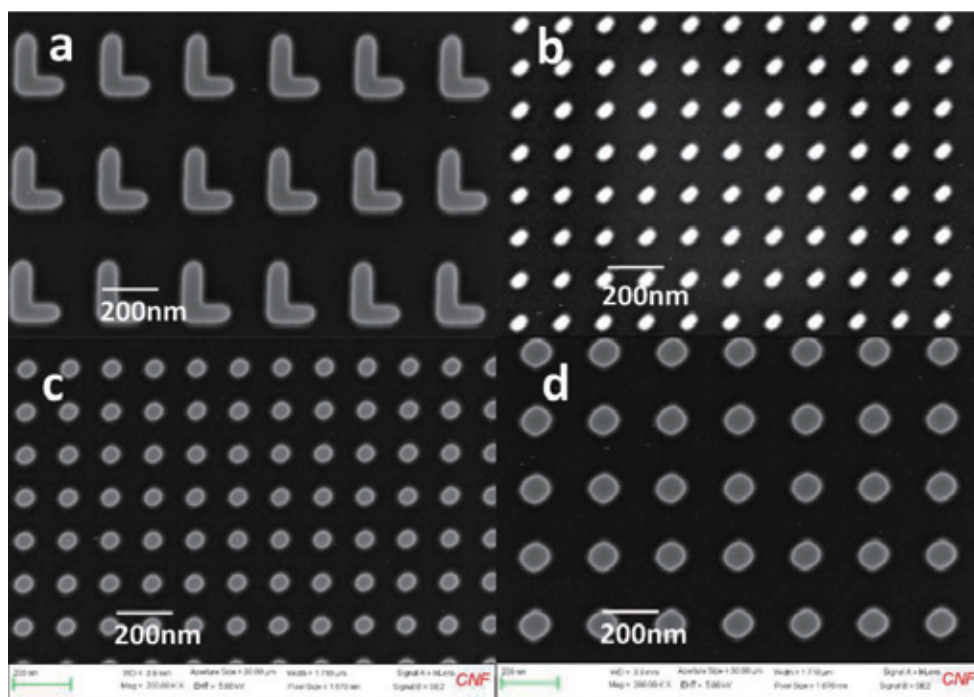
scaled below a few tens of nanometers. Note how much sharper the vertices of the red area are after corner PEC.

Process optimization also is key to getting the best results. We later modified our pre- exposure bake recipe by reducing baking time to 1 min and temperature to 90 °C for HSQ. This small process change further improved the resulting sharp corners of all the features as seen in Fig. 10(a), (b), and (c).

## Conclusion

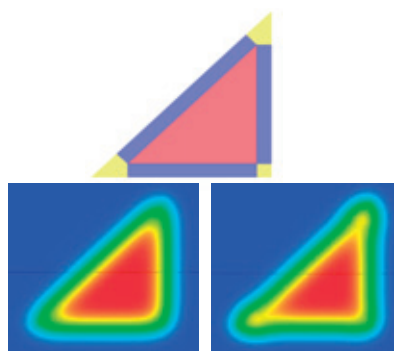
We have attempted to show that both excellent hardware and application specific software solutions are needed to optimally pattern challenging patterns especially at the nanoscale. JETStream software was introduced as an open-source scripting environment and library created by staff at the Cornell NanoScale Facility for generating otherwise challenging designs, or introducing systematic design variables in a time saving manner. In addition, both JETStream and GenISys BEAMER software were shown to be very useful software tools for solving difficult lithography problems such as writing on non-planar substrates or resolving exposures of geometric features which tend to blur when their size is shrunk below 40 nm, even when standard proximity correction methods are used.

**Fig. 7**



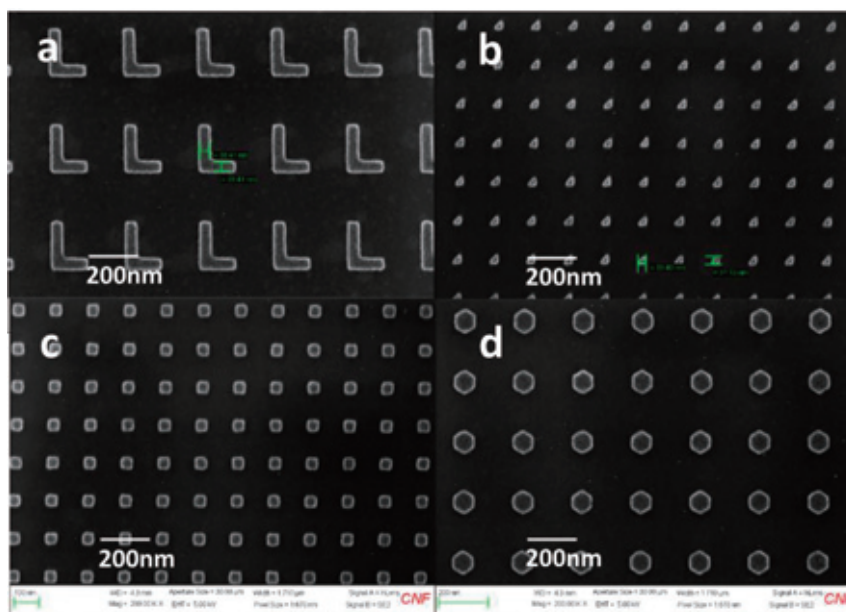
Scanning electron micrographs of developed e-beam lithography features in HSQ resist using only BEAMER PEC data correction for (a) L shapes, (b) right angled triangles, (c) squares and (d) hexagons.

**Fig. 8**



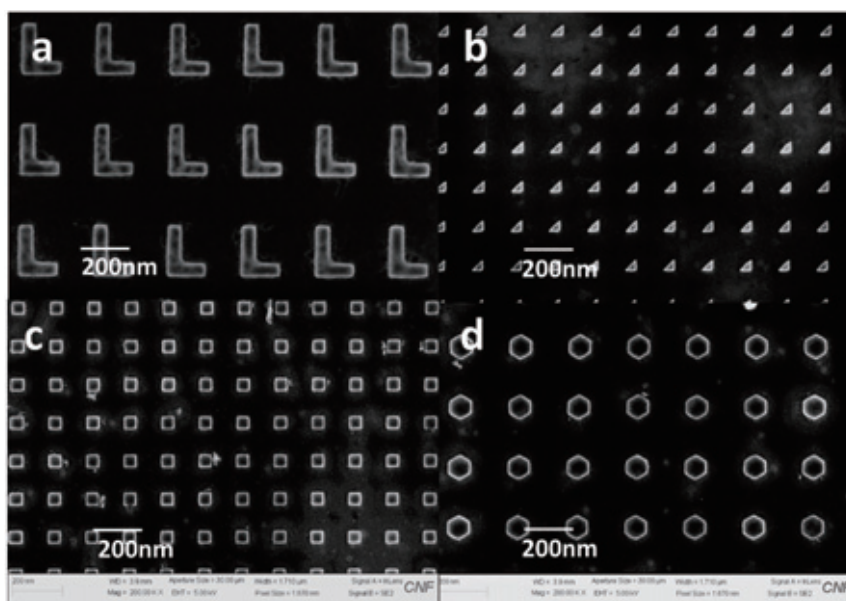
Detail of single triangle used in the exposure series in which the data underwent Corner PEC correction after standard PEC. The enhanced lithography results are due to the dose changes to the nano fractured CAD data that offset the non-ideal behavior of the resist at the nanoscale.

Fig. 9



Scanning electron micrographs of developed HSQ resist exposed using both Proximity correction and Corner PEC (a) L shapes, (b) right angled triangles, (c) squares and (d) hexagons.

Fig. 10



Scanning E-beam microscopy images of developed HSQ features using BEAMER corner-PEC and lower temperature bake of HSQ- a) L-shapes b) right angled triangles, (c) squares and (d) hexagons.

## Acknowledgments:

This work was performed at the Cornell NanoScale Science & Technology Facility, a member of the National Nanotechnology Coordinated Infrastructure (NNCI), which is supported by the National Science Foundation (Grant NNCI-1542081). We wish to acknowledge the kind and generous help of our friends at JEOL Ltd. and JEOL USA, INC. and in particular the discussion with Mr. Kato, JEOL applications engineer in Peabody, MA. We would also like to acknowledge Roger McCay, GenISys, Inc. for his help with BEAMER's corner PEC module.

## References

- [ 1 ] JETStream is made openly available by CNF at <https://confluence.cornell.edu/pages/viewpage.action?pageId=336378904> and by John Treichler at <https://drive.google.com/drive/folders/0BxNDiyrykU0reWIHZXRISnZzd1U>. Please credit CNF and John if used in your work.
- [ 2 ] BEAMER v5.6.2 is a commercially available software product from GenISys GMBH, <https://genisys-gmbh.com/web/products/beamer.html>
- [ 3 ] Vishva Ray, Yukinori Aida, Ryo Funakoshi, Hitoshi Kato, Stella W. Pang, *J Vac Sci Technol* **B 30**, 06F303 (2012).
- [ 4 ] HSQ resist is a product of Dow Corning.
- [ 5 ] Joel K. W. Yang and Karl K. Berggren, "Using high-contrast salty development of hydrogen silsesquioxane for sub-10-nm half-pitch lithography", *J. Vac. Sci. Technol.*, **B 25**(6), 2007.

# Development of New Operando Measurement System by Combining Reaction-Science High-Voltage Electron Microscopy and Quadrupole Mass Spectrometry

Shunsuke Muto<sup>1,2,4</sup>, Shigeo Arai<sup>2</sup>, Testuo Higuchi<sup>3</sup>, Shigemasa Ohta<sup>4</sup>, and Koji Orita<sup>5</sup>

<sup>1</sup>Advanced Measurement Technology Center, Institute of Materials and Systems for Sustainability, Nagoya University

<sup>2</sup>High-Voltage Electron Microscopy Laboratory, Institute of Materials and Systems for Sustainability, Nagoya University

<sup>3</sup>JEOL Ltd. <sup>4</sup>JEOL USA, Inc. <sup>5</sup>Graduate School of Engineering, Nagoya University

The Reaction Science High-Voltage Scanning Transmission Electron Microscope (RS-HVSTEM), JEM RS1000K RS, in common use since 2010, is a unique high-voltage electron microscope (HVEM) equipped with an environmental gas cell with a differential pumping system. In this article, we introduce a combined environmental HVEM and quadrupole mass spectrometer (QMS) to detect product gas species associated with chemical reactions occurring in the microscope together with concurrent TEM observation. We demonstrate preliminary results of detecting minute amounts of product gas species, associated with redox reactions, where the expected structural transformations are concurrently observed with TEM.

## Introduction

Current trends in the field of scanning/transmission electron microscopy (S/TEM) can be classified particularly into two main streams: atomic-level resolution imaging/analysis, and observation under an actual operation environment (previously termed '*in situ*' experiment but currently termed '*operando*' in a more active sense). They are both strongly demanded by fundamental science to push open unexplored areas and also by wider fields, particularly in industry, to investigate more practical aspects in nano-area analysis. The two combined fields render S/TEM-related analysis techniques indispensable to various materials analysis techniques requiring nanometric spatial resolution.

On the other hand, in spite of having the highest spatial resolution, analytical methods using high-energy electron probes generally suffer from a poor detection limit for trace elements: a typical value would be no larger than 0.1%, which is by no means satisfactory compared to, for instance, a few ppm, which is a typical dopant concentration in semiconductors. The poor detection limit is caused by the technique relying on measurement of energy exchange between electrons that occurs with a very small probability.

Analytical methods taking advantage of directly counting quanta emissions such as photons or atoms/ions are in general very sensitive to trace elements. It is thus very promising to

combine such a sensitive technique with the high spatial-resolution of TEM. In particular, mass spectroscopy (MS)-based techniques have detection limits generally as high as the ppm- or even ppb-level. Such MS-based techniques do not intrinsically show good affinity with other solid-state analysis methods like TEM, because they detect atoms and/or molecules of interest by ionizing them in the spectrometer. However, the field of *in situ* or *operando* measurements, an emphasis is placed on detecting dynamical response of the sample of interest to an external field as well as the conventional structural and chemical analyses in vacuum. In particular, the field of 'environmental TEM (E-TEM)' where gas-solid reactions are directly observed, has long desired to detect trace chemical reaction products occurring at nanometric areas concurrently with TEM observation/analysis.

The Reaction Science High Voltage Scanning Transmission Electron Microscope (RS-HVSTEM; JEOL JEM1000K RS), that has been in common use since 2010, is a unique megavolt-class S/TEM equipped with a gas environmental cell [1]. This instrument has very high utilization rate particularly by external and industrial researchers, where one can observe chemical reactions of thicker specimens [2-4] and mechanical responses [5] under gas pressures higher than those of typical 200-300 kV-class S/TEMs at very high spatial resolution. In addition, it takes advantage of its higher electron penetration power and wider pole-piece gap to ensure a higher degree of freedom for

dynamical observations of the samples of interest under flexible environments. The High-Voltage Electron Microscope Laboratory and JEOL together have implemented a combination of a high sensitivity quadrupole mass spectrometer (QMS) with a RS-HVSTEM and attempted live detections of consumption and emission of reaction gases associated with chemical reactions. Such attempts have been reported by several different groups using medium voltage TEMs [6-9], though have been never successful in structural change observation and product gas detection at the same time, associated with catalytic reactions.

In the present article we introduce the design and specifications of the HVSTEM-QMS system and demonstrate preliminary results, in which trace product gas emissions associated with redox reactions in the TEM were successfully detected.

## System Construction

A block diagram of the present HVSTEM-QMS system, where a JEOL JMS-Q1500GC QMS is implemented to the gas environmental cell of a JEM1000K RS is shown in **Fig. 1**. The gas environmental cell is designed so as to be inserted into the objective lens pole piece gap only in case of observation in a gas atmosphere, and retracted for the conventional TEM observation in vacuum [1]. The gas leakage from the E-cell to the TEM column is evacuated by differential pumping through the orifices at the top and bottom of the cell also working as the electron paths. As shown in yellow in Fig. 1 the pumping line of the cell is branched to the normal and QMS modes by implementing the two valves, V1 and V2, where at the QMS mode the gas molecules in the E-cell are introduced to QMS by closing V1 and opening V2 [10].

Outside views of the present system are shown in **Figs. 2**. The valves V1 and V2 are implemented on the backside of the E-cell, connected to QMS by a liner tube ~2-m long. The entire QMS operations, such as turning on/off, data acquisition, and displaying spectra on a monitor, are controlled by dedicated software on a Windows PC. The detailed specification and performance of the JMS-Q1500GC QMS are described in ref. [11]. In the actual experiments, ambient gas species such as O<sub>2</sub>, N<sub>2</sub>, CO<sub>2</sub>, Ar, H<sub>2</sub>O, and hydrocarbons are inevitably involved as the residual background gases in the E-cell, and it is essential to reduce such a background gas level to detect a small amount of the same gas species produced in the chemical reaction in TEM by the present system.

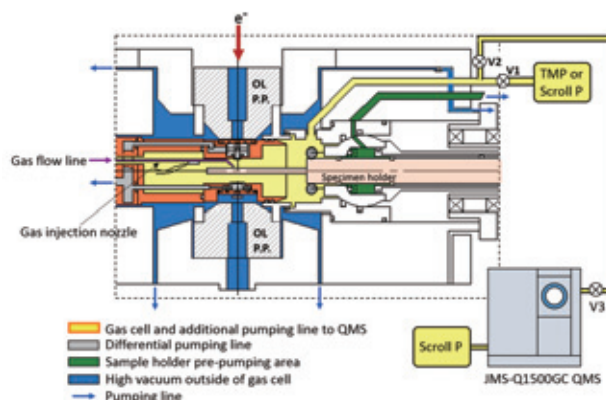
Snapshots of mass spectra of gas species for  $m/z$  ( $m$ : mass number of molecule;  $z$ : charge number) 14-21 (H<sub>2</sub>O-related), 26-33 (N<sub>2</sub> and O<sub>2</sub>), 38-45 (Ar and CO<sub>2</sub>), and 51-61 (hydrocarbon fragments: H. C.), live monitored in vacuum when the E-cell is introduced between the object lens pole piece gap are shown in **Fig. 3**. The residual gases and hydrocarbon fragments ( $m/z$  39, 41, 43, 55, and 57) are clearly observed just after the E-cell introduction (Fig. 3(a)), though those background peak intensities are significantly reduced after a few hours (Fig. 3(b)), when the vacuum is stabilized and trace reaction gases are detectable in the *operando* measurement.

## Experimental validation of HVSTEM-QMS system

### Pd nano-particle catalyst-assisted combustion of carbon nanotube under O<sub>2</sub> atmosphere

As the first feasibility test of the present HVSTEM-QMS system, we conducted oxidation of carbon nanotubes (CNTs) by Pd nano-particles under O<sub>2</sub> atmosphere to detect emission of

**Fig. 1**



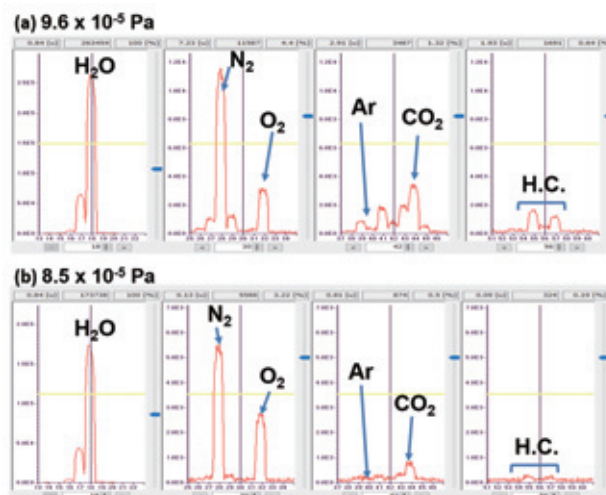
Schematic diagram of the present HVSTEM-QMS system (see text for detail). OL P. P.: Objective lens pole piece; TMP: turbo molecular pump; Scroll P: Scroll pump

**Fig. 2**



Present HVSTEM-QMS system, viewed from the front (a) and from the right backside (b).

**Fig. 3**



Snapshots of mass spectra of gas species at two different vacuum levels for  $m/z$  14-21 (H<sub>2</sub>O-related), 26-33 (nitrogen (N<sub>2</sub>), CO and oxygen (O<sub>2</sub>)), 38-45 (CO<sub>2</sub>) and 49-56 (hydrocarbon fragments: H. C.), live monitored in vacuum when the E-cell is introduced between the object lens pole piece gap. (a) just after the E-cell is introduced. (b) after evacuating the system for a few hours.

CO<sub>2</sub>. Carbon is supposed to be oxidized approximately above 800 °C in air. However, CO<sub>2</sub> emission starts by a catalytic reaction on a metal (e.g., Pd, Pt) surface under O<sub>2</sub> atmosphere at much lower temperatures between 200-400 °C [4], when the Pd particles move around as if they are eating CNTs (see Supplementary video in ref. [10]). Excerpts from the video recording of TEM observation are shown in **Fig. 4**.

A selected ion monitoring (SIM) chart for *m/z* 16 (double charged (*z* = 2) O<sub>2</sub>) and 44 (CO<sub>2</sub>) is shown in **Fig. 5**, where the sample was gradually heated under an O<sub>2</sub> atmosphere at a pressure of approximately 15 Pa (the full SIM chart in this experiment is available in Supplementary data of ref. [10]). The sample was prepared by grinding and dispersing a mixture of Pd nanoparticles and a bundle of CNTs in ethanol in a mortar and pestle, followed by painting them on a spiral tungsten filament in the Kamino sample heating holder [13]. As the temperature increased higher than 400 °C, Pd particles started moving around and the SIM chart exhibited increments of *m/z* 44 almost immediately. The CO<sub>2</sub> emission then saturated and subsequently decreased, eventually ceasing in correlation with slow-down of the particle motion. Assuming that the present reaction can be modelled by the subsequent chemical reactions like C  $\xrightarrow{k_1}$  CO<sub>2</sub>  $\xrightarrow{k_2}$  evacuation, where *k*<sub>1</sub> and *k*<sub>2</sub> are the associated reaction coefficients, and the concentrations of carbon, product CO<sub>2</sub> molecules and the total CO<sub>2</sub> evacuated by QMS from the gas cell are respectively set as *C*<sub>C</sub>(*t*), *C*<sub>CO<sub>2</sub></sub>(*t*), *C*<sub>evac</sub>(*t*), functions of time. The reaction rate equations can be then expressed as follows:

$$-\frac{dC_C}{dt} = k_1 C_C \quad (1)$$

$$\frac{dC_{CO_2}}{dt} = k_1 C_C - k_2 C_{CO_2} \quad (2)$$

$$\frac{dC_{evac}}{dt} = k_2 C_{CO_2} \quad (3)$$

The solutions of Eqs. (1)-(3) are obtained, setting *C*<sub>0</sub> as the initial CO<sub>2</sub> concentration, in the following forms:

$$C_C(t) = C_0 e^{-k_1 t} \quad (4)$$

$$C_{CO_2}(t) = \left( \frac{k_1 C_0}{k_2 - k_1} \right) (e^{-k_1 t} - e^{-k_2 t}) \quad (5)$$

$$C_{evac}(t) = C_0 \left( 1 + \frac{k_1 e^{-k_2 t} - k_2 e^{-k_1 t}}{k_2 - k_1} \right) \quad (6)$$

where the introduced oxygen pressure is assumed to be constant. The CO<sub>2</sub> emission curve in the SIM chart can be well fit by Eq. (5), as shown in Fig. 6, so that the reaction coefficients were estimated to be *k*<sub>1</sub> = 0.0038 ± 0.0002 s<sup>-1</sup> and *k*<sub>2</sub> = 0.031 ± 0.003 s<sup>-1</sup>. It follows from Eq. (2) that carbon is combusted approximately 0.4% per second and 3% of the generated CO<sub>2</sub> gas is evacuated every second. The QMS-SIM chart enables us as such to analyze the chemical reaction kinetics involved and derive the reaction coefficients and associated activation energies, with which we can discuss the reactions of interest by comparing the structural changes concurrently obtained in the TEM images.

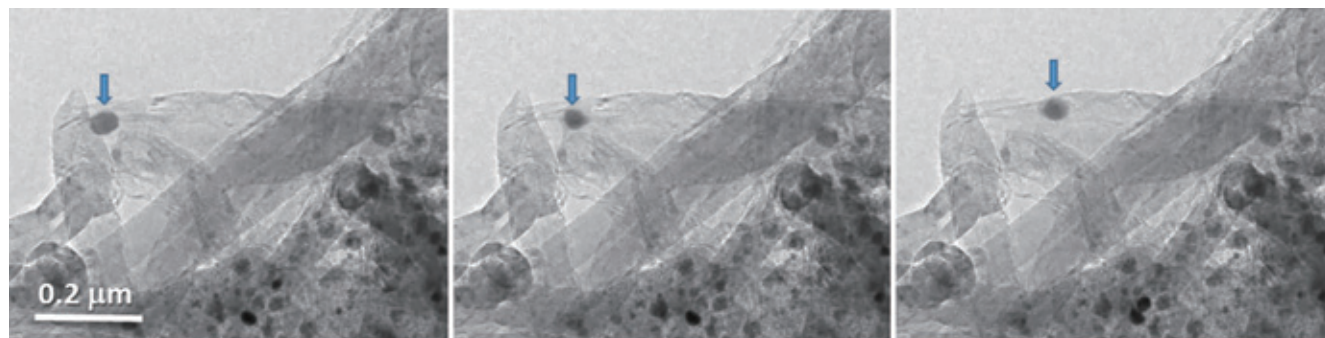
### Reduction of surface oxide layers of Rh nanoparticles in vacuum

To extend the present system for applications to more practical and interesting examples, it should be able to detect an even less amount of product gases in the TEM chamber. We thus attempted to detect oxygen emission associated with the thermal reduction of metal oxide nanoparticles in vacuum. The sample was ZrO<sub>2</sub>-supported Rh nanoparticles, which were fully or partly surface-oxidized in ambient atmosphere depending on their size, as shown in **Fig. 7(a)**. The sample was mounted on the Kamino heating holder as before, and gradually heated. **Figure 8** shows the SIM chart monitoring *m/z* 44 (CO<sub>2</sub>) and 32 (O<sub>2</sub>) (the full SIM chart in this experiment is also available in Supplementary data of ref. [10]). Interestingly, the oxygen emission associated with the reduction was not detected, although unambiguous CO<sub>2</sub> emission was observed to be synchronized with the onset of transformation from Rh oxide to metallic Rh at around 200 °C, as observed by TEM (Fig. 7(b)). The CO<sub>2</sub> emission promptly decayed after the heater current was turned off, suggesting that the decomposed oxygen was so active as to immediately react likely with the surrounding hydrocarbon into stable CO<sub>2</sub>, possibly derived from vacuum grease vapor in the sealing parts and residual organic solvent involved in the sample synthesis. The multi-peak feature of the CO<sub>2</sub> emission curve suggested that the reduction reaction depended on the particle size actually observed in the TEM observation.

### Summary

It was demonstrated that the present HVSTEM-QMS system succeeded for the first time in concurrent atomic resolution structural observation and detection of product gas emissions associated with gas-involved redox reactions in TEM, which

**Fig. 4**



TEM image snapshots of moving Pd nanoparticles dispersed on CNTs and heated to 400 °C in O<sub>2</sub> atmosphere. Each frame was extracted at the interval of one second from the video.

**Fig. 5**

QMS-SIM chart, monitoring  $m/z$  44 (black line:  $\text{CO}_2$ ) and  $m/z$  16 (red line: fragment of  $\text{O}_2$ ) during heating Pd/CNT system in  $\text{O}_2$  atmosphere. Green line shows the sample temperature as a function of time.

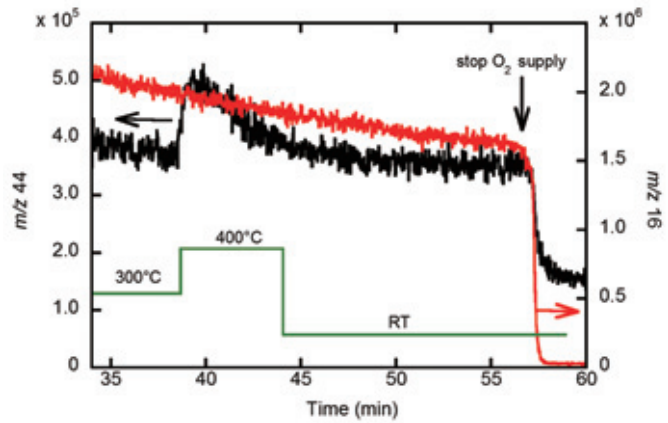


**Fig. 6**

Re-plot of QMS-SIM chart of  $m/z$  44 in Fig. 5, where the horizontal axis origin is set at the onset of  $\text{CO}_2$  emission. The solid red line is the best fit curve of Eq. (5) to the experimental points.

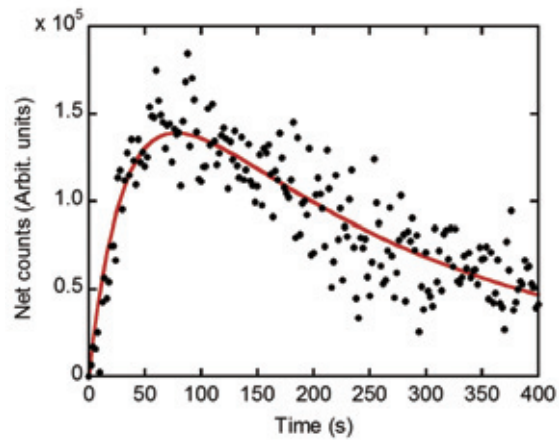


**Fig. 7**

(a) Surface-oxidized Rh nanoparticle supported by a  $\text{ZrO}_2$  particle at room temperature in vacuum. (b) Metallic Rh nanoparticle as a result of surface reduction at 200 °C in vacuum. Each phase was confirmed by electron energy-loss spectra (not shown).

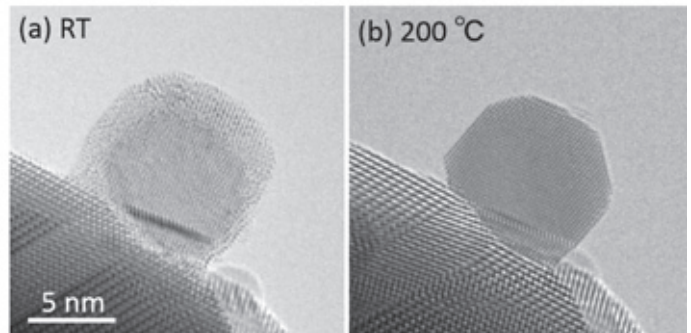
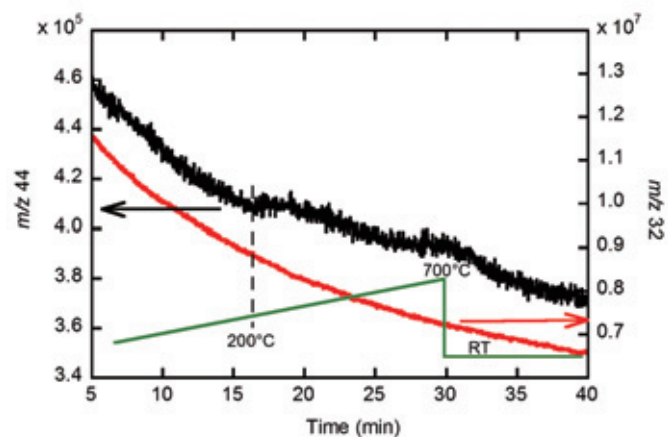


**Fig. 8**

QMS-SIM chart, monitoring  $m/z$  44 (black line:  $\text{CO}_2$ ) and  $m/z$  32 (red line:  $\text{O}_2$ ) during heating Rh oxide particles in vacuum. Green line shows the sample temperature as a function of time.



enabled analysis of the reaction kinetics based on SIM charts obtained of emission/consumption gas species. It should be emphasized that the present system development was achieved not just by combining the commercial instruments together but resulted from incessant efforts to reduce the amount of residual background gases by repeated purge procedures of the gas lines, improving the sealing O-rings quality, and tightening the connecting nuts. It is desirable that the gas evacuating efficiency coefficient  $k_2$  should be even more improved in the future. The sensitivity of the stand-alone QMS can reach the ppb order, though a quantitative estimation of the sensitivity of the present HVSTEM-QMS system would be a future task for us.

The present system will open a new world in *operando* measurements in the field of environmental TEM, and we have been already successful in detecting source gas consumption and product gas emissions associated with model catalytic reactions for automotive exhaustive gas purification [13-15]. We are now exploring combined measurements with chemical analysis such as electron energy-loss spectroscopy and further applications are underway.

## Acknowledgments

The authors thank Messrs. H. Tanaka, T. Suganuma, M. Ibe and Dr. H. Hirata, Toyota Motor Corporation for supplying us the Rh/ZrO<sub>2</sub> sample used in the present report.

This work was partly supported by Grants-in-Aid for Scientific Research on Innovative Areas "Nano Informatics" (grant number 25106004), and Kiban-kenkyu A (grant number 26249096) from the Japan Society of the Promotion of Science and partly by Nagoya University microstructural characterization platform as a program of "Nanotechnology Platform" of the Ministry of Education, Culture, Sports, Science and Technology (MEXT), Japan.

## References

- [ 1 ] Tanaka N, Usukura J, Kusunoki M, Saito Y, Sasaki K, Tanji T, Muto S, and Arai S (2013) Development of an environmental high-voltage electron microscope for reaction science. *Microscopy* **62**: 205-215.
- [ 2 ] Fujita T, Tokunaga T, Zhang L, Li D, Ito L, Arai S, Yamamoto Y, Hirata A, Tanaka N, Ding Y, and Chen M (2014) Atomic observation of catalysis-induced nanopore coarsening of nanoporous gold. *Nano Lett.* **14**: 1172-1177.
- [ 3 ] Kamatani K, Higuchi K, Yamamoto Y, Arai S, Tanaka N, and Ogura M (2015) Direct observation of catalytic oxidation of particulate matter using in situ TEM. *Sci. Rep.* **5**: 10161.
- [ 4 ] Yoshida K, Arai S, Matsumoto H, Shirai M, and Tanaka N (2018) Catalytic Etching of Multi - Walled Carbon Nanotubes Controlled by Oxygen Gas Pressure. *Chem. Cat. Chem.* **10**: 2205-2209.
- [ 5 ] Takahashi Y, Arai S, Yamamoto Y, Higuchi K, Kondo H, Kitagawa Y, Muto S, and Tanaka N (2015) Evaluation of interfacial fracture strength in micro-scale components *Exp. Mech.* **55**: 1047-1056.
- [ 6 ] Hansen P L, Wagner J B, Helveg S, Rostrup-Nielsen J R, Clausen B S and Topsøe H (2002) Atom-resolved imaging of dynamic shape changes in supported copper nanocrystals. *Science* **295**: 2053-2055.
- [ 7 ] Miller B K and Crozier P A (2014) Analysis of catalytic gas products using electron energy-loss spectroscopy and residual gas analysis for operando transmission electron microscopy. *Microsc. Microanal.* **20**: 815-824.
- [ 8 ] Bremmer G M, Zacharaki E, Sjøstad A O, Navarro V, Frenken J W M and Kooyman J (2017) In situ TEM observation of the Boudouard reaction: multi-layered graphene formation from CO on cobalt nanoparticles at atmospheric pressure. *Faraday Discuss.* **197**: 337-351.
- [ 9 ] Jinschek J R (2012) Atomic scale structure-function relationship of heterogeneous catalysts: investigation of gas-solid interactions by ETEM. *Microsc. Anal.* **26**: S5-S10 (AM).
- [ 10 ] Muto S, Arai S, Higuchi S, Orita K, Ohta S, Tanaka, H, Suganuma T, Ibe M and Hirata H (2019) Environmental high-voltage S/TEM combined with quadrupole mass spectrometer for concurrent in situ structural characterization and detection of product gas molecules associated with chemical reactions. *Microscopy* **67**: doi.org/10.1093/jmicro/dfy141.
- [ 11 ] <https://www.jeol.co.jp/en/products/detail/JMS-Q1500GC.html>.
- [ 12 ] Kamino T, Yaguchi T, Konno M, Watabe A, Marukawa T, Mima T, Kuroda K, Saka H, Arai S, Makino H, and Suzuki Y (2005) Development of a gas injection/specimen heating holder for use with transmission electron microscope. *Microscopy* **54**: 497-503.
- [ 13 ] Muto S, Arai S, Higuchi T and Ohta S (2017) *In situ* observation of catalytic reactions under gas atmosphere by reaction science high-voltage scanning transmission electron microscope equipped with quadrupole mass spectrometer. *3<sup>rd</sup> East Asia Microscopy Congress, EAMC3, Busan, C-7.*
- [ 14 ] Tanaka H, Iwasaki M, Arai S, Hirata H and Muto S (2018) Dynamic observations of surface behavior of Rh nanoparticles under reaction conditions by environmental transmission electron microscopy. *The 8<sup>th</sup> Tokyo Conference on Advanced Catalytic Science and Technology, TOCAT8, Aug. 5-10, Pacifico Yokohama, OB209.*
- [ 15 ] Muto S, Arai S, Higuchi T and Ohta S (2018) *In situ* detection of product gas molecules associated with catalytic reactions of fine metallic particles by environmental high-voltage TEM equipped with quadrupole mass spectrometer. *19<sup>th</sup> Intern'l Microscopy Congress, IMC19, Sept. 9-14, Sydney, IT5: 295.*

# Development of Low-Voltage TEM/STEM for Single Carbon Atom Analysis under the 3C Project

Kazu Suenaga National Institute of Advanced Industrial Science and Technology (AIST)

When I first used a transmission electron microscope (TEM) in my student hood to characterize carbon materials about 30 years ago, no one could imagine that we could ever be able to visualize individual carbon atoms. The recent unprecedented progress of TEM and its associated technologies has made it eventually possible to visualize individual carbon atoms as well as to analyze them. Here in this report, I summarize how our collaborative research group of JEOL, NIMS and AIST has developed a dedicated low-voltage TEM/STEM by designing the cutting-edge aberration correctors and ultimately succeeded the single atom analysis of individual carbon atoms.

## Introduction

Both high spatial resolution and high sensitivity are required to visualize materials made of the light element, such as carbon ( $Z=6$ ), by using a TEM. For elemental identification and electronic structure analysis, the core-level spectroscopy based on electron energy-loss spectroscopy (EELS) is definitely required in a STEM. Because the EELS utilizes the inelastic scattering of the incident electron beam with the specimens, it is essential to make the number of inelastic events efficiently happen for the highly sensitive detection of atomic species. Lowering the accelerating voltage is primarily important because the possibilities of inelastic scattering events do increase with lower accelerating voltage of the incident electrons. In 1980-1990s when I started researches involving characterization of carbon materials, there is a huge trend in TEM community to develop high voltage (HV-)TEM, with an acceleration voltage higher than a million volts, to realize higher spatial resolution in advantage of shorter wave-length of the probe electrons. There was, however, huge drawbacks in HV-TEM, which will make it hardly possible to visualize atomic structures of carbon materials. First, the electron damage of carbon materials is extremely fast when an HV-TEM is used. Second, regardless how good the spatial resolution is in HV-TEM, there will be almost no contrast of thin carbon materials because of extremely high transmissivity of high speed electrons. I personally learned from those days experience that it is critical that the incident electron interacts with the specimen in a highly efficient way to successfully visualize the light element materials with highest sensitivities.

In 2006 when our collaborative group started up, our primary goal was to make a TEM with a lowest possible acceleration voltage so that individual carbon atoms can be visualized and identified by increasing the electron-atom interactions. Lower accelerating voltage generally means inferior spatial resolution achievable by TEM. Then it is indispensable for this project to design new aberration correctors dedicated for this purpose. The

project was named “the 3C project” by Dr. Yoshiyasu Harada who was at the time President of JEOL, which stands for “C correction and Cs correction for Carbon materials”.

## Choice of acceleration voltage optimized for carbon materials

The light element materials largely suffer the electron beam damage, therefore HR-TEM imaging of biological and organic molecules are generally quite difficult to realize. One of the most crucial electron beam damages is the knock-on effect with which an atom will be kicked out by the physical impact of high speed electron with the momentum transfer. To moderate the knock-on damage, it is efficient to reduce the acceleration voltage of the incident electron beam. The threshold acceleration voltage for the knock-on effects is determined by the so-called displacement energy which is specific to the materials and/or elements. Lowering the acceleration voltage is very effective to reduce the knock-on damage but has a severe drawback. The bond break due to the ionization effect, known as the radiolysis, will become dominant at a specific acceleration voltage with which shows a resonance when the wavelength of the incident electrons becomes closer to the bond-length. In case of carbon materials, the inter-atomic distance of carbon, the C-C bonds, is varying roughly 1.2 to 1.4 Å. This bond length in resonance corresponds to the electron wave of 50 eV (= 0.05 keV). In other words, the selective bond breaks will not happen until the acceleration voltage comes down to 0.05 kV for C-C bonds. It is rather safe to use the acceleration voltage of 10 kV (or higher) where the bond break rate reduces by  $1/e^2$  then shows a gradual slope with higher acceleration voltage.

**Figure 1** represents our simulation results of calculated knock-on threshold energies of carbon atoms with different bonding states [1]. While the  $sp^2$  bonded carbon atoms of graphite (Fig. 1(e)) show the knock-on threshold of 80 kV, the carbon atoms that consist of nanotube (d) or fullerene (c) show the threshold of

50 kV. Furthermore, a radical carbon atom at the graphene edge, which has only two C-C bonds, shows a lowest threshold of ~35 kV. Therefore, the upper limit of acceleration voltage should be 35 kV so that a low-voltage TEM/STEM which is capable of visualizing the carbon atoms at the graphene edge without massive electron beam damage can be realized. The lower limit of acceleration voltage can be determined by the rate for the selective bond breaks, which is enough higher than 10 kV as described above. Eventually, our 3C project has found a clear goal to realize the low voltage TEM/STEM which resolves the C-C bonds of 1.2 – 1.4 Å within the narrow acceleration voltages of 15 – 35 kV.

### DELTA system: a dedicated high-order aberration corrector for low-voltage TEM/STEM

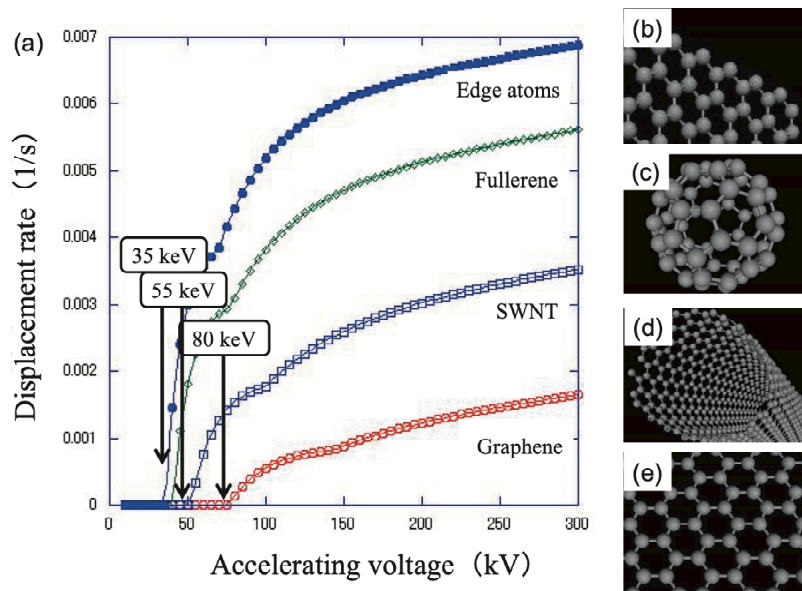
In order to achieve the high resolution at low acceleration voltage, a new aberration corrector is indispensable. Some companies like CEOS in Germany or NION in US have

commercialized the aberration correctors for TEM/STEM, which could work at relatively high acceleration voltages (100 kV or higher) and were not supposed to be used at lower acceleration voltages. At lower acceleration voltages, the chromatic aberration and the diffraction limit due to the higher order aberration should become greatly important and influential to the performance. Two-step hexapole system for the most popular aberration corrector at that time had a severe drawback because the fifth-order six-fold aberration ( $C_{56}$ , or  $A_5$ , or  $A_6$ ) will limit the opening angle  $\alpha$ , therefore the spatial resolution is strongly hindered by the diffraction limit. The six-fold aberration which is intrinsically dominant in the hexapole system can be expressed as,

$$C_{56} \propto \frac{M^2 \times Cs^2 \times t}{f^2}$$

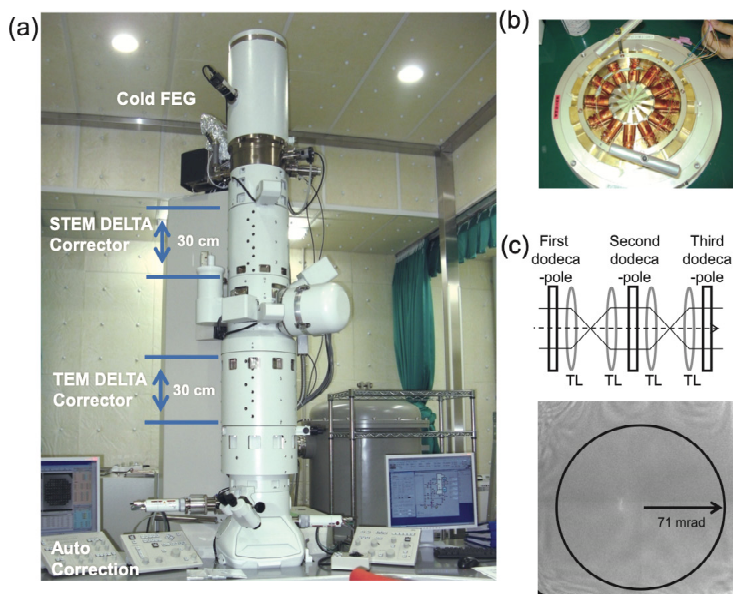
where  $M$ : demagnification rate of condenser mini lens and objective lens,  $t$ : thickness of multipoles,  $Cs$ : spherical aberration coefficient, and  $f$ : focal length of objective lens. In

**Fig. 1**



(a) Estimated knock-on threshold energies for various carbon materials with different configuration. Displacement energies ( $E_d$ ) previously reported were used for calculations. (b) Accelerating voltages less than 35 kV are indeed preferred for observing the graphene edge atoms and (c) the fullerene molecules, while the carbon nanotube and graphene bulk structures are more resistant up to (d) 55 and (e) 80 kV respectively.

**Fig. 2**



(a) Low-voltage TEM/STEM named 3C1, which achieves a world-best spatial resolution with respect to the wave length. (b) DELTA corrector consists of triple dodeca-pole elements. (c) Six-fold astigmatism will be cancelled by rotating three-fold astigmatism of each dodeca-pole. A phase flat region exceeds 73 mrad in  $\pi/4$  limit.

general,  $f$  is proportional to chromatic aberration coefficient  $C_c$  ( $f \propto C_c$ ), a smaller  $f$  means a larger  $C_{56}$ . It means the chromatic aberration and diffraction limit is a trade-off for the low-voltage TEM/STEM with the existing aberration correctors.

Dr. Hidetaka Sawada from JEOL has designed a new aberration corrector and overcome this drawback. It consists of a series of three steps of dodecapoles and is called the DELTA (Dodecapole ELEMENTS Triple Aberration corrector) system [2, 3]. This DELTA corrector is capable of rotating three-fold aberration ( $A_3$ ) and then the coupled six-fold aberrations can be cancelled by inducing magic angles between three serial  $A_3$  aberrations. Therefore one can use the polepiece with smaller  $C_c$  but avoid the diffraction limit which will strongly restrict the spatial resolution.

Introducing the DELTA corrector into the probe forming lens, a large opening angle  $\alpha$  can be used for STEM imaging (Fig. 2). We were able to realize the STEM imaging of graphene at 30 kV with the spatial resolution better than 1.4 Å which corresponds to the C-C bond length. Figure 3 shows the experimental results by Sawada in which the STEM imaging with the  $\alpha = 48$  mrad can resolve the 1.0 Å distance. This spatial resolution

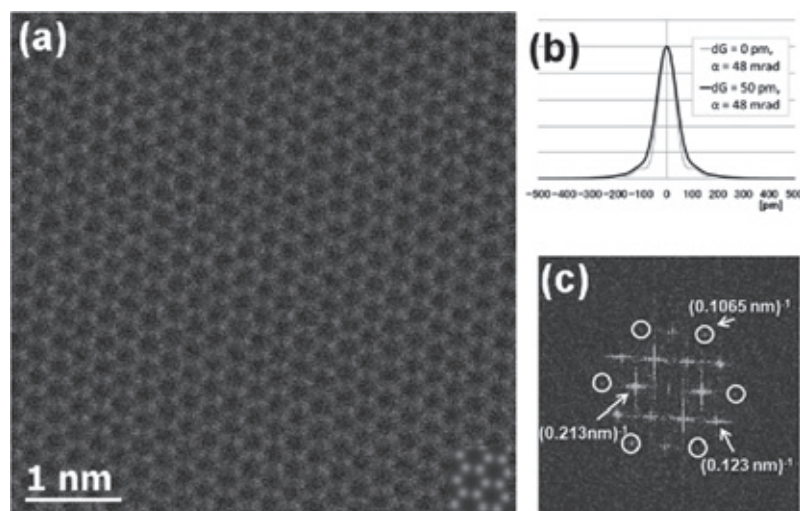
corresponds to the 15 times of the wavelength of an electron accelerated at 30 kV [4].

### Chemical analysis of individual molecules

The above mentioned low-voltage TEM/STEM has a great advantage when one aims to perform spectroscopy and chemical analysis on molecules. It does not induce massive electron beam damage if one work at 30 kV or lower. Figure 4 shows an EELS chemical mapping performed at 30 kV using the low-voltage STEM on metallofullerene molecules which contain a single metal atom in each fullerene cage. In 2000 we had already performed a similar experiment but using a 100 kV electron beam, and all the molecules were destroyed due to the massive electron beam damages after acquiring an EELS chemical map [5]. To the contrary, using the low-voltage TEM/STEM, one can employ the acceleration voltage of 30 kV which is obviously lower than the threshold energy of 35 kV and the fullerene molecules are not destroyed.

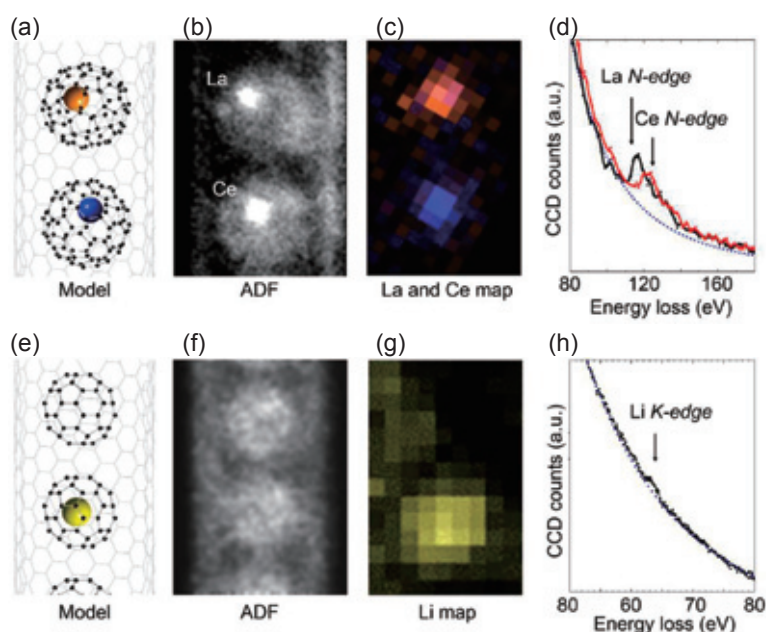
Figure 4(a-d) shows the chemical maps of metallofullerene

Fig. 3



(a) ADF image of graphene at 30 kV. Lower right corner shows a simulated image with a convergence angle of 48 mrad and Gaussian probe size of 50 pm. (b) Calculated probe shape with Gaussian probes of 0 and 50 pm. Probe dimensions are (FWHM) 92.8 pm,  $D_{50}$ : 167.5 pm, and  $D_{95}$ : 210.5 pm. (c) A Fourier transform of the STEM image.

Fig. 4



Detection of a single metal atoms in peapods (by STEM operated at 30 kV). (a, b) A model and an ADF image, respectively, for  $\text{La@C}_{62}$  and  $\text{Ce@C}_{62}$  peapods. and (e, f) Those for a  $\text{Li@C}_{60}$  peapod. In the ADF images, no visible contrast for the Li atom can be seen inside the fullerene cages in (f), while the La and Ce atoms are clearly imaged as bright spots in (c). However, the EELS chemical map in (g) composed by the Li *K-edge* around ~60 eV in (h) indicates the existence of a Li atom in the bottom  $\text{C}_{60}$  cage. Compared to the La and Ce EELS chemical maps in (c) composed by the La and Ce *N-edges* around ~120 eV in (d), the Li map seems more blurred because of the EELS delocalisation and the atomic movement in which the Li atom inside the cage escapes from the electron beam. The EELS elemental maps in (c) and (g) are smoothed by the convolution of a  $3 \times 3$  pixel matrix. Both experiments were performed at 30 kV.

molecules (La@C<sub>82</sub> or Ce@C<sub>82</sub>) by means of STEM-EELS. Single atoms of La (Z=57) or Ce (Z=58) are encapsulated in each fullerene cage of C<sub>82</sub>. These molecules are further encapsulated in a carbon nanotube, exhibiting the peapod structures (Fig. 4a). There is only one atomic number difference between La and Ce, therefore no distinct contrast can be found in the ADF image (Fig. 4b). On the other hand, in the chemical map (Fig. 4c) constructed from the EELS spectrum-imaging clearly distinguishes the single atoms of La and Ce, presented in the colour map in red and blue respectively.

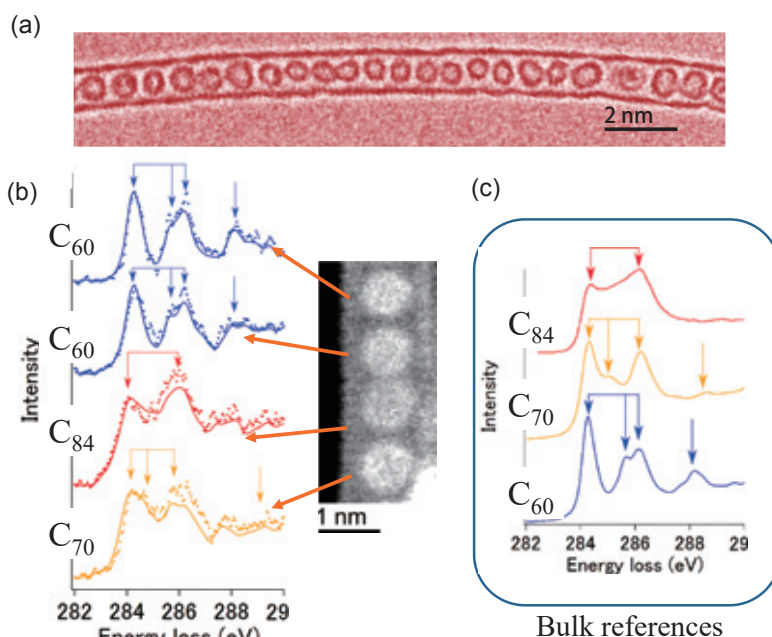
Another great advantage of low-voltage TEM/STEM is a potential capability to efficiently detect light elements. Figure 4(e-h) proves the successful detection of single Li atom (Z=3) in an EELS chemical map. In contrast to the case of La or Ce, the Li atoms cannot be visualized in the ADF image (Fig. 4f). The knock-on threshold of Li is supposed to be still lower than 30 kV, so that the Li atom can be intrinsically kicked out under the e-beam observation of low-voltage TEM/STEM. The Li atoms are therefore supposed to move around within the fullerene cage during the e-beam scan. Because the fullerene cage itself is not to be damaged under the 30 kV observation, the Li atom will remain inside the fullerene cage. It is noted that the ADF image of atoms requires the physical impact of electron beam with the target atoms, while the EELS signal arises even when the electrons pass by near the atoms. This is the so-called EELS signal delocalisation effect in which the atoms show the dielectric response due to the electrons passing nearby in a loof geometry and then an EELS signal indeed arises. Since Li has only a shallow edge around 60-70 eV, a relatively larger EELS signal delocalisation (a few Å) is expected, which helps to detect single Li atom in the EELS chemical map in a confined nanometer space even though it is hardly possible to image in the ADF contrast [6].

### ELNES fingerprints for individual molecules

EELS fine structure analysis to determine the molecular symmetry/structure at single molecule levels is of extreme

importance. ELNES (Energy Loss Near Edge Structure) will provide us the bonding information of specific elements in materials and/or the symmetry information of targeted molecules. This article picks up the carbon materials that indeed have many allotropes, which cannot be distinguished by the simple elemental analysis. A family of fullerene molecules is known as most typical carbon materials and each fullerene molecule consists of a few tens of carbon atoms with closed network. These fullerene molecules have wide ranges of different size and symmetry with various electronic states. In this section, we show an example that one can discriminate the fullerene molecules with different mass (size) and symmetry. The different carbon allotropes, C<sub>60</sub>, C<sub>70</sub>, and C<sub>84</sub> molecules, can be clearly identified in the individual molecular basis by ELNES analysis of carbon K-edge. Another peapod structure of different kinds of fullerene molecules co-doped into carbon nanotube was used for individual molecular spectroscopy (Fig. 5), where the carbon K-edge fine structure is measured from each molecule. These molecules are one dimensionally aligned with the intermolecular distance around 1 nm (Fig. 5(a)), which makes it possible to get an ELNES spectrum from each molecule. Figure 5b shows carbon K-edge fine structure taken from four adjacent fullerene molecules. Each ELNES exhibits distinct shapes with different peak positions which allow us to determine the structure or symmetry of carbon based molecules. Note that the contribution from carbon nanotube must have been removed from the ELNES structures in advance because the carbon nanotube also contributes to the carbon K-edge. The reference spectra of carbon K-edge are already acquired from the bulk crystal of known fullerene molecules. Such bulk spectra have higher signal-to-noise ratio because many of identical molecules contribute to the spectra and clearly show the distinct peak positions for C<sub>84</sub>, C<sub>70</sub> and C<sub>60</sub> (Fig. 5c from the top, indicated by arrows). By comparing the experimental spectra from individual molecules (Fig. 5b) with these reference spectra, one can identify the structures of individual fullerene molecules one-by-one [7]. Such a method to identify the ELNES with the known reference is called the fingerprinting method.

**Fig. 5**



(a) Representative HR-TEM image of fullerenes in a SWNT. (b) Spectra of four molecules compared to experimental spectra from bulk. The solid lines are spectra after Richardson-Lucy deconvolution. Two of the molecules are identified as C<sub>60</sub> and one as C<sub>70</sub>. The fourth molecule (red) spectrum shows broader peaks indicating a lower symmetry and closely matches that of C<sub>84</sub>, though not definitely assigned. The same common features can be seen in (d), where reference spectra from crystalline C<sub>60</sub>, C<sub>70</sub>, and C<sub>84</sub> are shown. [See also ref. [7] for details.]

## Single atom analysis of carbon atomic chains

An electron beam at 60 kV will remove the edge carbon atoms of freestanding graphene in a TEM and the one-dimensional carbon atomic chains which consist of a few to a few tens of carbon atoms will remain after [8]. This is an efficient way to sculp a freestanding carbon atomic chains in vacuum and is of great scientific importance since it provides us an opportunity to investigate structures and properties of authentic one-dimensional materials.

**Figure 6** shows the results of STEM-EELS experiments on a pair of carbon atomic chains. A STEM-ADF image (Fig. 6a) shows a strong dimerization of carbon atoms in chains [9]. Dimerization due to the Peierls distortion is very prominent in contrast to the known synthesized cumulene (...C=C=C=C...) or polyynes (...C≡C-C≡C...). This unordinary structure is surprisingly stable under TEM observation condition, then one is able to get an EELS from every carbon atom which is the constituent of the atomic chains and to analyze its EELS of carbon *K*-edge. In our experiment, a spectrum-imaging of carbon *K*-edge was performed covering the field of view of Fig. 6a as  $13 \times 10$  pixels. Thus obtained 130 EEL spectra were classified into three cases; green for  $sp^2$  carbon atoms, blue for edge carbon atoms and red for the atomic chain. These three different carbon atoms exhibit different ELNES with distinct  $\pi$  peak positions (Fig. 6c). We can therefore make spatial maps for all the different electronic state for each  $\pi$  peak. The ELNES of the carbon atomic structure shows a good agreement with the theoretically predicted one by CASTEP.

## Introduction of monochromator

The 3C project is named after the three C, the third of which means the Cc (chromatic aberration). We once designed a tandem Cc and Cs corrector for the image forming lens and proved the principle showing the successful Cc correction in the range of  $\pm 25$  V at 30 kV acceleration voltage [10]. It is however hard to practically use this CcCs corrector because of the alignment difficulty and the intrinsic instability. We have therefore introduced a monochromator as an alternative for the CcCs tandem corrector. A double Wien filter type monochromator designed by Dr. Masaki Mukai from JEOL

located just after the Shottky gun before the accelerating tube is found extremely stable and relatively easy to operate [11]. When the monochromator is coupled with the DELTA corrector for imaging, the contrast transfer function (CTF) will show a great shape with far first zero and reduced dumping function, which are helpful to realize a higher spatial resolution in TEM [12, 13]. **Figure 7(a)** shows the 3C2 machine with the double Wien filter type monochromator. The monochromator has a fixed dispersion plane of  $12.3 \mu\text{m}/\text{eV}$  and a series of slits with different width. The energy resolution can be improved down to 30 meV at the cost of strongly diminished beam current (Fig. 7d). Figure 7c shows an example of HR-TEM image of graphene recorded by the 3C2 machine with the DELTA corrector and monochromator. The dark spots correspond to the individual carbon atoms, which shows a great improvement if compared with the HR-TEM image recorded by a 120 kV TEM without Cs corrector in 2004[14].

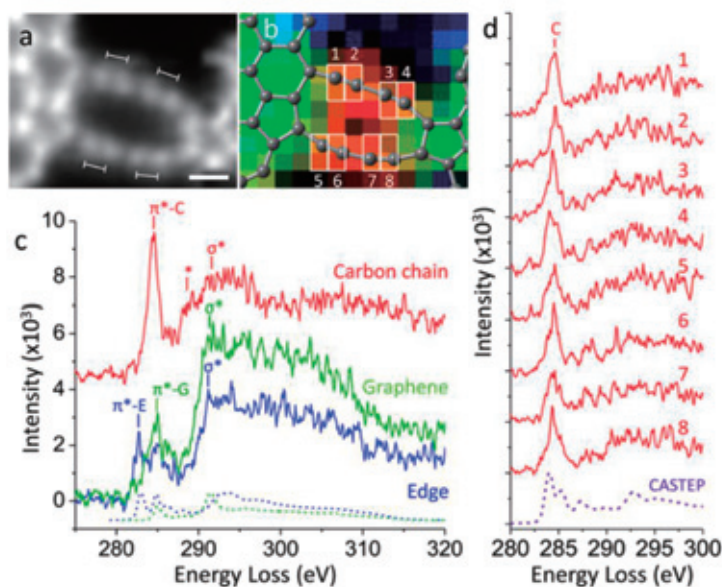
## Ending remark

This article summarizes achievements of our 3C project which has been conducted since 2006. We have successfully designed a dedicated low-voltage TEM/STEM in order to visualize and analyze individual carbon atoms. Further developments of electron microscopy hardware obviously require new designs of aberration correctors and monochromators which are fully dependent of much sophisticated electron optics. Realizing a Cc corrector for the probe forming lens and an improved monochromated electron source with higher beam current is still remaining for our project.

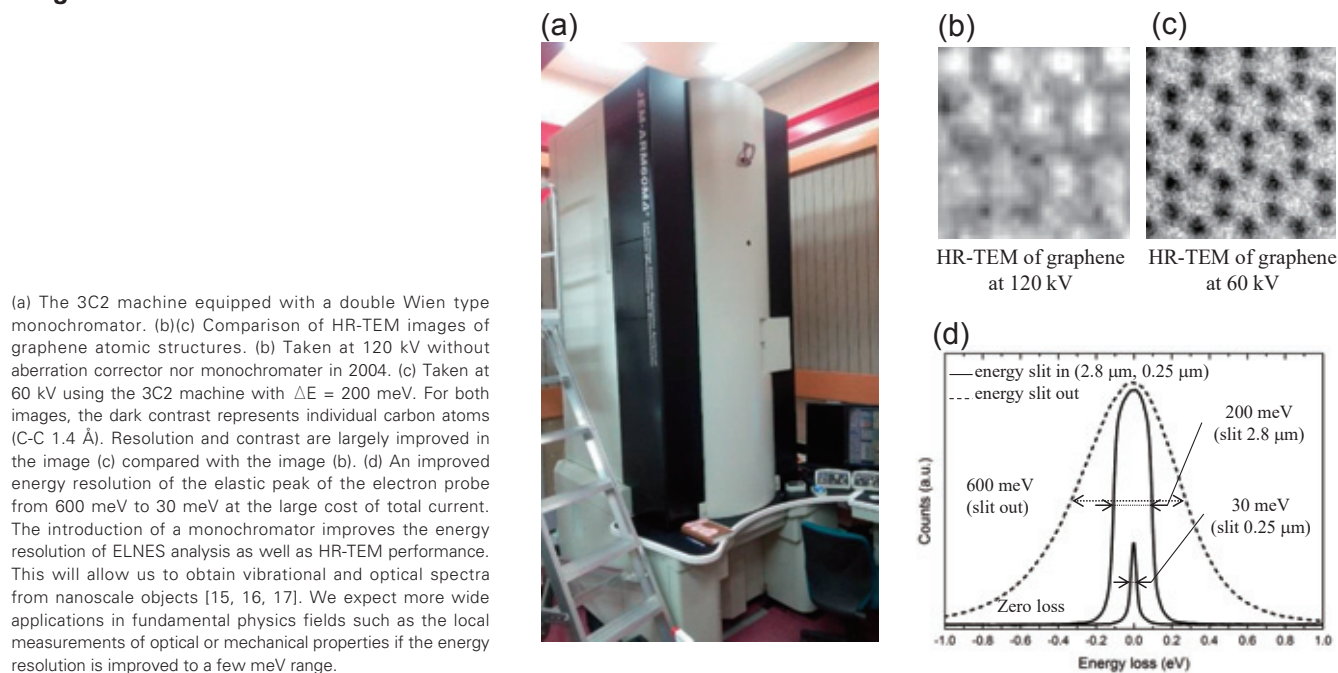
## Acknowledgements

Triple C project has been supported by JST and JSPS, and is still undergoing. Prof. Michiyoshi Tanaka is greatly appreciated for continuous encouragements. The work presented here are all collaborated with Drs. Yukihiro Kondo, Toshikatsu Kaneyama, Hidetaka Sawada, Takeo Sasaki, Shigeyuki Morishita, and Masaki Mukai from JEOL as well as Dr. Koji Kimoto from NIMS. Drs. Yung-Chang Lin, Ryosuke Senga and Luiz Tizei from AIST have conducted the experimental researches presented here.

**Fig. 6**



(a) ADF image of two parallel carbon chains. Scale bar is 2 Å. (b) The corresponding EELS color mapping overlapped with the extracted atomic model. The 2D spectrum imaging contains  $13 \times 10$  pixels in EELS map and simultaneous ADF image consists of subpixel scan ( $16 \times 16$ ). Three color indexes in the EELS color integrated with different energy widths correspond to  $sp^1$ -chain (red, 283.4–284.5 eV),  $sp^2$ -graphene (green, 284.6–299.6 eV), and graphene edges (blue, 281.4–282.9 eV). The acquisition time for each spectrum is 0.2 s/pixel. (c) Spectra shown are extracted from the sum of 10 pixels from the EELS map shown in (b). The simulated EEL spectra of graphene and edge are presented by green and blue dashed lines, respectively. (d) Atom-by-atom EELS spectra corresponding to each atom in the carbon chain.

**Fig. 7**

## References

- [ 1 ] K. Suenaga, Y. Iizumi and T. Okazaki, “Single atom spectroscopy with reduced delocalization effect using a 30 kV-STEM”, *European Physical Journal Applied Physics*, **54** (2011) 33508 (4 pages), DOI: 10.1051/epjap/2011100414
- [ 2 ] H. Sawada, T. Sasaki, F. Hosokawa, S. Yuasa, M. Terao, M. Kawazoe, T. Nakamichi, T. Kaneyama, Y. Kondo, K. Kimoto and K. Suenaga, “Correction of higher order geometrical aberration by triple 3-fold astigmatism field”, *Journal of Electron Microscopy* **58** (2009) pp.341-347, DOI: 10.1093/jmicro/dfp033
- [ 3 ] H. Sawada, T. Sasaki, F. Hosokawa, S. Yuasa, M. Terao, M. Kawazoe, T. Nakamichi, T. Kaneyama, Y. Kondo, K. Kimoto and K. Suenaga, “Higher-order aberration corrector for an image-forming system in a transmission electron microscope”, *Ultramicroscopy*, **110** (2010) pp.958-961, DOI: 10.1016/j.ultramic.2010.01.010
- [ 4 ] H. Sawada, T. Sasaki, F. Hosokawa and K. Suenaga “Atomic-resolution STEM imaging of graphene at low voltage of 30kV with resolution enhancement by using large convergence angle”, *Phys. Rev. Lett.*, **114** (2015) 166102 DOI: 10.1103/PhysRevLett.114.166102
- [ 5 ] K. Suenaga, M. Tencé, C. Mory, C. Colliex, H. Kato, T. Okazaki, H. Shinohara, K. Hirahara, S. Bandow and S. Iijima, “Element-selective single atom imaging”, *Science*, **290** (2000) pp.2280-2282, DOI: 10.1126/science.290.5500.2280
- [ 6 ] R. Senga and K. Suenaga, “Single-atom electron energy loss spectroscopy of light elements”, *Nature Communications*, (2015) 6: 7943 | DOI: 10.1038/ncomms8943
- [ 7 ] L. Tizei, Z. Liu, M. Koshino, Y. Iizumi, T. Okazaki and K. Suenaga, “Single molecular spectroscopy: Identification of individual fullerene molecules”, *Phys. Rev. Lett.*, **113** (2014), 185502 (2014) doi:10.1103/PhysRevLett.113.185502
- [ 8 ] C. Jin, H. Lan, L. Peng, K. Suenaga and S. Iijima, “Deriving Carbon Atomic Chains from Graphene”, *Physical Review Letters*, **102** (2009) 205501 (4 pages), DOI: 10.1103/PhysRevLett.102.205501
- [ 9 ] Y.-C. Lin, S. Morishita, M. Koshino, C.-H. Yeh, P.-Y. Teng, P.-W. Chiu, H. Sawada, and K. Suenaga, “Unexpected Huge Dimerization Ratio in One-Dimensional Carbon Atomic Chains”, *Nano Letters*, **17** (2017) pp.494-500, DOI: 10.1021/acs.nanolett.6b04534
- [ 10 ] F. Hosokawa, H. Sawada, Y. Kondo, K. Takayanagi and K. Suenaga, “Development of Cs and Cc correctors for transmission electron microscopy”, *Microscopy* **62** (2013) pp.23-41, doi: 10.1093/jmicro/dfs134
- [ 11 ] H. Kurata, “Electronic State Analysis by Monochromated STEM-EELS”, *JEOL News* **53** (2018) pp.25-29
- [ 12 ] S. Morishita, M. Mukai, K. Suenaga and H. Sawada, “Resolution enhancement in transmission electron microscopy with 60 kV monochromated electron source”, *Applied Physics Letters* **108**, 013107 (2016) doi: 10.1063/1.4939653
- [ 13 ] S. Morishita, M. Mukai, K. Suenaga and H. Sawada, “Atomic Resolution Imaging at an Ultralow Accelerating Voltage by a Monochromatic Transmission Electron Microscope”, *Physical Review Letters*, **117**, 153004 (2016) DOI: 10.1103/PhysRevLett.117.153004
- [ 14 ] A. Hashimoto, K. Suenaga, A. Gloter, K. Urita and S. Iijima, “Direct evidence for atomic defects in graphene layers”, *Nature*, **430** (2004) pp.870-873, DOI: 10.1038/nature02817
- [ 15 ] R. Senga, T. Pichler, Y. Yomogida, T. Tanaka, H. Kataura, and K. Suenaga, “Direct Proof of a Defect-Modulated Gap Transition in Semiconducting Nanotubes”, *Nano Letters*, **18** (2018) pp.3920-3925 DOI: 10.1021/acs.nanolett.8b01284
- [ 16 ] R. Senga, T. Pichler, and K. Suenaga, “Electron Spectroscopy of Single Quantum Objects To Directly Correlate the Local Structure to Their Electronic Transport and Optical Properties”, *Nano Letters*, **16** (2016) pp.3661-3667 DOI: 10.1021/acs.nanolett.6b00825
- [ 17 ] R. Senga et al., arXiv:1812.08294 [cond-mat.mtrl-sci]

# High-Field DNP Using Closed-Cycle Helium MAS System

Yoh Matsuki and Toshimichi Fujiwara | Institute for Protein Research, Osaka University

Dynamic nuclear polarization (DNP) using cross effect (CE) for the electron to nuclear polarization transfer can enhance the sensitivity of magic-angle sample spinning (MAS) solid-state NMR by more than 100-fold, and is becoming increasingly popular at moderate external magnetic field and temperature conditions such as  $B_0 = 9.4$  T,  $T = 100$  K. Nevertheless, the decreasing CE-DNP efficiency with increasing external field strength has been posing a serious concern in promoting the technique toward very high-field conditions ( $B_0 \gg 10$  T) for higher spectral resolution. Although ultra-low temperature (ULT) DNP technique that utilizes cold helium (He)-based MAS is an effective means for recovering the decreased DNP efficiency at high fields, the conventional system that boils liquid He for producing the cold spinner gas was impractical for routine applications due to its high running cost and poor long-term stability. To overcome these issues, we have developed a novel closed-cycle cold He MAS DNP probe system, and reported in 2015. Since then, we have been continually improving it for faster MAS at lower temperatures, and for higher sensitivity gain. In this article, we review the current status of the system illustrated with some of the latest DNP data taken at  $B_0 = 16.4$  T and  $T \ll 100$  K.

## Introduction

Dynamic nuclear polarization (DNP) transfers large electron spin polarization to the nuclear spin of interest, being able to enhance the sensitivity of magic-angle sample spinning (MAS) NMR by orders of magnitude. This electron-to-nuclear polarization transfer is achieved by perturbing the electron spin resonance (ESR) of an exogenous/endogenous paramagnetic center in the sample using the resonant microwave irradiation. For the polarization transfer, at least one of the known DNP mechanisms, namely Overhauser effect, solid effect, cross effect (CE) or thermal mixing, should be operative. Among them, the CE process involving two electron and one nuclear spins has been used most widely at high field conditions for its relatively high efficiency. In the CE process, the differential electron polarization is transferred to the nuclear spin, thus the selective saturation of one of the two dipolar-coupled electron spins is the key requirement for improving the overall signal enhancement.

Implementing CE-DNP usually needs the following three items: (i) First of all, a polarizing agent (small open-shell compound bearing unpaired electron(s)) as the source of the electron spin polarization. Often times, it is dissolved into a frozen glassy matrix, e.g. glycerol-water mixture, together with the analyte such as proteins. The advent of biradical polarizing agents has boosted the efficiency of the CE-based DNP at high fields [1, 2], and is still under active development. (ii) Secondly, a microwave oscillator and a transmission system that delivers the generated microwave to the DNP NMR probe. In order to perform DNP at high-fields, e.g. for a "500 MHz NMR", high-power (several watts) and high-frequency (~330 GHz) microwave is necessary, which defines one of the

challenges in the instrumentation for high-field DNP. In 1993, the introduction of cyclotron maser (gyrotron) oscillators as a valid and efficient microwave source [3] has opened up the DNP technique to high-field conditions ( $B_0 > 5$  T). Since then, gyrotrons capable of long-term stable oscillation with a smooth tunability, producing high-frequency high-power output, and being compact and inexpensive has been the technical focuses in the field [4-6]. (iii) Last but not least is an NMR probe system that realizes fast MAS under cryogenic sample temperatures (~100 K or lower). The low temperature helps to elongate the electron longitudinal relaxation time  $T_{1e}$ , facilitating saturation of the ESR. Although the conventional MAS at ~100 K can be relatively easily achievable using cold  $N_2$ -based MAS systems, improvement of the DNP efficiency at high fields requires MAS at ultra-low temperatures (ULT), i.e.  $T \ll 100$  K using helium (He)-based MAS instruments. Different physical properties of gas He (GHe) versus gas  $N_2$  and high commercial price of He give rise to major challenges in instrumentation and in practical applications. In this article, we will review the current status of our closed-cycle He MAS DNP NMR probe system, and discuss the overall sensitivity gain achievable using the present system at  $B_0 = 16.4$  T.

## Cryogenic platform for high-field DNP

### A bottleneck in high-field DNP

After the seminal paper in 1993 that reported the first "high-field" DNP measurement at 5 T, the highest field condition for DNP remained at 9.4 T [7] until 2010 when the authors have reported the first over-10 T DNP ( $B_0 = 14.1$  T; 395 GHz - 600 MHz DNP - NMR) [8]. After the report, the highest field

strength for DNP has reached 21 T (2017) only within 7 years. Currently, high-field DNP-NMR spectrometers, including our 16.4 T DNP spectrometer (2015), are up and running internationally at 9.4 T (263 GHz - 400 MHz), 11.8 T (330 GHz - 500 MHz), 14.1 T (395 GHz - 600 MHz), 16.4 T (460 GHz - 700 MHz), 18.8 T (527 GHz - 800 MHz), 21 T (592 GHz - 900 MHz).

Despite the remarkable success, a common issue for the high-field DNP has also become evident: the efficiency of the CE-based DNP decreases with increasing external field strength much more steeply than most of us expected (**Fig. 1**) [9]. Possible causes include the progressive decrease of the electron relaxation time at high fields. This issue not only seriously degraded the cost efficiency of high-field DNP systems, but also raised a major concern for the applicability of the current DNP methodologies to very high-field conditions,  $B_0 \gg 10$  T.

### He MAS DNP

The issue of the degrading DNP efficiency at high fields may be resolved if the experiment can be performed at much lower temperatures, i.e.  $T \ll 100$  K, than currently widely achieved using the conventional air/nitrogen-based MAS system. This requires a DNP NMR probe that can cool and spin the sample using cold He gas which does not liquefy until 4.2 K. Although significant technical challenges are foreseen for cold He MAS due to the very different physical properties of He versus  $N_2$ , DNP at ultra-low temperatures (ULT) has a number of advantages: (i) Longer electron spin relaxation time facilitates the saturation of the electron spin transition, and raise the efficiency of the CE process. (ii) The static nuclear polarization increases in inverse proportion to the sample temperature according to the Curie's law. (iii) The thermal noise decreases since the sample, RF coil and the detection circuit are all kept at low temperature. In fact, the authors has experimentally demonstrated in 2012 that the signal enhancement factor by CE-DNP increases exponentially with decreasing sample temperature using a prototype liquid He (LHe)-boiling MAS DNP NMR system [10].

Another long-standing issue was how to transform this LHe-boiling ULT DNP system to a practical and routinely applicable technology. Although instruments for ULT MAS NMR using cold GHe has been reported since the 1970's, they are all based on a boiling-off or heat-exchange to LHe for producing the cold spinner and temperature-controlling GHe, including our prototype system mentioned above [11-14]. However, this LHe-boiling MAS had a serious limitation in achieving a (long-term) stability of the sample temperature and MAS rate. Furthermore, the operation cost was far from acceptable level for practical applications, e.g. for biological samples that often requires a week-long data acquisition for multi-dimensional spectroscopy.

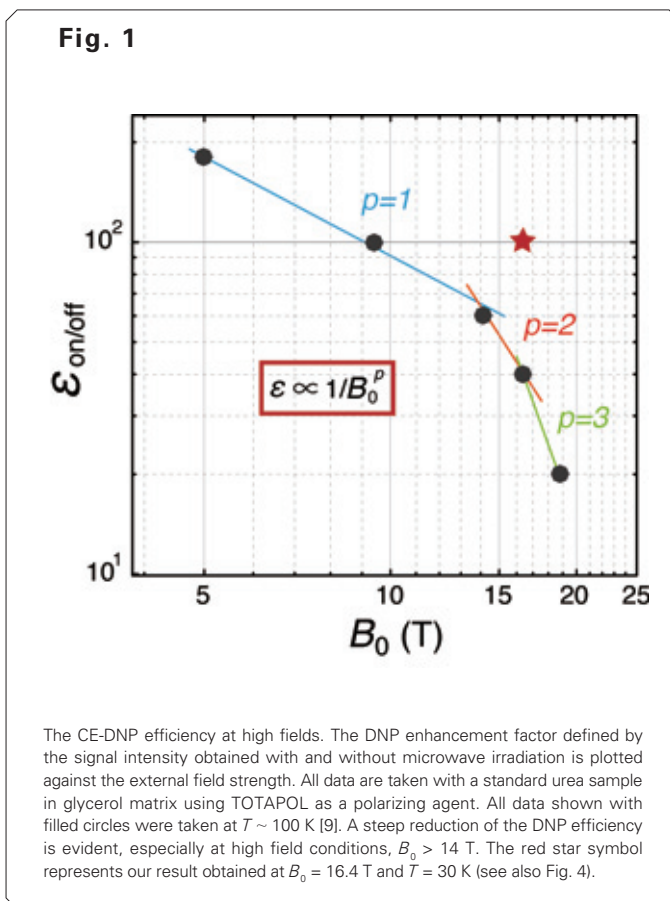
More specifically, the issues were the following. The LHe container (He dewar) is usually pressurized for producing the high-pressure spinner gases, and cannot be re-filled during the measurements. Thus, e.g. a 100 L-container can sustain the ULT MAS measurements for ~10 h for the longest. In addition, since the latent heat of LHe is as small as 1/70 of that for  $N_2$ , it is difficult to obtain a stable evaporation, sensitively affected by the thermal convection in the He dewar and the change in the thermal invasion from dewar's outer wall with decreasing liquid level during the measurement. In addition, it is generally difficult to find valves and pressure regulators with a cryogenic specification with enough accuracy and agility. Even for a system that utilizes LHe only for heat-exchanging of the spinner GHe flow, fluctuation or slow drift of the sample temperature

and/or MAS rate is unavoidable at the cryogen refill and with a slowly decreasing liquid level while LHe is consumed during the measurement. High commercial price of He gives even heavier headache. Since the LHe-boiling MAS experiments usually consume more than 200 L of LHe for 5 days of ULT MAS NMR measurements, it is not realistic to use it for DNP measurements throughout the year. Apart from the problems related to the ULT MAS, high-voltage parts in the RF circuits such as coils and variable capacitors often suffer from discharge arcing in the He environment, making long  $^1H$  decoupling during signal acquisition difficult.

### Closed-cycle He MAS DNP

An elegant and highly efficient approach overcoming these issues has recently been provided by the authors' group, reporting the first example of a closed-cycle He MAS NMR probe system [15-17]. The system does not require any LHe, but it compresses and buffers GHe, and regulates the gas flow rate, cools it "on the fly" using electric gas chillers, and then sends it to the NMR probe for sample cooling and spinning. The GHe exhaust from the probe will not be stored nor liquefied, but directly returned to the original compressor, realizing a continuous recirculating gas flow to sustain ULT MAS without consuming any He (patent pending). The instrumental details are as following.

The closed-cycle He MAS NMR probe system consists of a Cryogenic Helium Circulation (CHC) unit and a dedicated DNP NMR probe (**Fig. 2**). The CHC unit consists of a pair of heat exchanger vessels and a rack for the gas compressors, buffer tanks, and regulators. The GHe for ULT MAS is introduced to the CHC unit from a gas cylinder through a dedicated clean gas lines, and can be sent to a liquefier or liquefaction center after the experiment if necessary. The bearing and driving He

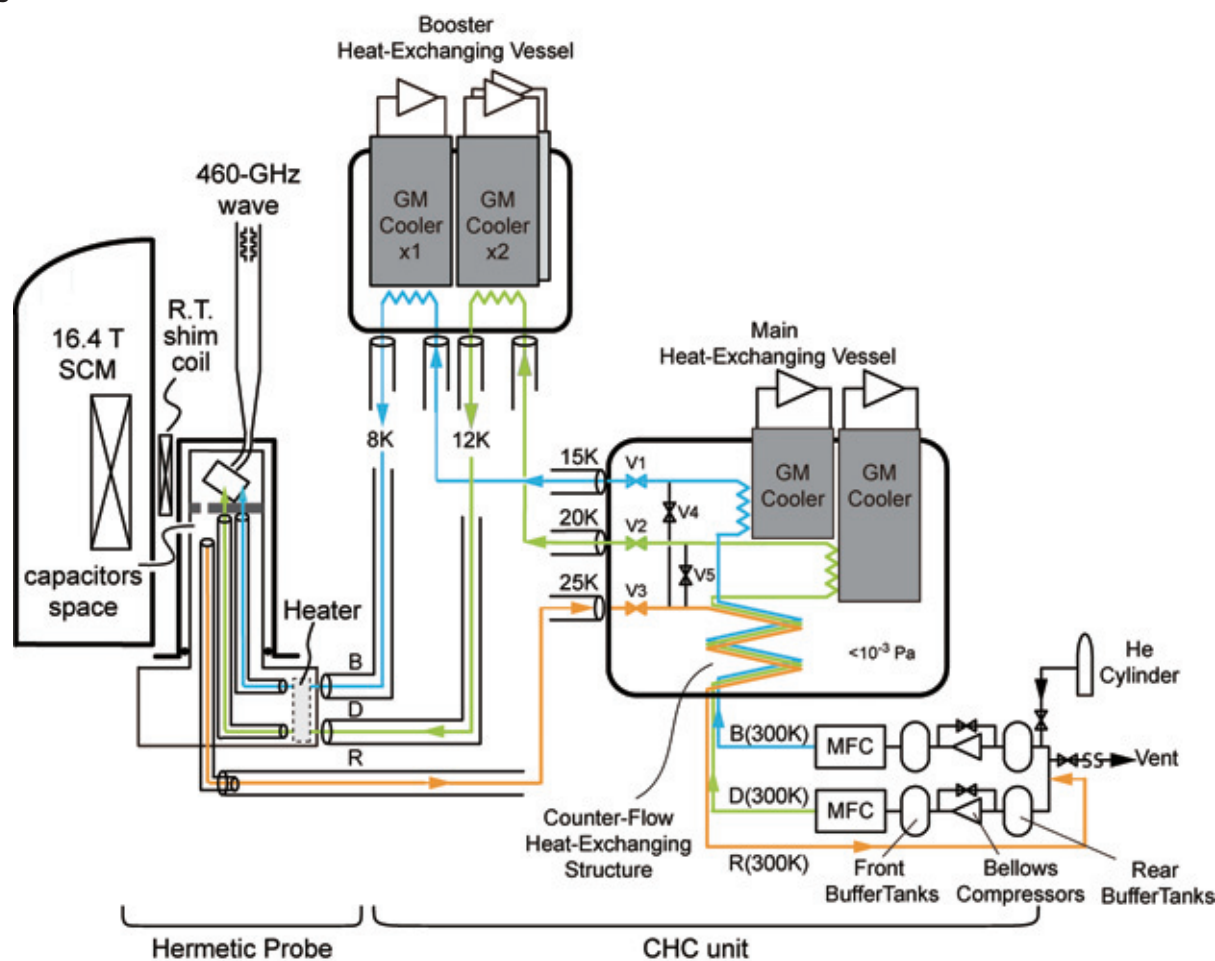


gases are independently compressed by one and two bellows compressors, respectively, buffered, regulated with a mass-flow controller, and then sent to the main heat-exchanger followed by the booster heat-exchanger for cooling. The bellows compressors require no oil lubricant and have an advantage that it does not contaminate the spinner gases over a long-term use. For the cooling of the bearings and the driving gas flows, respectively, two and three 10 K Gifford-MacMahon (GM) coolers are employed. The GM coolers are installed in the vacuum vessel together with the heat-exchanger copper coils. With this system, it was possible to cool total  $\sim 350$  L/min of room temperature GHe “on the fly” down to  $\sim 9$  K using  $\sim 38$  kW of electricity. The relationship between sample temperature and required power consumption will be described in detail in the next section. Thus-cooled GHe is then sent to the NMR probe through the vacuum-insulated flexible tubes for sample cooling and spinning (minimum sample temperature is lower than 15 K). The gas discharged from the probe is still very cold ( $\sim 30$  K), thus used for cooling the room temperature GHe in the first-stage of the main heat-exchanger vessel. As a result, the temperature of the return gas becomes ambient before coming back to the original compressor. This cooling-power recycling design enabled an efficient use of the cooling capacity of the refrigerant, and reduced the size of the entire system. The return gas in ambient temperature also enabled to use buffer tanks and pressure/mass-

flow regulators with a room-temperature specification that are inexpensive and high in performance.

The whole system including the NMR probe is designed to be completely hermetic, and keeps out the atmospheric nitrogen and moisture which contaminate the circulating GHe. As a result, a stable and long-term He MAS can be sustained for more than 4 weeks (as we experimentally confirmed) without any GHe leakage or condensation followed by frost formation anywhere of the system. To improve the heat insulation, each gas transfer line in the NMR probe is vacuum-jacketed, and the space between the probe’s cylindrical body and a probe jacket is also evacuated. Low-temperature GHe exit from the MAS module after the sample cooling and spinning is directed to a space just below the sample chamber where the variable/chip capacitors for RF circuit tuning/matching are located. The gas is then collected and discharged from the probe through a 6 mm-diameter exhaust pipe located just below the capacitor’s space so that a slightly pressurized He atmosphere is formed around the high voltage parts of the RF circuit. This reduces the mean free path for He atoms and suppresses discharge arcing (patent pending). Currently, the RF circuit is doubly tunable to  $^1\text{H}$  and  $^{13}\text{C}$ , and high-resolution measurements using the cross polarization (CP) under high-power  $^1\text{H}$  decoupling are possible. A probe triply-tunable to  $^1\text{H}$ ,  $^{13}\text{C}$  and  $^{15}\text{N}$  is under development. The 460 GHz microwave for DNP enters from

Fig. 2



A schematic diagram of the closed-cycle He MAS probe system. The paths of the bearing gas, driving gas, and the return gas are shown by blue, green and orange lines, respectively. Approximate minimum gas temperatures are also indicated. For the measurements at  $T = 35$ -100 K, the booster heat exchanger is not necessary. By closing valves V1 -V3 and opening V4 and V5, it is possible to cool the main heat exchanger without the NMR probe connected.

the probe top and is transmitted to the sample chamber through the above-mentioned vacuum layer around the probe body using a double vacuum-tight  $\text{Si}_3\text{N}_4$  windows with optimized microwave transmission (patent pending). Finally, the wave is irradiated toward the sample rotor from the side through the RF coil.

### Operational characteristics of closed-cycle He MAS

We use sample rotors made of  $\text{Si}_3\text{N}_4$  that is highly transparent to microwaves with low dielectric constant ( $\epsilon' \sim 10$ ) and loss tangent ( $\tan \delta \sim 0.0003\text{--}0.002$ ), and is relatively high in thermal conductivity ( $\kappa \sim 30$  W/mK). The diameter of the rotor is 3.2 mm. The sample is center-packed using Teflon and Kel-F spacers. The Kel-F spacer is made hollow to contain microcrystals of KBr for in-situ temperature measurement in the sample tube based on the  $^{79}\text{Br}$  NMR at any time during the experiment. The rotor ends are closed with Vespel caps that are designed to become tight at cryogenic temperatures but loose at room temperature enabling repeated use of the caps (patent pending).

To start operating the system, the probe is inserted to the NMR magnet, connected with the CHC unit before the entire system is purged with high-purity (99.999%) GHe. First, a low flow ( $\sim 2$  L/min) GHe is maintained through the whole system including the CHC unit and the probe for about 10 min until the He purity gauge installed at the vent valve indicates "100%". Next, the vent valve is closed and the system is pressurized to  $\sim 150$  kPa (in gauge), and then the pressure is relieved to atmospheric pressure. By repeating this compression-release cycle about 10 times, the gas in the system can be fully replaced with high purity helium. Finally,  $\sim 25$  L of "persistent" GHe is introduced, and then the pumps and the GM coolers are started for a cooling process. The total amount of GHe required for the purging procedure and the "persistent" gas for a ULT MAS DNP measurement is only roughly 500 L (corresponding to  $\sim 0.7$  L of liquid He). Thus, a standard  $14$  m<sup>3</sup> GHe cylinder usually lasts roughly 2 to 3 months.

The initial cooling process from room temperature down to  $\sim 20$  K takes  $\sim 6$  h. Therefore, it is always a good idea to start the cooling process the day before the DNP NMR measurements by starting the GM coolers before going home and leave the system overnight. During this unattended cooling process, it is safe to use low flow for the spinner gases (e.g. 20 L/min for bearing and 10 L/min for driving) to keep the MAS rate to less than about 2 kHz. In the next morning, the sample temperature and the MAS rate can be set to a desired value, and waiting for about half an hour to equilibrate is usually enough before start measurements.

Once the heat exchangers that have very high heat capacity are cooled, the subsequent cooling process becomes quicker, thus a sample exchange can be performed relatively efficiently as follows. First, the GM coolers and compressors are stopped, and then the probe is disconnected from the CHC unit. Next, the probe is purged with room temperature, dry nitrogen gas is flowed (20 L/min) until the whole probe is warmed up to room temperature. The heat capacity of the probe is low, and this takes only  $\sim 20$  minutes or so. After the probe is removed from the magnet for a sample exchange, it is reconnected with the CHC unit again, purged with GHe before restarting the cooling process. Now, it takes only  $\sim 1$  h until the probe stabilizes again at  $\sim 20$  K. The sample rotor can be set in this way in the morning while starting the initial overnight cooling process with an empty probe. In order to expedite sample exchange, a probe system with a cryogenic sample exchange capability is also under development.

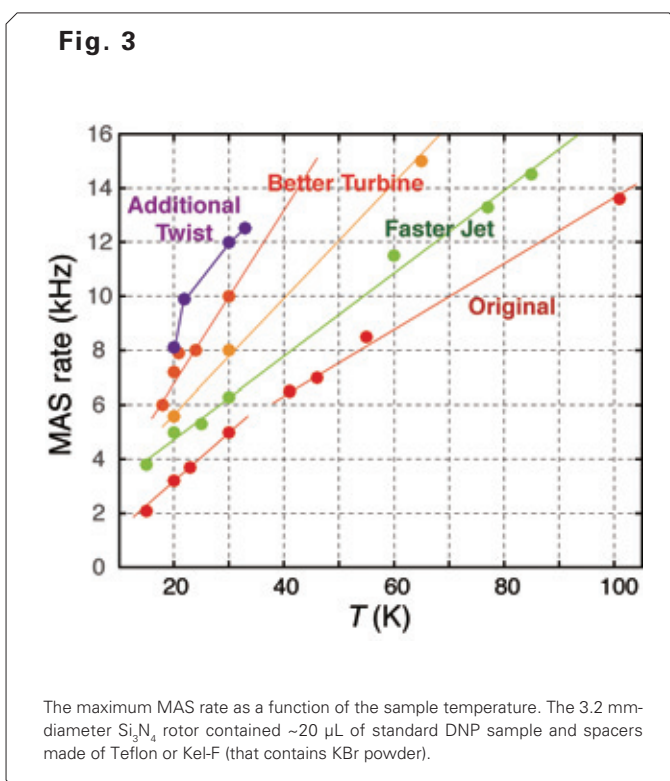
## Results and Discussion

### Performance of closed-cycle He MAS

**Figure 3** plots the MAS rate as a function of the sample temperature obtained with the closed-cycle He MAS probe system at various phases of the development. The sample temperature is seamlessly variable between 20 K and 200 K. Although the maximum MAS rate was about  $\sim 5$  kHz at 30 K in the early days, it is as of the time of writing (March, 2019) more than doubled to  $\sim 12$  kHz through improvements of the nozzle design to increase the velocity of the He jets that pushes the turbine and of the turbine design itself based on the fluid dynamics simulations.

One of the advantages of the closed-cycle He MAS system is its high long-term stability of the measurement conditions. Since no boiling or liquefaction process of helium is involved in the system, the flow rate for the spinner gas flows is intrinsically highly stable. The sample temperature and the MAS rate can be further stabilized using mass-flow regulators and temperature controllers. The typical stability of temperature and MAS rate was  $\pm 0.5$  K and  $\pm 2$  Hz in standard deviation, respectively, at any temperature between 20 and 200 K. During the 30-days of continuous operation, there was no significant drop in the gas flow rate and pressure was observed, and thus it seems a longer operation is also possible.

The second advantage of the closed-cycle MAS system is its low operation cost. The amount of electricity required for the GM coolers is 192 kWh/day for each cooler, and required number of coolers depends on the desired sample temperature. While all five coolers (906 kWh/day) are required for measurements at ultra-low temperatures (15–35 K), only two (384 kWh/day) or one cooler is enough for low (35–100 K) and high temperature (100–200 K) experiments, respectively. Compared with the conventional method using LHe boil-off, the helium consumption is 1/100 or less, and the operation cost is 1/30 in the low to ultra-low temperature regimes. Even compared with the conventional method for the 100 K-MAS that uses



“inexpensive” liquid N<sub>2</sub> (consuming ~500 L/day of liquid N<sub>2</sub> for producing and cooling the spinner gas), the operation cost of the closed-cycle He MAS system is less than the half based on our local supply prices for the electricity and liquid N<sub>2</sub>.

### Sensitivity gain by ULT DNP at 16.4 T

The CE-DNP efficiency that decreases with increasing field strength can be recovered at ULT conditions. **Figure 4** plots the temperature dependence of the sensitivity gain obtained by CE-DNP at  $B_0 = 16.4$  T for a standard urea sample in a glycerol matrix. For the biradical polarizing agent, TOTAPOL (black data) or AMUPol (gray data) was used. The ratio of the signal intensity obtained with and without microwave irradiation,  $\epsilon_{\text{on/off}}$ , steeply increased with decreasing sample temperature, and both TOTAPOL and AMUPol yielded  $\epsilon_{\text{on/off}} \sim 100$  at 30–37 K (Fig. 4a). This can be explained by a longer electron longitudinal relaxation time  $T_{1e}$  at lower temperatures, facilitating the saturation of the ESR.

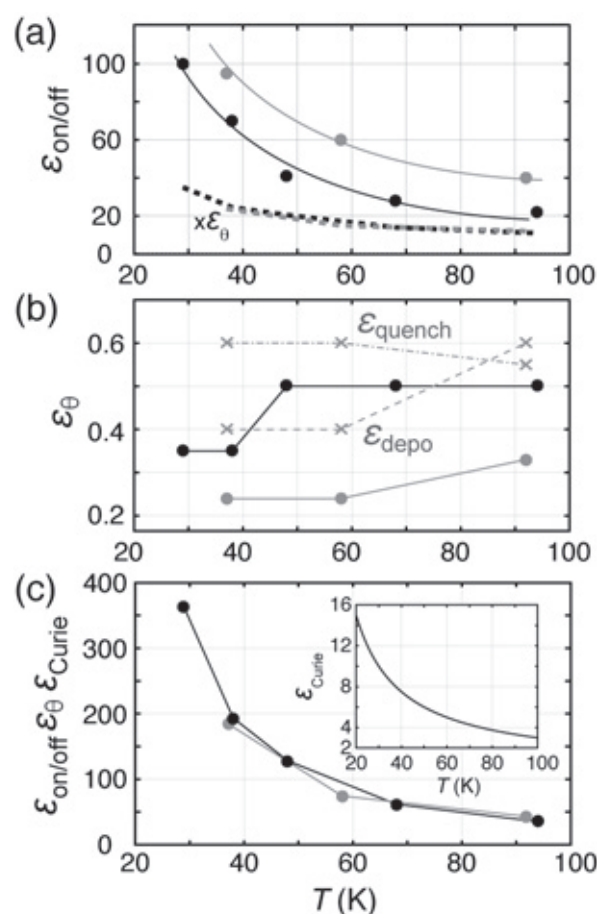
The other factors that affect the overall NMR sensitivity include the so-called quenching and the depolarization effects: it is known that for a radical-doped sample, the intensity of an NMR signal observed without microwave irradiation is smaller than that for an un-doped sample due to the paramagnetic relaxation (quenching) and the MAS-induced depolarization effect of the electron and nuclear spin polarization at equilibrium (depolarization) [18, 19]. Figure 4 (b) plots the temperature dependence of the product of these factors  $\epsilon_{\text{quench}} \times \epsilon_{\text{depo}}$ . For AMUPol, the product was 0.32 at 90 K and 0.25 at 30 K (22% drop), and for TOTAPOL it decreased from 0.5 at 90 K to 0.35 at 30 K (30% drop), with both agents showing a declining tendency with the temperature drop. On the whole, AMUPol yielded smaller “off signal” for a doped sample than TOTAPOL. From the breakdown of  $\epsilon_{\text{quench}}$  and  $\epsilon_{\text{depo}}$  observed for AMUPol (Fig. 4b, gray data), it can be seen that the extent of the depolarization increases with the temperature drop. This suggests again that  $T_{1e}$  becomes longer at lower temperatures. Taking into account the generally smaller off-signal with AMUPol, it can be seen that TOTAPOL and AMUPol give a similar effective sensitivity gain although AMUPol gives ~20 units higher  $\epsilon_{\text{on/off}}$  than TOTAPOL in the entire temperature range examined (Fig. 4a, dash lines).

The net sensitivity gain  $\epsilon_{\text{net}}$  taking account of the signal enhancement by DNP ( $\epsilon_{\text{on/off}}$ ), the increase in the Curie magnetization ( $\epsilon_{\text{Curie}}$ ), as well as the decreased off-signal intensity ( $\epsilon_{\theta} = \epsilon_{\text{quench}} \times \epsilon_{\text{depo}}$ ) reaches a factor of 400 at  $T = 30$  K,  $B_0 = 16.4$  T (Fig. 4c). Compared with the maximum reported net sensitivity gain for the conventional 100 K-DNP,  $\epsilon_{\text{net}} \sim 400$  @ 9.4 T [20] and  $\sim 75$  @ 16.4 T [21], the 30 K-DNP realizes ~5 times larger net sensitivity at the same field condition of 16.4 T. It is also seen that the 30 K-DNP fully recovers the decrease of the CE-DNP efficiency caused by the increase of the magnetic field from 9.4 T to 16.4 T. Other reported methods for improving the DNP efficiency at high fields include the development of polarizing agents (e.g. TOTAPOL vs AMUPol) that improved  $\epsilon_{\text{on/off}}$  by 1.5- to 2-fold [22] and the use of smaller diameter sample rotors (2.5 mm or 1.3 mm sample tube) that gave 2-fold increase in  $\epsilon_{\text{on/off}}$  due to the improved microwave irradiation efficiency [23]. Therefore, it can be said that the ULT DNP provides significantly larger improvement of the net gain  $\epsilon_{\text{net}}$  (~5 times) than the other approaches. Moreover, the net gain is expected to increase further. In our recent experiments, it has been shown that  $\epsilon_{\text{on/off}}$  can be more than doubled from improved microwave transmission within the probe, which should be published in a forthcoming paper.

### 30 K-DNP vs conventional 100 K-DNP

**Figure 5** illustrates the superiority of the 30 K-DNP over the conventional 100 K-DNP. Shown is a <sup>13</sup>C cross-polarization (CP) spectra obtained at inner rotor temperatures of 38 K (blue) and 98 K (red) under the same microwave irradiation condition. Sample was 120 μg of natural abundance (“non-labeled”) L-proline dissolved into a standard DNP matrix. For such small amount of non-labeled substance, the signal-to-noise (S/N) ratio is not sufficient with the 100 K-DNP. On the other hand, the 30 K-DNP enables to clearly observe all the natural abundance <sup>13</sup>C signals of proline above the noise level only in 8 scans. The absolute sensitivity with the 30 K-DNP was 5 times higher than that with the 100 K-DNP, which corresponds to 25 times acceleration of the accumulation time. The <sup>1</sup>H longitudinal relaxation time  $T_{1H}$  was 6.5 sec at both 90 K and 30 K, showing that the ULT DNP does not hurt the unit time sensitivity as is often concerned. In our experiences, samples doped with paramagnetic polarizing agent rarely exhibit  $T_{1H}$  at 30 K appreciably longer than that at 90 K.

**Fig. 4**



Sensitivity gain by CE-based DNP at 16.4 T. Temperature dependence of (a) the DNP enhancement factor  $\epsilon_{\text{on/off}}$ , (b) the paramagnetic quenching and the MAS-induced depolarization factor  $\epsilon_{\theta} = \epsilon_{\text{quench}} \times \epsilon_{\text{depo}}$ , (c) the net sensitivity gain  $\epsilon_{\text{net}}$ . The sample was 2 M <sup>13</sup>C-urea dissolved in a standard DNP matrix (d<sub>5</sub>-glycerol/D<sub>2</sub>O/H<sub>2</sub>O = 6.5/2.5/1; w/w/w). The polarizing agent was 20 mM TOTAPOL (black) or 20 mM AMUPol (gray). The MAS rate was 6 kHz at all temperatures. In (b), the breakdown of  $\epsilon_{\theta}$  into  $\epsilon_{\text{quench}}$  and  $\epsilon_{\text{depo}}$  is also shown for AMUPol. (c) The insertion shows the temperature dependence of Curie effect  $\epsilon_{\text{Curie}}$ . The submillimeter wave was transmitted with a quasi-optical transmission system, and was about 3 W at the probe input.

## Closed-cycle He MAS DNP in a historical context

**Figure 6** is a historical overview of the overall sensitivity gain which also takes into account the sensitivity gain from the rise in the external field strength ( $\epsilon_{B_0}$ ) for high-field DNP. Here,  $\epsilon_{B_0}$  is the relative sensitivity gain with respect to  $B_0 = 1$  T, thus defined as  $\epsilon_{B_0} = (B_0)^{3/2}$ , where  $B_0$ (T) is the magnetic field strength used for the DNP measurement. The circles  $\circ$  and  $\bullet$  indicate MAS DNP data using air or nitrogen MAS, clearly showing the advance in the sensitivity gain from the introduction of gyrotron in the mid 90's until the first decade of 2000. The following star symbols ( $\star$ ) show data from 2010 onwards for the DNP using cold He MAS that enabled a further advance in the sensitivity gain at higher fields ( $B_0 > 10$  T). Note that recent advances due to the Overhauser DNP in insulating solids ( $\triangle$ ) and those using Trityl-TEMPO hetero-biaradical ( $\blacktriangledown$ ) both do not still match the 30 K-DNP for the sensitivity gain.

## Conclusion

We here reviewed the closed-cycle He MAS DNP NMR probe system and its performance in DNP measurements at  $B_0 = 16.4$  T and  $T \ll 100$  K. Improving the DNP efficiency at high field conditions is the key requirement for successful analyses of large and complex chemical systems such as proteins, and

the development of an ULT MAS probe system is at the core of such endeavor. In this article, indeed, we have illustrated that the ULT DNP technique is one of the most successful approaches so far in improving the DNP efficiency at high fields. Furthermore, establishing the long-term stable and low running-cost ULT MAS platform was an essential breakthrough in making high-field DNP available to a wider range of applications/users. As one of the highlights in this point, the first commercial DNP NMR spectrometer utilizing the closed-cycle He MAS system manufactured by JEOL Ltd. will be installed in a customer site in 2019, stipulating the beginning of the next-generation high-field DNP based on the advanced ULT MAS probe system.

Meanwhile, a number of further technical developments are envisaged. This includes polarizing agents specialized in high-field and/or ULT conditions, advanced microwave and RF wave irradiation schemes, innovative sample-irradiation mechanisms in a probe, DNP probes with a cold preamplifier to name a few. On the methodology front, the unique properties of highly polarized spins, not only the sensitivity gain, should be utilized to elucidate mesoscopic-scale distance and/or molecular orientation information. This will contribute to the new step toward "structural life science" that aims to understand biological processes more as a system, rather than focusing on the individual biomolecules as currently possible.

**Fig. 5**

Superiority of the 30 K-DNP versus the conventional 100 K-DNP. Shown are the  $\{^1\text{H}\}$ - $^{13}\text{C}$  CP spectra taken with 120  $\mu\text{g}$  (1  $\mu\text{mol}$ ) of non-labeled proline dissolved in a standard DNP matrix using  $^{13}\text{C}$ -depleted  $d_5$ -glycerol. The temperature inside the sample rotor was 38 K (blue) and 98 K (red). The temperature rise in the sample rotor due to the microwave irradiation was about 8 K in both cases. The MAS at a rate of 8.6 kHz and  $^1\text{H}$  decoupling at 65 kHz were used. The number of scans was 8 with the recycling delay of 9 s. The asterisks ( $\star$ ) indicate spinning side bands.

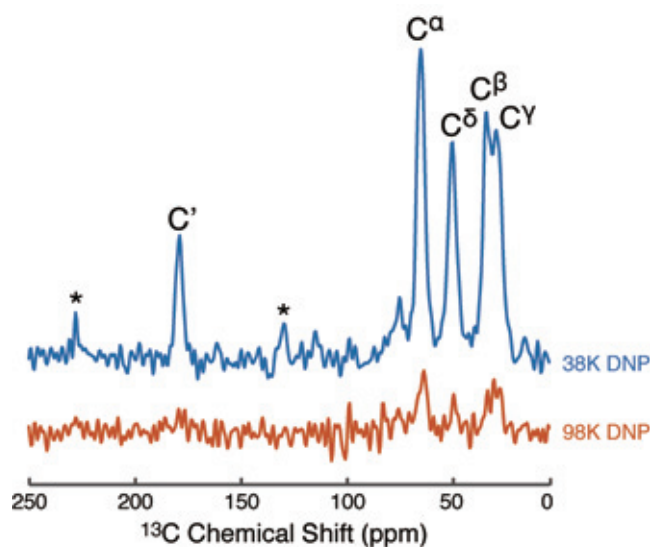
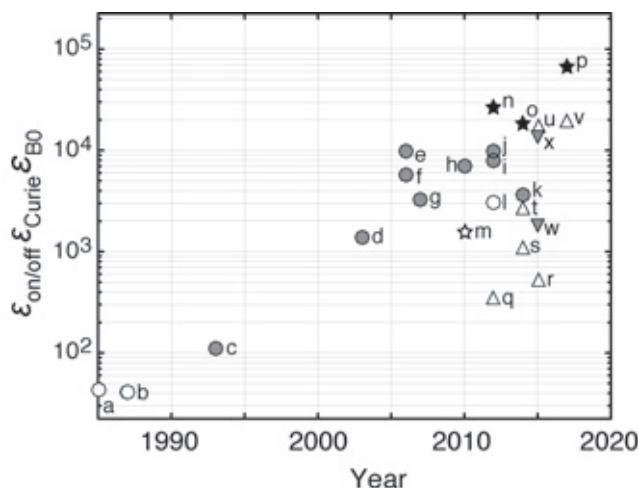


**Fig. 6**

Recent history of the effective sensitivity gain by high-field MAS DNP. The effective sensitivity gain (vertical axis) takes into account the gain due to the rise of the magnetic field. See the main text for more detail. The horizontal axis plots the year of the initial report for DNP measurements at a given external field strength. Filled stars ( $\star$ ) report the CE-DNP data reported by the authors using  $\text{N}_2$ - or He-MAS at  $B_0 > 10$  T (m [8]; n [10]; o [16]; p [24]). The white and the gray circles ( $\circ$ ,  $\bullet$ ) are the SE- or CE-DNP data reported by the authors using  $\text{N}_2$ -MAS (a [25]; b, g [26]; c [3]; e, f [27]; d [7]; h [20]; i [28]; j [21]; k [29]; l [30]). White triangles  $\triangle$  are for OE-DNP ( $q^{31}$ ; s,  $t^{32}$ ; r,  $u^{33}$ ;  $v^{34}$ ), and gray triangle  $\blacktriangledown$  are data by hetero-biaradical (w, x [9]).



## Acknowledgments

This research was conducted at Institute for Protein Research, Osaka University supported by JST SENTAN Program (H271030) and the NMR platform program by MEXT Japan (480790). We also thank JEOL RESONANCE Inc. and CryoVac Co. for invaluable technical supports that enabled successful developments described above.

## References

- [ 1 ] Hu, K. N. Polarizing agents and mechanisms for high-field dynamic nuclear polarization of frozen dielectric solids. *Solid State Nucl. Magn. Reson.* **40**, 31–41 (2011).
- [ 2 ] Matsuki, Y. *et al.* Dynamic nuclear polarization with a rigid biradical. *Angew. Chemie - Int. Ed.* **48**, 4996–5000 (2009).
- [ 3 ] Becerra, L. R., Gerfen, G. J., Temkin, R. J., Singel, D. J. & Griffin, R. G. Dynamic nuclear polarization with a cyclotron resonance maser at 5 T. *Phys. Rev. Lett.* **71**, 3561–3564 (1993).
- [ 4 ] Scott, F. J. *et al.* Frequency-agile gyrotron for electron decoupling and pulsed dynamic nuclear polarization. *J. Magn. Reson.* **289**, 45–54 (2018).
- [ 5 ] Idehara, T., Khutoryan, E. M., Ogawa, I., Matsuki, Y. & Fujiwara, T. Modulation and Stabilization of the Output Power and Frequency of FU Series Gyrotrons. **9**, 117–130 (2016).
- [ 6 ] Hornstein, M. K. *et al.* Second Harmonic Operation at 460 GHz and Broadband Continuous Frequency Tuning of a Gyrotron Oscillator. *IEEE Trans. Electron Devices* **52**, 798–807 (2005).
- [ 7 ] Bajaj, V. S. *et al.* Dynamic nuclear polarization at 9T using a novel 250 gyrotron microwave source. *J. Magn. Reson.* **160**, 85–90 (2003).
- [ 8 ] Matsuki, Y. *et al.* Dynamic nuclear polarization experiments at 14.1 T for solid-state NMR. *Phys. Chem. Chem. Phys.* **12**, 5799–5803 (2010).
- [ 9 ] Mathies, G. *et al.* Efficient Dynamic Nuclear Polarization at 800 MHz/527 GHz with Trityl-Nitroxide Biradicals. *Angew. Chemie - Int. Ed.* **54**, 11770–11774 (2015).
- [10] Matsuki, Y. *et al.* Helium-cooling and -spinning dynamic nuclear polarization for sensitivity-enhanced solid-state NMR at 14 T and 30 K. *J. Magn. Reson.* **225**, 1–9 (2012).
- [11] Concistrè, M., Johannessen, O. G., Carignani, E., Geppi, M. & Levitt, M. H. Magic-angle spinning NMR of cold samples. *Acc. Chem. Res.* **46**, 1914–1922 (2013).
- [12] Hackmann, A., Seidel, H., Kendrick, R. D., Myhre, P. C. & Yannoni, C. S. Magic-angle spinning NMR at near-liquid-helium temperatures. *J. Magn. Reson.* **79**, 148–153 (1988).
- [13] Hall, D. A. *et al.* Polarization-enhanced NMR spectroscopy of biomolecules in frozen solution. *Science (80- )*. **276**, 930–932 (1997).
- [14] Samoson, A. *et al.* New Horizons for Magic-Angle Spinning NMR. *Top. Curr. Chem.* **246**, 15–31 (2004).
- [15] Matsuki, Y., Nakamura, S., Fukui, S., Suematsu, H. & Fujiwara, T. Closed-cycle cold helium magic-angle spinning for sensitivity-enhanced multi-dimensional solid-state NMR. *J. Magn. Reson.* **259**, 76–81 (2015).
- [16] Matsuki, Y., Idehara, T., Fukazawa, J. & Fujiwara, T. Advanced instrumentation for DNP-enhanced MAS NMR for higher magnetic fields and lower temperatures. *J. Magn. Reson.* **264**, 107–115 (2016).
- [17] Matsuki, Y. & Fujiwara, T. Cryogenic Platforms and Optimized DNP Sensitivity. *eMagRes* **7**, 9–24 (2018).
- [18] Corzilius, B., Andreas, L. B., Smith, A. A., Ni, Q. Z. & Griffin, R. G. Paramagnet induced signal quenching in MAS-DNP experiments in frozen homogeneous solutions. *J. Magn. Reson.* **240**, 113–123 (2014).
- [19] Thurber, K. R. & Tycko, R. Perturbation of nuclear spin polarizations in solid state NMR of nitroxide-doped samples by magic-angle spinning without microwaves. *J. Chem. Phys.* **140**, 184201 (2014).
- [20] Rosay, M. *et al.* Solid-state dynamic nuclear polarization at 263 GHz: Spectrometer design and experimental results. *Phys. Chem. Chem. Phys.* **12**, 5850–5860 (2010).
- [21] Barnes, A. B. *et al.* Dynamic nuclear polarization at 700 MHz/460 GHz. *J. Magn. Reson.* **224**, 1–7 (2012).
- [22] Sauvée, C. *et al.* Highly efficient, water-soluble polarizing agents for dynamic nuclear polarization at high frequency. *Angew. Chemie - Int. Ed.* **52**, 10858–10861 (2013).
- [23] Jaudzems, K. *et al.* Dynamic Nuclear Polarization-Enhanced Biomolecular NMR Spectroscopy at High Magnetic Field with Fast Magic-Angle Spinning. *Angew. Chemie - Int. Ed.* **57**, 7458–7462 (2018).
- [24] Matsuki, Y. & Fujiwara, T. Advances in high-field DNP methods. in *Experimental Approaches of NMR Spectroscopy: Methodology and Application to Life Science and Materials Science* 91–134 (2017). doi:10.1007/978-981-10-5966-7\_4
- [25] Wind, R. A., Duijvestijn, M. J., van der Lugt, C., Manenschijn, A. & Vriend, J. Applications of dynamic nuclear polarization in <sup>13</sup>C NMR in solids. *Prog. Nucl. Magn. Reson. Spectrosc.* **17**, 33–67 (1985).
- [26] Bajaj, V. S. *et al.* 250 GHz CW gyrotron oscillator for dynamic nuclear polarization in biological solid state NMR. *J. Magn. Reson.* **189**, 251–279 (2007).
- [27] Song, C., Hu, K. N., Joo, C. G., Swager, T. M. & Griffin, R. G. TOTAPOL: A biradical polarizing agent for dynamic nuclear polarization experiments in aqueous media. *J. Am. Chem. Soc.* **128**, 11385–11390 (2006).
- [28] Barnes, A. B., Nanni, E. A., Herzfeld, J., Griffin, R. G. & Temkin, R. J. A 250 GHz gyrotron with a 3 GHz tuning bandwidth for dynamic nuclear polarization. *J. Magn. Reson.* **221**, 147–153 (2012).
- [29] Koers, E. J. *et al.* NMR-based structural biology enhanced by dynamic nuclear polarization at high magnetic field. *J. Biomol. NMR* **60**, 157–168 (2014).
- [30] Corzilius, B., Smith, A. A. & Griffin, R. G. Solid effect in magic angle spinning dynamic nuclear polarization. *J. Chem. Phys.* **137**, 054201 (2012).
- [31] Haze, O., Corzilius, B., Smith, A. A., Griffin, R. G. & Swager, T. M. Water-soluble narrow-line radicals for dynamic nuclear polarization. *J. Am. Chem. Soc.* **134**, 14287–14290 (2012).
- [32] Can, T. V. *et al.* Overhauser effects in insulating solids. *J. Chem. Phys.* **141**, 064202 (2014).
- [33] Lelli, M. *et al.* Solid-State Dynamic Nuclear Polarization at 9.4 and 18.8 T from 100 K to Room Temperature. *J. Am. Chem. Soc.* **137**, 14558–14561 (2015).
- [34] Chaudhari, S. R. *et al.* Dynamic nuclear polarization at 40 kHz magic angle spinning. *Phys. Chem. Chem. Phys.* **18**, 10616–10622 (2016).

# Application of "operando-ESR" to organic electronics materials

Junto Tsurumi *NIMS*

Shun Watanabe Department of Advanced Materials Science, Graduate School of Frontier Sciences, The University of Tokyo, National Institute of Advanced Industrial Science and Technology (AIST)-University of Tokyo Advanced Operando-Measurement Technology Open Innovation Laboratory (*OPERANDO-OIL*), *AIST* and *JST, PRESTO\**

An electron is an elementary particle that has a negative electric charge and angular momentum, namely spin. Materials science researchers have developed various methods to explore the functionalities of charge and spin. In condensed matter, various electronic properties of electrons' charge are investigated by a range of spectroscopy techniques and transport measurements. A silicon-based electronics is the most representative example, where various functionalities have been realized by a precise control of charges. On the other hand, the way of accessing an electron's spin is limited so far. Electron Spin Resonance (ESR), which is a technique in the family of magnetic resonance spectroscopy, is a unique analytical method that is able to detect electron spin directly in both solid and solution, and is employed as a powerful tool in characterizing physical properties of various materials. In this article, we review an "operando-ESR" technique, in particular its application to organic semiconductors that are expected to be next generation electronic materials.

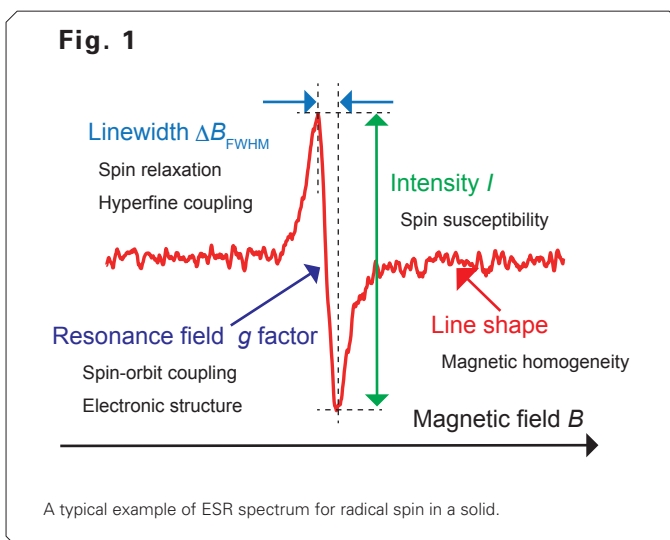
## Introduction: ORGANIC COMPOUNDS AND ELECTRON SPIN RESONANCE

Electron Spin Resonance (ESR) is a spectroscopic method for detecting unpaired electron spins either in a solid or in liquid sample. Electron spins placed in an external magnetic field are oriented parallel or antiparallel to the magnetic field, resulting in an energy difference (the Zeeman effect). When this energy difference matches the energy of the electromagnetic wave, the electron spin absorbs the electromagnetic wave, and an ESR spectrum is observed. Since ESR was first observed in 1945 [1], it has been applied in various scientific fields such as physics, chemistry, medicine [2]. Because ESR is highly selective for the unpaired electron spin, it is possible to determine the magnitude of magnetic interaction and magnetic moment around the electron spins. Target materials are generally paramagnetic substances and organic compounds with the unpaired electron spin [3].

Since organic compounds can be converted into free radicals by chemical reaction with light, heat, and impurities, they can be studied with ESR spectroscopy. High selectivity of free radicals in ESR spectroscopy can be applied to spin labeling in biomaterials, chemical reaction path tracking, etc [4]. Although the spin labeling detected by ESR has been often performed in a solution, the ESR method is applicable to both solid and liquid samples. In solution, the observed radical spins are isolated from each other. That is, it is assumed that the magnetic interaction between radical spins and adjacent molecules is small. In a solid, on the other hand, radical

spins are subjected to the average magnetic interaction of the surrounding material [3]. Since magnetic interactions in such organic solids can vary widely, such as nuclear spin species and their anisotropy, ESR spectroscopy in the solid state allows the ability to extract unique properties related to solid state electronic phenomena.

**Figure 1** shows an example of the ESR signal in a solid (thin film) of an organic molecule. Typically, the vertical axis represents the ESR signal intensity, and the horizontal axis represents the magnetic field  $B$ . It should be noted here that the obtained ESR spectra are a derivative of the absorption



curve. The central magnetic field of the signal represents the resonance field, which gives unique  $g$ -factor. In organic compounds generally composed of light elements such as carbon, the  $g$ -factor is often observed near the  $g$ -factor of free electron spin, but it depends on the spin-orbit interaction and the density-of-states. It should also be noted that the accuracy of the microwave frequency and applied magnetic field is important, as the  $g$ -shift from that of the free electrons requires to be measured with at least five significant figures of precision. ESR signals in solution are known to split by hyperfine interactions from the proton nuclear spins. In a solid, these hyperfine interactions are often averaged and a single component absorption signal can be obtained due to interactions from adjacent molecules as well as intramolecular interaction cannot be neglected. Even when the single component of the ESR signal is obtained, the shape of the absorption signal (typically, Gaussian, Lorentzian, etc.) is also important in evaluating the magnetic interaction surrounding the electron spins (described later). The intensity of the absorption signal is proportional to the spin susceptibility. In the case of solution ESR, the spins that contribute to ESR are localized electron spins, which are in the Curie paramagnetic state. In this case, it is possible to quantify spins (spin counting) because ESR signal intensity is proportional to the total amount of electron spins. On the other hand, it should be noted that degenerated electrons in a solid show Pauli paramagnetism. This yields that ESR signal intensity is not proportional to the total amount of electron spins. Thus, it is possible to determine the details of the electronic state from ESR measurement in solids.

Electrons consist of two degrees of freedom, charge and spin. Charge and spin should correlate with each other, particularly in electrons that form the Bloch wave in solids. Therefore, it should be possible to obtain information on the electron charge by precisely observing the behavior of electron spin. From the early years of defects research in silicon electronics, understanding of the electron charge has been deepened through in-depth understanding of physical properties of electron spin [5]. For example, ESR has been used for observation of defects in silicon crystals, etc [6]. In this paper, we introduce the latest research results applying ESR to electronic materials. In particular, focusing on the state-of-the-art research on *in-situ* spectroscopic measurement (*operando* measurement) in the operation of electronic devices, using an example of organic semiconductors that are expected to be next-generation electronic materials [7].

## ORGANIC SEMICONDUCTORS AND PRINTED ELECTRONICS

The modern electronics industry is based on silicon and other inorganic semiconductors. With the miniaturization of transistors, the operation speed and the degree of integration have dramatically improved. An advanced information-oriented society has been established in which a vast amount of information can be exchanged via a network. In recent years, the concept of the Internet of Things (IoT) has been launched, and everything in the real world, as well as in the virtual space, is digitized and managed by the network. Since the IoT society requires an infinite number of sensor devices that collect various information, new semiconductor materials that can be mass-produced, and cheaper than inorganic semiconductors are required. In inorganic semiconductors, atoms are strongly bonded to each other by a covalent bond, while in organic semiconductors, the molecules assemble by weak

intermolecular interaction. Therefore, organic semiconductors are resistant to mechanical bending and distortion, and can be applied to flexible sensor devices that have been difficult to realize in conventional inorganic semiconductors. Moreover, since film formation by a simple printing process is possible by dissolving organic semiconductors in an organic solvent, it can be produced at lower cost than inorganic semiconductors that require a vacuum process [8, 9].

Due to the remarkable developments in synthetic chemistry and materials science in recent years, mobility of organic semiconductors, an index of the device performance, exceeds  $10 \text{ cm}^2 \text{ V}^{-1} \text{ s}^{-1}$  [10–12]. On the other hand, the electron transport of the organic semiconductor having high mobility could not be explained by the conventional model in which electrons are strongly localized in a molecule (so-called hopping conduction model) [13]. Therefore, band transport in which electrons are delocalized along a molecular crystal has been proposed and is being confirmed using various spectroscopies. In fact, organic single-crystalline materials with mobilities exceeding  $1 \text{ cm}^2 \text{ V}^{-1} \text{ s}^{-1}$  have a clear correlation ( $\mu = e\tau_p/m^*$ ,  $\tau_p$ : momentum relaxation time and  $m^*$ : the effective mass). Generally, in band transport, the momentum relaxation time is expressed as the temperature function  $\tau_p \propto T^{-q}$  ( $q$ : exponent). It is expected that the charge scattering mechanism can be identified by examining the negative temperature dependence of mobility. However, in organic semiconductors, the effects of static disorder (defects and grain boundaries) become more pronounced at lower temperatures, and it has been difficult to explore the intrinsic temperature dependence of mobility [14]. As described above, in order to understand the charge transport mechanism in organic semiconductors, it is necessary to elucidate the electron scattering/relaxation mechanism. To do so, we attempted to predict charge relaxation through spin relaxation using the ESR method, which is the main focus of this paper.

## DEVELOPMENT OF *operando*-ESR

Relaxation of electron charge and spin is closely correlated to each other. It is expected that the momentum relaxation time which determines the drift velocity of charge can be predicted by measuring the time in which the information of the spin is lost (spin relaxation time). In general, the mechanism of spin relaxation of electrons in solids is classified into four models; Elliott-Yafet (EY) mechanism, D'yakonov-Perel (DP) mechanism, Bir-Arnov-Pikus (BAP) mechanism, and hyperfine-interaction [15]. Among them, the DP mechanism describes spin relaxation in solids with no crystallographic inversion symmetry, and the BAP mechanism is a model for spin relaxation processes derived from the exchange interaction on electrons and holes. Therefore, in organic semiconductors with inversion symmetry, it is sufficient to consider only the EY mechanism and hyperfine interactions [16]. In particular, the EY mechanism is a spin relaxation mechanism that occurs by incorporating spin-orbit interaction into the periodic system Hamiltonian, and describes spin relaxation in the scattering center [17, 18]. Therefore, investigating whether the spin relaxation mechanism in the organic semiconductors follows the EY mechanism is nothing more than evaluating the band conduction. Here, *operando*-ESR method is effectively used for directly observing the spin dynamics of charge carriers accumulated in the organic transistor. The word "*operando*" means "operating" in Latin, and the *operando* spectroscopy method literally refers to the spectroscopy method on the operating device.

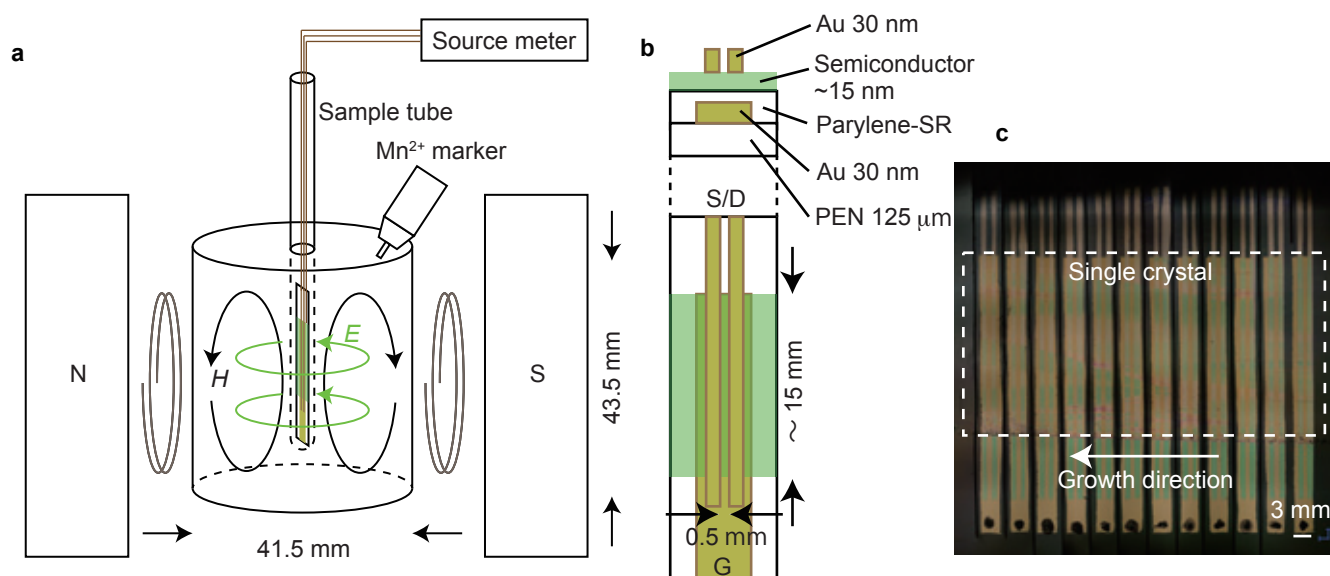
**Figure 2** a shows a schematic illustration of *operando*-ESR measurements. We observed ESR of charge carriers induced in the channel by the gate voltage application during the operation of organic devices (transistors). The *operando*-ESR method was first reported by Marumoto and Kuroda *et al* in 2004, and since then has been discussed about molecular orientation and spatial extent of carrier wave functions [19–21]. However, in the conventional *operando*-ESR method, only grains, trap sites, and strongly localized spins in molecules have been discussed, and there have been only a few examples of spin dynamics studies in delocalized electron spins in organic single crystals. This is due to the spatial limitation of the microwave resonator (cavity) used in ESR observation. The diameter and the size of the cylindrical microwave cavity commonly used in X-band ESR (microwave frequency  $\sim 10$  GHz) is approximately 40 mm, and 43.5 mm (Fig. 2a). In order to obtain a uniform spin system with sufficient sensitivity, it is necessary to prepare an organic single crystal in which crystal axes are perfectly aligned in this cavity. Therefore, high quality single crystals are essential. In addition, in order to measure the ESR spectrum with sufficient sensitivity for the spin dynamics studies, it is necessary for at least about  $10^{11}$  to  $10^{12}$  of spin to be present in the cavity. Since the spin density that can be injected using a general solid gate is at most  $10^{12}$   $\text{cm}^{-2}$ , the active layer area used for the *operando*-ESR measurement is at least  $1$   $\text{cm}^2$ . In this research, we used the organic semiconductor molecule 3,11-dialkyl[2,3-*d*:2',3'-*d'*]benzo[1,2-*b*:4,5-*b'*]dithiophene ( $\text{C}_{10}$ -DNBDT-NW) [12] developed by our research group. A large area single crystal transistor can be obtained by applying ink of organic semiconductor molecules on the gate insulating layer and controlling the drying direction (continuous edge cast method) [12, 22]. It is possible to form a several square centimeter single crystal thin film, as shown in Fig. 2c. Each transistor shown in Fig. 2c is a top gate bottom contact device structure shown in Fig. 2b. The charge carrier is accumulated in the range of  $15$  mm  $\times$   $2$  mm. By integrating seven of these

transistors having identical transistor characteristics, it is possible to measure ESR in a large area single crystal transistor whose substantial active layer exceeds  $2$   $\text{cm}^2$ . The actual *operando*-ESR measurement was performed with an X-band electron spin resonance spectrometer, JEOL JES-X310, by combining a helium temperature control unit.

The ESR spectrum modulated by the gate voltage ( $V_G$ ) at room temperature is shown in Fig. 3a. The ESR signal intensity increases monotonously with respect to  $V_G$ , and the spin injected in the channel is measured with good sensitivity. The spin density is estimated from the integrated intensity of the ESR spectrum, and agrees perfectly with the carrier density estimated from the capacity of the gate insulator  $C_i$  and  $V_G$  (Fig. 3b) [7]. In addition, the carrier density in the band conduction state was measured using the Hall effect measurement, and also agrees with the spin density. From these measurements, it is concluded that all the spins detected by the *operando*-ESR measurement undergo band conduction.

Next, we would like to focus on a signal shape of the obtained ESR spectrum. All ESR spectra measured at temperatures from 300 K to 4 K could be fitted with a single Lorentzian (Fig. 4a). This suggests that all the observed spins share the same magnetic circumstance, and can be treated as a homogeneous spin system [23]. Contrary, when each electron spin is surrounded by different magnetic environments due to hyperfine interaction with nuclear spins, the ESR signal becomes Gaussian, and can be treated as an inhomogeneous spin system. From the temperature dependence of ESR spectra (Fig. 4b), the temperature dependence of the full width at half maximum is estimated (shown in Fig. 4c). At a low temperature below 50 K, a negative temperature dependence was confirmed, in which the spectrum shape sharpens as the temperature rises. This temperature dependence is similar to the tendency observed in many organic polycrystals, and it can be interpreted as the observation of "motional narrowing" caused by the movement of localized spins. On the other hand,

**Fig. 2**



(a), Schematic illustration of *operando*-ESR measurement. (b), Organic field-effect transistors (OFETs) fabricated onto a flexible substrate are placed into an ESR sample tube. (c), Photograph of the fabricated OFETs. Seven OFETs are integrated into the ESR tube to gain a signal-to-noise (SN) ratio.

at a high temperature above 50 K, the temperature dependence of the linewidth exhibits different temperature dependence predicted from motional narrowing. This suggests that when the kinetic energy of the carrier is sufficiently higher than the localized level, spin relaxation by spin-orbit coupling (SOC) becomes dominant. These two spin relaxation mechanisms can be discussed by separating them into spin-lattice relaxation and spin-spin relaxation time. Thus, the temperature dependence of the ESR linewidth originates from the two mechanisms: hyperfine interaction and SOC. In addition, the contribution of each mechanism will be discussed in more detail by measuring the spin relaxation time and the momentum relaxation time.

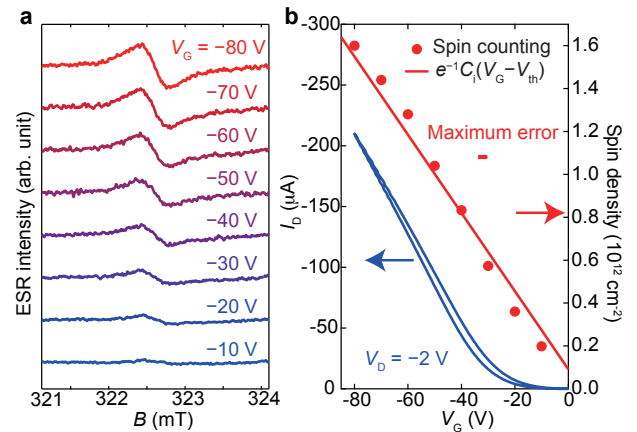
## MEASUREMENT OF MOMENTUM AND SPIN RELAXATION TIME

ESR is microwave-induced oscillation in a spin system that includes a relaxation phenomenon, and is described by Bloch's equation [3, 23]. The dynamics of spins, that is, the spin relaxation process, is incorporated into the Bloch equation, and the energy relaxation of spins is defined as spin-lattice relaxation (longitudinal relaxation) and relaxation of spin phase coherence as spin-spin relaxation (lateral relaxation). The spin-lattice relaxation time  $T_1$  and the spin-spin relaxation time  $T_2$  are generally determined using spin echo (a pulsed magnetic resonance method), but can be obtained under static conditions. Under the assumption that the ESR spectrum is obtained from a homogeneous spin system, that is, the relaxation mechanism of all spins is the same,  $T_2$  is given by  $T_2 = 2/(\gamma B_{\text{FWHM}})$  using the linewidth of the ESR spectrum  $B_{\text{FWHM}}$  and the gyromagnetic ratio  $\gamma$ . Further,  $T_1$  can be obtained by measuring the microwave intensity dependence of the ESR intensity (continuous wave saturation method) [23]. As shown in Fig. 5, when the frequency of spin excitation between Zeeman splitting levels is equal to the frequency of spin return to the ground state, the integrated intensity of the ESR spectrum is saturated. From the microwave intensity necessary for saturation of the ESR spectrum,  $T_1$  can be determined by back-calculating the spin relaxation frequency. Furthermore, the momentum relaxation time  $\tau_p$  representing the carrier scattering frequency is determined from the equation  $\mu = e\tau_p/m^*$ . Here,  $m^*$  is the effective mass and is estimated to be  $m^* = 1.05m_0$  by density functional theory based on the crystal structure obtained from a single crystal X-ray structure analysis of  $\text{C}_{10}\text{-DNBDT-NW}$ .

## SPIN RELAXATION MECHANISM IN SINGLE CRYSTAL ORGANIC SEMICONDUCTORS

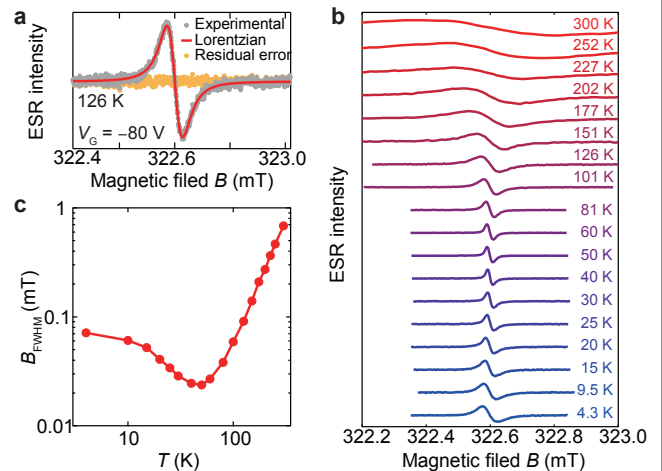
The spin relaxation mechanism in single crystal organic semiconductors is discussed by comparing the spin relaxation time  $T_1$ ,  $T_2$  and the momentum relaxation time  $\tau_p$  in  $\text{C}_{10}\text{-DNBDT-NW}$  single crystal thin film. Figure 6a summarizes the temperature dependence of  $T_1$ ,  $T_2$ , and  $\tau_p$  obtained in the previous measurements. Note that  $\tau_p$  is displayed in the form  $\tau_p T^2$  to facilitate comparison with the spin relaxation time. This figure utilizes a double logarithmic scale, and the power-law dependence is displayed as a straight line.  $T_1$  and  $T_2$  are shown on the left axis, and  $\tau_p T^2$  is shown on the right axis. The parallel straight lines indicate that there is a proportional relationship to the temperature dependence because the numbers of digits of the left and right axes are aligned. Therefore, it is concluded that  $T_1$ ,  $T_2$  and  $\tau_p T^2$  are proportional in the temperature range where  $\tau_p$  is measured.

Fig. 3



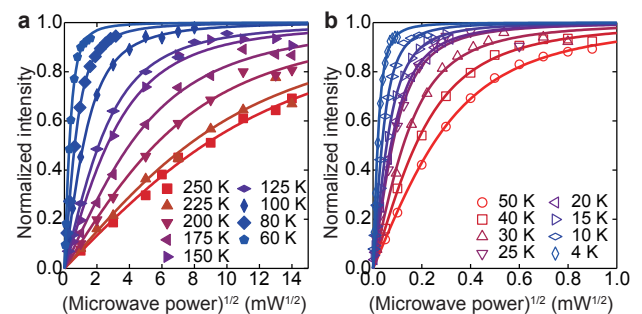
(a), ESR spectra measured at various gate voltages ( $V_G$ ). (b), Spin density estimated from the intensity of the ESR signals (red circles) and from the capacitance of the gate insulator (red line), in addition to the transfer curve at room temperature (blue line).

Fig. 4



(a), Typical example of fitting results. (b), Temperature dependence of ESR spectra recorded with  $V_G = -80$  V, where an external magnetic field is applied perpendicular to the substrate. (c), Temperature dependence of ESR linewidth.

Fig. 5



ESR intensities as a function of the square root of the irradiated microwave power at (a) high temperature (60–250 K), and (b) low temperature (4–50 K). The solid curves represent the fitting results.

Next, we will discuss the correlation between the three relaxation times. In conclusion, the correlation of  $T_1 \propto T_2 \propto \tau_p T^{-2}$  is consistent with that predicted by Elliott-Yafet (EY) mechanism. The EY mechanism describes the spin conserving/flipping probability at an ordinary scattering event with the presence of SOC, where SOC makes an admixture of the eigenstates of the spin-up  $|\uparrow\rangle$  and spin-down states  $|\downarrow\rangle$ . In the simplest two-band model, the following relationship holds between spin relaxation time and momentum relaxation time [17, 18].

$$\frac{1}{T_2} \sim \frac{1}{T_1} = \alpha \frac{1}{\tau_p}, \quad (1)$$

where  $\alpha$  is the probability of spin-flipping at the scattering event and described as,

$$\alpha = \Delta g^2 \left(\frac{m^*}{m_0}\right)^2 \left(\frac{\langle E_k \rangle}{E_G}\right)^2, \quad (2)$$

$\Delta g$  is the shift from the free electrons'  $g$  value, and represents the strength of the spin-orbit interaction.  $m^*/m_0$  is the ratio of the effective mass to the free electron mass, which originates from the density-of-states.  $\langle E_k \rangle$  is an energy average value of carriers contributing to scattering, and represents the

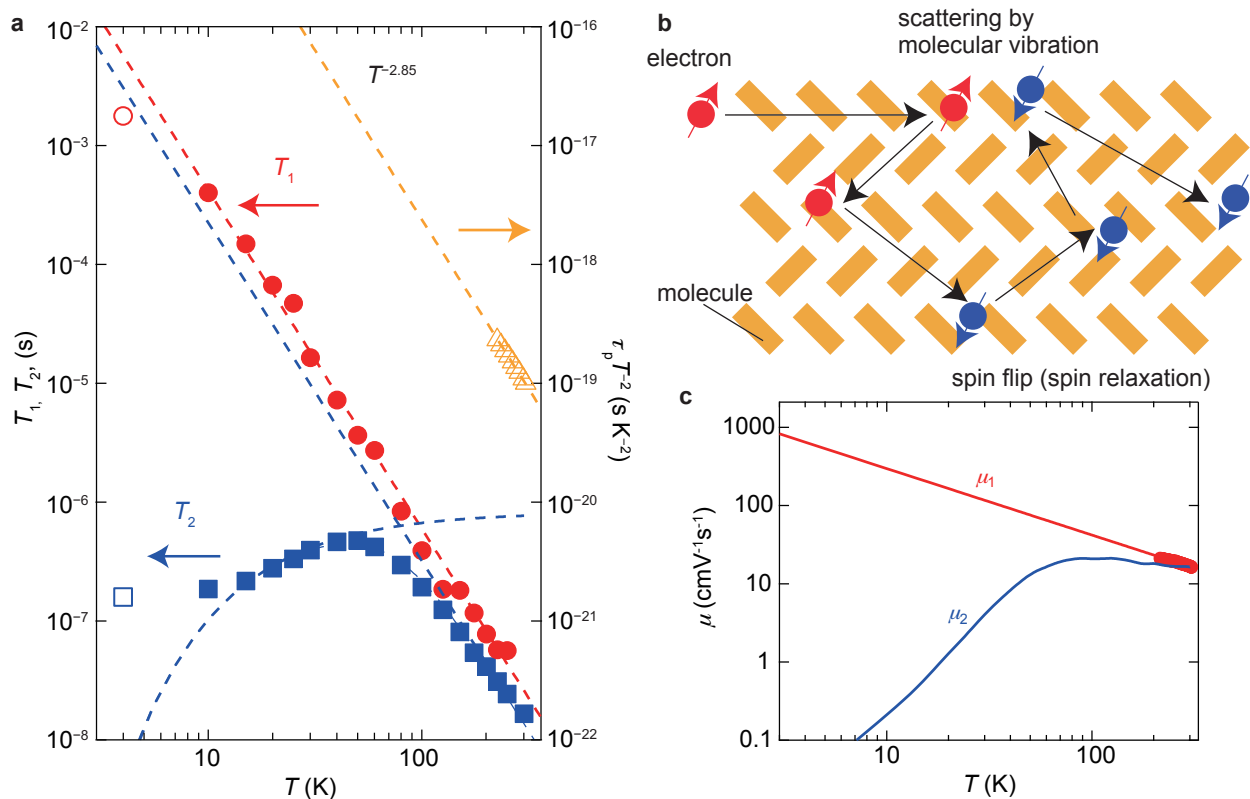
strength of interaction with other band levels.  $E_G$  is an energy gap with another level having the same wave number. For metals and degenerate semiconductors,  $\langle E_k \rangle$  is identical to the Fermi level, and for non-degenerate semiconductors, it is approximated to be  $\langle E_k \rangle = k_B T$ . Thus, the relation between spin relaxation time and momentum relaxation time in the organic semiconductor which is a non-degenerate semiconductor is

$$T_2 \sim T_1 \propto \tau_p T^{-2}, \quad (3)$$

This correlation agrees with the experimental result obtained by the *operando*-ESR measurement. The theoretical value of the spin-flipping probability  $\alpha$  in C<sub>10</sub>-DNBDT-NW is estimated to be  $6.0 \times 10^{-7}$  from the formula (2) using  $g = 2.011$ ,  $m^* = (m_b^* m_c^*)^{1/2} = 1.4 m_0$ , and  $E_G = 0.4$  meV. The experimentally-obtained spin-flipping probability  $\alpha$  is the ratio of momentum relaxation time to spin relaxation time  $\tau_p/T_1 = 9.4$  fs/25.9 ns =  $3.6 \times 10^{-7}$ ,  $\tau_p/T_2 = 9.4$  fs/16.6 ns =  $5.6 \times 10^{-7}$ , which are in a good agreement with the spin-flipping probability expected from the EY mechanism. In other words, it was found that spin-orbit interaction causes spin-flip with a probability of once a three million time carriers are scattered by phonon [7].

In the high temperature region above 100 K, the spin-lattice relaxation time  $T_1$  changes monotonically according to  $T_1 \propto T^{-2.85}$ . On the other hand,  $T_2$  becomes shorter as the temperature drops below 50 K. This is because  $T_2$  is influenced not only

**Fig. 6**



(a), Temperature dependence of the momentum and spin relaxation times in C<sub>10</sub>-DNBDT-NW. The momentum relaxation time  $\tau_p$ , estimated from the drift mobility and effective mass, is plotted as  $\tau_p T^{-2}$  (yellow triangles), and fitted by the line of  $T^{-2.85}$  (yellow dashed line). The spin-lattice relaxation time  $T_1$ , estimated by the continuous wave saturation method, is displayed as red circles and fitted by  $T^{-2.85}$  (red dashed line). The spin-spin relaxation time  $T_2$  is displayed as blue squares. (b), Schematic illustration of EY spin relaxation mechanism. (c), Temperature dependence of carrier mobilities estimated from  $\mu_1 = eT_1 T^2/m^*$  (red) and  $\mu_2 = eT_2 T^2/m^*$  (blue).

by the spin relaxation by the EY mechanism but also by the hyperfine interaction mechanism. As described above, in the low temperature region, the contribution of carrier trapping in the localized level cannot be ignored, and the influence of the hyperfine interaction of the localized electron spin appears. From the fitting with the thermal activation function  $1/T_2 \propto \exp(-E_a/k_B T)$ ,  $E_a$  is estimated to be 1.8 meV, which corresponds to a temperature of about 20 K, and supports that carrier conduction around room temperature can be described by trap-free band conduction. On the other hand, since  $T_1$  is hardly affected by hyperfine interactions in solids, it can be assumed that spin relaxation is reflected purely by phonon scattering. Then, the temperature dependence of  $T_1$  is well represented by a single power law from room temperature down to 4 K, and it can be seen that carriers are scattered by a single scattering mechanism in a wide temperature range. Taking this into consideration, it is assumed that the proportional relation equation (3) between  $\tau_p$  and  $T_1$  holds up to 4 K, and the low temperature carrier dynamics that cannot be measured by the transistor are inferred. The demonstrated *operando*-ESR measurement would be useful to fully understand the charge transport mechanism in organic semiconductors under low-temperature regimes. Transport measurements often suffer from cracks in organic single-crystal materials, presumably due to thermal expansion coefficient mismatch between the organic material and inorganic substrate; therefore, it has been extremely difficult to accurately determine the drift mobility (this is also why  $\tau_p$  was no longer evaluated below 200 K).

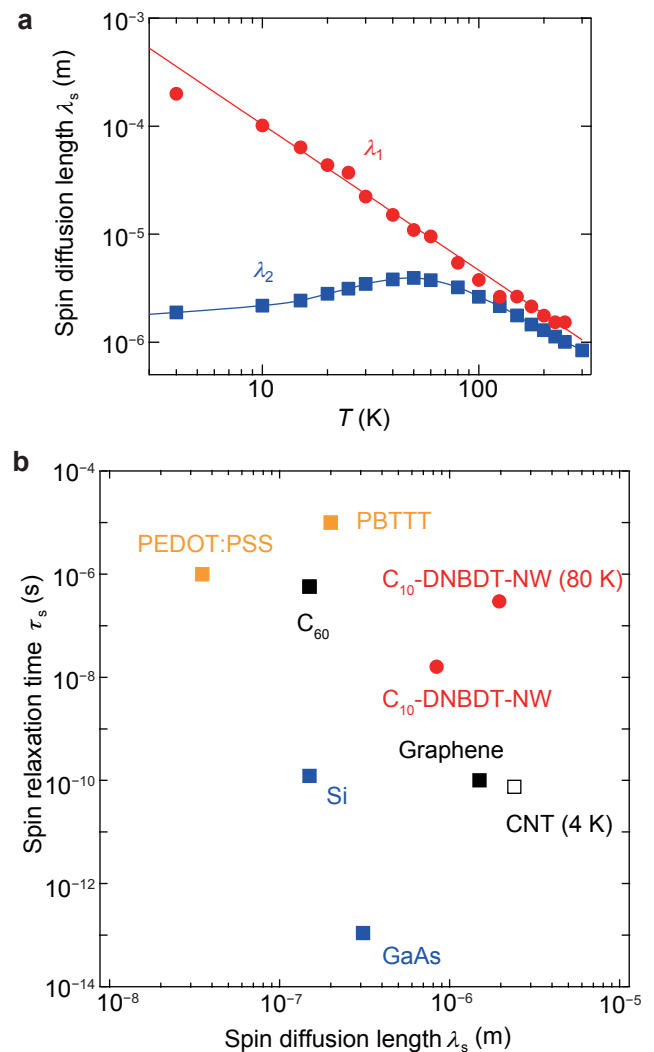
The relaxation time estimated from the temperature dependence of  $T_1$  and the equation (ref eq. 3) can be proportional to the mobility when the trap is completely filled or when an ideal transistor without a trap is used. With this assumption, the mobility is given by  $\mu = e\tau_p/m^* = eT_1 T^2/m^*$ . Therefore, the mobility keeps rising at low temperature according to  $T^{-0.85}$ , and it can be predicted that the mobility may reach  $650 \text{ cm}^2 \text{ V}^{-1} \text{ s}^{-1}$  (Fig. 6c). Although there is room for improvement in mobility at low temperature by the selection of the insulating layer and improvement of the crystal growth method, it can be seen that trap-free and nearly ideal electrical conduction can be realized at room temperature.

## SPIN TRANSPORT IN ORGANIC SEMICONDUCTORS

Finally, the spin diffusion length of the organic semiconductor is discussed. Since many organic semiconductors consist of only light elements with small atomic numbers, the spin relaxation time is overwhelmingly longer compared to inorganic semiconductors [16, 24]. Therefore, organic semiconductors are expected to be used as spin media that can store spin information for a long time, which allows robust spin transport. However, the spin relaxation length  $\lambda_s$  cannot be long [24] because typical organic semiconductors that have been generally used so far have low mobility.  $\lambda_s$  is expressed as  $\lambda_s = (D\tau_s)^{1/2}$ . Here,  $D = k_B T \mu / e$  is the diffusion constant, and  $\tau_s$  is the spin coherence time. The spin coherence time is strictly the spin relaxation time measured electrically using a spin device (such as a non-local spin valve). With experimental values of  $T_2 = 16.6 \text{ ns}$  and  $\mu_{\text{Hall}} = 16.5 \text{ cm}^2 \text{ V}^{-1} \text{ s}^{-1}$  at room temperature, the spin diffusion length is estimated to be approximately  $\lambda_s = 840 \text{ nm}$ . Surprisingly,  $\lambda_s$  may approach  $2.0 \mu\text{m}$  at 50 K, which is derived from  $T_2 = 470 \text{ ns}$  and  $\mu_{\text{Hall}} = 13 \text{ cm}^2 \text{ V}^{-1} \text{ s}^{-1}$  (Fig. 7a). The measured spin diffusion length of  $\text{C}_{10}$ -DNBDT-NW is longer than those of silicon and gallium

arsenide and comparable to that of graphene (Fig. 7b) [24]. The present organic single crystals can be a novel spin media in which spins can be transferred along with coherent, band-like carriers. Therefore, the coexistence of ultra-long spin coherence times due to light-atom compositions and coherent charge transport can be expected. The EY spin relaxation mechanism in organic single-crystal semiconductors was experimentally verified unambiguously by the combination of *operando*-ESR and transport measurements on gate-induced carriers. Observation of the missing relationship between charge and spin relaxations is expected to shed light on opportunities to realize sophisticated spintronic devices based on organic single crystals, where extraordinarily long spin diffusion lengths can be expected due to the coexistence of ultra-long spin coherence times and relatively high band-like mobility. Tuning the strength of SOCs by almost infinite chemical engineering opens up possibilities for further lengthening of the spin coherence time and spin diffusion length.

Fig. 7



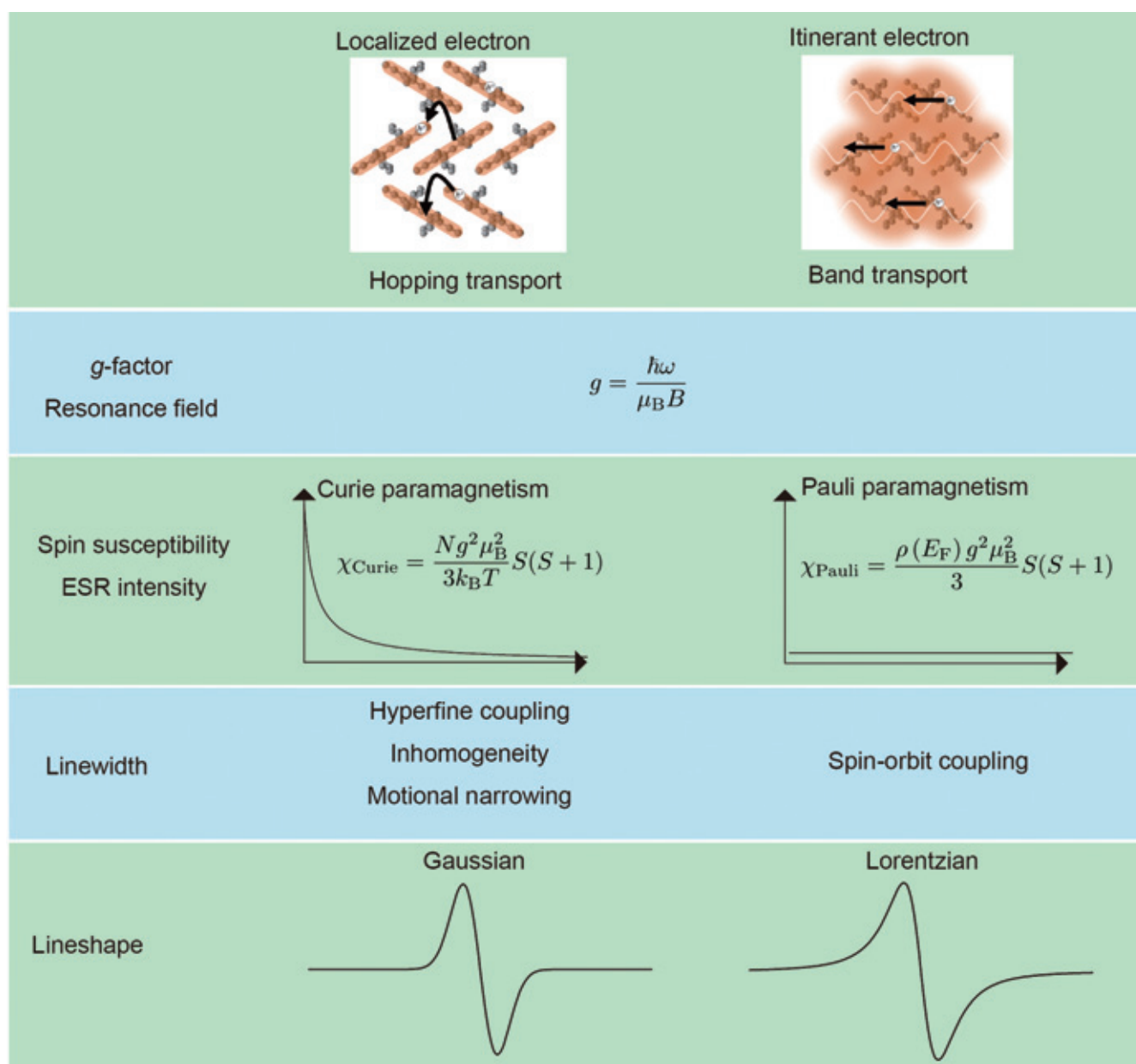
(a) Temperature dependence of spin diffusion lengths estimated from  $\lambda_1 = \sqrt{D_1 T_1}$  (red), and  $\lambda_2 = \sqrt{D_2 T_2}$  (blue), where  $D$  is the diffusion constant,  $D_1 = k_B T \mu_1 / e$ , and  $D_2 = k_B T \mu_2 / e$ . (b) Comparison of spin relaxation time and spin diffusion length for various materials.

## Conclusion

Based on the above findings, information obtained by *operando*-ESR measurement of organic semiconductors is summarized in **Fig. 8**. The electric conduction of an organic semiconductor is roughly classified into hopping conduction in which localized carriers undergo thermal-activated transport, and band-like conduction in which carriers are delocalized into several molecules or more. Band-like electrical conduction has been verified in some high mobility single crystals by Hall effect measurement and temperature dependence of mobility. In this report, we have demonstrated that the spin relaxation mechanism can also be explained by the band conduction model in the single crystal of C<sub>10</sub>-DNBDT-NW. In ESR measurement, it is possible to estimate the *g*-factor from the position of the resonance field for both localized

and delocalized spins. However, it should be noted that the *g*-factors measured in the case of polycrystalline samples may be angularly averaged due to anisotropy of *g*-factor. The spin susceptibility is determined from the double integration of the ESR spectrum. In the case of localized spins, Curie susceptibility, in which the magnetic susceptibility is inversely proportional to temperature, is confirmed because of strong electrostatic repulsion between carriers. In the case of itinerant spin, on the other hand, degenerate spin systems often exhibit Pauli paramagnetic behavior. The linewidth of the spectrum reflects the spin relaxation of the carriers. Since a large amount of hydrogen atoms exist in the organic semiconductor, localized carriers are strongly affected by hyperfine interactions. Also, when there is molecular orientation disorder in the solid, non-uniformity of anisotropic *g*-factor may increase the linewidth. It should be noted that when the

**Fig. 8**



Summary of parameters obtained from ESR measurements in solid-state films.

carrier is trapped in a localized level much deeper than  $k_B T$ , the line-shape follows the Gaussian. As the temperature rises and carriers are able to move between the traps, the effects of hyperfine interactions are averaged out, resulting in motional narrowing. At this time, the line-shape gradually approaches the Lorentzian. When spins undergoing band-conduction *i.e.*; the situation is considered as the upper limit of motional narrowing, ESR line-shape becomes Lorentzian, where the contribution of hyperfine interactions is suppressed and spin relaxation by SOC becomes dominant.

In this paper, we clarified the conduction mechanism in high mobility organic single-crystalline semiconductors through the results of the *operando*-ESR, and discussed the potential of organic semiconductors as a spin media. In organic semiconductors with a large number of hydrogen atoms, the experimental results that spin relaxation is dominated by the EY mechanism seem to be counterproductive at first glance. It indeed reflects how close the carrier conduction behaves to the band conduction in high mobility organic semiconductors. In addition to the advances in materials science for high mobility organic semiconductors, the improved methods for a mass production of high-quality single-crystals have made it possible to conduct *operando*-ESR measurements. It is expected that the conduction mechanism of the organic semiconductor will be clarified in more detail by performing the *operando*-ESR measurement of various organic semiconductors in the future. Materials sciences of organic semiconductors have been remarkably developed in recent years, and for the development of semiconductors with higher mobility, it is strongly required to elucidate factors that limit carrier conduction and scattering mechanisms. *Operando*-ESR measurement is a powerful tool to study spin dynamics, and it is expected that the importance of ESR measurement will increase in the future.

## Acknowledgments

The work presented in this paper was carried out primarily at Department of Advanced Materials Science, The University of Tokyo. We would like to express our gratitude to Prof. Jun Takeya and Prof. Toshihiro Okamoto.

## References

- [ 1 ] Zavoisky, E. Spin-magnetic resonance in paramagnetics. *J Phys USSR* **9**, 211–245 (1945).
- [ 2 ] Weil, J. A. & Bolton, J. R. *Electron paramagnetic resonance: elementary theory and practical applications* (John Wiley & Sons, 2007).
- [ 3 ] Slichter, C. P. *Principles of magnetic resonance*, vol. 1 (Springer Science & Business Media, 2013).
- [ 4 ] Berliner, L. J. & Reuben, J. *Spin labeling: theory and applications*, vol. 8 (Springer Science & Business Media, 2012).
- [ 5 ] Feher, G. Electron spin resonance experiments on donors in silicon. i. electronic structure of donors by the electron nuclear double resonance technique. *Physical Review* **114**, 1219 (1959).
- [ 6 ] Watkins, G. & Corbett, J. Defects in irradiated silicon. i. electron spin resonance of the si-a center. *Physical Review* **121**, 1001 (1961).
- [ 7 ] Tsurumi, J. *et al.* Coexistence of ultra-long spin relaxation time and coherent charge transport in organic single-crystal semiconductors. *Nature Physics* **13**, 994 (2017).
- [ 8 ] Forrest, S. R. & Thompson, M. E. Introduction: organic electronics and optoelectronics. *Chemical Reviews* **107**, 923–925 (2007).
- [ 9 ] Saganuma, K. *Introduction to printed electronics*, vol. 74 (Springer Science & Business Media, 2014).
- [10] Takeya, J. *et al.* Very high-mobility organic single-crystal transistors with in-crystal conduction channels. *Applied Physics Letters* **90**, 102120 (2007).
- [11] Hasegawa, T. & Takeya, J. Organic field-effect transistors using single crystals. *Science and Technology of Advanced Materials* **10**, 024314 (2009).
- [12] Mitsui, C. *et al.* High-performance solution-processable n-shaped organic semiconducting materials with stabilized crystal phase. *Advanced Materials* **26**, 4546–4551 (2014).
- [13] Tessler, N., Preezant, Y., Rappaport, N. & Roichman, Y. Charge transport in disordered organic materials and its relevance to thin-film devices: a tutorial review. *Advanced Materials* **21**, 2741–2761 (2009).
- [14] Podzorov, V. *et al.* Intrinsic charge transport on the surface of organic semiconductors. *Physical Review Letters* **93**, 086602 (2004).
- [15] Zutic, I., Fabian, J. & Sarma, S. D. Spintronics: Fundamentals and applications. *Reviews of Modern Physics* **76**, 323 (2004).
- [16] Watanabe, S. *et al.* Polaron spin current transport in organic semiconductors. *Nature Physics* **10**, 308 (2014).
- [17] Pikus, G. & Titkov, A. Optical orientation, modern problems in condensed matter science. *Meier F., Zakharchenya BP., editors* **8** (1984).
- [18] Yafet, Y. g factors and spin-lattice relaxation of conduction electrons. In *Solid State Physics*, vol. 14, 1–98 (Elsevier, 1963).
- [19] Marumoto, K., Muramatsu, Y., Ukai, S., Ito, H. & Kuroda, S.-i. Electron spin resonance observations of field-induced polarons in regioregular poly(3-octylthiophene) metal–insulator–semiconductor diode structures. *Journal of the Physical Society of Japan* **73**, 1673–1676 (2004).
- [20] Marumoto, K., Kuroda, S.-i., Takenobu, T. & Iwasa, Y. Spatial extent of wave functions of gate-induced hole carriers in pentacene field-effect devices as investigated by electron spin resonance. *Physical Review Letters* **97**, 256603 (2006).
- [21] Matsui, H., Hasegawa, T., Tokura, Y., Hiraoka, M. & Yamada, T. Polaron motional narrowing of electron spinresonance in organic field-effect transistors. *Physical Review Letters* **100**, 126601 (2008).
- [22] Yamamura, A. *et al.* Wafer-scale, layer-controlled organic single crystals for high-speed circuit operation. *Science Advances* **4**, eaao5758 (2018).
- [23] Alger, R. S. *Electron paramagnetic resonance: techniques and applications* (interscience publishers, 1968).
- [24] Dediou, V. A., Hueso, L. E., Bergenti, I. & Taliani, C. Spin routes in organic semiconductors. *Nature Materials* **8**, 707 (2009).

# YOKOGUSHI (Multifaceted) Analysis of Biomimetic Materials by Using PyGC/MS and XPS – Characterization of Biomimetic Lacquer –

Noriyasu Niimura Application Management Department, JEOL Ltd.

Japanese lacquer has attracted attention in the field of biomimetic material development due to its outstanding durability. Four types of biomimetic lacquer films were developed and characterized by using pyrolysis-gas chromatography/mass spectrometry (PyGC/MS), X-ray photoelectron spectroscopy (XPS) and the pencil hardness testing method. The structure and polymerization mechanisms of the biomimetic lacquer films were revealed to be similar to those of the natural lacquer film. They must be tough enough to be used as preservative surface coating materials.

## Introduction

Since the resolution of Sustainable Development Goals (SDGs) in the United Nations in September 2015, the international trend towards a sustainable society has been changing from a side stream to a mainstream. Biomimetics is an interdisciplinary field where engineering, chemistry and biology are applied to the development of functional materials and machines that mimic biological processes. It has been attracting attention as a platform for the development of new low environmental impact technology. Actually, in the “Fifth Environmental Basic Plan” formulated by the Government of Japan in April 2018, six priority strategies that cross the various fields are set up. In “Development of technology applying natural laws and mechanisms” of “Strategy #5: Development and dissemination of technologies supporting sustainability”, promotion of development of low impact environmental technologies utilizing biomimetics is described [1].

Within this context, we focused on Japanese lacquer, which is one of traditional crafts in Japan. Japanese lacquer is a sap obtained from lacquer tree. It has been used as a coating material for a long time, because it has outstanding durability in addition to its elegant appearance. It was reported that lacquer sap contains urushiol as the main constituent [2-4]. The other constituents are plant gum, glycoprotein, laccase enzyme and water. Japanese lacquer is a complex natural coating material based on the interaction and polymerization of these constituents [5]. Urushiol is a catechol derivative having C15 hydrocarbon chains consisting of a mixture of alkane, monoenes, dienes and trienes mainly at the 3-position of catechol. Its composition has been investigated in detail [6-8]. It polymerizes into lacquer film by laccase catalyzed oxidative coupling and autoxidation [9-11]. The structural study of the lacquer film related to the toughness function was reported [12-17].

In this study, urushiol analogs were synthesized and polymerized by laccase enzyme and autoxidation to produce biomimetic lacquer films [18-22]. The biomimetic lacquer films were characterized by using two-stage pyrolysis-gas chromatography/mass spectrometry (Py-GC/MS) [23-25], X-ray photoelectron spectroscopy (XPS) and pencil hardness testing method, and compared with natural lacquer film.

## 1. Experimental

### 1.1. Samples

#### 1.1.1. Biomimetic lacquer films

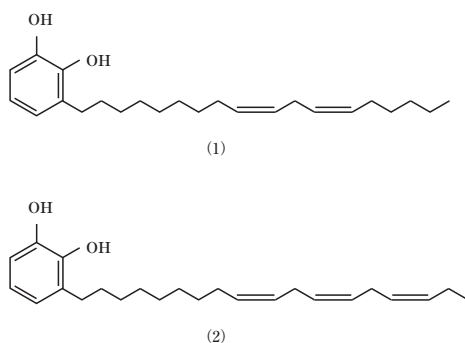
Urushiol analogs A–D were produced from linseed oil, tung oil, linoleic acid and linolenic acid, respectively, by alkylation and intermolecular cyclization [26]. The composition of urushiol analogs A and B are shown in **Table 1** and **2**, respectively. The structural formulas of urushiol analog C: 3-[(9Z, 12Z)-9, 12-octadecadienyl] catechol and urushiol analog D: 3-[(9Z, 12Z, 15Z)-9, 12, 15-octadecatrienyl] catechol are shown in **Fig. 1**.

**Table 1** The composition of urushiol analog A.

3(R)catechol, R=	%
$C_{14}H_{29}$ , $C_{16}H_{33}$	4.0–9.0
$C_{18}H_{37}$	2.0–8.0
$C_8H_{16}CH=CHC_8H_{17}$	13.0–37.6
$C_8H_{16}CH=CHCH_2CH=CHC_5H_{11}$	4.5–29.1
$C_8H_{16}CH=CHCH_2CH=CHCH_2CH=CHC_2H_5$	25.8–53.0
$C_{20}H_{41}$	0.2–1.0

**Table 2 The composition of urushiol analog B.**

3(R)catechol, R=	%
$C_nH_{2n+1}$ (n=12–20)	3.5–8.0
$C_8H_{16}CH=CHC_8H_{17}$	4.0–15.8
$C_8H_{16}CH=CHCH=CHC_6H_{13}$	8.7–10.8
$C_8H_{16}CH=CHCH=CHCH=CHC_4H_9$	77.0–81.8

**Fig. 1 Structural formulas of urushiol analogs C and D.**

(1) urushiol analog C: 3-[(9Z, 12Z)-9, 12-octadecadienyl] catechol  
 (2) urushiol analog D: 3-[(9Z, 12Z, 15Z)-9, 12, 15-octadecatrienyl] catechol

The respective urushiol analogs were added to an acetone powder, which was separated as acetone insoluble material from the sap of a lacquer tree containing the non-oily parts, i.e., plant gum, glycoprotein and laccase enzyme, in water-isopropyl alcohol and stirred. The respective mixtures had a viscosity suitable for coating, and after coating on a glass plate, it was dried in a humidity-controlled chamber filled with a relative humidity (RH) of 80% at 25–30 °C for 10 h. In this process, the respective mixtures polymerized into biomimetic lacquer films A–D. Then, they were removed from the chamber and placed in air for 3 years.

### 1.1.2. Natural lacquer film

Fluid sap exuded from the *Toxicodendron vernicifluum* lacquer tree was treated using the traditional Kurome and Nayashi methods [27] and coated on a glass plate followed by hardening in a humidity-controlled chamber with an RH of 80% at 25–30 °C for 10 h. It was then removed from the chamber and placed in air for 3 years.

### 1.2. PyGC/MS measurements

A stainless steel capillary column (30 m × 0.25 mm I.D., 0.25 μm film thickness, dimethylpolysiloxan 100%) was used for separation of GC. A helium carrier gas flow of 50 mL/min at the pyrolyzer was reduced to 1 mL/min at the capillary column by using a splitter. The sample (0.5 mg) was placed in a platinum sample cup and the cup was set on the top of the pyrolyzer kept at near room temperature. The sample cup was introduced into a furnace at 400 °C, and then the temperature programming of the GC oven was started. The GC oven was programmed at a constant rate of temperature rise 20 °C/min in a range from 40–330 °C. After the first pyrogram was

recorded, the sample cup was retracted to the initial position. The furnace was then reset to 500 °C. For the second analysis, the sample cup was dropped into the furnace at 500 °C, and the temperature program of the GC oven was restarted. Scanning mass spectra were recorded using electron ionization with ionization energy of 70 eV.

### 1.3. XPS measurements

The measurements were carried out with the monochromatized Al K $\alpha$  X-rays. The analyzer passing energy was 10 eV (resolving energy 0.65 eV at Ag 3d<sub>5/2</sub>). The calibration of binding energy was conducted by setting the peak of C-C coupling in the C 1s spectrum at 285.0 eV. The X-ray power was 100 W and the measurement time was 10 min. As previously reported, these measurement conditions do not cause radiation damage to the lacquer film [28]. In elemental analysis, Scofield cross-section values [29] and Tanuma inelastic mean free path (IMFP) values [30, 31] were used to quantify the XPS results. The peaks were fitted by a procedure based on independent variation of parameters such as peak position, full width at half maximum (FWHM), peak height, and mixed-ratio Gauss/Lorentzian peak line shape [32]. Curve fitting was performed using the damped non-linear least squares method [33]. Background subtraction was carried out according to the Shirley method [34–40].

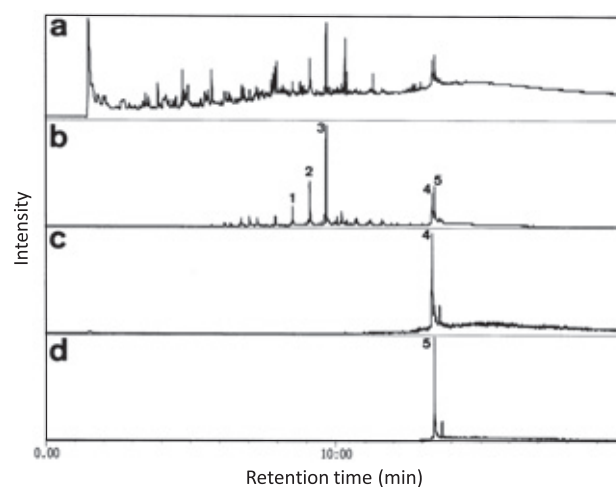
## 2. Results and discussion

### 2.1. PyGC/MS measurements

#### 2.1.1. Pyrolysis at 400 °C

The natural lacquer film and biomimetic lacquer films were pyrolyzed at 400 °C. The total ion current chromatogram (TICC) and extracted ion chromatograms (EICs: *m/z* 123, 318, 320) of the natural lacquer film are shown in Fig. 2.

The EICs show peaks 1–5. They were identified as the pyrolysis products of urushiol, i.e., 3-pentylcatechol (*Mr* 180), 3-hexylcatechol (*Mr* 194) and 3-heptylcatechol (*Mr* 208); and urushiols, i.e., 3-pentadecenylcatechol (*Mr* 318) and 3-pentadecylcatechol (*Mr* 320) based on the mass spectra.

**Fig. 2 TICC and EICs of the natural lacquer film obtained by pyrolysis at 400 °C.**

a) TICC b-d) EICs (*m/z* 123, 318, 320)  
 1: 3-pentylcatechol (*Mr* 180) 2: 3-hexylcatechol (*Mr* 194)  
 3: 3-heptylcatechol (*Mr* 208) 4: 3-pentadecenylcatechol (*Mr* 318)  
 5: 3-pentadecylcatechol (*Mr* 320)

The TICC and the EICs ( $m/z$  123, 334, 360, 362) of the biomimetic lacquer films A and B are shown in **Fig. 3** and **4**.

The EICs show peaks 1–6. They were identified as the pyrolysis products of urushiol analogs, i.e., 3-hexylcatechol ( $M_r$  194), 3-heptylcatechol ( $M_r$  208) and 3-octylcatechol ( $M_r$  222); and the monoenyl and saturated urushiol analogs, i.e., 3-hexadecylcatechol ( $M_r$  334), 3-octadecylcatechol ( $M_r$  360) and 3-octadecylcatechol ( $M_r$  362) based on mass spectra.

The TICC and EIC ( $m/z$  123) of the biomimetic lacquer films C and D are shown in **Fig. 5** and **6**. The urushiol analogs were not detected, but their pyrolysis products were detected in the respective lacquer films.

As shown above, monoenyl and saturated urushiol analogs were detected from the biomimetic lacquer films A and B as well as from the natural lacquer film, but not from biomimetic lacquer films C and D. These urushiol analogs are thermally decomposed components of the terminal alkyl- and alkenylcatechol side chains of the respective biomimetic lacquer films. As a result, the biomimetic lacquer A and B were found to be terminated with monoenyl and saturated urushiol analogs as well as natural lacquer. On the other hand, the biomimetic lacquer C and D are not terminated with monoenyl and saturated urushiol analogs.

#### 2.1.2. Pyrolysis at 500 °C after Pyrolysis at 400 °C

The biomimetic lacquer films and the natural lacquer film were pyrolyzed at 500 °C after pyrolysis at 400 °C. The TICC and EIC of the natural lacquer film are shown in **Fig. 7**. Peak pairs of alkenylphenols (much smaller peaks on the left side) and alkylphenols (larger peaks on the right side) were detected in the EIC ( $m/z$  108) as shown in Fig. 7b. The alkenylphenols and alkylphenols having the longest side chain were pentadecylphenols and pentadecylphenols. These alkenylphenols and alkylphenols are the pyrolysis products of the nucleus-side chain C-O coupling urushiol polymers, because the dimerization of urushiol was reported to proceed through the laccase-catalyzed nucleus-side chain C-O coupling as well as the C-C coupling [31]. Since the C-O coupling polymers should mainly terminate with alkyl- and monoenylphenol, pentadecylphenols and pentadecylphenols are formed from such terminal groups. Pyrolysis mechanisms producing 2-heptenylphenol, 2-heptylphenol, 3-pentadecylphenol and 2-pentadecylphenol are shown in **Fig. 8**.

The TICCs and EICs of the biomimetic lacquer films A–D are shown in **Fig. 9–12**. Peak pairs of alkenylphenols and alkylphenols were detected in the respective EICs ( $m/z$  108) as in the case of the natural lacquer film. In the biomimetic lacquer films A and B, the alkenylphenols and alkylphenols having the longest side chain are octadecylphenols, octadecylphenols, eicosenylphenols and eicosylphenols. These alkenylphenols and alkylphenols are pyrolysis products of nucleus-side chain C-O coupling urushiol analog polymers and are formed from terminal groups such as natural lacquer films. On the other hand, in the biomimetic lacquer films C and D, these components were not detected, because the urushiol analogs C and D are dienyl- and trienylcatechol.

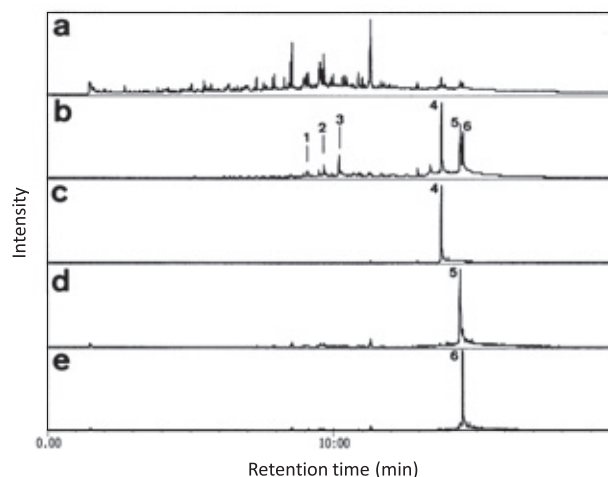
Based on these results, it became clear that the polymerization of the respective urushiol analogs proceeds through the laccase-catalyzed nucleus-side chain C-O coupling as does the natural urushiol. It was also revealed that the biomimetic lacquer films A and B are mainly terminated with alkyl- and monoenylphenol, but the biomimetic lacquer films C and D are not.

In the natural lacquer film, alkenes and alkanes which have longer carbon chains than the side chain of urushiol were

detected as shown in Fig. 7. The polymerized products generated by the autoxidative side chain-side chain C-C coupling of natural urushiol are pyrolyzed, and the long chain alkanes and alkenes are produced as a result.

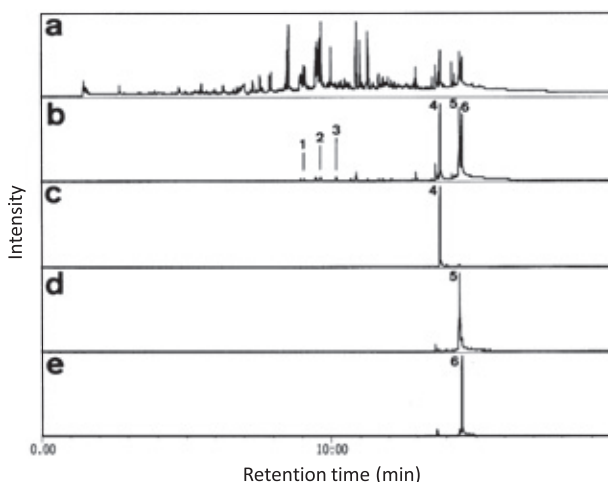
In the biomimetic lacquer films, alkenes and alkanes which have the longer carbon chain than the side chain of urushiol analog were detected as shown Fig. 9–12. These are pyrolysis products of the autoxidative side chain-side chain C-C coupling polymer of the urushiol analogs, because the urushiol analogs have the unsaturated

**Fig. 3 TICC and EICs of the biomimetic lacquer film A obtained by pyrolysis at 400 °C.**



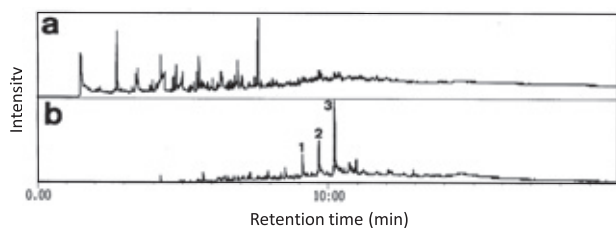
a) TICC b-e) EICs ( $m/z$  123, 334, 360, 362)  
 1: 3-hexylcatechol ( $M_r$  194) 2: 3-heptylcatechol ( $M_r$  208)  
 3: octylcatechol ( $M_r$  222) 4: 3-hexadecylcatechol ( $M_r$  334)  
 5: 3-octadecylcatechol ( $M_r$  360) 6: 3-octadecylcatechol ( $M_r$  362)

**Fig. 4 TICC and EICs of the biomimetic lacquer film B obtained by pyrolysis at 400 °C.**



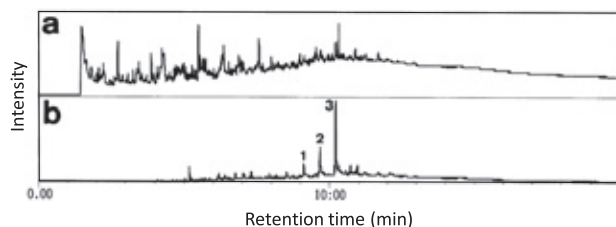
a) TICC b-e) EICs ( $m/z$  123, 334, 360, 362)  
 1: 3-hexylcatechol ( $M_r$  194) 2: 3-heptylcatechol ( $M_r$  208)  
 3: octylcatechol ( $M_r$  222) 4: 3-hexadecylcatechol ( $M_r$  334)  
 5: 3-octadecylcatechol ( $M_r$  360) 6: 3-octadecylcatechol ( $M_r$  362)

**Fig. 5** TICC and EIC of the biomimetic lacquer film C obtained by pyrolysis at 400 °C.



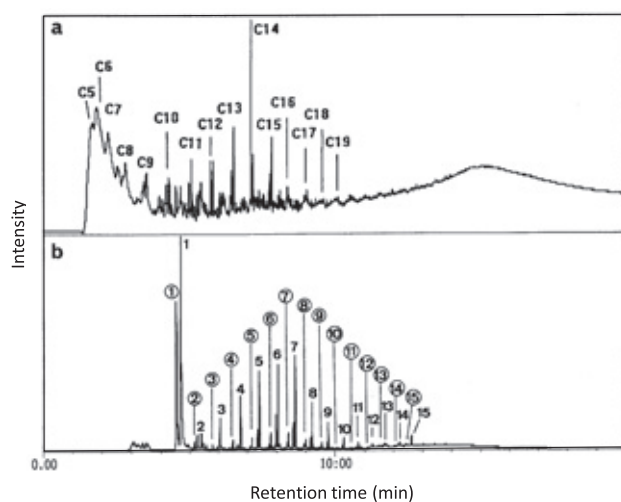
a) TICC b) EIC ( $m/z$  123)  
 1: 3-hexylcatechol ( $M_r$  194) 2: 3-heptylcatechol ( $M_r$  208)  
 3: 3-octylcatechol ( $M_r$  222)

**Fig. 6** TICC and EIC of the biomimetic lacquer film D obtained by pyrolysis at 400 °C.



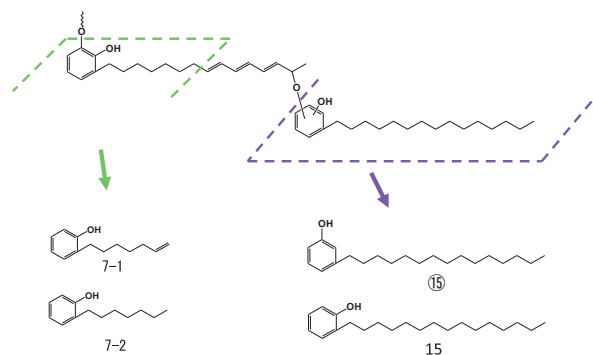
a) TICC b) EIC ( $m/z$  123)  
 1: 3-hexylcatechol ( $M_r$  194) 2: 3-heptylcatechol ( $M_r$  208)  
 3: 3-octylcatechol ( $M_r$  222)

**Fig. 7** TICC and EIC of the natural lacquer film obtained by pyrolysis at 500 °C after pyrolysis at 400 °C.



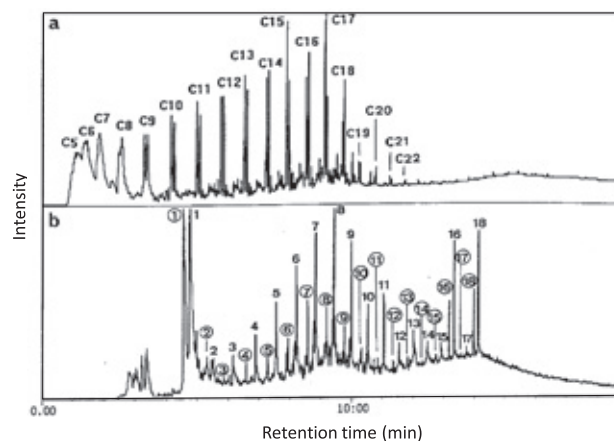
a) TICC  
 C5: pentane C6: 1-hexene C7: heptane  
 C8–C19: 1-alkenes and alkanes ( $C_8$ – $C_{19}$ )  
 b) EIC ( $m/z$  108)  
 ① 3-methylphenol  
 ②–⑮ : 3-alkenylphenols and 3-alkylphenols (side chains:  $C_2$ – $C_{15}$ )  
 1: 2-methylphenol  
 2–15: 2-alkenylphenols and 2-alkylphenols (side chains:  $C_2$ – $C_{15}$ )

**Fig. 8** Pyrolysis mechanisms producing 2-heptenylphenol, 2-heptylphenol, 3-pentadecylphenol and 2-pentadecylphenol.



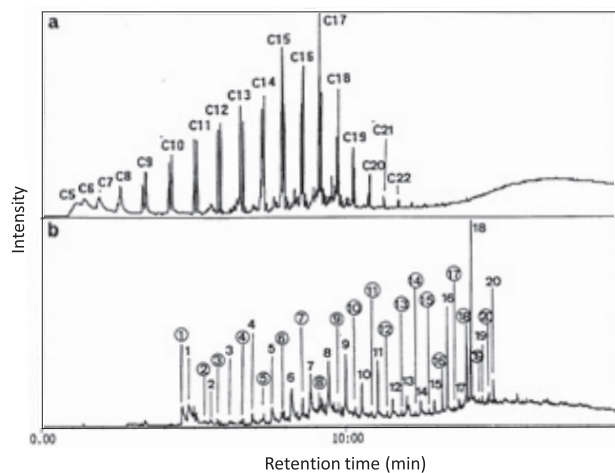
7-1: 2-heptenylphenol  
 7-2: 2-heptylphenol  
 ⑮ : 3-pentadecylphenol  
 15: 2-pentadecylphenol

**Fig. 9** TICC and EIC of the biomimetic lacquer film A obtained by pyrolysis at 500 °C after pyrolysis at 400 °C.



a) TICC  
 C5: pentane C6: 1-hexene C7: heptane  
 C8–C22: 1-alkenes and alkanes ( $C_8$ – $C_{22}$ )  
 b) EIC ( $m/z$  108)  
 ① 3-methylphenol  
 ②–⑮ : 3-alkenylphenols and 3-alkylphenols (side chains:  $C_2$ – $C_{18}$ )  
 1: 2-methylphenol  
 2–18: 2-alkenylphenols and 2-alkylphenols (side chains:  $C_2$ – $C_{18}$ )

**Fig. 10** TICC and EIC of the biomimetic lacquer film B obtained by pyrolysis at 500 °C after pyrolysis at 400 °C.



a) TICC

C5: pentane C6: 1-hexene C7: heptane  
C8–C22: 1-alkenes and alkanes (C<sub>8</sub>–C<sub>22</sub>)

b) EIC (*m/z* 108)

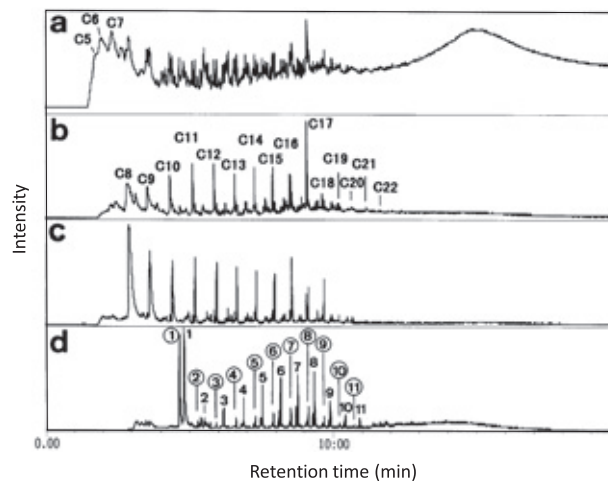
① 3-methylphenol

②–⑩: 3-alkenylphenols and 3-alkylphenols (side chains: C<sub>2</sub>–C<sub>20</sub>)

1: 2-methylphenol

2–20: 2-alkenylphenols and 2-alkylphenols (side chains: C<sub>2</sub>–C<sub>20</sub>)

**Fig. 12** TICC and EICs of the biomimetic lacquer film D obtained by pyrolysis at 500 °C after pyrolysis at 400 °C.



a) TICC b, c) EICs (*m/z* 83, 85)

C5: pentane C6: 1-hexene C7: heptane

C8–C22: 1-alkenes and alkanes (C<sub>8</sub>–C<sub>22</sub>)

d) EIC (*m/z* 108)

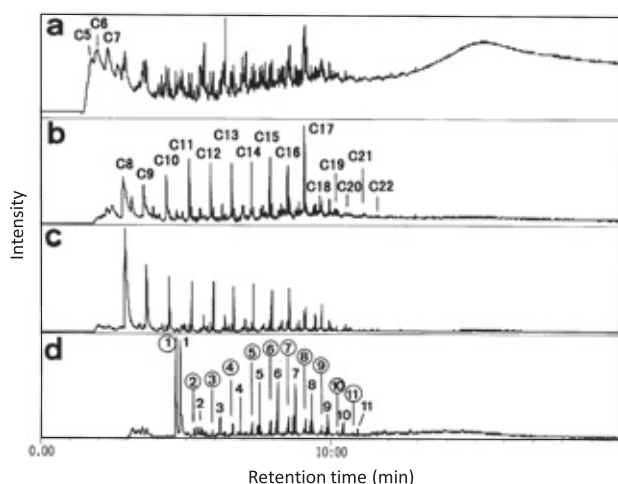
① 3-methylphenol

②–⑩: 3-alkenylphenols and 3-alkylphenols (side chains: C<sub>2</sub>–C<sub>11</sub>)

1: 2-methylphenol

2–11: 2-alkenylphenols and 2-alkylphenols (side chains: C<sub>2</sub>–C<sub>11</sub>)

**Fig. 11** TICC and EIC of the biomimetic lacquer film C obtained by pyrolysis at 500 °C after pyrolysis at 400 °C.



a) TICC b, c) EICs (*m/z* 83, 85)

C5: pentane C6: 1-hexene C7: heptane

C8–C22: 1-alkenes and alkanes (C<sub>8</sub>–C<sub>22</sub>)

d) EIC (*m/z* 108)

① 3-methylphenol

②–⑩: 3-alkenylphenols and 3-alkylphenols (side chains: C<sub>2</sub>–C<sub>11</sub>)

1: 2-methylphenol

2–11: 2-alkenylphenols and 2-alkylphenols (side chains: C<sub>2</sub>–C<sub>11</sub>)

side chains as does natural urushiol. These side chains lead to the cross-linking reaction of the urushiol analogs.

## 2.2. Pencil Hardness Testing

Pencil hardness testing is one method for the physical evaluation of polymer films. The hardness of the respective lacquer films was thus measured. The natural lacquer film is the hardest among these lacquer films showing a pencil hardness of 9H. The second hardest film is the biomimetic lacquer film D exhibiting the pencil hardness of 7H. The biomimetic lacquer films A and C are the third hardest showing the pencil hardness of 4H. The softest film is the biomimetic lacquer film B with the pencil hardness of 2B.

The monomer of biomimetic lacquer film D is urushiol analog D: 3-[(9Z, 12Z, 15Z)-9, 12, 15-octadecatrienyl] catechol. The number of double bonds in the side chain of urushiol analog D is the greatest among the urushiol analogs in this research. The number of double bond in the side chain of 3-[(9Z, 12Z)-9, 12-octadecadienyl] catechol, which is the monomer of biomimetic lacquer film C, is the second among the urushiol analogs. The urushiol analog A, which is the monomer of the biomimetic lacquer film A, is a mixture of trienylcatechol, dienylcatechol, monoenylcatechol and alkylcatechols. Therefore, the number of double bonds in the side chain of urushiol analog A might be the same as that of urushiol analog C. Based on these results, it can be said that the hardness of the film depends on the number of double bond in the side chain of the urushiol analog. The order of the pencil hardness demonstrates the same tendency as that of the number of double bond in the side chain of the respective urushiol analogs, except for the biomimetic lacquer film B. Though the

urushiol analog B contains a greater amount of trienylcatechols than the urushiol analog A, its hardness is softest among the biomimetic lacquer films. However, there is a difference between the respective olefinic side chains. The side chains of the urushiol analog B consist of a conjugated double bond, but those of the urushiol analog A do not consist of a conjugated double bond. This must be the one reason why the biomimetic lacquer film B is the softest even though it contains much amount of trienylcatechol.

### 2.3. XPS Analysis

#### 2.3.1. Elemental Analysis

Elemental analysis of the biomimetic lacquer films was carried out and the results were compared with those of natural lacquer film to investigate the relationship between the hardness and elemental composition of the biomimetic lacquer films. **Table 3** shows the results of the elemental analysis. The concentration of oxygen and nitrogen of the biomimetic lacquer film D was the highest among the biomimetic lacquer films. That of biomimetic lacquer film C was the second highest. The third was that of biomimetic lacquer film A.

That of biomimetic lacquer film B was the lowest. This order shows almost the same tendency as that of the pencil hardness test. The harder lacquer film has the higher concentration ratio of oxygen and nitrogen. The softer lacquer film has the lower concentration. Therefore, it can be said that on the biomimetic lacquer films, oxidative polymerization enhances the hardening reaction and that plant gum and glycoproteins are concentrated in the surfaces of lacquer films with the progress of polymerization [41]. On the other hand, in comparing biomimetic lacquer film D and natural lacquer film, the pencil hardness of the biomimetic lacquer film D is softer than that of the natural lacquer film, but the concentration of oxygen and nitrogen of the biomimetic lacquer film D is higher than that of the natural lacquer film. The pencil hardness depends not only on the concentration ratio of oxygen and nitrogen but also another factor. The length of the side chain of urushiol may be one of the factors, because the side chain of natural urushiol is mainly C<sub>15</sub>, but that of urushiol analog D is C<sub>18</sub>.

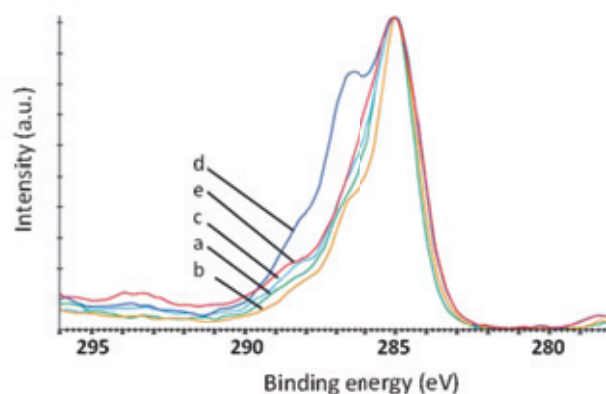
#### 2.3.2. C 1s Spectra

C 1s spectra were analyzed to investigate the chemical bonding states. C 1s spectra of the respective lacquer films are shown in **Fig. 13**. The shape of the respective spectra is different from one another. These spectra were deconvoluted to investigate the proportion of functional groups. The respective C 1s spectra were deconvoluted into COO (289.7 eV), C=O (288.7 eV), C-O-C (287.5 eV), C-OH (286.3 eV), C-N (285.9 eV), C-C (285.0 eV) and C=C (283.9 eV) [12-18].

The results of the deconvolution are shown in **Table 4**. The content of COO, C=O, C-O-C, C-OH and C-N functional groups in the biomimetic lacquer film D is the highest among the biomimetic lacquer films. That in the biomimetic lacquer film C is the second highest. The third highest is that in the biomimetic lacquer film A. That in the biomimetic lacquer film B is the lowest. This order shows the same tendency as the pencil hardness and the concentration of oxygen and nitrogen which were previously discussed. The content of COO, C=O, C-O-C, C-OH and C-N functional groups is higher in the harder lacquer film.

It was reported that on the natural lacquer films, C-O-C functional groups increase because of the laccase-catalysed oxidative polymerization and COO, C=O, C-O-C and C-OH functional groups increase because of autoxidation [41]. The polymerization producing these functional groups proceeds with the hardening of the natural lacquer film. On the other hand, the plant gum and glycoprotein are concentrated in the surface of the lacquer film during hardening. These components have COO, C=O, C-O-C, C-OH and C-N functional groups. This is the other reason why these functional groups increase during hardening. Therefore, the result obtained in this research, i.e., the content

**Fig. 13 C 1s spectra of the respective lacquer films.**



a (green): biomimetic lacquer film A  
 b (brown): biomimetic lacquer film B  
 c (light blue): biomimetic lacquer film C  
 d (blue): biomimetic lacquer film D  
 e (red): natural lacquer film

**Table 3 Elemental analysis of lacquer films (atomic %).**

lacquer film	O	N	C
natural lacquer film	23.5	3.5	73.0
biomimetic lacquer film A	18.1	3.0	78.9
biomimetic lacquer film B	17.8	2.0	80.2
biomimetic lacquer film C	23.3	3.3	73.4
biomimetic lacquer film D	27.0	3.9	69.1

**Table 4 Content of COO, C=O, C-O-C, C-OH and C-N in the lacquer films (%).**

lacquer film	COO	C=O	C-O-C	C-OH	C-N
natural lacquer film	2.0	4.8	10.3	25.3	2.2
Biomimetic lacquer film A	1.1	3.6	6.5	21.3	0.8
Biomimetic lacquer film B	0.8	3.2	5.2	17.0	0.7
Biomimetic lacquer film C	1.3	3.8	7.2	23.2	0.9
Biomimetic lacquer film D	2.3	5.7	14.8	33.7	3.2

of COO, C=O, C-O-C, C-OH and C-N functional groups in the harder lacquer film is higher, support that laccase-catalysed oxidative polymerization and autoxidation producing these functional groups proceeds the hardening of the biomimetic lacquers, and the plant gum and glycoprotein are concentrated in the surface of the biomimetic lacquer films during hardening as is true of natural lacquer film.

## Conclusions

Four kinds of biomimetic lacquer films were characterized by using PyGC/MS, XPS and the pencil hardness testing method.

Based on the results obtained by using PyGC/MS, it was concluded that the biomimetic lacquer A and B are terminated with the monoenyl and saturated urushiol analog components, but the other films are not. However, the polymerization of the respective urushiol analogs proceeds through the laccase catalyzed nucleus-side chain C-O coupling and the autoxidative side chain-side chain C-C coupling as does the natural lacquer film.

Additionally, based on the results obtained by using XPS and the pencil hardness testing method, it was concluded that laccase catalyzed oxidative polymerization and autoxidation proceed the hardening of the biomimetic lacquer. The plant gum and glycoprotein are concentrated in the surface of the biomimetic lacquer film during hardening as is true of natural lacquer film. Furthermore, the urushiol analog, whose side chain has more double bonds, polymerizes into harder lacquer film and concentrates more oxygen and nitrogen at the film surface.

Since the structure and polymerization mechanisms of the biomimetic lacquer films are very similar to those of the natural lacquer film, these biomimetic lacquer films must be tough enough to be used as preservative surface coating materials like the natural lacquer film. We will study the toughness of these films in the next stage.

## Acknowledgments

The author is grateful to Professor Tetsuo Miyakoshi of Meiji University for his cooperation in carrying out this research.

## References

- [ 1 ] Ministry of the Environment Japan, 2018, outline of the Fifth Basic Environment Plan [accessed 15 Oct 2018]. Available at: <[https://www.env.go.jp/policy/kihon\\_keikaku/plan/plan\\_5/attach/ref01-2.pdf](https://www.env.go.jp/policy/kihon_keikaku/plan/plan_5/attach/ref01-2.pdf)>
- [ 2 ] J. Kumanotani, K. Inoue, M. Achiwa and L. W. Chen, *Polym. Sci. Technol.*, **33**, 163 (1986).
- [ 3 ] N. Niimura, *Int. J. Mass Spectrom.*, **284**, 93 (2009).
- [ 4 ] N. Niimura, *Thermochimica Acta*, **532**, 164 (2012).
- [ 5 ] J. Kumanotani, *Zairyoukagaku* (in Japanese), **19**, 88 (1982).
- [ 6 ] Y. Yamauchi, R. Oshima and J. Kumanotani, *J. Chromatogr.* **243**, 71 (1982).
- [ 7 ] J. Bartus, W. J. Simonsick, C. Garner, T. Nishiura, T. Kitayama, K. Hatada and O. Vogel, *Polym. J.*, **26**, 67 (1994).

- [ 8 ] N. Niimura, T. Miyakoshi, J. Onodera and T. Higuchi, *Archaeometry*, **41**, 137 (1999).
- [ 9 ] N. Niimura, T. Miyakoshi, J. Onodera and T. Higuchi, *J. Chem. Soc. Jpn.* (in Japanese), **9**, 724 (1995).
- [ 10 ] N. Niimura, T. Miyakoshi, J. Onodera, T. Higuchi, *J. Anal. Appl. Pyrolysis*, **37**, 199 (1996).
- [ 11 ] N. Niimura, T. Miyakoshi, J. Onodera and T. Higuchi, *Rapid Commun. Mass Spectrom.*, **10**, 1719 (1996).
- [ 12 ] N. Niimura and T. Miyakoshi, *Coating Technology* (in Japanese), **33**, 204 (1998).
- [ 13 ] N. Niimura and T. Miyakoshi, *J. Mass Spectrom Soc. Jpn.*, **51**, 439 (2003).
- [ 14 ] N. Niimura and T. Miyakoshi, *Talanta*, **70**, 146 (2006).
- [ 15 ] N. Niimura, *Int. J. Polym. Anal. Charact.*, **17**, 540 (2012).
- [ 16 ] N. Niimura, *The Industrial Coating* (in Japanese), **185**, 64 (2003).
- [ 17 ] N. Niimura, *The Industrial Coating* (in Japanese), **217**, 53 (2009).
- [ 18 ] T. Miyakoshi, H. Kobuchi, N. Niimura and Y. Yoshihiro, *Bull. Chem. Soc. Jpn.*, **64**, 2560 (1991).
- [ 19 ] N. Niimura, T. Miyakoshi, J. Onodera and T. Higuchi, *Int. J. Polym. Anal. Charact.*, **4**, 309 (1998).
- [ 20 ] N. Niimura, Y. Kamiya, T. Sato, I. Katano and T. Miyakoshi, *J. Jpn. Oil Chem. Soc.*, **47**, 171 (1998).
- [ 21 ] N. Niimura and T. Miyakoshi, *Surf. Interface Anal.*, **29**, 381 (2000).
- [ 22 ] N. Niimura, T. Miyakoshi and Y. Iijima, *Analytical Science 2001 Supplement*, 17, i155, (2001).
- [ 23 ] N. Niimura and T. Miyakoshi, *Int. J. Polym. Anal. Charact.*, **8**, 47 (2003).
- [ 24 ] N. Niimura and T. Miyakoshi, *J. Mass Spectrom Soc. Jpn.*, **51**, 229 (2003).
- [ 25 ] N. Niimura and T. Miyakoshi, *Int. J. Polym. Anal. Charact.*, **10**, 141 (2005).
- [ 26 ] T. Miyakoshi, *Proceedings of the International Symposium on Oriental Lacquers*, 65 (1993).
- [ 27 ] K. Taneda, *Mokuzaikogyou* (in Japanese), **40**, 10 (1985).
- [ 28 ] N. Niimura, Y. Iijima and T. Miyakoshi, *Bunsekikagaku* (in Japanese), **42**, 605 (1993).
- [ 29 ] J. H. Scofield, *J. Electron Spectrosc. Relat. Phenom.*, **8**, 129 (1976).
- [ 30 ] S. Tanuma, C. J. Powell and D. R. Penn, *Surf. Interface Anal.*, **11**, 577 (1988).
- [ 31 ] S. Tanuma, C. J. Powell and D. R. Penn, *J. Vac. Sci. Technol.*, **A8**, 2213 (1990).
- [ 32 ] Y. Iijima, T. Sato, K. Hiraoka, Y. Ichinohe and Y. Nihei, *Advances in X-ray Chemical Analysis*, **26**, 237 (1995).
- [ 33 ] S. Tanuma, C. J. Powell and D. R. Penn, *Surf. Interface Anal.*, **11**, 577 (1988).
- [ 34 ] J. Shama, W. L. Garrett, F. J. Owens and V. L. Vogel, *J. Phys. Chem.*, **86**, 1657 (1982).
- [ 35 ] L. P. Buchwalter, B. D. Silverman, L. Witt and A. R. Rossi, *J. Vac. Sci. Technol.*, **A5**, 226 (1987).
- [ 36 ] L. D. Setiwan, H. Baumann and D. Gribbin, *Surf. Interface Anal.*, **7**, 188 (1985).
- [ 37 ] P. Sundberg, R. Larsson and B. Folkesson, *J. Electron Spectrosc. Relat. Phenom.*, **46**, 19 (1988).
- [ 38 ] S. Sapieha, M. Verreault, J. E. Klenberg-sapieha, E. Sacher and M. R. Wertheimer, *Appl. Surf. Sci.*, **44**, 165 (1990).
- [ 39 ] D. Briggs and G. Beamson, *Anal. Chem.*, **64**, 1729 (1992).
- [ 40 ] M. Stradal and D. A. I. Goring, *Can. J. Chem. Eng.*, **53**, 427 (1975).
- [ 41 ] N. Niimura, Y. Iijima and T. Miyakoshi, *Surf. Interface Anal.*, **24**, 237 (1996).

# Development of Cryo High-Resolution Transmission Electron Microscope CRYO ARM™ 300, Equipped with Cold Field Emission Gun for Structural Biology

Sohei Motoki EM Business Unit, JEOL Ltd.

This paper reports a 300 kV cryo-electron microscope, CRYO ARM™ 300, recently developed. This system features various kinds of automated functions mainly for acquiring data for single particle analysis of high resolution and high throughput. We report each feature of the function for this CRYO ARM™ 300, and show the recent application result of high resolution.

## Introduction

Structures of biological macromolecules (proteins, DNA, RNA, etc.) are important for understanding their function, since the structures significantly relates their functions. This suggests that the structures may tell the ways to develop a new drug. Up to the present, X-ray crystallography has been mainly used for high resolution structural analysis of proteins. Quite recently, CRYO Electron Microscope (CRYO EM) has also attracted attention for the structural analysis owing to rapid technological progress such as a new analysis software program and an image detection camera [1].

In 1983, in collaboration with Professor Yoshinori Fujiyoshi (Tokyo Medical and Dental University), we began the development of CRYO EM equipped with a top entry type helium stage, and the first generation CRYO EM was completed in 1986 [2]. The microscope enabled high resolution imaging at 4.2 K. Since that time, CRYO EM has been continuously developed into seventh generation machines through improvements such as automatic sample loader and in-column omega type energy filter addition. These microscopes made many contributions to structural biology. They are, for example, elucidation of the structure and function of aquaporin-1 [3], acetylcholine receptor [4], and other membrane proteins [5-7].

In recent years, a single particle analysis (SPA), which enables analyzing the protein structure, is getting increased attention, because no crystalline sample is required. With the advent of direct electron detection cameras that provide low dose imaging and allow correction of sample drift and beam-induced motion, the SPA now has become to have an ability to generate three dimensional density maps of proteins at close to atomic resolution [8, 9].

However, to have good reconstruction by the SPA, a large amount of image data collected by an automatic acquisition system is indispensable for improvement of the signal to noise ratio (S/N) by averaging in image processing. In 2011, we began development of a new 200 kV CRYO EM (JEOL, JEM-Z200FSC) equipped with a Schottky type thermal field emission gun (TFEG), focusing on automatic data collection system with Professor Namba of Osaka University. And this prototype was completed in 2016. In 2017, we have begun to develop 300 kV CRYO EM (JEOL, CRYO ARM™ 300 (JEM-Z300FSC)) (see **Fig. 1**). **Table 1** shows the main specifications of the CRYO ARM™ 300. This microscope has made it possible to acquire high resolution data by adopting a highly stable column design and highly coherent and stable cold field emission gun (CFEG) inherited from the previously developed aberration corrected microscope (JEOL, JEM-ARM300F). We also improve the autoloader for cryo samples (CRYO SPECPORTER™: CSP), which was developed previously as a prototype for JEM-Z200FSC, resulting in realization of a CRYO EM of higher usability. We introduce the features of the CRYO ARM™ 300 one by one from the next section.

## Cold Field Emission Gun (CFEG)

Biological samples such as proteins consist only of light elements. Therefore, it is hard to obtain enough scattering contrast because of small scattering powers of the light elements. In addition to this, the images are in low signal to noise ratio, since the images are acquired at low dose to prevent sample damage due to the electron beam. To enhance the image contrast at the low spatial frequency, generally the images are acquired with large defocus of ~1 μm. The enhanced contrast

at low frequency is required for particle picking, since with no particle picking, we cannot proceed to the next stage of SPA. However, with the given large defocus, the envelope function of temporal coherence ( $\epsilon_c$ ) on spatial frequency, which limits the amplitude extent of the phase contrast transfer function (PCTF), rapidly decays at higher frequency, resulting in the loss of the high resolution information of the protein structures. CFEG improves this situation because its energy spread is small (see Fig. 2). Energy spread of the 300 kV CFEG is 0.35 eV, which is less than half of Schottky TFEG. This small energy spread reduces the rapid decrease of  $\epsilon_c$  in the high frequency region and it allows one to obtain information at higher spatial frequency as shown in PCTF.

## CRYO Stage

Figure 3 shows a schematic drawing around the specimen stage of the CRYO ARM™ 300. To cool down the sample to 100 K or less, the sample stage connects to the 3 L liquid nitrogen tank placed outside the TEM column, via a flexible heat conductor. This flexibility prevents to transmit the vibrations generated in the tank to the sample stage. And, the sample is surrounded by cryo-shields cooled to be at 95 K or less, with liquid nitrogen, for preventing growth of ice contamination on the sample surface. The shield adsorbs water molecules. Moreover, the cryo shield is shaped to be chimney type extended along the beam pass, to promote the adsorption of ice to the shield. The holes of the chimney pipe are designed to be placed as far as possible from the sample, make reduce of the solid angle looking from the holes to a sample. This effectively reduces the probability to hit the sample by water molecules. Finally, the microscope surely provides the ice contamination growth rate reduced to be 0.5 nm/h or less.

## CRYO SPECPORTER™

Figure 4 shows the structure of CRYO ARM™ sample automatic transport system (CRYO SPECPORTER™; CSP). This transport system consists of longitudinal and lateral transport rods, each of which has a chuck to grip the sample cartridge. These rods allow mutual transportation of the sample cartridge between the sample storing positions in the pre-evacuation and CSP chambers, which are those of the parking stage, sample-exchange-cartridge, transfer-cup and observation position in the microscope column.

We designed this microscope to be shared with multiple users and made it convenient to share by the following features. The system provides a capability of loading and unloading of up to four sample cartridges at a time. And the vacuum of the CSP chamber, always keeps at the order of  $10^{-5}$  Pa, when the separation valve between the specimen pre-evacuation and CSP chambers is closed. This guarantees that the loading and unloading of the sample cartridges inside the CSP chamber are doable with no vacuum degradation. In other words, it is possible to load/unload arbitrary one to four loading positions of sample exchange cartridges out of the twelve positions, with no disturbing the positions of other cartridge storing samples. And also we can introduce a sample to the parking stage from outside using pre-evacuation through transfer cup. The microscope thus-designed to be shared with multiple users has great benefit in the following case. In a situation when you have a sample suitable for SPA in the CSP and your use time of the microscope is going to be over, and another researcher requests to observe his sample. The researcher can store his sample to a vacant position,

and another researcher can introduce a new sample into the CSP without the unloading of his sample.

## Hole Free Phase Plate (HFPP) and Omega filter

It is generally difficult to apply small proteins (~100 kDa) for SPA. As protein particles become smaller, the thickness of ice relatively increases, the difference of mass density between the particles and ice decreases, and it makes difficult to identify the particles to be picked up. In addition, as described above, the CRYO EM image obtained under low dose condition to prevent electron beam damage has low S/N ratio. If the particle position

Fig. 1 Appearance of CRYO ARM™ 300



Opening a door in the center part of the microscope cover, sample loading position appears. After placing the specimen transfer cup at the sample loading position, specimen magazine is automatically loaded into CRYO SPECPORTER™ when the button on the touch panel is turned on. Inside the cover there is stored an automated liquid nitrogen filling system besides the main column of the microscope. The inner surface of the cover is soundproofed.

Table 1 Main specifications of CRYO ARM™ 300

Electron Gun	Cold field emission gun (Cold FEG)
Accelerating voltage	300 kV
Energy filter	In-column Omega energy filter
Cryo stage	
Coolant	Liquid nitrogen, Automated liquid nitrogen filling system built in
Specimen cooking temperature	100 K or less
Temperature measurement	Near specimen, Cryo-shield, Near LN <sub>2</sub> tank
Specimen movement	
X, Y	Motor drive (movements: ± 1 mm) Piezoelectric elements (movements: ± 0.5 μm)
Z	Motor drive (movements: ± 0.2 mm)
Tilt-X	Motor drive (tilts: ± 70°)
Rotation within the specimen plane	Settable to 0° or 90°
CRYO SPECPORTER	
Specimen loading system	Air-lock
Specimen exchange system	Automated cryo-transfer system built-in
Cooling temperature (specimen exchange chamber)	105 K or less
Specimen exchange cartridge	Up to 4 specimens can be changed at one time
Specimen parking stage	Up to 12 specimens can be held

cannot be recognized, it makes impossible to deduce 3D structure or picking the particles for the SPA analysis.

For such small proteins, a Hole Free Phase Plate (HFPP) works as a powerful solution. The HFPP is a carbon film with a thickness of 15 nm and is inserted into the back focal plane of the objective lens. A 0th order diffraction spot formed at the back focal plane of the objective lens makes localized voltage on the HFPP due to secondary electron emission. The electric potential formed on the HFPP makes the electron phase of transmitted wave advance and makes electron phase shift by  $\pi/2$  radians. As a result, the PCTF changes from a sine function to a cosine function, which includes more information at low spatial frequency region in PCTF representing the particle's shape.

Furthermore, if zero-loss imaging in which inelastic scattered electrons are cut with an omega filter, the background component in the phase contrast image can be reduced and makes S/N improved.

## JADAS (JEOL Automated Data Acquisition System)

In order to obtain high resolution SPA results, it is necessary to acquire hundreds to thousands of CRYO EM images, that is, automated data acquisition software is essentially required.

It is necessary to adjust the optical axis and set parameters of the Minimum Dose System (MDS) for low dose operation before starting automatic data acquisition. These adjustment and settings are in pre-programmed workflow of the JADAS (JEOL Automated Data Acquisition System) recipe. Therefore, user can set such list of recipes using graphical user interface (GUI) of JADAS. **Figure 5** shows the procedure displayed when selecting each list.

After the start of automatic data acquisition, JADAS detects the position of the Quantifoil™ automatically, determines the adequate area with good ice thickness automatically, and selects the place acquiring data. With a typical sequence (JADAS has various sequences in editable recipes), move the specimen to each hole position, execute autofocus, and acquire data. The system repeats automatically the procedure for other holes.

## Application results

**Figure 6(b)** shows a SPA result of Apoferritin obtained by the CRYO ARM™ 300 at RIKEN Spring-8 center in Japan. The sample of the Apoferritin was derived from mouse and it consists of only the heavy chain expressed and purified. The 120,295 particles used for the reconstruction were picked up from the acquired 840 images using JADAS, and were used to make a 3D model by RELION (MRC Laboratory of Molecular Biology). The resolution in Fourier Shell Correlation (FSC) = 0.143 is 1.54 Å (see Fig. 6(c)). The fact that center holes of the six- and five-membered tryptophan rings are visible clearly indicates the high resolution of the reconstructed map.

## Conclusion

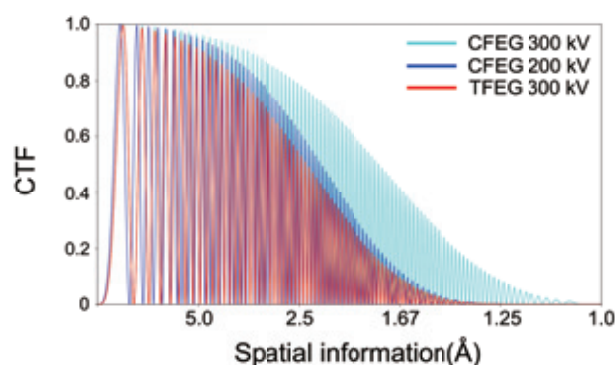
We developed a new CRYO EM (CRYO ARM™ 300 / JEM-Z300FSC) with an accelerating voltage of 300 kV for the main purpose of 3D structural analysis by SPA. We showed that each technical item on CRYO ARM™ 300 is effective for the SPA together with the application data. As the number of users of CRYO ARM™ 300 increase in the future, we expect

new requests from users with various levels and purposes. We think that it is necessary to understand the real intent of those requests well and reflect them to CRYO ARM™ 300 for its improvement.

## Acknowledgments

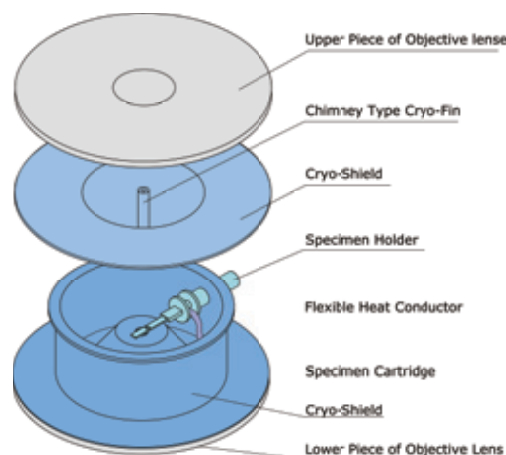
To develop CRYO ARM™ 300, a large number of people involved in the R&D, sales, manufacturing, procurement, production management, service, etc. in JEOL Ltd. were involved. We acknowledge all the JEOL staffs for their efforts in the development of the CRYO ARM™. And we thank Drs. T Kato, F Makino, T Nakane, K Yonekura and K Namba for providing application results, and thank Drs. H Yanagisawa and M Kikkawa for providing the plasmid of mouse Apoferritin.

**Fig. 2**



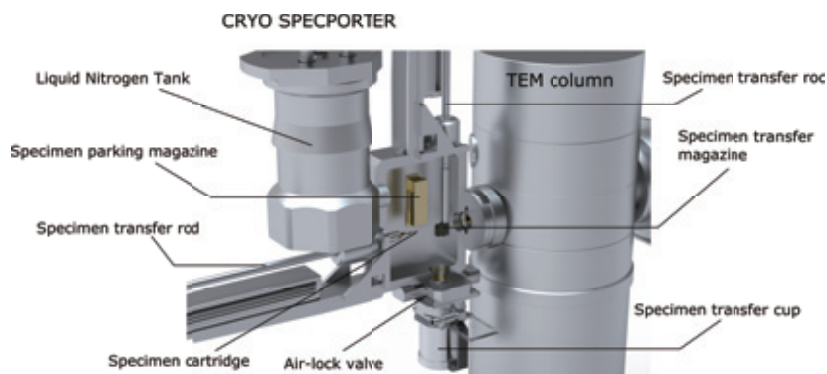
Simulated Phase Contrast Transfer Function (PCTF) of 300 kV CFEG, 200 kV CFEG, and 300 kV Schottky-FEG. Calculated using  $C_s = 2.7$  mm,  $C_c = 2.8$  mm,  $\Delta E = 0.4$  eV (CFEG),  $\Delta E = 0.9$  eV (Schottky-FEG). Comparing the respective information limits, we can see the 200 kV Cold-FEG surpasses 300 kV Schottky-FEG slightly and the 300 kV Cold-FEG surpasses 300 kV Schottky-FEG significantly.

**Fig. 3 Scheme around specimen stage of CRYO ARM™ 300**



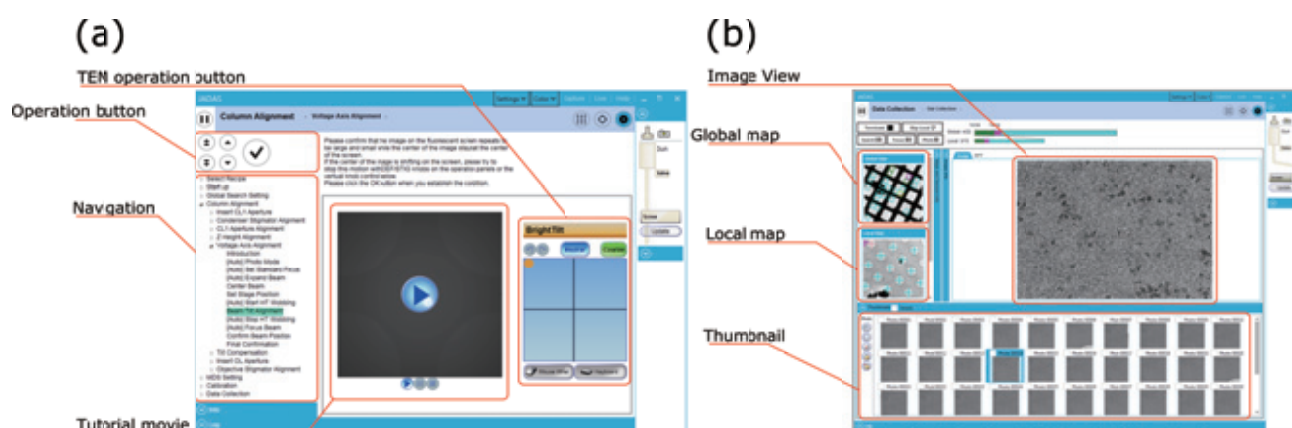
For preventing ice contamination, cryo shield surrounds the sample cartridge. Furthermore, a chimney type cryo shield is installed to reduce the arrival of water molecules from the vertical direction to the specimen.

**Fig. 4 Schematic of CRYO SPECPORTER™ (CS)**



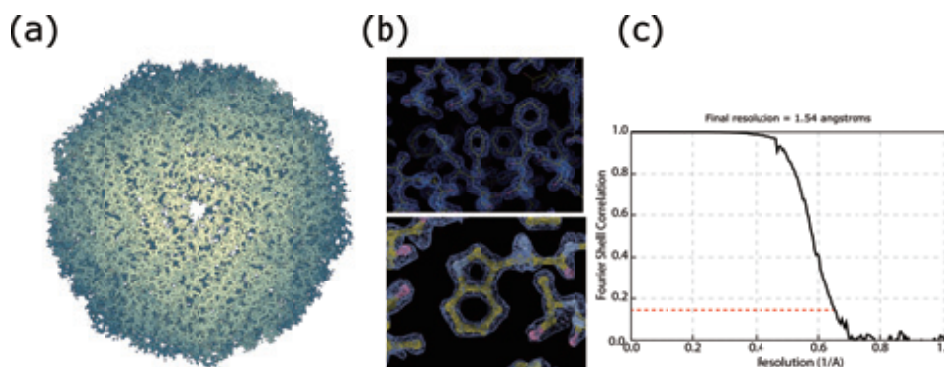
After pre-evacuation in the transfer cup, the air lock valve opens and the specimen magazine in the transfer cup is loaded into the CS. The specimen cartridge in the transfer magazines are set to the specimen storage magazine. Up to 12 cooled samples can be stored in the specimen storage magazine.

**Fig. 5 Screen shots of JADAS GUI**



(a) GUI of set up mode for data collection. It is designed to complete setup simply by following the navigation necessary for automated data acquisition using only 5 operation buttons. An explanation corresponding to each item is displayed with animation if user needs. (b) GUI of data acquisition mode. Once regions on the specimen you want to acquire data is selected on the low magnification TEM image (global map), JADAS automatically acquire the medium magnification TEM image (local map screen), detect the hole on the grid, estimates the adequate holes to be selected and collect images efficiently.

**Fig. 6**



(a) Three-dimensional density map of Apoferritin derived from mouse. (b)-upper panel. Results obtained by fitting the atomic structure of amino acids to the acquired three-dimensional density map. (b)-lower panel. Density map of tryptophan showing clear holes in their five- and six-membered rings. (c) Fourier Shell Correlation (FSC), which shows resolution of 0.154 Å at FSC = 0.143.

## References

- [ 1 ] Subramaniam S., Earl LA., Falconieri V., Milne JL., Egelman EH.: *Curr. Opin. Struct. Biol.* **41**, 194-202 (2-16).
- [ 2 ] Fujiyoshi Y.: *JEOL News* **41**, 13-21 (2009).
- [ 3 ] Fujiyoshi Y.: *Adv. Biophys.* **35**, 25-80 (1998).
- [ 4 ] Murata K., Mitsuoka K., Hirai T., Walz T., Agre P., Heymann JB., Engel A., Fujiyoshi Y.: *Nature* **407**, 599-605 (2000).
- [ 5 ] Kimura Y., Vassilyev DG., Miyazawa A., Kidera A., Matsushima M., Mitsuoka K., Murata K., Hirai T., Fujiyoshi Y., Unwin N.: *Nature* **389** 206-211 (1997).
- [ 6 ] Miyazawa A., Fujiyoshi Y., Unwin N.: *Nature* **423**, 949-955 (2003).
- [ 7 ] Gonen T., Cheng Y., Sliz P., Hiroki Y., Fujiyoshi Y., Harrison SC., Walz T.: *Nature* **438**, 633-638 (2005).
- [ 8 ] Bartesaghi A., Merk A., Banerjee S., Matthies D., Wu X., Milne JLS., Subramaniam S.: *Science* **348**, 1147-1151 (2015).
- [ 9 ] Liao M., Cao E., Julius D., Cheng Y.: *Nature* **504**, 107-112 (2013).
- [ 10 ] Namba K., Kato T.: *JEOL News* **50**, 2-7 (2018).
- [ 11 ] Hosogi N.: *JEOL News* **52**, 49-52 (2017).

# Observation and Analysis at Low Accelerating Voltage Using Ultra High Resolution FE-SEM JSM-7900F

Hironobu Niimi, Yusuke Sakuda, Natsuko Asano, Shunsuke Asahina

EP Business Unit, JEOL Ltd.

JEOL has continued to develop the scanning electron microscopes (SEMs) over 50 years since the release of JSM-1 in 1966. SEM is used in a wide range of fields such as research, development and quality assurance because it can obtain fine uneven structures and compositional information on the sample surface. Recently, it is requisite for high spatial resolution (hereinafter referred to as resolution) in the surface observation, charging reduction, sample damage reduction and surface analysis to the SEM. We show the new techniques for satisfying these requirements using low accelerating voltage and its applications in this paper.

## Introduction

The SEM is an instrument which detects secondary electrons (SEs), backscattered electrons (BSEs), characteristic X-rays and cathode luminescence emitted from the sample surface at each primary-electron irradiated position. Thus, it is possible to know the surface morphology, composition, crystal orientation and elemental information by using SEM.

For recent SEM, it is increasingly popular to use low accelerating voltage so as to observe more information on surfaces and to reduce the charging and damages. However, these requirements necessitate employment of advanced techniques.

In this paper, we show new techniques and applications using SEM at low accelerating voltage.

## 1. Low accelerating voltage observation

Ultra low accelerating voltage SEM is a powerful method for the surface observation and reduction for both charging and sample damage. Then, we will discuss recent ideas to improve the resolution in this session.

In general, the accelerating voltage below 5 kV is called a low accelerating voltage and the accelerating voltage below 1 kV is called an ultra low accelerating voltage. In this paper, the accelerating voltage of 5 kV or less is called "low acceleration voltage."

### 1.1. Effect of low accelerating voltage observation

We consider why low accelerating voltage SEM is necessary for various requirements. **Figure 1** shows the results of calculated penetration depths for the primary electrons into the

solid. Each penetration depth in graphite is compared for the accelerating voltage of 15 kV and 1 kV. The results show that the penetration depth at 1 kV is about 1/100 of that at 15 kV. Correspondingly, the diffusion volume of electrons after the electron beam penetrates into the sample is as small as 1/10<sup>6</sup> in volume ratio. Therefore, it is possible to obtain information only from the sample surface at the lower accelerating voltage.

Regarding to charging reduction, we usually apply conductive coating to insulators. However, in the case of an insulator having a fine nano structure, the structure of surface is embedded by coated materials [1], and this makes it difficult to observe such structures by SEM. It should be noted that charging is reduced at low accelerating voltage such as that below several hundred volts. With this extremely low voltage, it is possible to observe insulators with a fine structure without coating [2].

There are several damages from thermal heat, contamination and bombardment by the incident electrons at higher accelerating voltages. Then, high accelerating voltage observation must be paid attention to specimen damages. The use of low accelerating voltage suppresses the structural deformation of the surfaces of electron-beam sensitive materials, such as soft materials.

### 1.2. High resolution observation at low accelerating voltage

There are several issues for low accelerating voltage observation. One of the issues is a probe diameter which gives spatial resolution of the SEM image. The probe diameter  $d$  on the sample plane is expressed as the formula

$$d^2 = (Md_s)^2 + (0.6\lambda/\sin\alpha)^2 + (0.5C_s\alpha^3)^2 + (C_c\alpha\left(\frac{\Delta E}{E}\right))^2 \quad (1),$$

where  $M$  is the magnification of illumination system,  $d_s$  is the

electron source diameter,  $\lambda$  is the wavelength of an electron,  $\alpha$  is the convergence angle of an electron,  $C_s$  is the spherical aberration coefficient,  $C_c$  is the chromatic aberration coefficient,  $\Delta E$  is an energy spread of the primary electron and  $E$  is an energy of the primary electron. The first term is the Gaussian source diameter magnified on the sample plane, the second term is the diffraction limit, the third term is the spherical aberration, and the fourth term is the chromatic aberration. From the chromatic aberration of the fourth term in the formula (1), the probe diameter becomes larger as  $E$  becomes smaller. This is the main reason for the reduction in resolution due to the effect of chromatic aberration at low accelerating voltage.

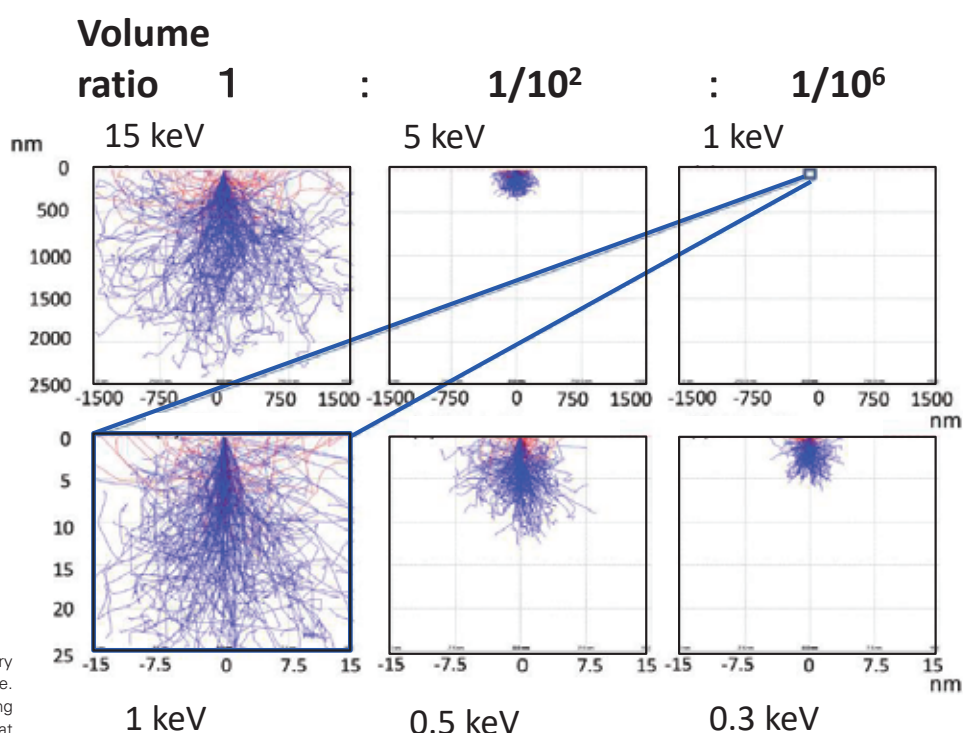
A deceleration method of applying a bias voltage  $-E_b$  to a specimen has been used as a method of reducing chromatic aberration at low accelerating voltage. It is known that the

chromatic aberration coefficient decreases at the ratio of  $E_i/E_g$  by reducing the kinetic energy of the primary electron on the sample [3]. Here,  $E_g$  is the voltage of the electron gun and  $E_i$  is the incident voltage, and this relationship is expressed by

$$E_i = E_g - E_b \quad (2).$$

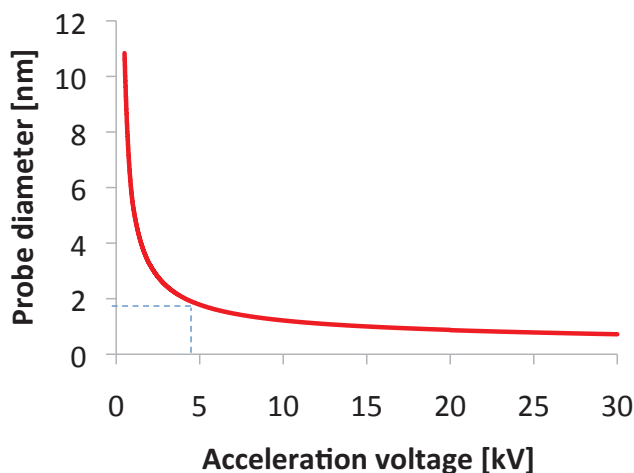
In other words, the chromatic aberration coefficient decreases as  $E_b$  increases if  $E_i$  is constant. Therefore, high resolution observation becomes possible even at a low accelerating voltage. The theoretical calculation (Fig. 2) shows that the probe diameter decreases from that of the primary electron at the voltage higher than 5 kV. Therefore, it is possible to keep a small probe diameter even at a low incident voltage by applying the bias voltage to -5 kV.

Fig. 1



Comparison of penetration depth of the primary electrons into solid for each accelerating voltage. Comparing the penetration depth at accelerating voltage between 15 kV and 1 kV, the depth at 1 kV is smaller than 15 kV by 1/100.

Fig. 2



Dependence of probe diameter on accelerating voltage. The horizontal axis represents the accelerating voltage, and the vertical axis represents the probe diameter. When the accelerating voltage is 5 kV or more, the probe diameter is reduced to 1/5.

## 2. Features of JSM-7900F

We describe an objective lens for high resolution imaging at low accelerating voltage, an electron gun for obtaining large current favorable for analysis and a TTL (Through The Lens) detector system for a highly efficient collecting detector.

We also show the optimized resolution that can be obtained by controlling the convergence angle of the primary electron beam to the specimen using ACL (Aperture Control Lens). Furthermore, we outline the new electron optical control system, called Neo Engine.

### 2.1. FE-electron gun

A thermionic-emission type tungsten filament was conventionally used as the electron source of the electron gun. Electrons are emitted by bending a tungsten wire to a V shape and heating it to 2800 K. On the other hand, a field emission type electron source is used for high resolution SEM. This is because the energy spread of electrons emitted by field emission is approximately 1/6 times that of thermo-electrons emitted from the tungsten filament [1]. Therefore, the chromatic aberration can be reduced because  $\Delta E$  of the fourth term in the formula (1) becomes smaller. The field emission type includes a cold cathode electron source (Cold Field Emission: CFE) and a thermal field emission electron source (Thermal Field Emission: TFE). Here we explain only TFE which is the main electron

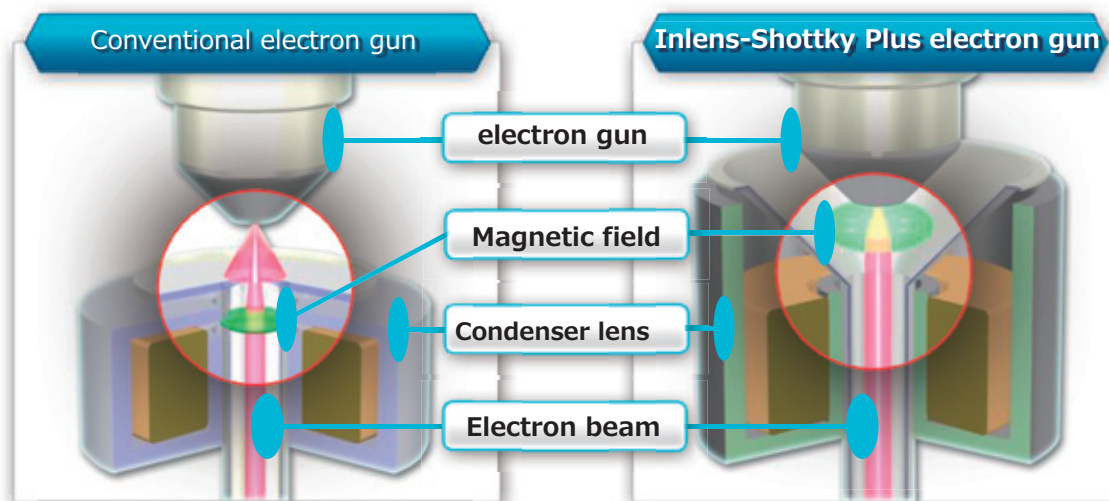
gun of the recent FE-SEM in this paper. TFE reduces the work function by coating Zr and O on the single crystal tungsten tip. It is easy to emit electrons from the tip of single crystal tungsten by this result. By heating the electron source to 1700 to 1800 K and applying a high voltage between the electron source and the extraction electrode, the vacuum barrier is lowered by the Schottky effect to emit electrons. Since TFE is heated, it can prevent gas adsorption and can emit an electron beam stably for a long time. Furthermore, our developed in-lens Schottky Plus electron gun can emit the beam of larger probe current for the conventional TFE because the primary electrons are converged by placing the tip of the electron source in the magnetic lens. **Figure 3** shows a conventional thermal field emission electron gun and an in-lens Schottky Plus electron gun. By using an in-lens Schottky Plus electron gun, it became possible to emit the primary electron beam with a large current of 500 nA or more.

### 2.2. Electrostatic/electromagnetic field superposed objective lens

The objective lens is used to focus the primary electron beam on the sample surface. In the conventional out-lens (**Fig. 4 (a)**), the magnetic field does not leak on the sample surface. Therefore, it was difficult to improve the resolution due to a difficulty in decreasing an aberration.

On the other hand, a semi-in-lens (**Fig. 4 (b)**) is an objective lens which is developed for improving the resolution. In this

**Fig. 3**



Comparison of conventional electron gun and in-lens Schottky Plus electron gun. Compared to the conventional type, the in-lens Schottky Plus electron gun places the tip of the electron gun in the magnetic field so as to produce a large probe current by converging the electron beam when the primary electrons are emitted.

**Fig. 4(a) Schematic diagram of out-lens.**

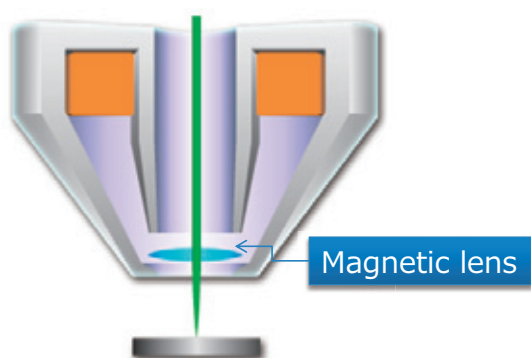
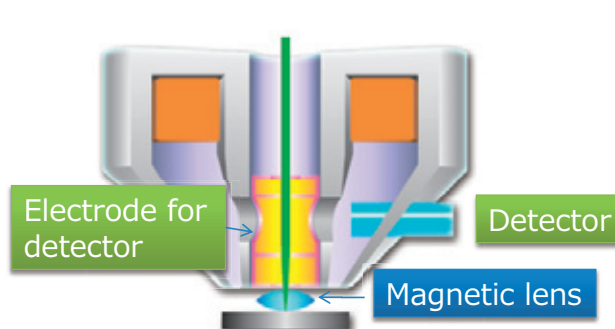


**Fig. 4(b) Schematic diagram of semi-in-lens.**



lens, the magnetic field leaks to the surface of the sample and improves the resolution. Also, it contributes to the improvement of the detection efficiency of the secondary electrons because it is possible to collect the secondary electrons to the inside of the objective lens by using the Larmor motion [4] of the electron in the magnetic field. Therefore, the TTL system is adopted in the semi-in-lens. Here, the TTL system is a method of detecting electrons while the electrons pass through an objective lens. However, it is difficult to observe the SEM image for the magnetic material under the influence of the leakage magnetic field. Also in Electron Back Scatter Diffraction (EBSD) [1] [5], the trajectory of backscattered electrons (BSEs) receives the influence of the leakage magnetic field in the crystal orientation analysis. This makes accurate EBSD analysis difficult.

Therefore, we consider a method to maintain high resolution even if the magnetic lens is the out-lens. The answer is a method of superimposing a positive electrostatic field on a magnetic lens. A decelerating field is generated at the exit of the objective

lens by using this method, so the chromatic aberration coefficient of the objective lens can be reduced [3]. Furthermore, it is possible to capture electrons emitted from the sample surface by this method. Therefore, an electrostatic/electromagnetic field superposed objective lens, called SHL (Super Hybrid Lens) is developed as shown in Fig. 4 (c) [6]. Since SHL has a little influence on trajectory of BSEs due to a small-leakage magnetic field with keeping high resolution, a TTL detector can be used, and small aberration at low accelerating voltages can be realized. Adopting the SHL for JSM-7900F enabled both observation and analysis with high resolution.

### 2.3. Detectors

Everhart-Thornley (E-T) detector is used as the most common method for collecting electrons generated from a sample. The E-T detector applies a positive voltage to a mesh electrode attached to the tip of the detector and captures electrons. The collected electrons are converted into light by a scintillator and then multiplied/converted into electric signals by a photomultiplier. The E-T detector is characterized by its ability to image at high scanning rates. The lower detector (LED) shown in Fig. 5 corresponds to the E-T detector.

On the other hand, there is a semiconductor detector often used to detect and image backscattered electrons. This corresponds to the backscattered electron detector (BED) shown in Fig. 5. Electrons with a kinetic energy of 1 keV or more are incident on the semiconductor device to form electron-hole pairs in the device, which become electrical signals.

Furthermore, the TTL detector, which is used with an electrostatic/electromagnetic field superposed objective lens, can efficiently capture secondary electrons (SEs) by placing it on the optical axis directly above the objective lens. Moreover, the TTL detector can capture more SEs by the upper secondary electron detector (USD), and also only BSE by the upper detector (UED) by combining an energy filter to UED and USD, as shown in Fig. 5. Figure 6 shows the range in which the TTL detector collects the electrons emitted from the sample. The TTL detector of JSM-7900F can also capture SEs more efficiently by using

**Fig. 4(c) Schematic diagram of the electrostatic/electromagnetic field superposed objective lens.**

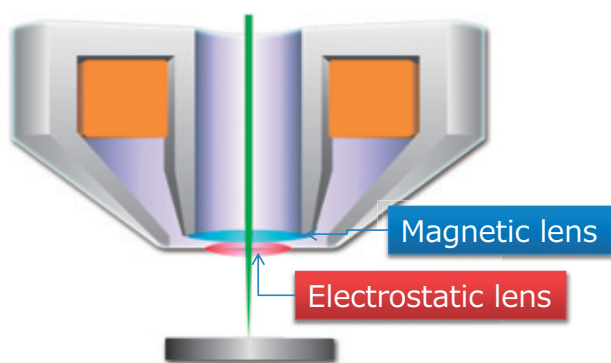
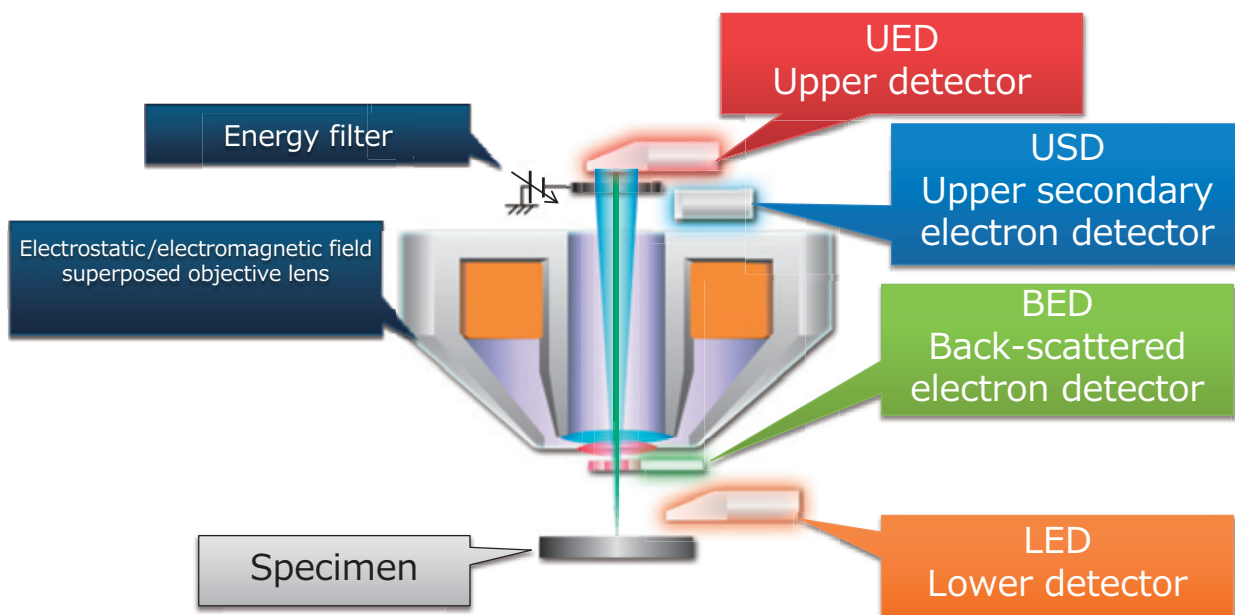
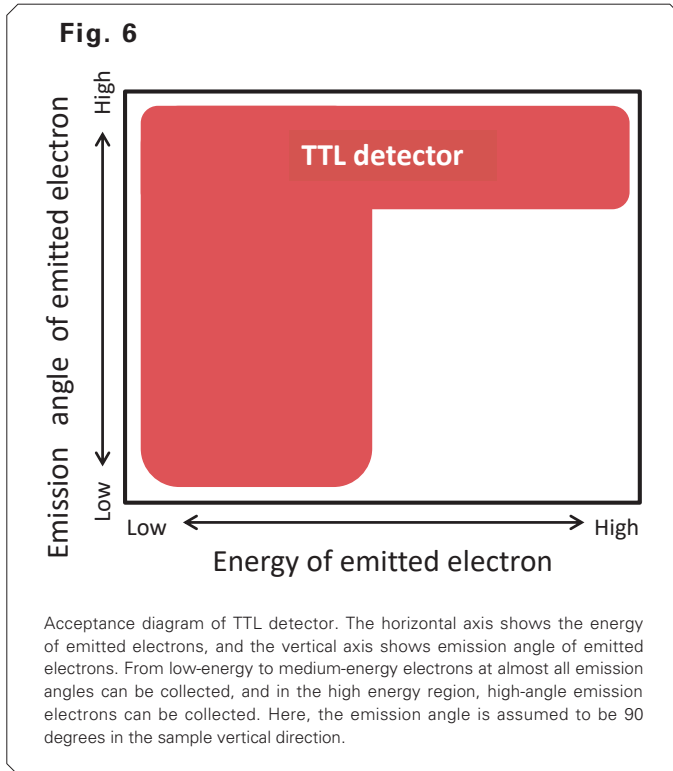


**Fig. 5 Arrangement of each detector.**



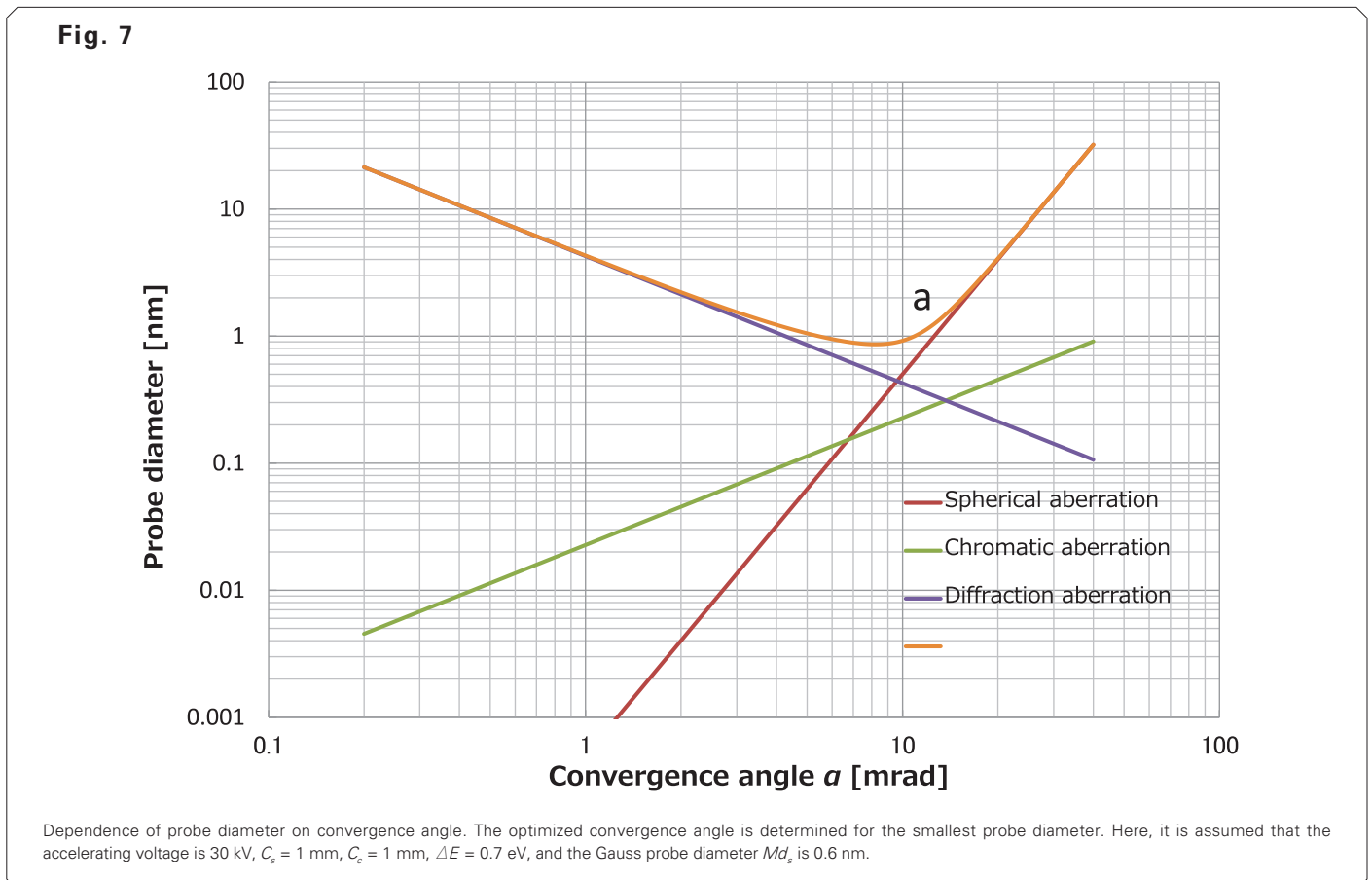
the deceleration method. When a bias voltage (negative voltage) is applied to the sample surface, SEs generated from the sample surface are accelerated and easily enter the TTL detector. Here in Fig. 6, the vertical axis is the emission angle of generated electrons (vertical direction is 90 deg.) and the horizontal axis is the energy of generated electrons.



### 2.4. Optimization of probe diameter using Aperture angle Control Lens

The probe diameter  $d$  is expressed by the formula (1) as described above. In this formula, the convergence angle  $\alpha$  is included in the second term, the third term, and the fourth term, respectively. Assuming that the accelerating voltage is 30 kV,  $C_s = 1$  mm,  $C_c = 1$  mm,  $\Delta E = 0.7$  eV, and the Gaussian probe diameter of the magnified source  $Md_s$  is 0.6 nm, the probe diameter  $d$  shown as brown curve a is obtained by the formula (1). Here the vertical axis is the probe diameter  $d$  [nm] and the horizontal axis is the convergence angle  $\alpha$  [mrad] of the electron beam. It is important to control the convergence angle of the primary electron beam because there is an optimized angle for the convergence angle as shown in Fig. 7. From this principle, we place a lens (ACL: Aperture angle Control Lens) directly above the objective lens to control the convergence angle  $\alpha$  of the primary electron beam.

Figure 8 shows an example of the effect of ACL. The figure on the left side in Fig. 8 is an SEM image of a laminated capacitor. The acquisition conditions are an accelerating voltage of 5 kV and a magnification of  $\times 20,000$ . The line profile along the red line for each probe current is shown in the right side in Fig. 8. It can be seen from Fig. 8 that the line profile has almost the same line width from 500 pA to 50 nA. This is because the minimum probe diameter for each probe current is obtained by adjusting the optimized convergence angle using the ACL for each probe current. Figure 9 shows the calculation result of the normalized probe diameter with ACL and without ACL. As seen in Fig. 9, the change in the normalized probe diameter for each probe current is smaller with ACL compared to without ACL. Especially, the normalized probe diameter with ACL is 1/7 compared to that of without ACL at a probe current of 20 nA.



## 2.5. Usability improvement

In the surface observation, the first procedure is to reduce the contamination to a sample. In JSM-7900F, the sample is loaded and unloaded using the sample exchange chamber with keeping the sample chamber at a high vacuum of about  $10^{-4}$  Pa. As a result, while the sample chamber is kept at a high vacuum, it is possible to rapidly transfer the sample and to reduce the contamination to the sample.

In FE-SEM, the accelerating voltage and probe current may be greatly changed depending on the observation conditions. Even in such a case, it is important to be able to stably acquire an SEM image. Furthermore, an appropriate electron trajectory is calculated for each condition in this instrument and the calculation results are immediately reflected on the instrument to control the electron trajectory. We developed a new electron optical control engine (Neo Engine) in order to improve usability or throughput provided by JSM-7900F. Neo Engine improves an electron optical control system and automatic functions such as autofocus. As a result, it is possible to obtain

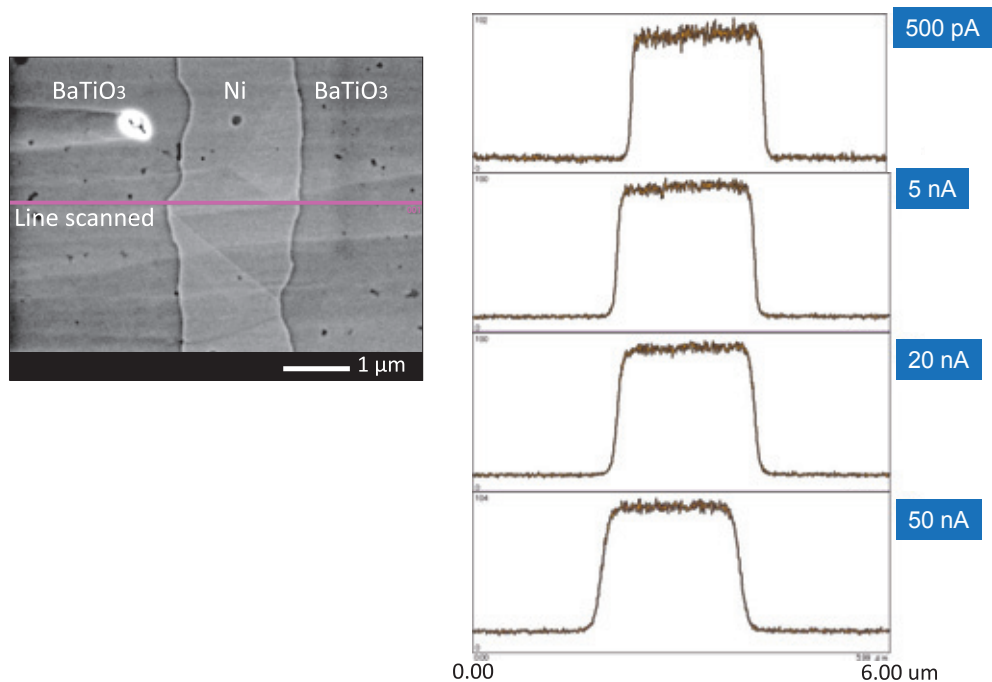
stable images even at low accelerating voltage.

## 3. Analysis at low accelerating voltage

In general, it is difficult to perform elemental analysis and crystal orientation analysis under low accelerating voltage conditions which are optimized for surface observation (this is like a trade-off). On the other hand, electron beam damage can be reduced by decreasing the accelerating voltage, enabling acquisition of the surface information. For this reason, analysis under low accelerating voltage conditions has been desired by many users.

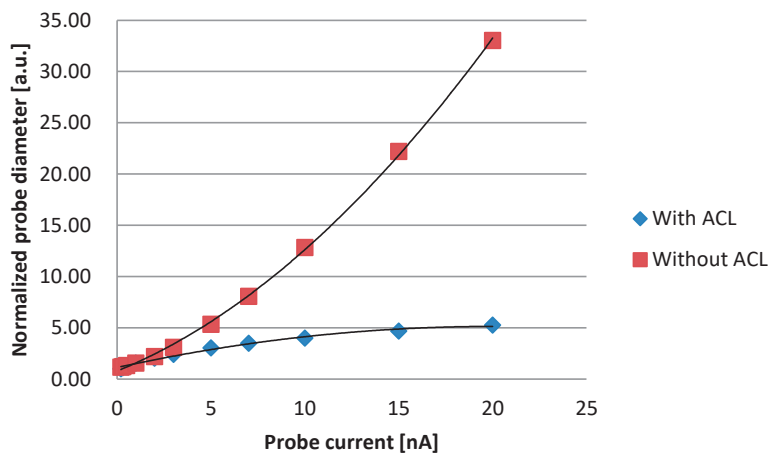
Recently, by the development of new surface analysis methods, it has become possible to acquire elemental and crystal orientation information under low accelerating voltage conditions that were difficult to obtain before. In this section, we introduce a new surface analysis method, namely soft X-ray emission spectroscopy and a low accelerating voltage EBSD method using a new detector.

**Fig. 8**



Change in line profiles displayed in SEM image for each probe current. The line profile of the red line portion of the left SEM image is shown on the right graph for each probe current. The acquisition conditions are an accelerating voltage of 5 kV and a magnification of  $\times 20,000$ . The sample is a laminated capacitor.

**Fig. 9**



Comparison of probe diameters for each probe current with and without control of convergence angle using ACL. The probe diameters controlled with ACL are indicated by blue colors, whereas the diameters without ACL control are indicated by red colors. The accelerating voltage is assumed to be 5 kV.

### 3.1. Soft X-ray emission spectroscopy

Recently, Soft X-ray Emission Spectroscopy (SXES) used in FE-SEM has been developed that detects characteristic X-rays in soft X-ray region [7] [8]. In the field of analysis, attempts have been made to detect low energy characteristic X-rays below 1 keV [7] [8]. Taking Al as an example, it is usual to detect and analyze Al-K $\alpha$  line (1.486 keV) in conventional EDS analysis [1]. On the other hand, SXES is capable of not only elemental analysis near the surface but also chemical state analysis by detecting signals mainly due to electron transitions near the valence band such as metal Al-L line (0.073 keV).

The measurement principle is shown in **Fig. 10**. First, the characteristic X-rays emitted from the sample are collected by the collector mirror and guided to the diffraction grating. Characteristic X-rays with a wide range of energies can be separated simultaneously [9] because unequally spaced grooves are formed in this diffraction grating. Furthermore, SXES can be performed even under a low accelerating voltage condition of below 1 kV because the detected characteristic X-ray energy becomes small. Therefore, SXES is attracting attention as a new surface analysis method.

### 3.2. Low accelerating voltage EBSD method

EBSD is one of the methods for analyzing crystals in SEM. When a crystal is irradiated with primary electrons, the primary electrons are scattered inside the crystal and BSEs are emitted from the surface after the primary electrons are diffracted by the crystal lattices. A pseudo-Kikuchi pattern or an EBSD pattern can be observed (**Fig. 11**) by projecting the emitted electrons to the screen. In an actual instrument, the signal yield efficiency is improved by tilting the sample to 70 degrees in the SEM sample chamber, and the acquisition efficiency of the EBSD pattern is improved by placing the detector near the sample (**Fig. 12**). It is possible to know the crystal orientation of the region irradiated with the primary electrons because EBSD pattern varies depending on crystal orientation. If this analysis is performed over the entire sample surface, the crystal orientation of each region in the sample can be represented in the map (**Fig. 13**).

In addition, it is possible to identify crystal species as well as crystal orientation by using the EBSD method. This method is widely used for analysis of metals and ceramics because it can obtain a wide range of information such as crystal grain size, shape and distortion.

Currently, various EBSD detectors are commercially available from several companies. In conventional detectors, it was necessary to set the accelerating voltage of the SEM as high as 15 to 20 kV in order to obtain the EBSD pattern with sufficient intensity for analysis. However, using the EBSD detector (Symmetry made by Oxford instruments) composed of the latest CMOS devices, sufficient EBSD analysis is possible even in the low accelerating voltage of about 3 to 5 kV. In this way, sample damage is reduced compared to the previous conditions, and it became possible to obtain crystal information near the surface.

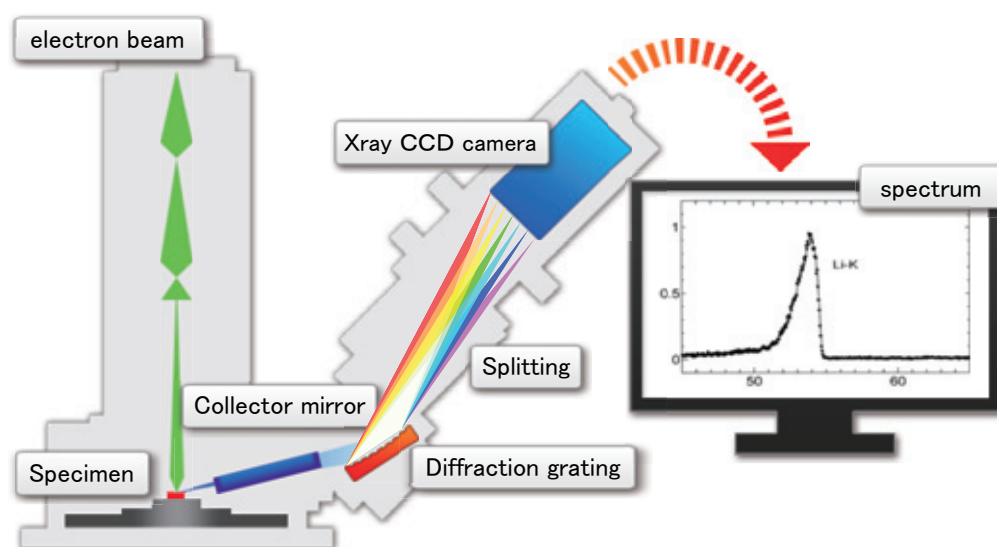
## 4. Applications

We introduce that low accelerating voltage observation is effective for high-resolution surface imaging of mesoporous silica SBA-15 for both charging and contamination reduction. In addition, we introduce soft X-ray emission spectroscopic analysis at low accelerating voltage as an application of surface analysis and also, crystal orientation analysis of biomineral using EBSD at low accelerating voltage.

### 4.1. High resolution observation of mesoporous silica surface using low accelerating voltage SEM

Surface information can be obtained because the penetration depth of the primary electron beam into the sample becomes small by lowering the incident voltage (see Section 1.1, "Effect of low accelerating voltage observation"). Furthermore, charging and electron beam damages are suppressed even if the low accelerating voltage SEM imaging is conducted for insulators. Here, we introduce the advantages of the low accelerating voltage SEM observation in mesoporous silica (SBA-15) which is one of nano porous materials.

**Fig. 10 Measurement principle of Soft X-ray Emission Spectrometer (SXES).**



Mesoporous silica (SBA-15) is a typical porous material with nano scale pores, which is attracting attention for applications such as adsorbents and catalysts. The pore diameter of SBA-15 is about 10 nm and it is made of amorphous  $\text{SiO}_2$ . Usually, it is difficult to apply conductive coating because the pore structure has a three-dimensional connection between nano-sized structures. Therefore, it is one of the materials whose surface observation by SEM is difficult.

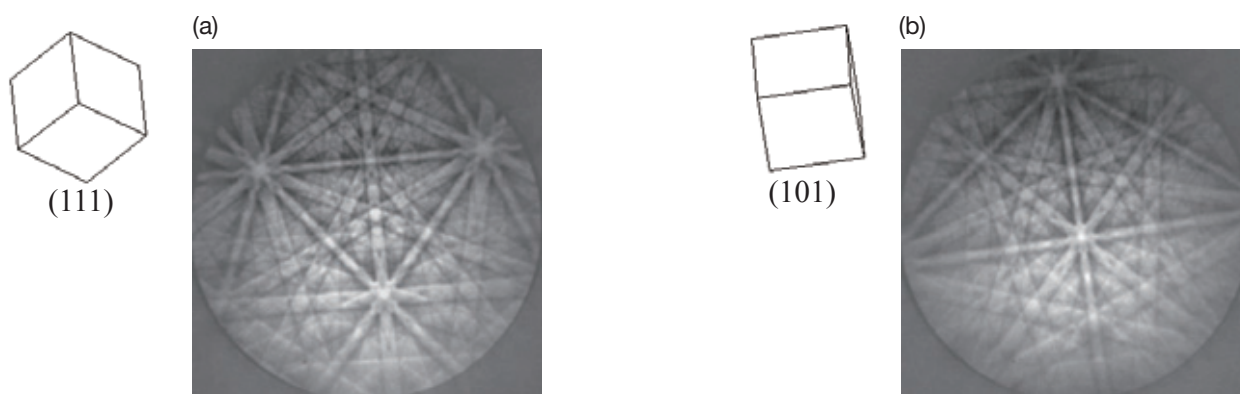
The samples was dispersed in ethanol that is dropped on a carbon stub and heated for about 15 minutes on a hot plate at 200 °C as pretreatment. **Figure 14** shows the results of observing SBA-15 under different conditions. Figure 14 (a) is an SEM image of SBA-15 observed with an incident voltage of 0.3 kV (sample bias -5 kV) with a probe current of 7 pA. An ordered meso pore structure of 10 nm is clearly visible. We succeeded to suppress the influence of charging and then obtained the feature of nanostructure by both low incident voltage and low probe current. On the other hand, strange contrast is seen, caused by the influence of charging from an image acquired at an incident voltage of 1.5 kV (sample bias -5 kV) (Fig. 14 (b)). Furthermore, Fig. 14 (c) shows the image taken at an incident

voltage of 0.3 kV (sample bias -5 kV) immediately after the image of Fig. 14 (b) was taken. Imaging is performed for the sample surface under the same conditions as in Fig. 14 (a) after imaged at a high incident voltage. The nanostructures of the surface are not clearly observed at a high incident voltage. The sample pretreatment is very important for this study because we believe that the low voltage observation is sensitive to surface as shown in Fig. 14 (c). For this reason, it is recommended to observe the sample at low accelerating voltages immediately after the sample is subjected to synthesis or production without conductive coating.

#### 4.2. Low accelerating voltage soft X-ray emission spectroscopic analysis

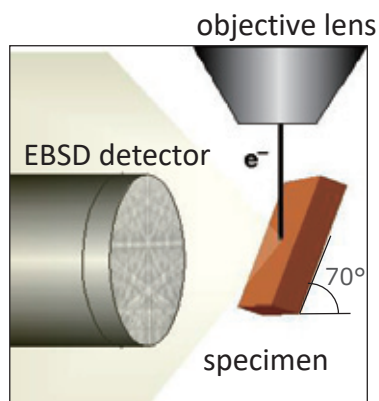
By combining both the low accelerating voltage SEM (Section 1.2, “High resolution observation at low accelerating voltage”) and the SXES technique (Section 3.1, “Soft X-ray emission spectroscopy”), it becomes possible to perform elemental analysis and chemical state analysis of the sample surface. In order to excite the characteristic X-rays from the sample, the primary electron beam with its incident voltage higher than the

**Fig. 11**



(a) Example of Kikuchi patterns in (111) and (101) of silver crystal. The Kikuchi patterns are different depending on the crystal orientation.  
 (b) Example of silver crystal orientation map. It is understood that the pattern is different depending on the crystal orientation.

**Fig. 12**



Positional relationship between specimen and EBSD detector inside specimen chamber.

**Fig. 13 Silver crystal orientation map.**



critical excitation voltage of the detectable elements, must be irradiated onto the sample. However, the incident voltage of 2 to 3 times or more than this critical excitation voltage is desirable for consideration of excitation efficiency of the X-rays. For example, characteristic X-rays of C-K $\alpha$  line can be excited even under at a low accelerating voltage of about 0.5 to 1 kV because the critical excitation voltage for C-K $\alpha$  is 0.277 keV.

SXES point analysis results of graphite and diamond are shown in **Fig. 15**. It can be seen that spectral shapes and peak positions are different depending on the chemical state difference even for the same carbon material [10].

Next, we introduce as an example of depth profile analysis without polishing a sample. It is possible to vary the penetration depth of electrons into the sample by changing the accelerating voltage as described above. Therefore, it is able to acquire surface information and bulk information by changing the accelerating voltage. A sample used is a SiO<sub>2</sub> film about 100 nm thick, formed on a Si substrate. Silicon species of Si and SiO<sub>2</sub> also differ in spectra peak position depending on the chemical bonding state as shown in **Fig. 16** as in the case of carbon.

**Figure 17** compares different SXES spectra at various accelerating voltages. The Si substrate is the main source of spectral information at 7 kV and the SiO<sub>2</sub> film is the main source of spectral information at 1 kV. It is possible to perform chemical state analysis for the depth information non-destructively by changing the accelerating voltage using FE-SEM and SXES. Furthermore, spectrum acquisition with incident voltage of 100 V is possible by combining deceleration method, as described in recent reports [11].

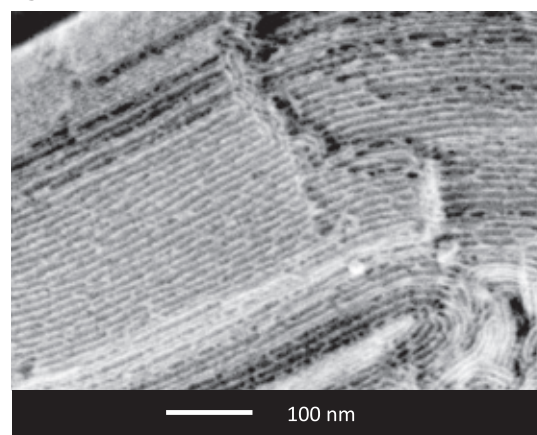
#### 4.3. Analysis of biomineral by low accelerating voltage EBSD method

Low accelerating voltage SEM is a powerful tool to observe and analyze the original nanostructures without artifacts. However, a nacreous layer formed inside the shell is easily damaged by irradiating the electron beam. Therefore, it has considered difficult for crystal orientation analysis by EBSD because this method requires high accelerating voltage of about 15-20 kV. For solving this limitation, we report a low accelerating voltage EBSD analysis of the nacreous layer by using a new EBSD detector that adopts the new type CMOS device.

We used an Ar ion beam cross-section specimen preparation instrument (IB-19520CCP or CCP). EBSD is a surface sensitive measurement method that acquires top-surface information, only about 50 nm deep from the surface, depending on the material though. Thus, it is essential to prepare a smooth sample without damage. Our CCP incorporates a liquid nitrogen sample cooling mechanism. This method can reduce the sample damage due to heat generated by irradiating ion beam. We carry out CCP milling with keeping the sample temperature at lower than -120 °C. The Os coat of 1 nm was applied using an Os coater (OPC 80 T from Filgen Co.) after completion of the milling.

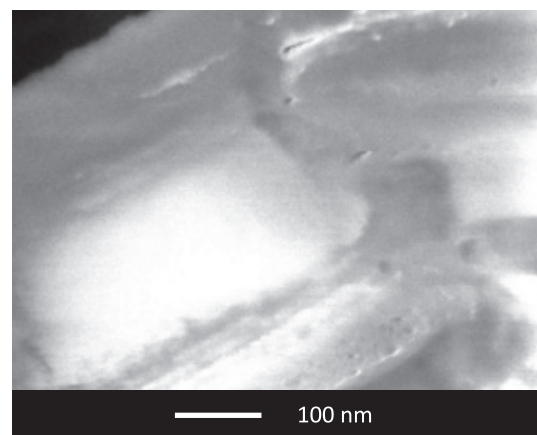
**Figure 18** shows results of acquiring the EBSD crystal phase maps for the nacreous mother-of-pearl layer cross section under two conditions at conventional high accelerating voltage condition of 10 kV (a) and low accelerating voltage of 5 kV (b). The pink color parts indicate that crystal species can be identified well. The black parts indicate that the species could not be identified. It can be seen that we can acquire a map with high quality under the low accelerating voltage condition. To the contrary, the EDS map acquired at high accelerating voltage provides lower quality. This is because the damage to the sample by an electron beam is large under this high voltage condition

**Fig. 14(a)**



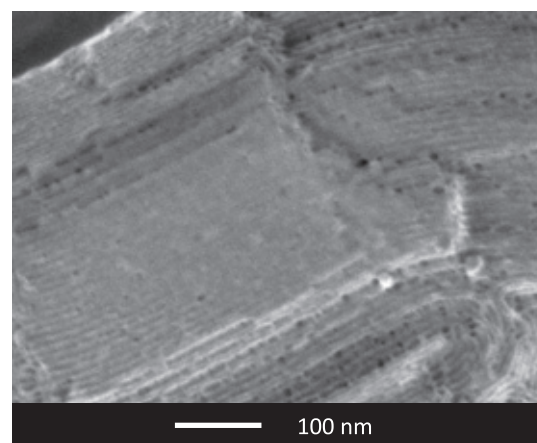
(a) SEM image of mesoporous silica (SBA-15) at low accelerating voltage. Acquisition conditions are as follows: the incident voltage is 0.3 kV, the probe current is 7 pA, the sample bias voltage is -5 kV. The structure of mesoporous silica can be clearly observed.

**Fig. 14(b)**



(b) SEM image of mesoporous silica (SBA-15) at low accelerating voltage. Acquisition conditions are as follows: the incident voltage is 1.5 kV, the probe current is 7 pA, the sample bias voltage is -5 kV. Nano fine structures cannot be seen because the mesoporous silica is charged.

**Fig. 14(c)**



(c) SEM image of mesoporous silica at a low accelerating voltage (incident voltage 0.3 kV) after the image of Fig. 14 (c) (accelerating voltage 1.5 kV) was taken. Acquisition conditions are as follows: the probe current is 7 pA, the sample bias voltage is -5 kV. It can be seen that the nano fine structures are embedded by contamination immediately after imaged again at 0.3 kV.

and it is necessary to sufficiently separate the measurement points from each other by taking large scanning width for sample damage reduction. This result confirms that the sample damage is smaller under low accelerating voltage condition. Therefore, we can increase the number of pixel points by a factor of 4 for the map acquisition at low accelerating voltage. This leads to the acquisition of a map with higher quality.

## Conclusion

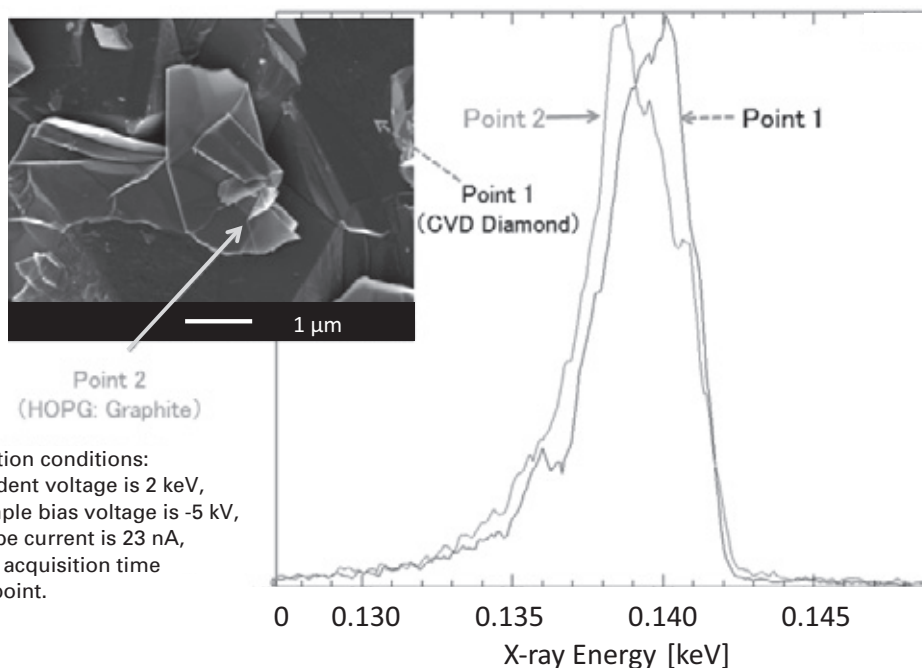
In this paper, we showed a method to realize high resolution surface observation, charging reduction, sample damage

reduction and surface analysis by low accelerating voltage required for the latest SEM and its applications.

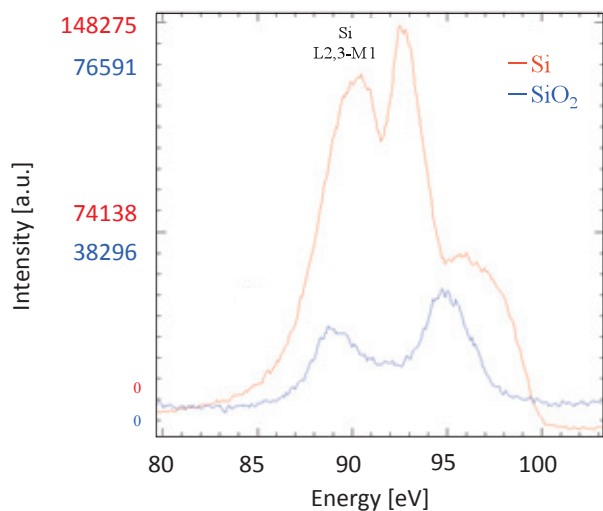
As for the instrumentation, the chromatic aberration is reduced and resolution is improved by using the deceleration method based on the definition formula of resolution according to the instrumentation. We also introduced the latest techniques such as objective lens, FE electron gun and detectors. In addition, it was also shown that the ACL behaves an important role to keep high resolution.

We introduced the high resolution surface observation of mesoporous silica as an observation example with a low accelerating voltage SEM. In this case, we discussed about

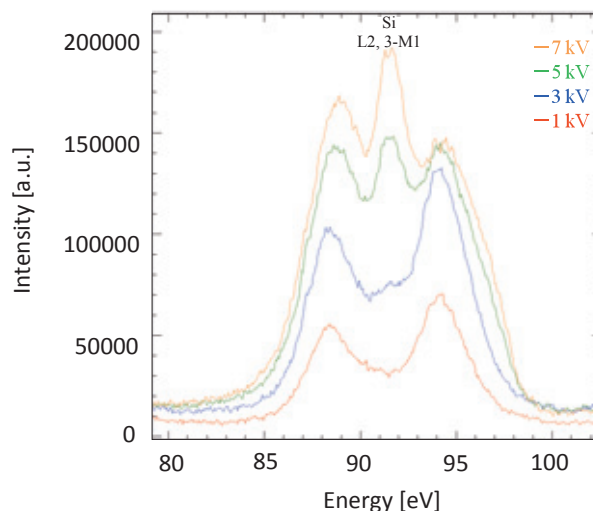
**Fig. 15 Soft X-ray emission spectra of graphite and diamond.**

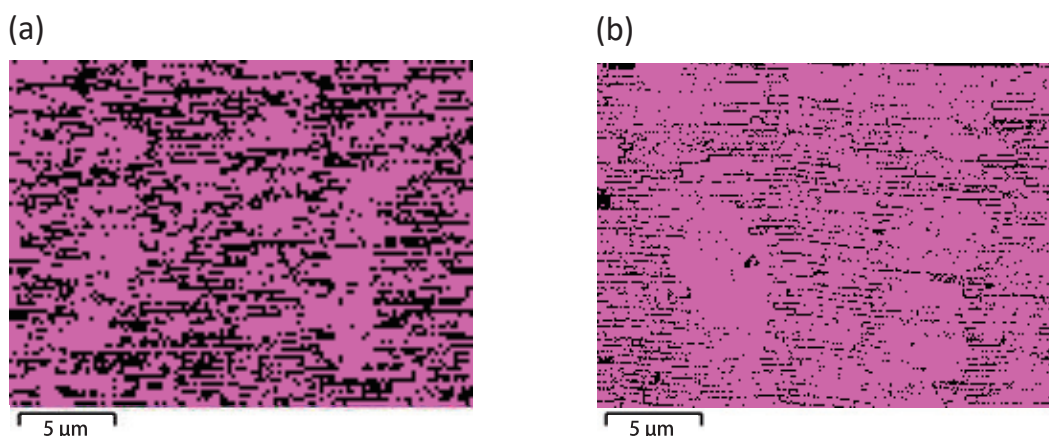


**Fig. 16 Standard soft X-ray emission spectra of Si and SiO<sub>2</sub>.**



**Fig. 17 Soft X-ray emission spectra under incident voltage variations, acquired from SiO<sub>2</sub> film with thickness of 100 nm on Si substrate.**



**Fig. 18**

(a) EBSD phase map of pearl oyster cross section obtained at a high accelerating voltage of 10 kV. Acquisition conditions: the probe current is 2 nA, Number of measurement points is 10,890 points, Step size is 200 nm.  
 (b) EBSD phase map of pearl oyster cross section obtained at a low accelerating voltage of 5 kV. Acquisition conditions: the probe current is 5.7 nA, Number of acquisition points is 43,740 points, Step size is 100 nm.

pretreatment of the sample as well as setting conditions of the instrument to avoid charging. Furthermore, elemental analysis using SXES is possible in combination with SEM, its accelerating voltage being as low as 1 kV or less. We also introduced a surface analysis method with SXES which can analyze the chemical state.

We introduced an example of successfully studying the crystallography of biomineral with reducing damage to the sample by using the EBSD method at low accelerating voltage. Until now, EBSD mapping with high quality in the nacreous layer was considered to be difficult. However, highly-stable FE-SEM JSM-7900F, with an effective combination of the low accelerating voltage EBSD method with a new type of detector and CCP, solved this difficulty. We showed successful results of high-quality EDS map of a nacreous layer.

Based on the above descriptions, the ultra-high resolution FE-SEM JSM-7900F can answer all of users requirements. That supports high resolution imaging at low accelerating voltage and a variety of analyses, such as surface analysis, crystal orientation analysis, elemental analysis, and chemical state analysis. Thus, the innovative JSM-7900F acts as a surface analysis instrument that surpasses the concept of conventional FE-SEM.

## Acknowledgments

In writing this paper, for mesoporous silica to Prof. Osamu Terasaki of ShanghaiTech University, for EBSD to Mr. Hirofumi Morita of Oxford Instruments, for SXES to Dr. Hideyuki Takahashi and Masaru Takakura, for low accelerating voltage technology to Mr. Tetsuro Nagoshi, we were given a deep discussion. We would like to take this opportunity to express my gratitude to everyone concerned.

## References

- [ 1 ] “Scanning Electron Microscopy and X-Ray Microanalysis” J. I. Goldstein, D. E. Newbury, P. Echlin, D. C. Joy, C. E. Lyman, E. Lifshin, L. Sawyer and J. R. Michael, Springer Publishing, Third edition, pp657, p 35, pp297-353, 2007.
- [ 2 ] <https://www.jeol.co.jp/applications/detail/811.html>
- [ 3 ] “Some approaches to low-voltage scanning electron microscopy”, I. Mullerova, M. Lenc, *Ultramicroscopy*, **41**, PP399-410 (1992).
- [ 4 ] “INTRODUCTION TO PLASMA PHYSICS AND CONTROLLED FUSION”, F. F. Chen, Vol.1: Plasma Physics, Plenum Press published, Second Edition, pp19-21, (1984).
- [ 5 ] “Scanning Electron Microscopy –Physics of Image Formation and Microanalysis–”, L. Reimer, Springer Published, Second edition, pp368-370, p173, (1998).
- [ 6 ] “Recent progress in scanning electron microscopy for the characterization of fine structural details of nano materials”, M. Suga, S. Asahina, Y. Sakuda, H. Kazumori, H. Nishiyama, T. Nokuo, V. Alfredsson, T. Kjellman, SM. Stevens, HS. Cho, M. Cho, L. Han, S. Che, MW. Anderson, F. Schuth, H. Deng, OM. Yaghi, Z. Liu, HY. Jeong, A. Stein, K. Sakamoto, R. Ryo, and O. Terasaki, *Progress in Solid State Chemistry*, vol. **42**, no. 1-2, pp. 1-21, 2014.
- [ 7 ] “Development of a sub-eV resolution soft-X-ray spectrometer for a transmission electron microscope”, M. Terauchi, H. Yamamoto and M. Tanaka, *Journal of Electron Microscopy*, **50**(2), pp101-104, (2001).
- [ 8 ] “Direct observation and analysis of york-shell materials using low-voltage high-resolution scanning electron microscopy: Nanometal-particles encapsulated in metal-oxide, carbon, and polymer”, S. Asahina, M. Suga, H. Takahashi, H. Y. Jeong, C. Galeano, F. Schüth, and O. Terasaki, *APL Materials* vol. **2**, p113317, DOI: 10.1063/1.4902435, (2014).
- [ 9 ] “Newly Developed Soft X-ray Emission Spectrometer, SS94000SXES”, M. Takakura, T. Murano, and H. Takahashi, *JEOL News*, vol. **50**, no. 1, July, (2015).
- [ 10 ] Y. Sakuda, S. Asahina, T. Togashi and M. Kurihara, *Kinzoku*, **88**, (11), pp892-897, (2018) in Japanese .
- [ 11 ] “Soft X-ray Depth Chemical State and Quantitative Analysis with Variable Low Incident Voltage”, H. Takahashi, S. Asashina, Y. Yamamoto, Y. Sakuda, M. Takakura, T. Murano, M. Terauchi, Proc. of 72<sup>nd</sup> Annual Meeting of the Japanese Society of Microscopy, vol. **51**, Supplement 1, p131, (2016) in Japanese.

# Development of an Integrated Analysis Method for the JMS-T200GC High Mass-Resolution GC-TOFMS by Electron Ionization and Soft Ionization Methods

Masaaki Ubukata and Yoshihisa Ueda MS Business Unit, JEOL Ltd.

We have developed a new software package with a new workflow for identifying unknown compounds from GC-high resolution MS (GC-HRMS) data. In this newly designed workflow, unknown compounds are determined by correlating the data results obtained by using a hard ionization method such as Electron Ionization (EI) and a soft ionization method such as Field Ionization (FI) with high-resolution mass spectrometry.

The new data reduction software 'msFineAnalysis' was used to identify unknown compounds in the data from pyrolysis/GC-HRMS analysis of vinyl acetate resin. The new workflow implemented in this software improved the accuracy of identification and eliminated misidentification of unknown compounds.

## Introduction

When a sample composed of unknown compounds is analyzed by using GC-MS (gas chromatograph mass spectrometer), the compound peaks separated by the GC are identified by using their corresponding mass spectra. Electron Ionization (EI) is widely used for GC-MS [1] because of the availability of mass spectral databases that contain hundreds of thousands of spectra for compounds that are frequently analyzed by GC-MS. EI mass spectra are typically acquired using the standard ionizing electron energy of 70 eV which produces fragmentation patterns that are directly related to the compound's structure. Additionally, the relative intensity ratios for the fragment peaks are always constant if the ionizing electron energy is kept constant. Consequently, the mass spectrum of the same compound acquired with the same ionization energy, exhibits a reproducible spectral pattern. Mass spectral database searches (commonly called "library searches") utilize this feature of EI for compound identification [2].

While mass spectral library searches are very simple to implement for identifying compounds acquired by GC-MS, this method has the following disadvantages. 1) For compounds having similar structures (in particular for compounds whose elemental compositions of substituents are slightly different from each other), the mass spectra acquired by using EI can be very similar, and therefore, the chemical compounds may not be identified from the library search result. 2) For compounds which are not included in the library search databases (i.e. pyrolyzed products detected by pyrolysis analysis), it is impossible to identify them with a library search. In case 1),

if the molecular ion peaks are found in the mass spectra, it can be possible to determine the elemental composition of the target compound. However, because EI is a high-energy ionization method, the chemical structure of a given compound can fragment extensively, making it difficult, if not impossible, to observe the molecular ions. If a low-resolution mass spectrometer is used for the measurement, even if molecular ions are observed, their mass-to-charge ratios are only reported as integer values. An integer value for the molecular ion  $m/z$  is not sufficient for determining the elemental composition because there are many combinations of elemental masses that can have a specific integer mass. A high-resolution mass spectrometer (HRMS) can provide accurate mass measurements with a precision in the 3<sup>rd</sup> or 4<sup>th</sup> decimal place which in turn allows for more accurate elemental composition assignments. For case 2), identification of chemical compounds that are not present in the databases cannot be obtained by library searches alone so using the HRMS accurate mass information for molecular ions (as well as fragment ions) can help narrow down the possibilities.

In this work, we used the JMS-T200GC AccuTOF™ GCx-plus GC-high resolution time-of-flight MS (GC-HRTOFMS) equipped with both EI and Soft Ionization (SI) to generate molecular ions. We then used the newly developed software application 'msFineAnalysis' to combine the information obtained from the EI library searches with the SI molecular ion accurate mass and isotope analysis to identify the sample components [3, 4]. The details of the msFineAnalysis qualitative analysis work flow will be introduced along with the application of this software to the thermal analysis of resin products.

## Analysis Flow

**Figure 1** shows the qualitative analysis work flow using only library search by the conventional EI method (left) and using the new integrated analysis work flow utilized in the msFineAnalysis software (right). The procedures for the new analysis work flow are as follows:

1. For the data acquired by the EI and SI methods, the peaks in the total ion chromatogram (TIC) are detected to create mass spectra.
2. For the mass spectra acquired by each ionization method, each spectrum is associated with a corresponding chromatographic peak retention time, and then, the mass spectra with the same retention times are assigned as the same component.
3. The EI mass spectra are library searched for matches. ①
4. The SI mass spectra are used to determine the molecular ions for each analyte. ②
5. An accurate mass analysis is done for each of the detected molecular ions. This analysis involves directly comparing the possible elemental composition formulas to the statistically-significant EI library search results from Step 3 in order to narrow down the most likely elemental composition candidates for a given analyte. ③
6. An isotope pattern analysis is conducted to further refine the molecular ion elemental composition candidates. ④
7. Using these possible molecular ion composition formulas as the search constraints, an accurate mass analysis is performed for the fragment ions in the EI mass spectra. If a given molecular ion formula is not correct, then the EI fragment ions will not show good matches and will result in a low EI fragment ion interpretation ratio.
8. The interpretation ratio is used to further refine the molecular-ion formula candidates. ⑤
9. Finally, all of these analysis results are integrated together into a qualitative analysis report for the peaks detected in the sample. ⑥

## Analysis Examples: Pyrolysis data analysis of vinyl acetate resin

### (1) Analytical Condition

A JMS-T200GC equipped with a pyrolyzer was used to measure a commercially-available vinyl acetate resin. A combination EI and Field Ionization (FI) source was used with the system to measure the samples. The measurement conditions for the GC-HRTOFMS and pyrolyzer are listed in **Table 1**. Since an EI/FI combination ion source was used for this work, it was not necessary to exchange sources when switching between the EI and FI methods.

The EI and FI sample measurements were subjected to the new msFineAnalysis work flow. Afterwards, these analysis results were compared to an analysis with only EI library search results to confirm the improved capabilities of this new, innovative analysis work flow.

### (2) Analysis Results

The EI and SI total ion current chromatograms (TICCs) for the resin sample were automatically analyzed by msFineAnalysis using the analysis work flow shown in Fig. 1. In total, 33 components were detected during the sample measurement (**Fig. 2**). Each component was categorized according to the reliability of its identification results. The three classification types are shown as different colors in the report (**Fig. 3**).

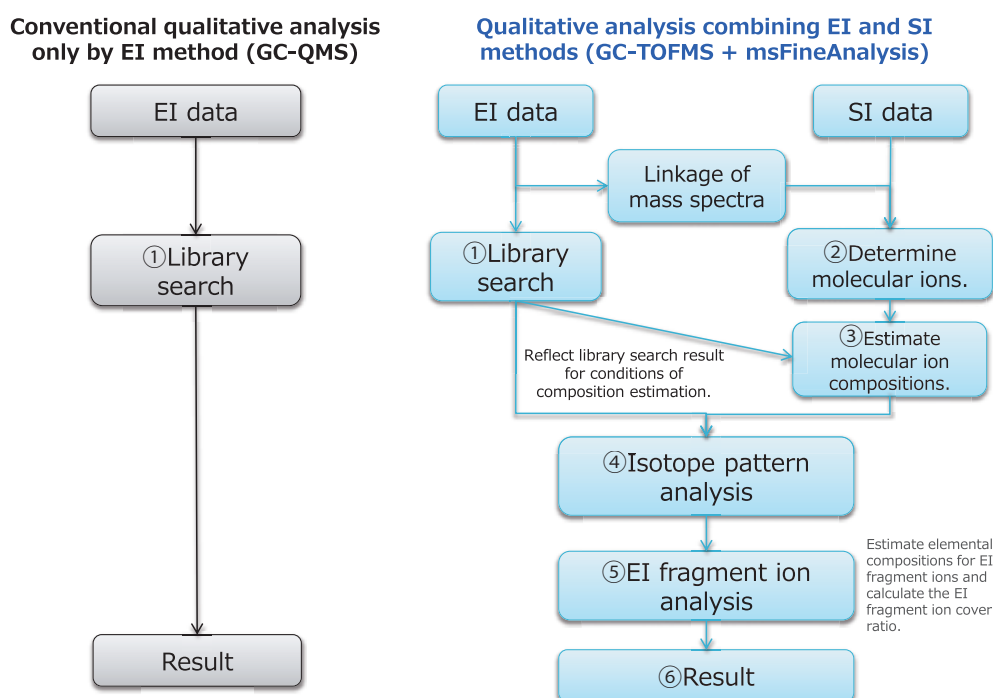
Green: EI search result had high similarity score and matched the identified SI molecular ion. High probability that the analyte has been identified correctly.

Orange: Multiple candidates with significant molecular elemental composition formulas were obtained.

White: No significant molecular composition formula was obtained.

A comparison between the integrated analysis results acquired by msFineAnalysis and the conventional GC/EI analysis

**Fig. 1 Analysis flow comparison with conventional GC-MS qualitative analysis**



results are shown in **Fig. 4**. Conventional EI data analysis only resulted in the high-confidence identification of one-fourth of the components. However, the new msFineAnalysis work flow, which also included molecular ion formula estimation and isotopic analysis, enabled the determination of more than 90% of the components. Furthermore, the new software used the EI fragment ion formulas to obtain additional structural information for the analytes. For the library-registered components (similarity: high), the new analysis method showed highly reliable qualitative analysis results that involved combining the library search results and the molecular composition formulas. Even for unknown components that do not show a good library match (similarity: low) and are thus difficult to identify by using the conventional GC/EI method (left in Fig. 1), msFineAnalysis also estimated the molecular composition formulas obtained with soft ionization. Consequently, the new analysis method, irrespective of high or low similarity, uses the accurate mass

molecular ion information to estimate elemental compositions that can further refine the candidate identification. Furthermore, these results showed that msFineAnalysis provides a very effective work flow for the qualitative analysis of GC-MS data.

To demonstrate the details of the new analysis method, we will present two kinds of identification examples that are typical for qualitative analysis.

### (3) Example 1: Peaks detected at a retention time around 2.49 min

Mass spectra acquired by EI and FI are shown in **Fig. 5**. A library search of the EI mass spectra resulted in several matches. However, all of the matching spectra had similarity scores of less than 700, indicating that there is a low probability that the related peaks correspond to these compounds. On the other hand, the SI mass spectra showed clear peaks at  $m/z$  106.06 and  $m/z$  128.12. The  $m/z$  128.12 (larger  $m/z$ ) was selected as the

**Table 1 Measurement Condition**

[Pyrolysis condition] Pyrolysis Temperature	600 °C
[GC Condition] Column Oven Temperature Injection Mode	DB-5msUI, 15 m × 0.25 mm, 0.25 μm 50 °C (1 min) - 30 °C /min - 330 °C (1.7 min) Split mode (100:1)
[MS condition] Spectrometer Ion Source Ionization	JMS-T200GC (JEOL Ltd.) EI/FI combination ion source EI+ : 70 eV, 300 μA FI+ : -10 kV, 6 mA/10 msec, Carbotec emitter

**Fig. 2 Total Ion current chromatograms for Py-GC/TOFMS analysis of vinyl acetate sample**

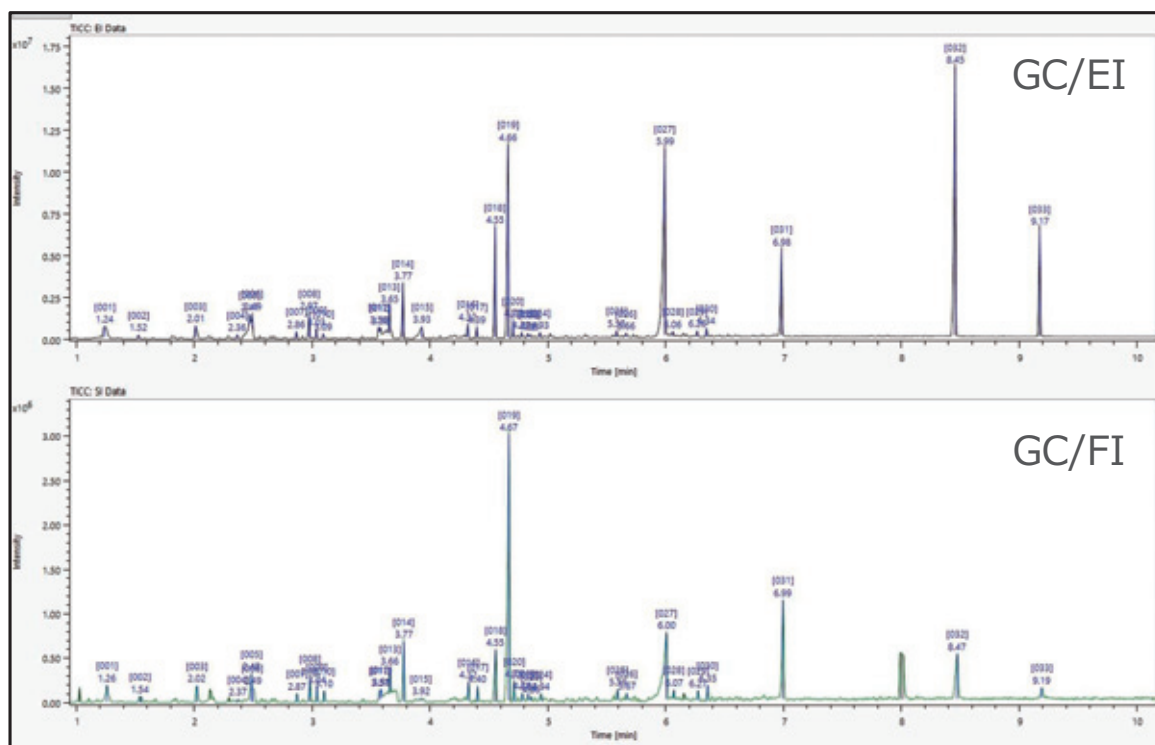


**Fig. 3 Data analysis results of vinyl acetate sample by msFineAnalysis software**

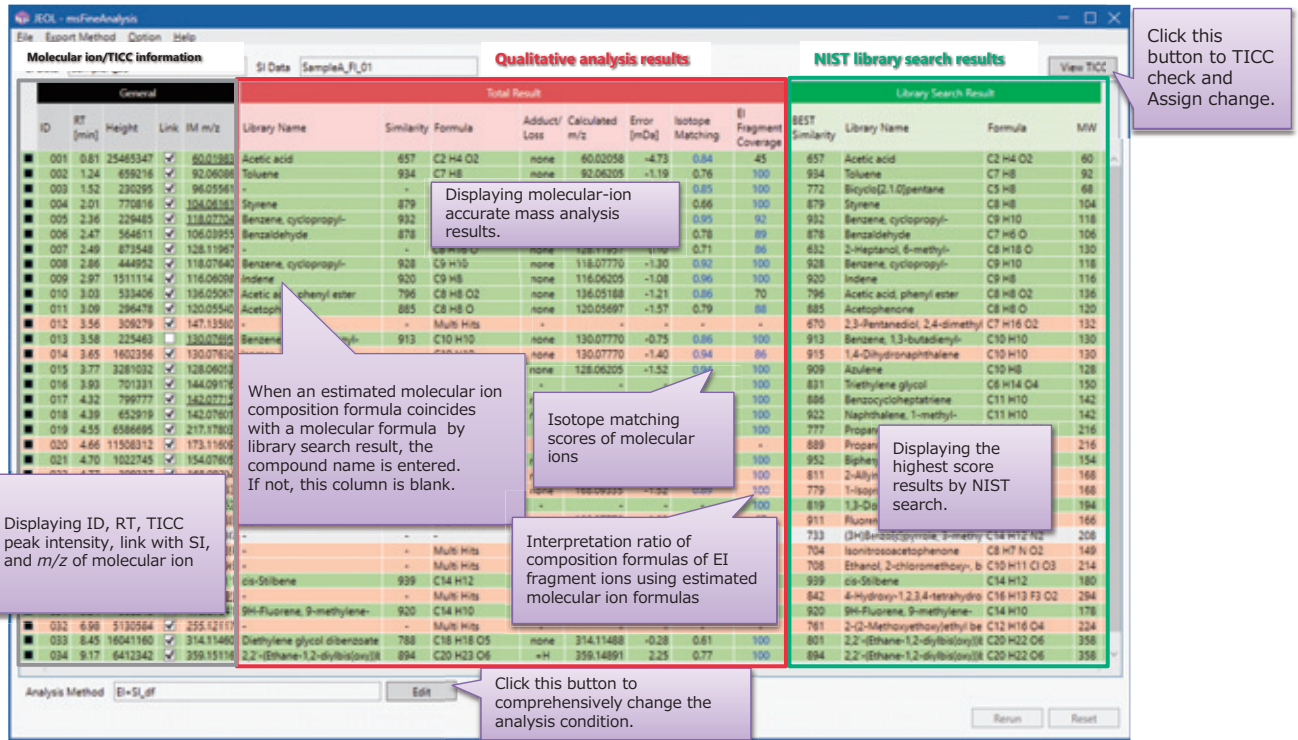
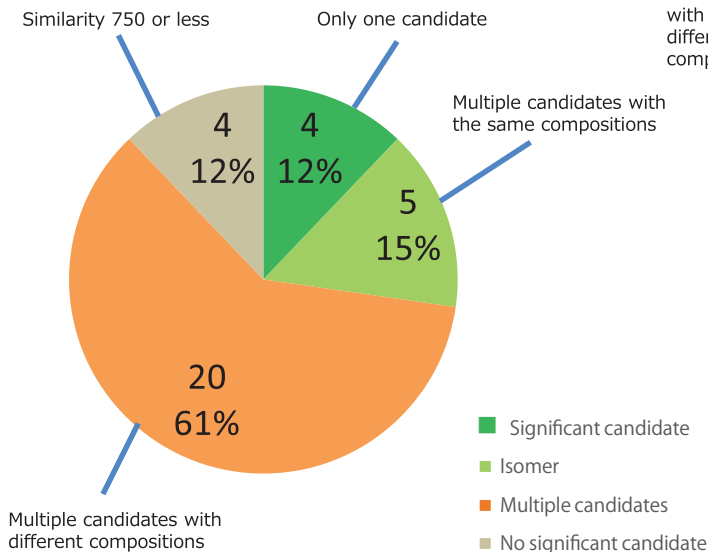
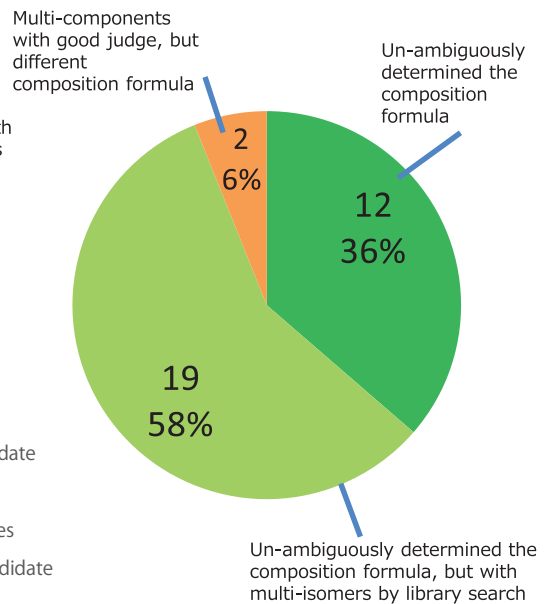


**Fig. 4 Comparison of number of peaks that were identified between conventional data analysis flow and new work flow with msFineAnalysis software**

**Conventional GC-MS qualitative analysis**  
(by NIST library search, similarity threshold : 750)



**Integrated analysis of EI and SI methods**  
(by msFineAnalysis, able/disable to determine composition)



molecular ion peak, and its accurate mass was used to estimate an elemental composition of  $C_8H_{15}O$  (error 0.1 mDa). Next, this composition " $C_8H_{15}O$ " was used as the element limits to estimate the fragment ion formulas in the EI mass spectrum. The results showed that 6 out of the 7 higher intensity peaks were likely a product of the " $C_8H_{16}O$ " elemental composition. These results also suggested that 1 of the 7 peaks may not be a peak derived from  $C_8H_{16}O$ . To explore this possibility, extracted ion current chromatograms (EICC) for both peak types ( $C_8H_{16}O$ : $m/z$  55.05, 97.10 and non- $C_8H_{16}O$ : $m/z$  75.04) were created, and the results showed that there was a clear difference in the chromatographic peak shapes/times in each chromatogram (Fig. 6). These results suggested that ion peaks produced by different chemical species were co-eluting at a retention time of  $\sim 2.49$  min. To test this hypothesis, a library search was conducted using only a mass spectrum produced from the latter part of the peak at 2.49 min, so as to exclude as much as possible the contribution from the co-eluted components. The search came up with "3-Penten-1-ol, 2,2,4-trimethyl- :  $C_8H_{16}O$ " with a similarity of over 800. Furthermore, the composition for this compound exactly matched the initially-estimated elemental composition of  $C_8H_{16}O$ .

The peak at 2.49 min analyzed by using the conventional GC/EI method (only library search of the EI mass spectra) did not provide enough information to narrow down the candidate compounds. However, the msFineAnalysis work flow using the combined EI and FI mass spectral information resulted in a single, strongly supported candidate "3-Penten-1-ol, 2,2,4-trimethyl-".

#### (4) Example 2: Peaks detected at a retention time around 8.15 min

Mass spectra acquired by EI and FI are shown in Fig. 7. A library search of the EI mass spectrum revealed one compound with a similarity of 801 (2,2'-(Ethane-1,2-diylbis(oxy)) bis(ethane-2,1-diyl) dibenzoate) along with 7 other compounds

with similarities of more than 750 (shown on Table 2). Consequently, it was difficult to make an unambiguous identification using only the library search results. The SI mass spectra showed a clear peak appearing at  $m/z$  315.12, suggesting that this peak is likely to be the molecular ion. Table 3 shows the possible elemental composition formulas calculated using the accurate mass of this peak. All four compositions had calculated values that were within 3 mDa of the measured value. Next, a comparison of Table 2 and Table 3 showed that "Diethylene glycol dibenzoate" (similarity of 788) had an elemental composition that matched  $C_{18}H_{18}O_5$ . Next, this composition " $C_{18}H_{18}O_5$ " was used as the element limits to estimate the fragment ion formulas for 5 high intensity peaks in the EI mass spectrum. All of the peaks produced elemental compositions (errors less than 3 mDa) consistent this compound (Table 4). These results all strongly support "Diethylene glycol dibenzoate" as the peak detected at retention time  $\sim 8.45$  min.

As described above, the peak detected at a retention time around 8.45 min was difficult to identify through an EI library search result alone, as there were a number of possible candidates with close similarity matches. However, the msFineAnalysis software, with its ability to combine EI and SI data analysis, resulted in a single, strongly supported candidate "Diethylene glycol dibenzoate".

## Summary

For the analysis of unknown compounds using GC-TOFMS with high-mass resolution, a new analytical work flow was devised that combined conventional EI library search, molecular ion elemental compositions acquired using a SI method (FI for this work), and the EI fragment ion accurate mass information to identify the targeted chemical species. This innovative analysis work flow led to the development of the new GC-HRMS analysis software msFineAnalysis.

Fig. 5 Mass spectra at around retention time 2.49 min measured by EI and FI

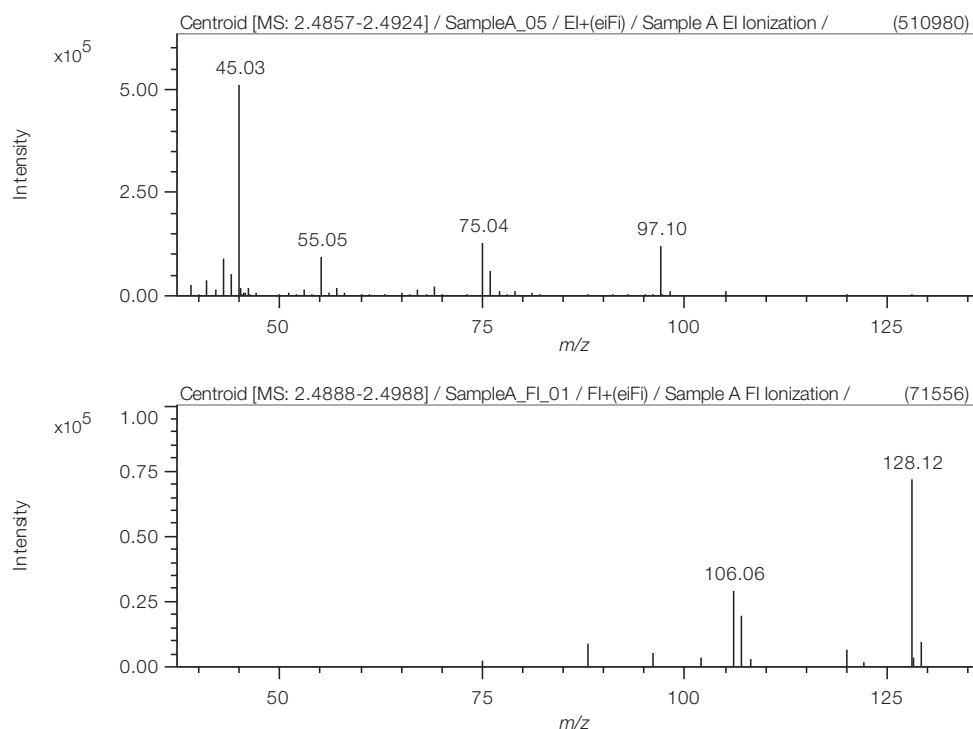


**Fig. 6 TICC and EICC at around retention time 2.49 min**

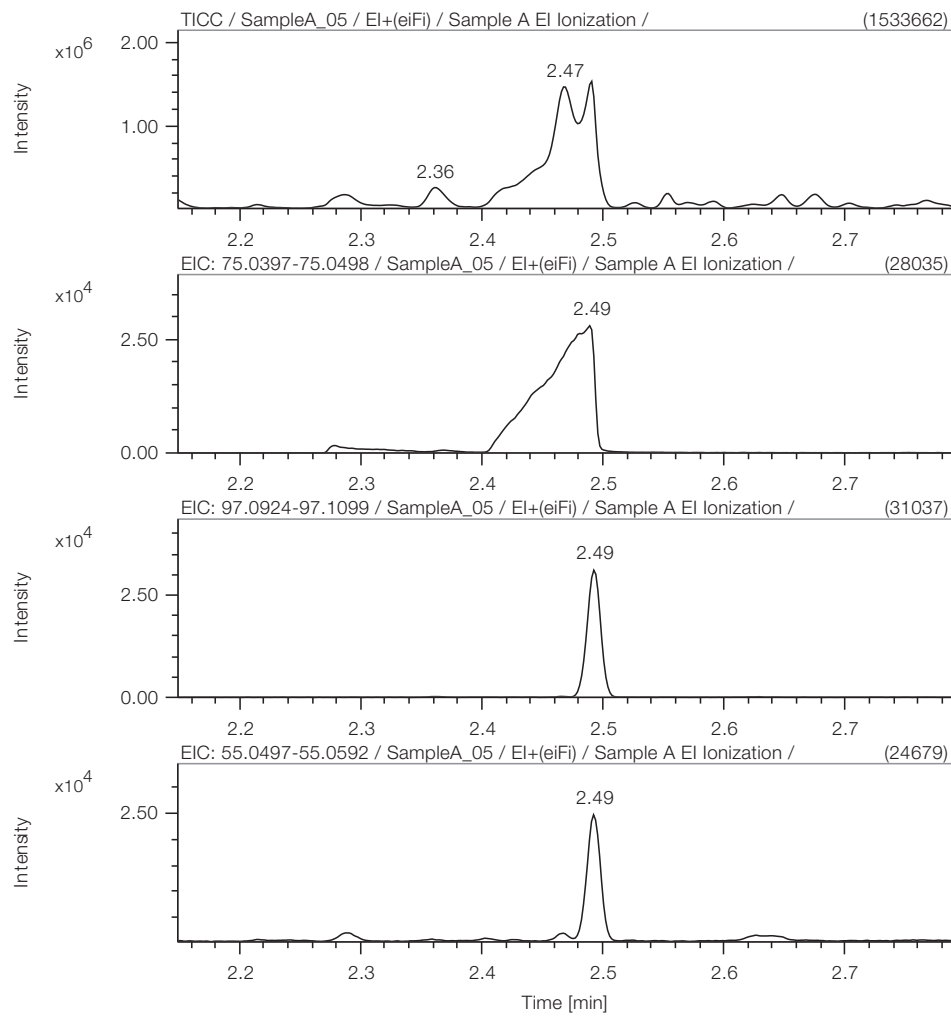


**Fig. 7 Mass spectra at around retention time 8.45 min measured by EI and FI**

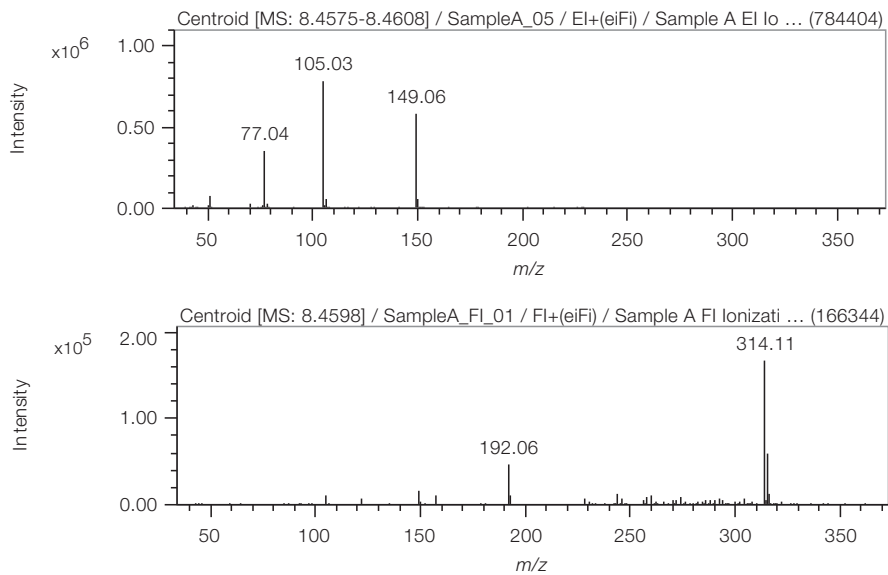


**Table 2 Results of library search for the mass spectrum of peak at 8.45 min retention time**

No	Compound Name	Similarity	Formula
1	2, 2'-(Ethane-1, 2-diylbis(oxy))bis(ethane-2, 1-diyl) dibenzoate	801	C <sub>20</sub> H <sub>22</sub> O <sub>6</sub>
2	Diethylene glycol dibenzoate	788	C <sub>18</sub> H <sub>18</sub> O <sub>5</sub>
3	1, 3-Dioxolane, 2-(methoxymethyl)-2-phenyl-	787	C <sub>11</sub> H <sub>14</sub> O <sub>3</sub>
4	Benzoic acid, 2-(3-nitrophenyl)ethyl ester	778	C <sub>15</sub> H <sub>13</sub> NO <sub>4</sub>
5	Benzoic acid, 2-(4-nitrophenoxy)ethyl ester	776	C <sub>16</sub> H <sub>13</sub> NO <sub>5</sub>
6	3, 6, 9, 12-Tetraoxatetradecane-1, 14-diyl dibenzoate	764	C <sub>24</sub> H <sub>30</sub> O <sub>8</sub>
7	Ethanol, 2-(4-phenoxyphenoxy)-, benzoate	752	C <sub>21</sub> H <sub>18</sub> O <sub>4</sub>
8	1, 3-Dioxolane, 2-phenyl-2-(phenylmethyl)-	750	C <sub>16</sub> H <sub>16</sub> O <sub>2</sub>
9	Benzoic acid, 2-(2-chlorophenoxy)ethyl ester	730	C <sub>15</sub> H <sub>13</sub> ClO <sub>3</sub>
10	3, 4-Pyridinedicarboxylic anhydride	703	C <sub>7</sub> H <sub>3</sub> NO <sub>3</sub>

**Table 3 Results of estimation of elemental composition for the MS peak of 314.11462**

Formula	Calculated <i>m/z</i>	Error/mDa
C <sub>18</sub> H <sub>18</sub> O <sub>5</sub>	314.11488	-0.26
C <sub>16</sub> H <sub>16</sub> N <sub>3</sub> O <sub>4</sub>	314.11353	1.09
C <sub>19</sub> H <sub>14</sub> N <sub>4</sub> O	314.11621	-1.59
C <sub>21</sub> H <sub>16</sub> NO <sub>2</sub>	314.11756	-2.94
C <sub>13</sub> H <sub>18</sub> N <sub>2</sub> O <sub>7</sub>	314.11085	3.77

**Table 4 The results of estimation of elemental compositions for the peaks in mass spectrum at 8.45 min peak**

<i>m/z</i> of peak	Formula	Error/mDa
51.02244	C <sub>4</sub> H <sub>3</sub>	-0.48
77.03809	C <sub>6</sub> H <sub>5</sub>	-0.49
105.03439	H <sub>7</sub> H <sub>5</sub> O	0.9
105.08898	C <sub>5</sub> H <sub>13</sub> O <sub>2</sub>	-2.02
149.05995	C <sub>9</sub> H <sub>9</sub> O <sub>2</sub>	0.25

Using this software for library-registered compounds (similarity: high), it is possible to provide highly reliable qualitative analysis results that combine the EI library search results with the SI molecular ion elemental composition results. Furthermore, the msFineAnalysis software made it possible to estimate the molecular ion elemental composition as well as the fragment ion elemental compositions for unknown compounds that do not show a good library match (similarity: low). These results provided a stronger foundation for identifying unknowns than using the conventional EI with library search method alone.

Irrespective of high or low similarity, the new analysis method enables the estimation of molecular composition formulas and to refine candidates for identification. Thus, msFineAnalysis is very effective for qualitative analysis of GC-HRMS (JMS-T200GC) data.

## References

- [1] Gohlke, R. S.; McLafferty, F.W. Early Gas Chromatography/Mass Spectrometry. *J. Am. Chem. Soc. Mass Spectrom.* 1993, **4**, 367-371.
- [2] Stein, S. E.; Ausloos, P.; Lias, S.G. Comparative Evaluations of Mass Spectral Databases. *J. Am. Chem. Soc. Mass Spectrom.* 1991, **2**, 432-437.
- [3] Ubukata, M.; Basics of Mass Spectrometry 2016 -Analysis of Unknown Compounds-, JEOL MS Users Meeting (2016) (in Japanese).
- [4] Ubukata, M.; Introduction of a New Product "JMS-T200GC AccuTOF™ GCx-plus" -Applications of Qualitative Analysis Software "msFineAnalysis", JEOL MS Users Meeting (2018) (in Japanese).

# Development of a Gas Chromatograph Triple Quadrupole Mass Spectrometer JMS-TQ4000GC

Kiyotaka Konuma MS Business Unit, JEOL Ltd.

The triple quadrupole Mass Spectrometer (MS) means a MS that locates two quadrupoles in tandem and places a collision cell (ion guide built-in) to perform ion cleavage between the two quadrupoles. The Gas Chromatograph (GC) triple Quadrupole MS (QMS), which is a combination of GC and triple QMS, features high sensitivity detection derived from high ion selectivity and is used recently for high-sensitivity quantitative analysis of trace components in the complex matrixes. JEOL has developed a new GC Triple QMS, JMS-TQ4000GC achieving high-speed and high-sensitivity detection by incorporating JEOL's unique short collision cell technology. The hardware, software and applications of the JMS-TQ4000GC are introduced in this article.

## Introduction

Recent increasing attention for challenges on food quality has triggered the fact that general people have been placing higher focuses on "food safety." The past monitoring results implemented by the Japanese government [1] indicated that the main factors for anxiety of people from the viewpoint of food safety are food additives and pesticides. Ministry of Health, Labor and Welfare, Japan, introduced the Positive List system in 2006 [2]. This list basically prohibited the sales of foods containing residual agricultural chemicals covering pesticides, food additives and animal drugs, whose volumes exceed the defined criterion according to the revision of Food Sanitation Law in 2003, Japan. In the Positive List system, not only for 283 kinds of the pesticides, additives and drugs whose residual criterion are defined (to be 0.01 ppm) in the Food Sanitation Law, but also for the other pesticides that are used in and outside Japan are subjected to the residual criterion of 0.01 ppm. Consequently, about 800 kinds of pesticides were subjected to the restriction of the residual criterion. Along with the implementation of the Positive List system, the kinds of pesticides that must conventionally be analyzed had dramatically extended, but analyzing them has been not easy. The reason why the analysis of the pesticide residues is challengeable is that instruments and methodology enabling high-sensitivity detection of these diversified pesticide compounds in the complex matrixes are strongly required. The QuEChERS method [3-5], which is generally used as a pre-treatment technique of measurement samples for this purpose, provides simple and fast operation. But in this method, a number of matrixes derived from samples remain in a sample extraction solution. In order to exclude these matrixes, if a complicated sample pre-treatment technique is used, the pesticides to be analyzed may have possibility to be removed. Therefore, this disadvantage leads to the needs of an advanced MS that can detect trace components of pesticides from the sample extraction solution even if the solution contains

many residual matrixes. To meet such a request, a newly-developed GC Triple QMS, JMS-TQ4000GC, incorporates a unique patented-technology of "short collision cell" for enabling ion accumulation and instantaneous ejection of all the accumulated ions, and thus accomplishes a compromise of high-speed analysis and high-sensitivity analysis (**Fig. 1**). This article introduces the overview of new technologies, "short collision cell" as well as other techniques, and applications of the JMS-TQ4000GC to the analysis of pesticide residues in foods.

## Experiments, Results and Discussion

### Features of hardware

#### Overview of "short collision cell"

The overview of the short collision cell is illustrated in **Fig. 2**. This innovative short collision cell adopts a set of quadrupoles with an extremely short total length of 15 mm, compared with an ion-guide used for a conventional collision cell. This feature dramatically shortens the ion ejection time from the collision cell, for compromising high-speed SRM (selected reaction monitoring) analysis and avoiding the interfering ions (cross-

**Fig. 1 JMS-TQ4000GC**



talk). Also, continuous ion accumulation and instantaneous ejection of the accumulated ions within the collision cell makes the ions into pulses, and data acquisition only for the time of ejection of these ion pulses leads to accomplishment of noise reduction and enhanced detection sensitivity. Such a unique “short collision cell” technology is patented (patent No.: US8692191, EP2469578, US8604420).

### Ion accumulation

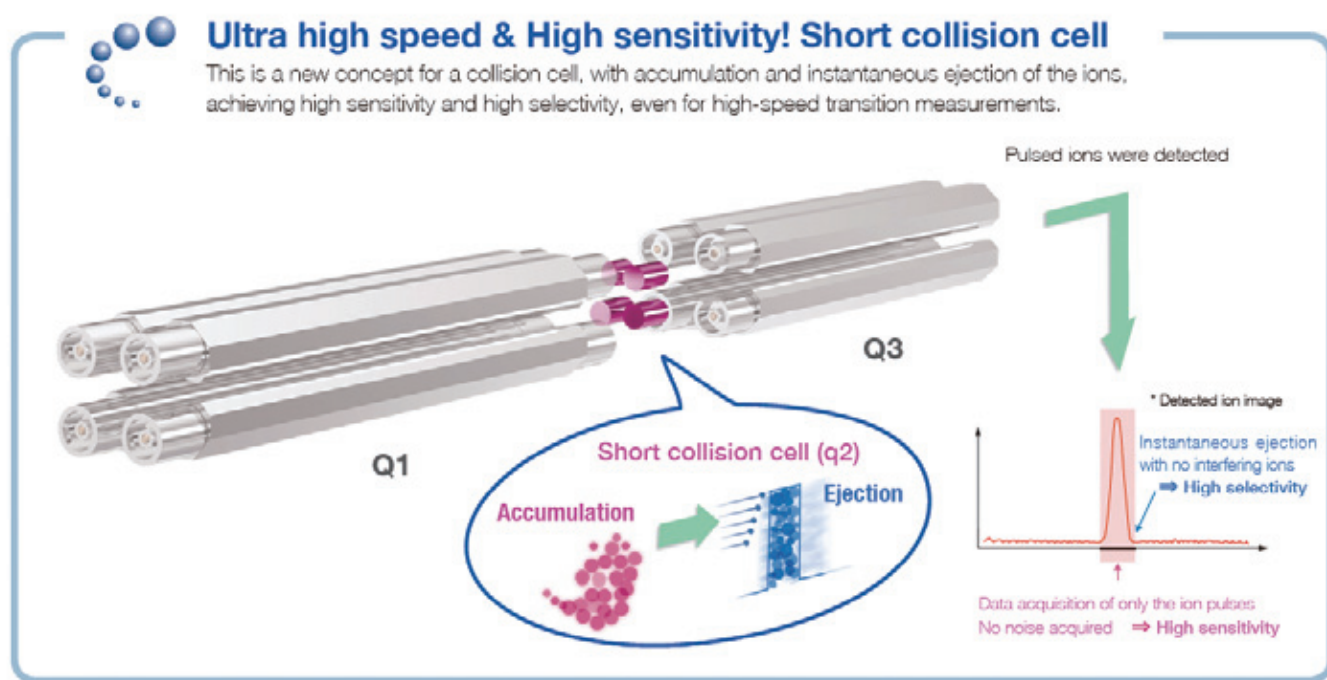
For ion accumulation within the collision cell, the short accumulation mode (High Speed mode) and the long accumulation mode (High Sensitivity mode) are selectable. In the case of the short accumulation time, the noise elimination time is also shortened and thus, high sensitivity SRM measurement up to 1,000 channels per second is possible although sensitivity enhancement is small. When the accumulation time is long (High

Sensitivity mode), the speed of SRM measurement is limited to 100 channels per second at the maximum, but the noise elimination time also becomes long, thus greatly enhancing the sensitivity (Fig. 3).

The High Speed mode is suitable for analyses focused on throughout, such as screening analysis of multi-components and multi-samples. In this article, the result of Fast GC analysis of pesticide residues in foods will be described later, as an example of the High Speed mode.

On the other hand, the High Sensitivity mode is suitable for analysis focused on detection sensitivity and the accuracy of quantification. Especially, this mode is effective for accurate quantitative analysis with the number of components being narrowed down after the screening. In this article, the result of comprehensive analysis of 266 components of pesticide residues in foods under the general acquisition condition will be

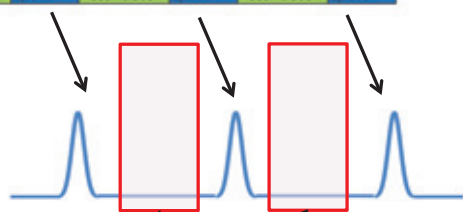
**Fig. 2 Overview of short collision cell**



(Patents : JP5296505, US8692191, EP2469578, US8604420)

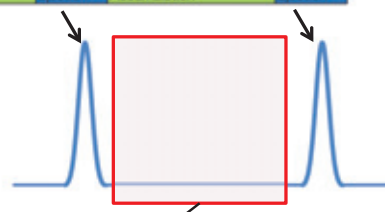
**Fig. 3 Overview of Ion accumulation**

● With a short accumulation time (High speed mode)



Enhancement of sensitivity is limited with a short time for the noise elimination

● With a long accumulation time (High sensitivity mode)



Enhancement of sensitivity is significant with a long time for the noise elimination

described later, as an example of the High Sensitivity mode.

#### Instrument detection limit (IDL)

The data of IDL in the SRM measurement (High Sensitivity mode) is shown in Fig. 4. The standard solution that contains 2 fg OFN (Octafluoronaphthalene) was measured for 8 times repeatedly to estimate IDL value. As a result, a good result of “IDL = 0.32 fg” was obtained.

#### Support functions by the software

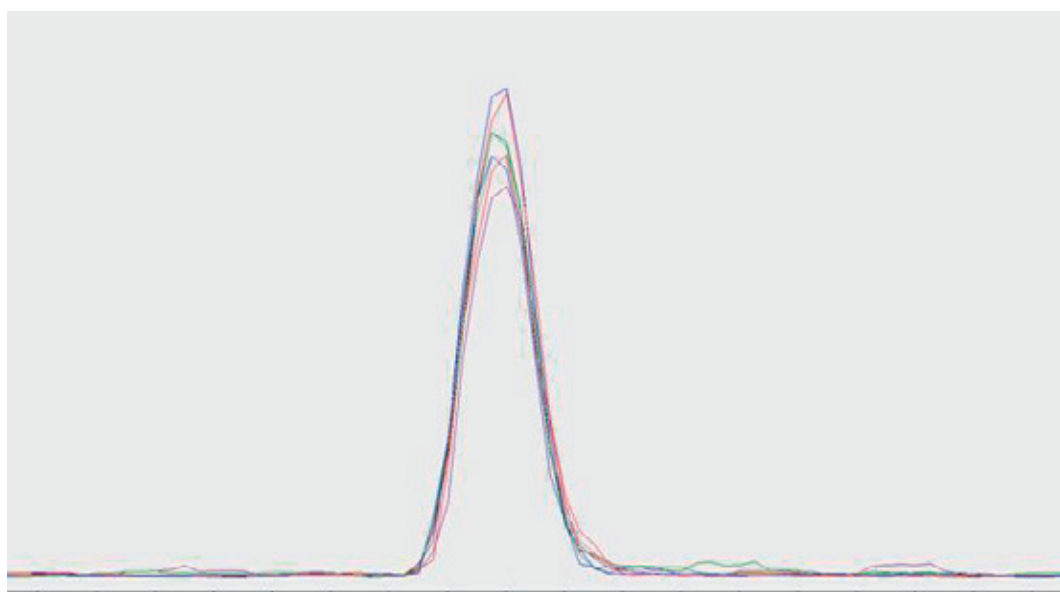
##### SRM Compound Data File

In the case of the comprehensive analysis of pesticides, many

items should be specified for each compound and thus, creation of new acquisition conditions requires a long time. The JMS-TQ4000GC comes with “SRM Compound Data File” in which various parameters of transition, collision energy (CE), etc., for SRM measurement are listed (Fig. 5). From the data files, a compound to be measured can be selected. Then, the SRM measurement condition, together with quantitative analysis conditions, can be created. At present, “SRM Compound Data File” incorporates more than 300 kinds of data files for pesticide components, as standard in the analysis of pesticide residues in foods by GC-MS. In the future, extension of the data files will be continued.

**Fig. 4 IDL with high sensitivity mode**

● OFN 2 fg, IDL=0.32 fg (n=8)



Average	Standard deviation	CV%	IDL [fg]
7290	388	5.32	0.32

**Fig. 5 SRM Compound Data File**

Compound Name	R.T. [min]	Type	Precursor <i>m/z</i>	Product <i>m/z</i>	CE [eV]	I/Q
Acetochlor	17.21	Qnt	146	131	15	1
		Ref.1	223	132	25	0.61
		Ref.2	146	130	25	0.89
Acrinathrin	23.47	Qnt	208	181	10	1
		Ref.1	181	152	20	0.92
		Ref.2	208	180	10	0.17
Aldrin	18.35	Qnt	263	193	25	1
		Ref.1	263	228	25	0.93
		Ref.2	293	222	25	0.5
Allethrin 1	18.93	Qnt	123	81	5	1
		Ref.1	123	95	10	0.51
		Ref.2	136	108	10	0.45

### Automatic creation of the SRM measurement condition

As the software of the JMS-TQ4000GC has an automatic creation function for SRM measurement condition, the user can easily reduce the time when creating the SRM measurement condition.

After the pesticide compound is selected from the aforementioned SRM Compound Data File, by simply selecting “Conventional SRM” that performs ordinary grouping or “p.d.SRM” that allocates the acquisition time for each channel, the SRM measurement condition is automatically created.

In the case of the comprehensive analysis of pesticides, a great number of components (more than several hundreds) should be measured at one time and thus, Conventional SRM may make the per-channel integration time insufficient, leading to degraded sensitivity. To the contrary, “p.d.SRM” enables allocation of the acquisition time for the respective channels depending on the peak elution times and thus, there arises no useless acquisition time, making it possible to avoid sensitivity degradation. The overview of Conventional SRM (ordinary grouping) and “p.d.SRM” is shown in Fig. 6.

### SRM optimization tool

If the operator intends to measure a new compound which is not included in the SRM Compound Data File, the SRM optimization tool is very effective. Using a single-scan result of the intended new compound, the scan method for the product ion can be automatically created and from this result, various parameters of transition and CE which are optimum for the SRM measurement of the intended compound, can automatically be detected. An example of actual SRM optimization is shown in Fig. 7. It is noted that the JMS-TQ4000GC also comes with this SRM optimization tool as standard configuration.

### Applications of JMS-TQ4000GC to analysis of residual pesticides in foods

#### Validity evaluation

In order to verify that a testing method is highly reliable for the analysis of pesticide residues in foods, it is needed to perform validity evaluation. Here, we show the validity evaluation result according to “Guideline for validity evaluation of testing methods on pesticide

residues in food”[6]. To be precise, we calculated the repeatability and intermediate precision from the quantitative analysis result of 266 components of pesticides for validity evaluation.

A sample used for measurement was a spinach extraction sample using the QuEChERS method. The pesticide standards were spiked at 0.01 ppm concentration into the sample solution extracted by QuEChERS. This spiked solution was applied for validity evaluation. The spiked solution was measured once a day (two parallel measurements). And the measurement was repeated for 5 days as branching test.

The repeatability and intermediate precision that were calculated from an obtained quantification result are shown in Fig. 8. Among 266 components of pesticides, as many as 263 components (99%) satisfied the repeatability standard of the Guideline; RSD within 25%. Also, 259 components (97%) satisfied the intermediate precision standard; RSD within 30%. This result confirmed that the quantification values acquired using the JMS-TQ4000GC has sufficient validity for high applicability to the analysis of pesticide residues in foods.

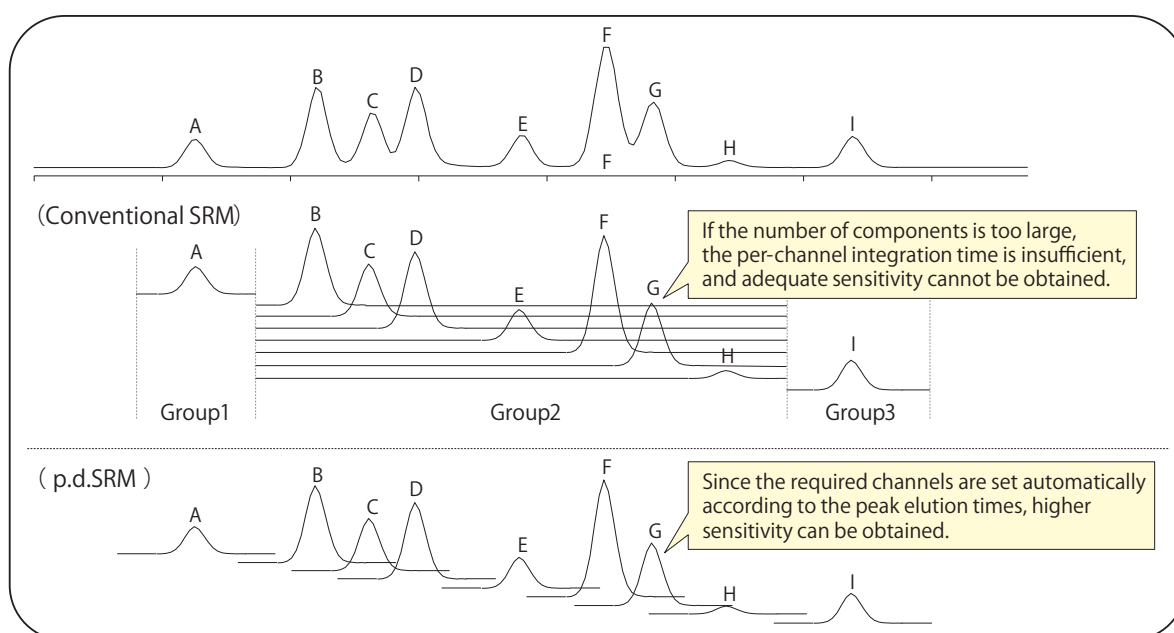
### Linearity of calibration curves

Standard mixture solutions containing 150 pesticides at several concentration range (from 0.001 ppm to 0.1 ppm) were measured to approve the linearity as calibration curve. The results for these measurements were summarized in Fig. 9. Even for a low-concentration sample of 0.001 ppm, it was possible to detect the compounds with sufficient sensitivity and thus, the correlation coefficient of the calibration curves created from the concentration range of 0.001 ppm to 0.1 ppm showed a good result, better than 0.999 for 144 compounds in 150 compounds as total. This result confirmed that the JMS-TQ4000GC is capable of accomplishing high linearity of calibration curves in the concentration range used normally for the analysis of pesticides in foods.

### Long-term stability

When performing the analysis of pesticides in foods, contamination of the ion source due to sample matrixes may cause sensitivity degradation. In this study, the spiked sample

Fig. 6 Overview of p.d. SRM



solution that was prepared by spiking the 266 pesticides standard at 0.01 ppm concentration into the sample solution extracted from spinach sample by QuEChERS were also used to evaluate the long-term stability. This spiked solution was measured 50 times sequentially.

Suitable pesticides were selected depending on their retention time from the earliest retention time to the latest one with 30 seconds interval, and their peak area variation were shown in Fig.10. The coefficient of variation (CV [%]) of peak areas for those 29 pesticides was within 5% and this result demonstrated a good reproducibility as long-term stability.

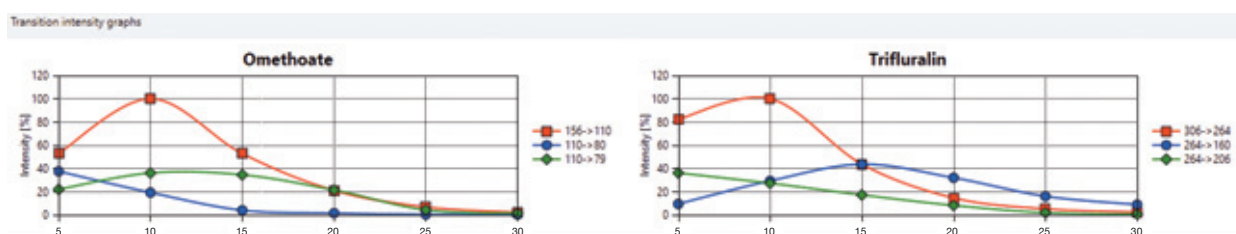
**Application to Fast GC condition**

High Speed mode (with short accumulation time) was adopted to apply the comprehensive analysis of 266 components of

pesticides to Fast GC condition. The analysis result is shown in Fig. 11. When implementing measurement under the conventional GC-MS condition according to the Guideline of the Japanese Ministry of Health, Labor and Welfare, the total acquisition time is about 40 min. But, the use of the Fast GC condition enabled the total acquisition time to be reduced to about 15 min. For screening analysis as well, analysis throughout is emphasized and thus, the concentration detection of 0.01 ppm (standard sample criterion) is considered to be essential. Taking this into account, a standard sample with concentration of 0.01 ppm was repeatedly measured and the sensitivity and reproducibility were confirmed. This result is shown in Fig. 12. For the standard sample with 0.01 ppm as well, it was confirmed that the JMS-TQ4000GC provides good shapes of chromatograms and high reproducibility.

**Fig. 7 Overview of SRM optimization tool**

● Optimized result can be confirmed by the graph of CE and Intensity of each transition



Sel.	Compound name	R.T. [min]	Type	Precursor m/z	Product m/z	CE [eV]	I/Q
<input checked="" type="checkbox"/>	Omethoate	9.93	Target	156	110	10	1
			Ref.1	110	80	5	0.37
			Ref.2	110	79	10	0.36
<input checked="" type="checkbox"/>	Trifluralin	10.63	Target	306	264	10	1
			Ref.1	264	160	15	0.43
			Ref.2	264	206	5	0.36
<input checked="" type="checkbox"/>	Dimethoate	11.4	Target	125	79	10	1
			Ref.1	229	87	10	0.46

Each parameter can be re-edited

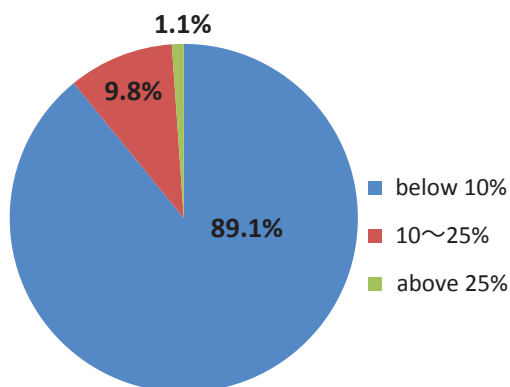
Register button

Register to the SRM compound data file

**Fig. 8 Calculation results of Repeatability and Intermediate Precision**

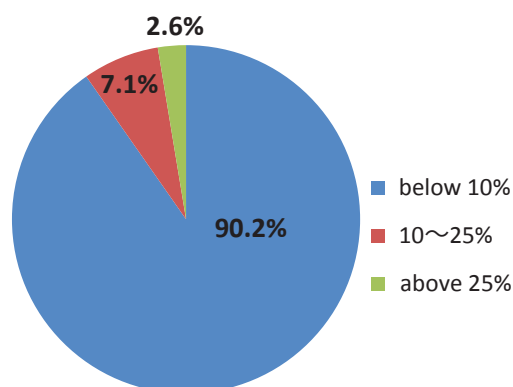
**Repeatability**

(266 components, 10ppb)



**Intermediate Precision**

(266 components, 10ppb)



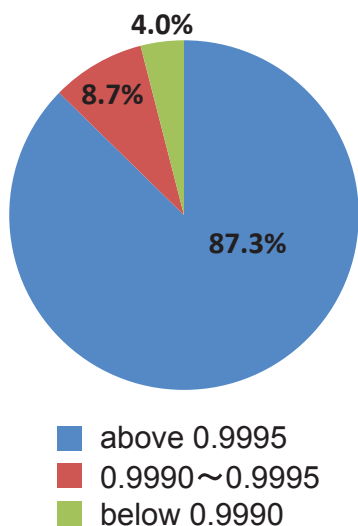
## Conclusion

We have developed a new Gas Chromatograph (GC) Triple Quadrupole Mass Spectrometer (QMS), JMS-TQ4000GC, which incorporates JEOL's unique short collision cell. Owing to this innovative "short collision cell" technology, the JMS-

TQ4000GC achieves high-speed and high-sensitivity detection. This GC Triple QMS, JMS-TQ4000GC allows for detection of trace components of pesticides in the complex matrices with high sensitivity. Thus, this mass spectrometer exhibits its sufficiently-high potential for the analysis of pesticide residues in foods, which has generally been difficult using mass

**Fig. 9 Linearity of calibration curves**

Distribution of correlation coefficients



Calibration curves and EIC of pesticides with 1ppb

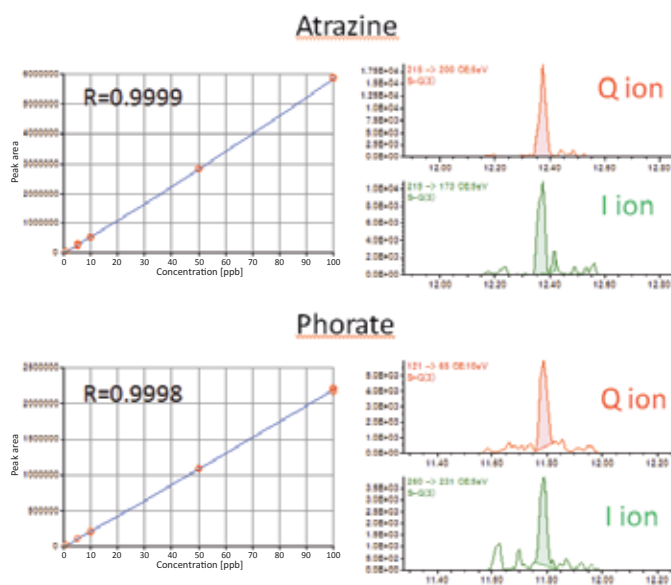
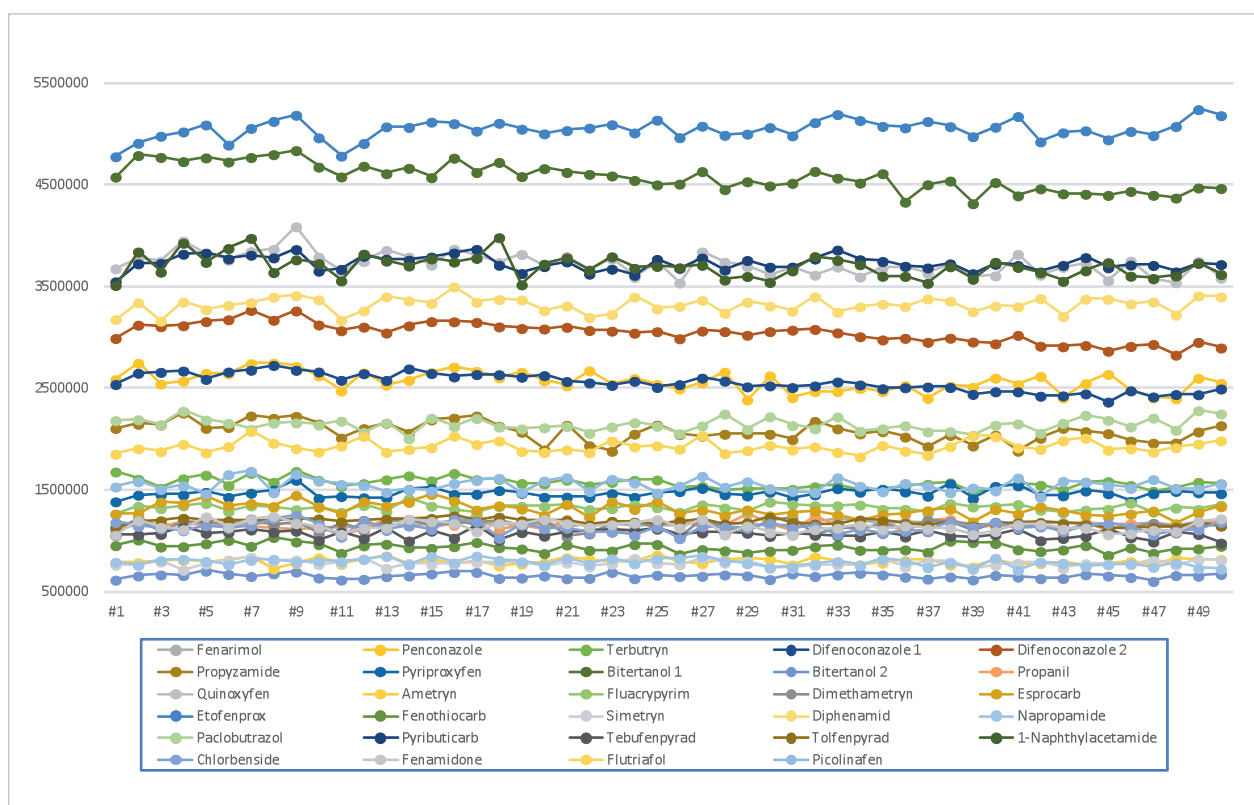


**Fig. 10 Reproducibility of the peak area**



spectrometers. Furthermore, the JMS-TQ4000GC has a wealth of support functions based on software technology, thus suitable for the users to analyze new kinds of compounds. We plan to enhance the performance and the software functionality of the JMS-TQ4000GC continually in the future.

**References**

- [ 1 ] Food Safety Commission of Japan website (in Japanese), [http://www.fsc.go.jp/monitor/monitor\\_report.html](http://www.fsc.go.jp/monitor/monitor_report.html)
- [ 2 ] Ministry of Health, Labor and Welfare website (in Japanese), [https://www.mhlw.go.jp/stf/seisakunitsuite/bunya/kenkou\\_iryuu/shokuhin/zanryu/index.html](https://www.mhlw.go.jp/stf/seisakunitsuite/bunya/kenkou_iryuu/shokuhin/zanryu/index.html)
- [ 3 ] Fast and Easy Multiresidue Method Employing Acetonitrile Extraction/Partitioning and “Dispersible Solid-Phase Extraction” for the Determination of Pesticide Residues in Produce, M. Anastassiades, et al., *J. AOAC Int.* **86**, No.2, 412-431(2003).
- [ 4 ] European standard EN 15662, Foods of Plant Origin-Determination of Pesticide Residues Using GC-MS and/or LC-MS/MS Following Acetonitrile Extraction/ Partitioning and Clean up by Dispersive SPE-QuEChERS method (2008).
- [ 5 ] AOAC Official Method, Pesticide Residues in Foods by Acetonitrile Extraction and Partitioning with Magnesium Sulfate (2007).
- [ 6 ] Ministry of Health, Labor and Welfare website (in Japanese), <https://www.mhlw.go.jp/topics/bukyoku/iyaku/syoku-anzen/zanryu3/dl/101224-1.pdf>

**Fig. 11 Analysis result of pesticides (266 components) with Fast GC condition**

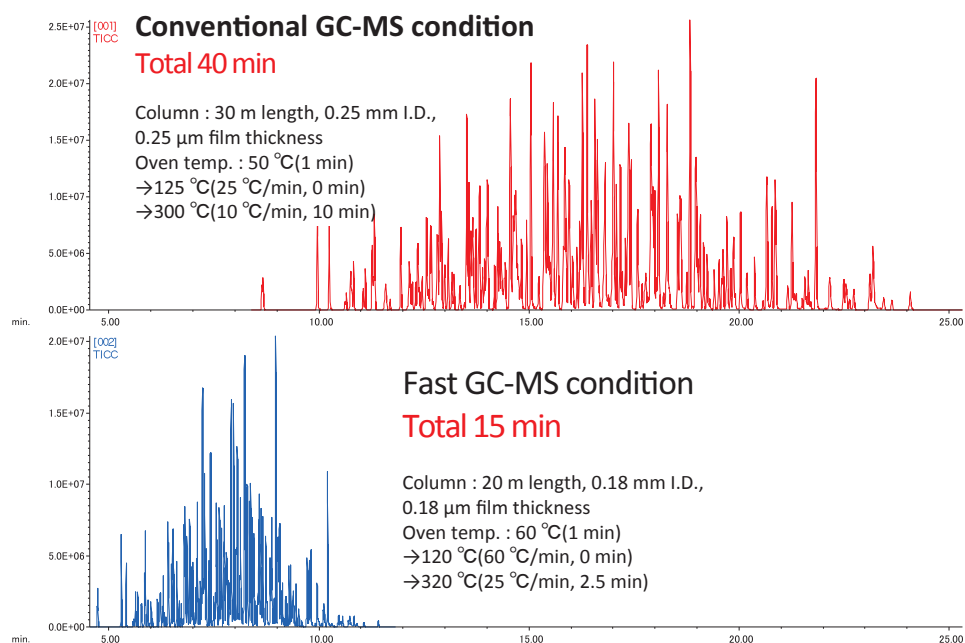
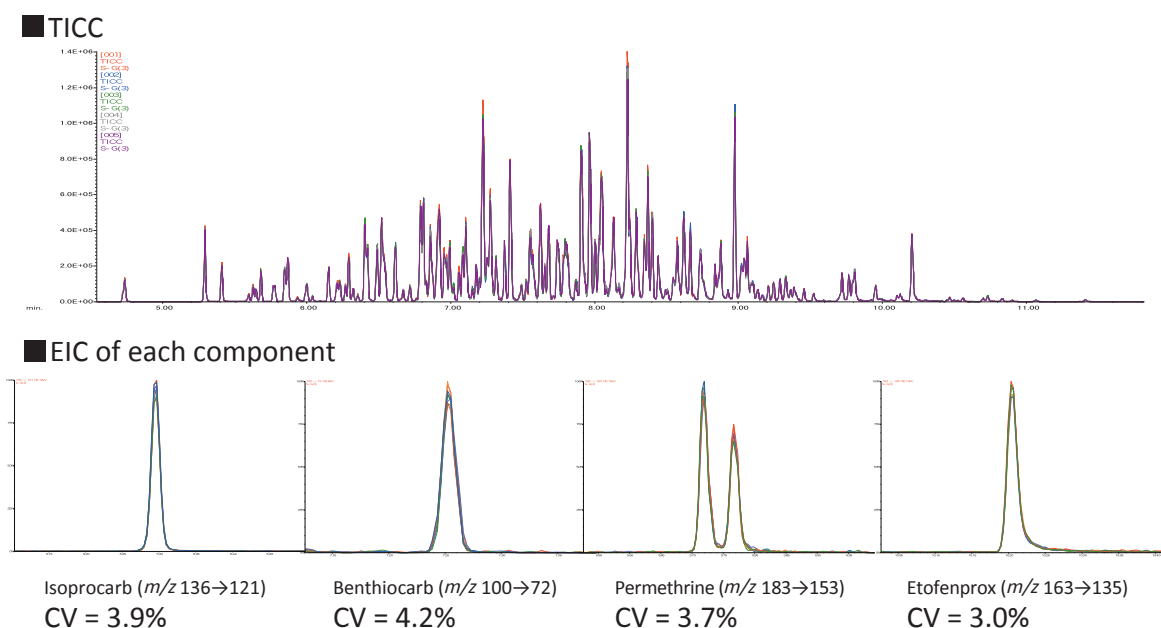


**Fig. 12 Sensitivity and reproducibility of standard samples (0.01 ppm)**



# Introduction of JEOL Products

## Benchtop Scanning Electron Microscope

### NeoScope™ JCM-7000

Optical Image to SEM observation  
with live **Elemental Analysis**

Accelerate your insight beyond an Optical Microscope



#### Contaminant analysis

- Easy to detect foreign material
- Easy to identify elemental composition

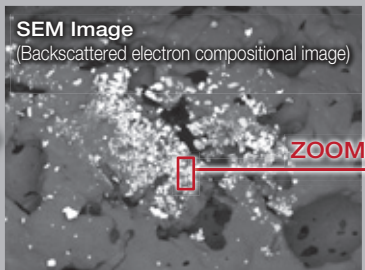
[Example] Analysis of black foreign material adhered on surface of food product

**OM image**



OM observation shows a black powder on specimen surface.

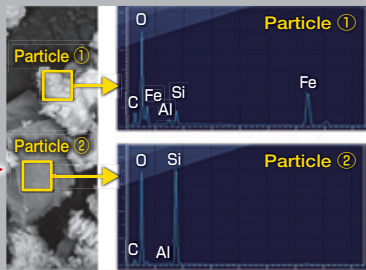
**SEM Image**  
(Backscattered electron compositional image)



**ZOOM**

SEM image from the same field of view (FOV) shows particles with different contrast indicating different compositions.

500 μm



**Particle ①**

**Particle ②**

O Fe Si Al Fe  
O Si  
C Al

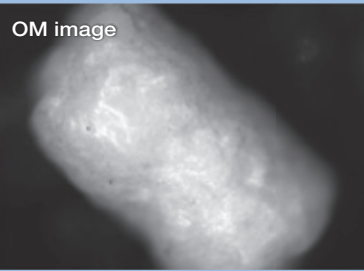
Enlarging the area of interest accesses instant live EDS analysis with main elements identified.

#### Quality control

- Observe detailed surface structures with high resolution and large depth of field not possible with OM imaging.

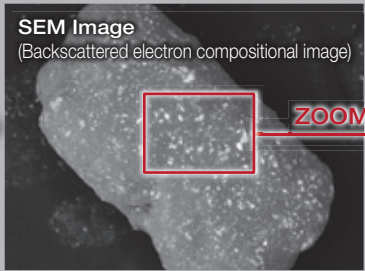
[Example] Distribution of lubricant on surface of pharmaceutical granules

**OM image**



In OM image, it is difficult to see the distribution of the lubricant on the granule surface and quality of its adhesion.

**SEM Image**  
(Backscattered electron compositional image)

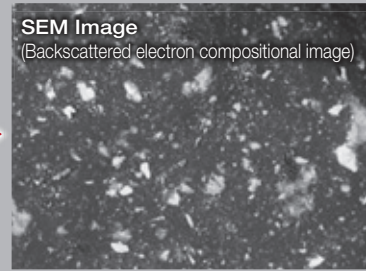


**ZOOM**

The superior depth of focus provided with SEM imaging over OM imaging along with the compositional contrast provided with the backscattered electron detector clearly shows the distribution of the lubricant on the surface of the granule.

200 μm

**SEM Image**  
(Backscattered electron compositional image)



Condition of the lubricant's adhesion can be observed with higher magnification.

# Easy-to-use SEM with seamless navigation and live analysis

## Zeromag<sup>\*1</sup>

Smooth transition from optical to SEM imaging.

Specimen: Salt

Backscattered electron topographic image

10 μm

500 μm

**Live Analysis<sup>\*2</sup>**

The main constituent elements in FOV are detected and displayed in real time with EDS.

<sup>\*1</sup> The stage navigation system (option) is required for Zeromag (optical image) image acquisition.  
<sup>\*2</sup> An EDS system (option) is required.

For other functions, please visit [https://www.jeol.co.jp/en/products/special\\_edition/2018/special02.html](https://www.jeol.co.jp/en/products/special_edition/2018/special02.html)

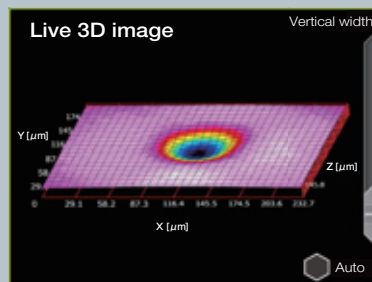
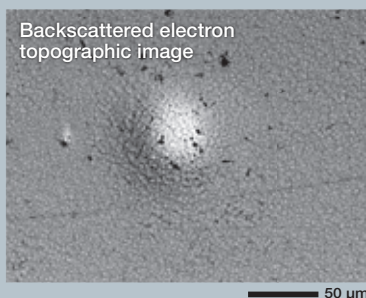


## "Live 3D" standard

JCM-7000 can display the live SEM and 3D images simultaneously. In addition to live 3D surface reconstruction, depth information can be observed as well.



【Example】 Indentation on a printed circuit board



### Optional accessories

- ◆ Tilt rotation motorized holder  
Tilt: -10° to +45°, Rotation: 360°
- ◆ Stage Navigation System
- ◆ EDS (energy dispersive X-ray spectrometer)



Breakthrough



JEOL science class support  
PR character "Rokumaru-kun"  
Copyright © 2019 JEOL Ltd.

Certain products in this brochure are controlled under the "Foreign Exchange and Foreign Trade Law" of Japan in compliance with international security export control. JEOL Ltd. must provide the Japanese Government with "End-user's Statement of Assurance" and "End-use Certificate" in order to obtain the export license needed for export from Japan. If the product to be exported is in this category, the end user will be asked to fill in these certificate forms.

**ARGENTINA**  
 COASIN S.A.C.IyF  
 Virrey del Pino 4071,  
 C1430CAM-Buenos Aires  
 Argentina  
 Tel. 54-11-4552-3185  
 Fax. 54-11-4555-3321

**AUSTRALIA & NEW ZEALAND**  
 JEOL (AUSTRALASIA) Pty.Ltd.  
 Suite 1, L2, 18 Aquatic Drive  
 - Frenchs Forest NSW 2086  
 Australia  
 Tel. 61-2-9451-3855  
 Fax. 61-2-9451-3822

**AUSTRIA**  
 JEOL (GERMANY) GmbH  
 Guts Aanger 30  
 85356 Freising, Germany  
 Tel. 49-8161-9845-0  
 Fax. 49-8161-9845-100

**BANGLADESH**  
 A.O. CHOWDHURY SCIENCE & SYNERGY PVT. LTD.  
 87, Suhrawardy Avenue, Floor 2  
 Baridhara, Dhaka1212  
 Bangladesh  
 Tel. 8802-9862272, 8953450, 8953501  
 Fax. 8802-9854428

**BELGIUM**  
 JEOL (EUROPE) B.V.  
 Planet II, Gebouw B  
 Leuvensesteenweg 542,  
 B-1930 Zaventem  
 Belgium  
 Tel. 32-2-720-0560  
 Fax. 32-2-720-6134

**BRAZIL**  
 JEOL Brasili Instrumentos Cientificos Ltda.  
 Av. Jaboaquara, 2958 5º andar conjunto 52,  
 04046-500 Sao Paulo, SP  
 Brazil  
 Tel. 55-11-5070-4000  
 Fax. 55-11-5070-4010

**CANADA**  
 JEOL CANADA, INC.  
 3275 1ere Rue, Local #8  
 St-Hubert, QC J3Y-8Y6, Canada  
 Tel. 1-450-676-9176  
 Fax. 1-450-676-6634

**CHINA**  
 JEOL (BEIJING) CO., LTD.  
 Zhongkeziyuan Building South Tower 2F,  
 Zhongguancun Nanshanjie Street No. 6,  
 Haidian District, Beijing, P.R.China  
 Tel. 86-10-6804-3321  
 Fax. 86-10-6804-6324

JEOL (BEIJING) CO., LTD., SHANGHAI BRANCH  
 Rm. 1505-1506, Benben Mansion No. 300, Xikang Road,  
 Shanghai 200040, China  
 Tel. 86-21-6248-4487 / 4868  
 Fax. 86-21-6248-4075

JEOL (BEIJING) CO., LTD., GUANGZHOU BRANCH  
 N1601, World Trade Center Building,  
 #371-375, Huan Shi Road East, Guangzhou,  
 Guangdong Prov. 510095, P.R.China  
 Tel. 86-20-8779-7846  
 Fax. 86-20-8778-4268

JEOL (BEIJING) CO., LTD., WUHAN BRANCH  
 Room A2118, Zhongshang Plaza Office Bldg.,  
 No. 7 Zhongnan Road, Wuhan,  
 Hubei, 430071, P.R.China  
 Tel. 86-27-9713-2597  
 Fax. 86-27-9713-2587

JEOL LTD. (BEIJING) CO., LTD., CHENGDU BRANCH  
 1807A Zongfu Building,  
 NO. 85 Zhongfu Road, Chengdu, Sichuan, 610016  
 P.R. China  
 Tel. 86-28-86622554  
 Fax. 86-28-86622564

**EGYPT**  
 JEOL SERVICE BUREAU  
 3rd Fl. Nile Center Bldg., Nawal Street,  
 Dokki, Cairo, Egypt  
 Tel. 20-2-3335-7220  
 Fax. 20-2-3338-4186

**FRANCE**  
 JEOL (EUROPE) SAS  
 Espace Claude Monet, 1 Allée de Giverny  
 78290, Croissy-sur-Seine, France  
 Tel. 33-13015-3737  
 Fax. 33-13015-3747

**GERMANY**  
 JEOL (GERMANY) GmbH  
 Guts Aanger 30  
 85356 Freising, Germany  
 Tel. 49-8161-9845-0  
 Fax. 49-8161-9845-100

**GREAT BRITAIN & IRELAND**  
 JEOL (U.K.) LTD.  
 JEOL House, Silver Court, Watchmead,  
 Welwyn Garden City, Herts AL7 1LT, U.K.  
 Tel. 44-1707-977117  
 Fax. 44-1707-373254

**GREECE**  
 N. ASTERIADIS S.A.  
 56-58 S. Trikoupi Str. P.O. Box 26140  
 GR-10022, Athens, Greece  
 Tel. 30-1-823-9383  
 Fax. 30-1-823-9367

**HONG KONG**  
 FARMINING LTD.  
 Unit No. 1009, 10/F, Prosperity  
 663 King's Road, North Point, Hong Kong  
 Tel. 852-2815-7299  
 Fax. 852-2581-4635

**INDIA**  
 JEOL INDIA PVT. LTD.  
 Unit No.805, 3rd Floor,  
 ABW Elegance Tower,  
 Jasola District Centre,  
 New Delhi 110 025, India  
 Tel. 91-11-4595-8000  
 Tel. 91-11-4595-8005  
 Tel. 91-11-4595-8017

JEOL INDIA PVT. LTD., Mumbai Office  
 214 E Square, Subhash Road,  
 Vile Parle (EAST),  
 Mumbai 400 057, India  
 Tel. 91-22-2612-9387

JEOL INDIA PVT. LTD., Bangalore Office  
 125, Brigade Road,  
 Unit No.402, Level 4, Palms Square,  
 Bangalore-560025, India  
 Tel. 91-80-4375-3351

JEOL INDIA PVT. LTD., Kolkata Office  
 Regus, The Legacy, 25 / A,  
 Shakespeare Sarani,  
 Kolkata - 700017, India  
 Tel. 91-98-3023-0484

JEOL INDIA PVT. LTD., Hyderabad Office  
 422, Regus Solitaire Business centre,  
 1-10-39 to 44, level 4, Gumidelli Towers, Old Airport Road,  
 Begumpet, Hyderabad - 500016, India  
 Tel. 91-40-6704-3708

**INDONESIA**  
 PT. TEKNOLABindo Penta Perkasa  
 Komplek Gading Bukit Indah Blok I/11  
 Jl. Bukit Gading Raya Kelapa Gading Permai,  
 Jakarta 14240, Indonesia  
 Tel. 62-21-45847057/58  
 Fax. 62-21-45842729

**ITALY**  
 JEOL (ITALIA) S.p.A.  
 Palazzo Paoinotti - Milano 3 City,  
 Via Ludovico il Moro, 6/A  
 20090 Basiglio(MI) Italy  
 Tel. 39-02-904143  
 Fax. 39-02-90414343

**KOREA**  
 JEOL KOREA LTD.  
 Dongwoo Bldg. 7F, 1443, Yangjae Daero,  
 Gangdong-Gu, Seoul, 05355, Korea  
 Tel. 82-2-511-5501  
 Fax. 82-2-511-2635

**KUWAIT**  
 Ashraf & CO. Ltd.  
 P.O. Box 3555 Safat 13036, Kuwait  
 Tel. 965-1805151  
 Fax. 965-24335373

**MALAYSIA**  
 JEOL (MALAYSIA) SDN.BHD.  
 508, Block A, Level 5,  
 Kelana Business Center,  
 97, Jalan SS 7/2, Kelana Jaya,  
 47301 Petaling Jaya, Selangor, Malaysia  
 Tel. 60-3-7492-7722  
 Fax. 60-3-7492-7723

**MEXICO**  
 JEOL DE MEXICO S.A. DE C.V.  
 Arkansas 11 Piso 2  
 Colonia Napoles  
 Delegacion Benito Juarez, C.P. 03810  
 Mexico D.F., Mexico  
 Tel. 52-5-55-211-4511  
 Fax. 52-5-55-211-0720

**Middle East**  
 JEOL GULF FZCO  
 P.O. Box No. 371107  
 Dubai Airport Free Trade Zone West Wing SWA No. G12,  
 Dubai, UAE  
 Tel. 971-4-609-1497  
 Fax. 971-4-609-1498

**PAKISTAN (Karachi)**  
 ANALYTICAL MEASURING SYSTEM (PVT) LTD. (AMS LTD.)  
 14-C Main Schar Commercial Avenue Lane 4,  
 Khyabran-e-Sakar,  
 D.H.A-VII, Karachi-75500, Pakistan  
 Tel. 92-21-35345581/35340747  
 Fax. 92-21-35345582

**PANAMA**  
 PROMIED S.A.  
 Parque Industrial Costa del Este  
 Urbanizacion Costa del Este  
 Apartado 0816-01755, Panama, Panama  
 Tel. 507-303-3100  
 Fax. 507-303-3115

**PHILIPPINES**  
 JATEC Philippines Corporation  
 28 Floor, The Enterprise Center Tower 2,  
 Ayala Avenue corner Pasco de Roxas,  
 Brgy. San Lorenzo, Makati City, 1226 Philippines  
 Tel. (632) 849 3904

**PORTUGAL**  
 Izsasa Portugal Lda.  
 R. do Proletariado, 1  
 2730-139 CARNAVEIXE, Portugal  
 Tel. 351-21-424-7300  
 Fax. 351-21-418-60-20

**QATAR**  
 Mannal Trading Company W.L.L.  
 ALI Emadi Complex,  
 Salwa Road P.O.Box 76, Doha, Qatar  
 Tel. +974 4455-8216  
 Fax. +974 4455-8214

**RUSSIA**  
 JEOL (RUS) LLC  
 Krasnoprolétaireskaya Street, 16,  
 Bld. 2, 127473, Moscow,  
 Russian Federation  
 Tel. 7-495-748-7791/7792  
 Fax. 7-495-748-7793

**SAUDI ARABIA**  
 ABDULREHMAN AL GOSAIBI G.T.C. (Riyadh)  
 Algosabi Building-Old Airport Road  
 P.O. Box 215, Riyadh-11411, Saudi Arabia  
 Tel. 966-1-477-7932

**SCANDINAVIA**  
 SWEDEN  
 JEOL (Nordic) AB  
 Hammarbacken 6A, Box 716, 191 27 Sollentuna  
 Sweden  
 Tel. 46-8-28-2800  
 Fax. 46-8-29-1647

**SINGAPORE**  
 JEOL ASIA PTE.LTD.  
 2 Corporation Road  
 #01-12 Corporation Place  
 Singapore 618434  
 Tel. 65-6565-9989  
 Fax. 65-6565-7552

**SOUTH AFRICA**  
 ADI Scientific (Pty) Ltd.  
 370 Angus Crescent  
 Northlands Business Park, 29 Newmarket Road  
 Northridge, Randburg, Republic of South Africa  
 Tel. 27-11-462-1363  
 Fax. 27-11-462-1466

**SPAIN**  
 IZASA Scientific SLU,  
 Argonases, 13, 28108 Alcobendas,  
 Madrid, Spain  
 Tel. 34 902 20 30 80  
 Fax. 34 902 20 30 81

**SWITZERLAND**  
 JEOL (GERMANY) GmbH  
 Guts Aanger 30  
 85356 Freising, Germany  
 Tel. 49-8165-77346  
 Fax. 49-8165-77512

**TAIWAN**  
 JIE DONG CO., LTD.  
 7F, 112, Chung Hsiao East Road,  
 Section 1, Taipei, Taiwan 10023 (R.O.C.)  
 Tel. 886-2-2385-2978  
 Fax. 886-2-2322-4655

For NMR & Mass Spectrometer Products  
 Widetron Technologies Corp.  
 No.8-2, No.77, Sec-2, Zhonghua E Rd.,  
 East Dist., Tainan City 701, Taiwan (R.O.C.)  
 Tel. 886-6-289-1943  
 Fax. 886-6-289-1743

(For Mass Spectrometer Products)  
 TechMax Technical Co. Ltd.  
 5F, No.11, Wuguang 2nd Rd., Wugu Dist.,  
 New Taipei City 248, Taiwan (R.O.C.)  
 Tel. 886-2-8990-1779  
 Fax. 886-2-8990-2559

For Semiconductor Products:  
 JEOL TAIWAN SEMICONDUCTORS LTD.  
 2F-2, No. 192, Dongguang Rd.  
 East Dist., Hsinchu City 30069,  
 Taiwan (R.O.C.)  
 Tel. 886-3-571-5656  
 Fax. 886-3-571-3151

**THAILAND**  
 BECTHAI BANGKOK EQUIPMENT & CHEMICAL CO., Ltd.  
 300 Phrayothin Rd. Phrayathai, Bangkok 10400,  
 Thailand  
 Tel. 66-2-615-2929  
 Fax. 66-2-615-2350/2351

JEOL ASEAN TECHNICAL CENTER (JATC)  
 MTEC building room 533  
 114 Moo9, Thailand Science Park  
 Phayathini Rd., Klong 1, Klong Luang,  
 Pathumthani 12120  
 THAILAND  
 Tel. 66-2-564-7738  
 Fax. 66-2-564-7738

**THE NETHERLANDS**  
 JEOL (EUROPE) B.V.  
 Lirweg 4, NL-2153 PH Nieuw-Vennep,  
 The Netherlands  
 Tel. 31-252-623500  
 Fax. 31-252-623501

**TURKEY**  
 Tekser A.S.  
 Kartal Cad. No: 55/3 Inonu Wa.,  
 Atasehir 34755, Istanbul, Turkey  
 Tel. 90-216-5798470  
 Fax. 90-216-5796475

**USA**  
 JEOL USA, INC.  
 11 Dearborn Road, Peabody, MA 01960, U.S.A.  
 Tel. 1-978-535-5900  
 Fax. 1-978-536-2203/2206

JEOL USA, INC. WEST OFFICE  
 5653 Stoneridge Drive Suite #110  
 Pleasanton, CA 94588, U.S.A.  
 Tel. 1-925-737-1740  
 Fax. 1-925-737-1749

**VENEZUELA**  
 GOMSA Service and Supply C.A.  
 Urbanizacion Montalban III  
 - Residencia Don Andres - Piso 7 - Apartamento 74  
 Avenida 3, entre calles 7 y 6  
 Montalban, Caracas, Venezuela  
 Tel. 58-212-443-4342  
 Fax. 58-212-443-4342

**VIETNAM**  
 TECHNICAL MATERIALS AND RESOURCES  
 IMPORT-EXPORT JOINT STOCK COMPANY (PEXCO)  
 Hanoi Branch  
 SALES & SERVICE  
 155-157 Lang Ha Street, Dong Da District, Hanoi, Vietnam  
 Tel. +84 (43) 862 0516  
 Fax. +84 (43) 853 2311